Palmitoyl-protein Thioesterase 1 in Developmental Plasticity and Infantile Neuronal Ceroid Lipofuscinosis

BY

KEVIN PATRICK KOSTER

B.S., University of Illinois at Chicago, 2014

THESIS

Submitted as partial fulfillment of the requirements

for the degree of Doctor of Philosophy in Neuroscience

in the Graduate College of the

University of Illinois at Chicago, 2021

Chicago, Illinois

Defense Committee:

Kuei Tseng, Chair

Akira Yoshii, Advisor

John Larson

Orly Lazarov

William Green, University of Chicago

This thesis is dedicated to my wife and best friend, Kimberly, for making me the person I am. Without her love, support, and sacrifice absolutely none of this would have been possible. I also dedicate this thesis to my son, Kub, and our future children.

AKNOWLEDGMENTS

I would like to thank my first mentor, Mary Jo LaDu, for giving me a chance to join her lab when I did not necessarily deserve one. Without that crucial moment, which I remember vividly, I cannot tell, and am rather pessimistic about, what I might have made of the following years. It is among the most important and formative periods of my life working under Dr. LaDu, and I am still internalizing the lessons I learned there to this day.

Secondly, I would like to thank Leon Tai, for patiently and closely advising me, both in the LaDu lab and in his own. Leon spent his valuable time to teach me how to work in a laboratory. We shared many early mornings drinking the strongest coffee known to humankind and for those days, I will always be grateful. His continued guidance is invaluable and something I will cherish for the rest of my career.

I would like to thank my PhD advisor and mentor, Akira Yoshii. Akira endowed me with an entirely different set of lessons for being a successful scientist. He undoubtedly pushed me, as a person and scientist, to a higher plane and for that I am sincerely grateful. Despite significant challenges in our respective personal lives, we maintained a great relationship and persevered to accomplish what we sought to. His work ethic and sheer persistence is a heroic example that I hope to emulate in my career.

I would also like to thank Kuei Tseng, often serving as my informal co-mentor and guiding not only the project, but me. He pushed me in several ways at critical junctures over the course of my PhD and has been an inspiration, for me, to what the ideal of a scientist can be. The precision in his thinking, planning, and execution is an aspiration of mine.

I would like to that my Thesis committee as well. Drs. John Larson, Orly Lazarov, and Bill Green. Their support at multiple points through my PhD shaped the project in important ways that I sincerely appreciate.

Lastly, I would like to thank the various students and personnel I had the pleasure to work with during my PhD. From my own lab, I would like to thank Roshan Srinivasan, Sami Alahmadi, Lorena Noriega, Amanda Niqula, Sarah Shaban, Ibrahim Mujahid, Lei Yu, and Hari Yagatili. We shared (Roshan and I in particular) a ton of agony, failure, and devastation, but also smiles, laughter, inside jokes, and elation that I will always remember fondly. Further, I thank Aashutosh Shetti, Terilyn Stephen, Eden Flores-Barrera, Ahmed Disouky, Zachery Morrissey, and the other students in the GPN for their impact on me, though I regrettably may not have always expressed the value I received from interacting with them. Aashu and I in particular shared many 6am discussions and venting sessions that were all but necessary for our continued persistence during the tough times of our respective projects.

This evolving community of people has very literally shaped the person I am, and I would not have changed a single thing.

KPK

CONTRIBUTION OF AUTHORS

Chapter 2 of this thesis is a reprinting of a publication including several authors in the journal *eLife*. The authors are, in order, Kevin P Koster, Walter Francesconi, Fulvia Berton, Sami Alahmadi, Roshan Srinivas, Akira Yoshii. The contributions of each author are as follows: experiments were conceived by KPK and AY. All experiments were performed or assisted by KPK. WF and FB performed electrophysiological recordings that constitute Figure 2.3 in the publication. RS and SA assisted with *in vitro* calcium imaging analysis that was represented in Figure 2.7 of the publication. KPK analyzed all data (except otherwise specified), prepared the figures, wrote the manuscript, and responded to reviewer comments with constant feedback from AY. KPK and AY edited and proofed the final manuscript.

All other experiments were performed by KPK. Exceptions are the electrophysiological recordings in Chapter 3, performed with assistance from collaborators Eden Flores Barrera and Emilce Artur de la Villarmois from the laboratory of Kuei Tseng, as well as the mass spectrometry, which was performed by Thu (Mi) T. A. Nguyen in the laboratory of Stephanie Cologna.

TABLE OF CONTENTS

LIST OF TABLES

LIST OF FIGURES

LIST OF ABBREVIATIONS

2-BP	**2-bromopalmitate**
ABE	**acyl-biotin exchange**
APEGS	**acyl-PEGyl exchange gel-shift assay**
APT1/2	**acyl-protein thioesterase 1/2**
AMPA	**α-amino-3-hydroxy-5-methyl-4 isoxazolepropionic acid**
APP	**amyloid precursor protein**
AKAP5	**A kinase anchoring protein 5**
ABHD	**α/β-hydrolase domain-containing protein**
AL	**autofluorescent lipopigment**
ALSM	**autofluorescent lysosomal storage material**
BACE1	**β-Site APP cleaving enzyme 1**
Bic	**bicuculline**
BP	**biological process**
Ca^{2+}	**calcium**
Cer	**cerulenin**
CLN1	**infantile neuronal ceroid lipofuscinosis**
CP	**calcium-permeable**
DIV	**days *in vitro***
DMSO	**dimethyl sulfoxide**
DR	**dark reared**
E	**embryonic day**
EPSP	**excitatory postsynaptic potential**
FRAP	**fluorescence recovery after photobleaching**
GFP	**green fluorescent protein**
HA	**hydroxylamine**
K^+	**potassium**
NCL	**neuronal ceroid lipofuscinosis**
NEM	**N-ethylmaleimide**
NFAT	**nuclear factor activated in T cells**
NMDA	**N-methyl-D-aspartate**
LTD	**long-term depression**
LTP	**long-term potentiation**
PSD	**postsynaptic density**
PAT	**palmitoyltransferase**
PBS	**phosphate-buffered saline**
PKA	**protein kinase A**
PKC	**protein kinase C**
PSD-95	**postsynaptic density protein 95**
PPT1	**palmityl-protein thioesterase 1 (human)**
Ppt1	**palmityl-protein thioesterase 1 (mouse)**
P	**postnatal day**
RT	**room temperature**
SAP102	**synapse associated protein 102**
TBS	**tris-buffered saline**
TMD	**transmembrane domain**
TNFα	**tumor necrosis factor α**
TTX	**tetrodotoxin**

LIST OF ABBREVIATIONS (CONTINUED)

VC	**vehicle control**
WT	**wild type**

SUMMARY

Infantile neuronal ceroid lipofuscinosis (CLN1) is a severe neurodegenerative disease that affects children. CLN1 is cause by mutations in the depalmitoylating enzyme palmitoyl-protein thioesterase 1 (PPT1). Protein palmitoylation and depalmitoylation are critical for synaptic function. However, the role of Ppt1-mediated depalmitoylation in neurodevelopmental plasticity and how loss of Ppt1 drives neurodegeneration in CLN1 is unclear. The central hypothesis was that PPT1 depalmitoylates postsynaptic proteins and that loss of PPT1 function compromises mechanisms of neurodevelopmental synaptic plasticity to drive features of CLN1. To address these questions, we studied plasticity mechanisms that underlie neural circuit development in the visual cortex of the *Ppt1*$^{-/-}$ mouse model of CLN1.

In a first set of experiments, the role of Ppt1 in the regulation of N-methyl-D-aspartate (NMDA) receptors was examined. The composition of NMDA receptors shifts during neurodevelopment coincident with the maturation of the visual cortical circuit. It was revealed that loss of Ppt1 leads to a stagnation of this developmental molecular pattern. This resulted in dysregulated synaptic calcium dynamics and left *Ppt1*$^{-/-}$ neurons vulnerable to excitotoxicity, partly due to hyperpalmitoylation of the immature NMDA receptor subunit GluN2B.

In a second line of experimentation, the role of Ppt1 in the synaptic scaling of α-amino-3-hydroxy-5-methyl-4-isoxazolepropionic acid (AMPA) receptors was examined. *Ppt1*$^{-/-}$ neurons demonstrated exaggerated synaptic upscaling of calcium-permeable AMPA receptors *in vitro* and *in vivo*. A postsynaptic scaffold implicated in synaptic scaling, A-kinase anchor protein 5 (Akap5), was over-palmitoylated in *Ppt1*$^{-/-}$ neurons. Further, this pathway linked for the first time dysregulated synaptic calcium to a neuroinflammatory cascade in CLN1.

Together, these findings emphasize a vital role for PPT1-mediated depalmitoylation in synaptic plasticity that underlies circuit formation and function in the developing nervous system.

1. INTRODUCTION

1.1. Neural homeostasis and synaptic plasticity

The human brain consists of approximately 86 billion neurons (Herculano-Houzel, 2012) that must form anatomically and functionally defined circuits to function appropriately. The activity of this organized neuronal circuitry encodes sensation, generates abstract thought, and produces motor programs that constitute behavior. Neurons within these circuits communicate at specialized cell-to-cell contact called synapses. The activity at these synapses governs how a given neuron, and by way of their connections, populations of neurons, communicate with each other. By definition, therefore, the molecular composition of synapses dictates how impinging signals are translated to neuronal activation. The brain-wide organization of the degree to which individual synapses influences the activity of given neurons is a major substrate of information encoding in the brain. This synaptic "strength," i.e., the extent to which its activation influences the potential activity of the neuron harboring it, is dynamic in the short- and long-term. This dynamicity is called synaptic plasticity.

Synaptic plasticity underlies how the brain reacts to the environment—allowing for adaptive changes in the perception and behavior of an organism to improve its survivability in the environmental niche. Synaptic plasticity dictates the developmental wiring of neuronal circuits by strengthening and maintaining necessary synaptic connections, while weakening or eliminating those that are unnecessary. It also underlies learning and memory, which are, in a reduced sense, the complex coordination of synaptic plasticity (Abraham et al., 2019; Citri and Malenka, 2008; Martin et al., 2000). This is especially important during neurodevelopment, when the brain is wiring and refining neural circuits to generate optimal behavior. It is not surprising then, that neurodevelopment represents a crucial time for the codification of neural circuits that contributes to the long-term health of the animal. Indeed, periods of intense synaptic plasticity that codify functional brain modules, such as vision or language, are considered "critical periods."

Critical periods exist for several brain functions, including those linked to sensory functions such as vision and somatosensation, as well as complex perceptual and motor functions, like language. Seminal work by Hubel and Wiesel on the visual system of cats and monkeys clearly demonstrate this point (HUBEL and WIESEL, 1964; Hubel and Wiesel, 1970; Hubel et al., 1976; LeVay et al., 1980). Monocular deprivation, which temporarily suppresses all instructive neuronal activity from one eye to the visual system, results in lifelong changes in the synaptic architecture of animal's visual cortex and, consequently, their ability to see (HUBEL and WIESEL, 1964)—but only when performed before a specific age (~3 months in cats). Performing this same manipulation after this critical period for visual cortical plasticity (later in life) has a substantially reduced effect, even when the eye is sutured for over a year (Hubel and Wiesel, 1970). Thus, beyond a threshold of neural circuit maturation that coincides with a discrete developmental period, the wiring of the system is solidified and relatively unsusceptible to large-scale reorganization. These findings and many others (comprehensively reviewed in (Hensch, 2004)) demonstrate that synaptic plasticity shapes neuronal circuitry particularly strongly during neurodevelopment and that this is crucial for sustained brain function.

1.2. Synaptic plasticity mechanisms

Several forms of synaptic plasticity have been discovered and are reasonably well-characterized, including both short-term and long-term processes (Citri and Malenka, 2008). Most attention has been paid to the long-term modes of plasticity, corresponding to changes that sustain for hours or even days. These fall into two formal categories, Hebbian plasticity and homeostatic plasticity.

1.2.1. Hebbian plasticity

Hebbian plasticity (Hebb, 2002) has received abundant attention because it has been long thought to be a basis for associative learning and at least some forms of memory (Abraham et al., 2019; Hebb, 2002). Hebbian plasticity is the process by which individual synapses

bidirectionally adjust their strength in response to stimulation patterns of corresponding intensity. Specifically, high intensity stimulation of a given synapse induces a long-term potentiation (LTP) (Bliss and Lomo, 1973), whereas as specific stimulus patterns, such as low-frequency stimulation, can induce long-term depression (LTD) (Ito et al., 1982) of the future synaptic response (Citri and Malenka, 2008). Following LTP of a given synapse, future stimulation of that same synapse produces a larger response while, in contrast, a future synaptic response is smaller following LTD. Neuroscientists have long paraphrased this phenomenon originally outlined by Donald Hebb as "neurons that fire together, wire together." Hebbian plasticity is local or even synapse specific. That is, LTP or LTD will occur at the particular synapses that link the presynaptic and postsynaptic neurons and not others on the same neuron. This can be a single synaptic connection or, if the axon of a given cell has multiple presynaptic terminals, at each of its postsynaptic partner sites. Hebbian plasticity is instantiated on the timescale of minutes following the inducing stimulus, and can persist for at least multiple hours, if not longer. Because of these properties, Hebbian plasticity is associative, i.e., the correlated activity of the pre- and postsynaptic neurons is what is captured by Hebbian mechanisms.

1.2.2. Homeostatic plasticity—synaptic scaling

In contrast, a recently characterized form of plasticity known as synaptic scaling is non-associative and widespread (Turrigiano and Nelson, 2004; Turrigiano et al., 1998). Synaptic scaling is a specific mechanism in the class of homeostatic plasticity, which refers to the fact that these forms of plasticity are often compensatory in nature, counterbalancing Hebbian plasticity mechanisms that are cumulative, additive and, therefore, subject to computationally devoid all-or-none outcomes (Turrigiano, 2017). Synaptic scaling, in contrast to Hebbian plasticity is the process by which synapses tune their responsiveness in opposite fashion to prolonged patterns of afferent activity in a neural circuit—low afferent activity induces increased postsynaptic sensitivity (potentiation), while periods of high activity decrease postsynaptic activity (depression)

(Turrigiano et al., 1998). This compensatory scaling is a global phenomenon whereby all (or most) synapses on neurons, often embedded within a population of neurons (e.g., visual cortex) that are reacting similarly, respond to a chronic activity level change. How synapses change their sensitivity in response to these changing activity patterns is a matter of the events that take place on the molecular scale.

1.3. Molecular mechanisms of synaptic plasticity

1.3.1. Postsynaptic glutamate receptors

The postsynaptic neuron receives chemical signals through binding of the excitatory neurotransmitter, glutamate, to its receptors. Upon binding, conformational changes in these receptors, 1) cause rapid movement of extracellular cations down their electrochemical gradient into the cell, depolarizing it and 2) activate downstream signaling molecules in the postsynaptic density (PSD), a region of tightly packed molecular complexes critical for receptor-mediated signal transduction. α-amino-3-hydroxy-5-methyl-4-isoxazolepropionic acid (AMPA) receptors mediate the vast majority of rapid, glutamate-mediated synaptic transmission and are the pillar of excitatory synapses. AMPARs respond to glutamate binding by opening a transmembrane pore, allowing influx of the cation, Na^+, and depolarization of the cell. As AMPARs open and close rapidly (1-2ms), they provide discrete postsynaptic depolarizing signals. In contrast, N-methyl-D-aspartate receptors (NMDARs), another ionotropic receptor, have greater affinity for glutamate than AMPARs, remain open substantially longer (50-300ms), and, critically, are permeable to calcium (Ca^{2+}).

1.3.1.1. AMPA receptors

AMPA receptors are glutamate-gated iontropic receptors composed of 4 subunits, GluA1-4, encoded by the genes *GRIA1-4*. Most functioning AMPA receptors, at least in studies of the hippocampus, are heteromers of GluA1/GluA2 or GluA2/GluA3 while a relatively small fraction of receptors are homomers of GluA1 (Lu et al., 2009; Wenthold et al., 1996).

The subunit composition of a given AMPA receptor effects its function by modulating its biophysical properties, the binding to transmembrane AMPAR regulatory proteins (TARPs) and by changing the character of posttranslational modifications that can be applied. For instance, the C-terminal tail of GluA1 and GluA4 are longer compared to GluA2 or GluA3 and can dominate the trafficking properties of long-tailed/short-tailed heteromers (discussed below).

Perhaps the best studied distinction in receptor properties is between GluA2-containing and GluA2-lacking receptors, particularly GluA1 homomers. GluA1 homomeric receptors exhibit a higher conductance, an inward rectification and, importantly, are permeable to Ca^{2+}, while GluA2/GluA1 heteromers generally are not (Burnashev et al., 1992). Therefore, GluA2-lacking AMPA receptors are referred to as calcium permeable (CP)-AMPA receptors (Diering and Huganir, 2018).

1.3.1.2. NMDA receptors

NMDA receptors are postsynaptic glutamate (and glycine/D-serine) receptors with unique features that position them well to serve as the mediators of synaptic plasticity. They are blocked by Mg^{2+} at or near the resting membrane potential of the neuron, making them impervious to ions until significant depolarization of the postsynapse is achieved. Once open, NMDA receptors pass not only sodium, but the critical neuronal second messenger, Ca^{2+}into the postsynapse with high conductance and a relatively long decay (tens to hundreds of milliseconds). In this way, NMDA receptors act as a coincidence detector for presynaptic neurotransmitter release and sufficient postsynaptic depolarization (Bourne and Nicoll, 1993). NMDAR-mediated Ca^{2+} influx activates signaling cascades critical for synaptic plasticity, reorganization of the postsynaptic structure, and via changes in the translation and transcription of proteins, learning and memory (discussed below).

NMDA receptors are tetrameric assemblies of seven potential subunits: GluN1 (*GRIN1*), the four GluN2 subunits, GluN2A-D (*GRIN2A-D*), and the two GluN3 subunits (*GRIN3A-B*)

(Hansen et al., 2018; Paoletti, 2011; Paoletti et al., 2013). However, the vast majority of NMDA receptors are composed of two glycine-binding GluN1 subunits and two glutamate-binding GluN2 subunits (A-D). Moreover, in part due to differential expression (Monyer et al., 1994), the majority of expressed receptors detected *in vivo* are either GluN1/GluN2A heterodimers, GluN1/GluN2B heterodimers, or GluN1/GluN2A/GluN2B triheteromers (Al-Hallaq et al., 2007; Chazot et al., 1994; Rauner and Köhr, 2011; Sheng et al., 1994). Due to this configuration i.e., that GluN1 subunits are obligatory while the GluN2 subunit can be one of several subtypes, the particular GluN2 subunit incorporated dictates many of the receptors' properties, including the conductance, the decay time, and the molecules that interact with the NMDA receptor at the PSD (Hansen et al., 2014; Paoletti et al., 2013). For instance, GluN1/GluN2B heteromers exhibit a lower glutamate affinity, lower open probability, but a substantially longer decay phase compared to GluN1/GluN2A receptors. The C-terminus of GluN2B also binds the key postsynaptic kinase, Ca^{2+} /calmodulin-dependent protein kinase II (CaMK2) with high affinity, whereas GluN2A does not (Barria and Malinow, 2005). Therefore, regulating the diversity of GluN2 subunits is crucial for determining the postsynaptic NMDA response and, in turn, for the features of postsynaptic plasticity that underlie circuit formation and dynamics. The role of GluN2 subunit identity in neurodevelopmental plasticity will receive special attention (**see section 1.3.4** and **Chapter 2**).

1.3.2. A brief history of NMDA receptor-dependent Hebbian plasticity

The molecular events that underlie synaptic plasticity mechanisms has been an area of intense and productive research over the past 30 years. In the first volume of the journal *Neuron*, pioneers in the field of molecular neuroscience Roger Nicoll, Julie Kauer, and Robert Malenka published a model of LTP that is to this day has been the standard (Nicoll et al., 1988). This model consolidated the findings of several seminal discoveries from multiple labs that defined with precision the molecular events that are necessary and sufficient for LTP, as follows: 1) the postsynapse is depolarized (Malinow and Miller, 1986; Wigström et al., 1986), 2) removing the

voltage-dependent blockade of N-methyl-D-aspartate (NMDA) receptors by Mg^{2+} (Mayer et al., 1984; Nowak et al., 1984), and 3) glutamate binds NMDA receptors (Collingridge et al., 1983), allowing the postsynaptic entry of calcium (Ca^{2+}) (Lynch et al., 1983). Calcium is among the most tightly regulated and critical cellular signals in neurons, activating cascaded of kinases, phosphatases, and other signaling molecules that translate the postsynaptic ion influx to long-term changes in protein number and function. Indeed, it is well established that activity of the postsynaptic kinase CaMK2 is necessary and sufficient to drive LTP in response to this calcium influx (Huganir and Nicoll, 2013). Activation of CaMK2 results in the phosphorylation of many molecules in the postsynaptic density (PSD) that drives LTP.

Shortly after LTP was characterized, Dudek and Bear identified NMDA receptor-dependent LTD in the hippocampus (Dudek and Bear, 1992). While the precise mechanisms of NMDA receptor-dependent LTD are still debated, the postsynaptic calcium level remains crucial. However, in contrast to LTP, it is thought that low levels of postsynaptic calcium, due to little depolarization of NMDA receptors during low-frequency afferent activity, favors the activation of phosphatases (Lisman, 1989), especially calcineurin (Mulkey et al., 1994). Activated calcineurin in turn dephosphorylates postsynaptic proteins, including CaMK2, resulting in LTD (Huganir and Nicoll, 2013).

In contrast to Hebbian plasticity, synaptic scaling is thought to be independent of NMDA receptor activity. Indeed, chronic blockade of synaptic activity by antagonizing NMDA receptors fails to induce scaling in multiple studies (O'Brien et al., 1998; Turrigiano et al., 1998). An alternate mechanism must therefore account for synaptic scaling induction.

The consequences of LTD or LTP induction are the increased or decreased sensitivity, respectively, of the activated synapse. This is achieved through modulation of many postsynaptic

molecules but ultimately, most changes in synaptic strength are a function of a change in the number of postsynaptic receptors.

1.3.3. NMDA receptor regulation in synaptic plasticity

A limited number of studies show that there is a delayed postsynaptic insertion of NMDA receptors in the synaptic membrane following LTP induction (Watt et al., 2004; Williams et al., 2007). Further, it has been demonstrated that during synaptic scaling, NMDA receptor-mediated currents are coregulated with those of AMPA receptors, such that upscaling increases NMDA currents and vice versa (Watt et al., 2000). These changes in NMDA receptor number may contribute to sustained changes in the strength of potentiated synapses, though little is known about this process.

Indeed, the current consensus is that NMDA receptors serve as the necessary initiation elements for forms of long-term plasticity by exerting control over other factors, like the postsynaptic Ca^{2+} levels and activation of posttranslational and transcriptional cascades. Because the triggering of most forms of postsynaptic plasticity requires NMDA receptors and their subunit composition defines their functional properties (**Section 1.3.1.2**), the regulation of which NMDA receptor subtypes dominate the synapses determines the degree, and features of, synaptic plasticity. This is especially true in the developing brain.

1.3.4. The neurodevelopmental GluN2 subunit switch NMDA receptors—a molecular mechanism for synaptic maturation

Although knowledge is limited on the regulation of NMDA receptors during classical forms of plasticity (e.g., Hebbian), there exists a much-studied pattern of NMDA receptor subunit regulation that is important for the maturation of synaptic transmission during neurodevelopmental plasticity. Originally referred to as the GluN2 subunit “switch,” it now seems clear that this process represents more of a “shift” in the early-life predominance of GluN2B-containing NMDA receptors

to those containing the GluN2A subunit during neural circuit development. This shift has been characterized in several brain regions in rodents, but especially the visual cortex (Carmignoto and Vicini, 1992; Monyer et al., 1994; Philpot et al., 2001; Quinlan et al., 1999; Sans et al., 2000; Sheng et al., 1994; Stocca and Vicini, 1998; Williams et al., 1993).

Visual cortical expression of GluN2B is high during the first few postnatal weeks of life and it therefore constitutes the majority of NMDA receptors at synapses (Monyer et al., 1994; Stocca and Vicini, 1998; Williams et al., 1993). This period corresponds to the critical period for visual cortical (ocular dominance) plasticity in mice. In the subsequent weeks (5-6 weeks of age), GluN2A expression and incorporation into NMDA receptors is evident, coincident with the decline of critical period plasticity (Chen et al., 2000; Erisir and Harris, 2003), although it is not absolutely required for closure of the critical period (Fagiolini et al., 2003).

The unique properties of these receptor subtypes make this a conceptually appealing molecular mechanism mediating the closure of the critical period by comprising a maturation of synaptic signals. Specifically, it is proposed that the slow-decaying activation and distinctive binding of CaMK2, among other factors, make GluN2B-containing NMDA receptors more promiscuous coincidence detectors necessary for developmental plasticity, whereas their replacement by GluN2A-containing receptors narrows the plasticity window (Bellone and Nicoll, 2007), which is important for circuit maturation (Yashiro and Philpot, 2008). Increasing the GluN2B/GluN2A ratio also biases synapses toward LTP and away from LTD (Lee et al., 2010b; Xu et al., 2009), which may cause associative wiring between neurons during early development that is refined later by incorporation of GluN2A (Yashiro and Philpot, 2008). This model has received corroboration from the finding that scaffold proteins undergirding the synaptic receptor architecture also show a distinct developmental shift in expression and PSD incorporation (Yoshii et al., 2003; Zundert et al., 2004). Given that this occurs during the critical period, disruptions in

the GluN2 shift may give rise to long-term, even life-long, aberrations in the neural circuits where it occurs. This is explored in more detail in **Chapter 2**.

While the details of NMDA receptor regulation are crucial for synaptic plasticity induction, the consequent changes in postsynaptic sensitivity primarily arise from the proteostasis, posttranslational modification, selective trafficking, and postsynaptic anchoring of AMPA receptors.

1.3.5. AMPA receptor regulation in synaptic plasticity

Because the AMPA receptor composition determines the biophysical properties of the receptor, changes in subunit composition contribute to synaptic plasticity mechanisms. As mentioned (**Section 1.3.1.1**), GluA1 and GluA4 are considered long-tailed AMPA receptors, while GluA2 and GluA3 have a short C-terminal tail. Early studies suggest these two subunit types may be differentially trafficked to synapses (Hayashi et al., 2000; Shi et al., 1999, 2001). GluA1-lacking receptors, such as GluA2/3 heteromers, are constitutively added to the synapse (Henley and Wilkinson, 2013; Shi et al., 2001). In comparison, GluA1-containing receptors are rapidly mobilized from the endoplasmic reticulum to the synapse in response to synaptic activity, especially induction of LTP (Shi et al., 1999, 2001). Although some controversy existed for several years regarding the requirement of the GluA1 C-terminal tail for hippocampal LTP (Granger et al., 2013), a definitive study demonstrated recently that it is indeed necessary and sufficient (Zhou et al., 2018).

Recent work has extended these findings, demonstrating a role for CP-AMPA receptors (GluA1 homomers) in synaptic plasticity mechanisms. The importance of CP-AMPA receptors in LTP is somewhat controversial, with conflicting results as to whether they are incorporated at potentiated synapses (Adesnik and Nicoll, 2007; Gray et al., 2007; Guire et al., 2008; Plant et al., 2006). However, the details of these studies reveal that CP-AMPA receptor contribution may be more easily detectable in young animals, accounting for the controversy (Diering and Huganir,

2018). Further, a recent report demonstrates that the transient incorporation of CP-AMPA receptors is important for LTD (Sanderson et al., 2016). The most consistent evidence for the involvement of CP-AMPA receptors in synaptic plasticity comes from studies of synaptic scaling (Cull-Candy and Farrant, 2021; Lee, 2012).

1.3.5.1. CP-AMPA receptor regulation in synaptic scaling

Although the role of CP-AMPA receptors have been controversial in Hebbian plasticity, a multitude of studies *in vitro* and *in vivo* demonstrate that they are directly involved in homeostatic synaptic scaling (Lee, 2012). The first clue that this was the case came from the finding that GluA1 is specifically upregulated by inactivity-induced synaptic scaling (Ju et al., 2004; Lissin et al., 1998; Thiagarajan et al., 2005). Physiological studies using the CP-AMPA receptor blockers philanthotoxin or NASPM added to these data, showing that CP-AMPA receptors are selectively incorporated into upscaled synapses (Sanderson et al., 2018; Thiagarajan et al., 2005). Furthermore, induction of synaptic upscaling *in vivo* by rearing mice in complete darkness (dark rearing), blunting afferent activity to the visual cortex, demonstrated a similar effect—CP-AMPA receptors were selectively increased at synapses in the upscaled visual cortex (Goel et al., 2006, 2011). Interestingly, the upscaling of CP-AMPA receptors requires phosphorylation of the GluA1 subunit at S845 *in vitro* and *in vivo* (discussed further below), demonstrating the importance of posttranslational modifications in the regulation of AMPA receptor trafficking in synaptic plasticity.

1.3.5.2. Control of AMPA receptors in synaptic plasticity by posttranslational modification

The differential trafficking of AMPA receptors is influenced strongly by the specific posttranslational modifications that can occur on the unique GluA C-terminal tails. Among the earliest proposed and tested mechanisms for the expression of LTP is the phosphorylation of AMPA receptor subunits (Malenka et al., 1989; Malinow et al., 1989). All subunits are phosphorylated on their cytoplasmic C-terminal tail on at least one site (Huganir and Nicoll, 2013).

Whereas GluA1 contains five recognized phosphorylation sites in this domain, GluA2 contains three, GluA3 has two, and GluA4 contains only one (Diering and Huganir, 2018). Phosphorylation at these residues affects receptor properties and trafficking in specific ways, and it is now clear that simultaneous modifications at these sites interact to determine the ultimate outcome on receptor function. These residues are phosphorylated by the postsynaptic kinases CaMK2, protein kinase A (PKA), protein kinase C (PKC), and others (Diering and Huganir, 2018; Huganir and Nicoll, 2013). Because of their ubiquity and prominent role in synaptic plasticity, most study has surrounded the effects of posttranslational modification of GluA1 and GluA2.

GluA2 contains phosphorylation sites at S863, Y876, and S880. Most study has defined the PKC site in GluA2, S880, as a crucial regulator of LTD (see **Section 1.4.1**) (Chung et al., 2000; Seidenman et al., 2003; Steinberg et al., 2006). GluA1 is phosphorylated at S818. S831, T840, S845, and S863. Of these sites, the PKA site, S845, the PKC site S818, and the PKC/CaMK2 site S831 are the best studied. Phosphorylation of S845 and S831 both play distinct roles in LTP but are not required for its induction (Lee et al., 2010a). The current understanding is that phosphorylation of S845 recruits GluA1-AMPA receptors to the perisynapse (see **section 1.4.1**) where they are primed for future synapse insertion, while S831 is more directly associated with GluA1-AMPA receptor targeting to the PSD (Diering and Huganir, 2018).

Since the discovery of synaptic scaling has occurred more recently than Hebbian forms, the underlying molecular mechanisms are not fully known. However, multiple studies confirm that phosphorylation of the GluA1 AMPA receptor subunit at S845 is necessary for inactivity-induced synaptic upscaling (Diering et al., 2014; Goel et al., 2011; Kim and Ziff, 2014). Work from independent labs demonstrates that during synaptic upscaling, the postsynaptic scaffold A-kinase anchor protein 5 (Akap5) is recruited to the PSD, thereby anchoring PKA in proximity to GluA1, which promotes phosphorylation of GluA1 at S845 and the stabilization of GluA1-containing

AMPA receptors at the synapse (Diering et al., 2014; Sanderson et al., 2018). Therefore, the coordinated activity of PKA by Akap5 is crucial for synaptic upscaling of CP-AMPA receptors.

Although each posttranslational modification is typically studied in isolation, the picture is emerging that these modifications cooperate to constitute something of a posttranslational modification receptor “code” of plasticity (Diering and Huganir, 2018). Importantly, different classes of posttranslational modifications often regulate each other, such that ubiquitination or palmitoylation (discussed below), for example, impact the propensity for additional modifications (Diering and Huganir, 2018). In some instances, distinct modification types compete directly for the same residue (Ho et al., 2011). Therefore, the impact of posttranslational modifications is achieved in large part through their effects on the selective transport, endo-, and exocytosis of AMPA receptors.

1.4. Endolysosomal trafficking of synaptic proteins

The endolysosomal system is a complex network composed of mobile, membranous vesicles (compartments) which are critical to cellular function. This system is responsible for trafficking proteins to their appropriate subcellular compartments (including the Golgi, ER, and plasma membrane) and recycling macromolecules.

In general, the endosomal compartment receives its cargo by either synthesis of new proteins, 2) autophagy, and 3) endocytosis. Once the cargo is obtained, it can be trafficked to its appropriate subcellular location, recycled to the plasma membrane, or targeted for degradation. There are, at least, five classes of membranous compartments in the endolysosomal system. 1) Early endosomes obtain the cargo by endocytosis and incorporate into 2) the multivesicular body. The multivesicular body is a sorting station for endolysosomal cargo within which proteins are modified via posttranslational modification and sorted for further transport. Cargo can then be transported from early endosomes or the multivesicular body to the plasma membrane through

3) recycling endosomes. Eventually, cargo is routed to 4) late endosomes, which fuse with 5) lysosomes. The lysosome is a highly acidic organelle that degrades proteins and represents the terminal stage of this multicompartment system. Thus, the integration of all these trafficking organelles together with protein degradation in the lysosome is called the endolysosomal system, which collectively manages the localization and amount of specific proteins, termed proteostasis.

As neurons are distinctly polar and expansive cells, the endolysosomal system must be integrated on the broad cellular and local levels. Endolysosomes serve specialized functions in synaptic communication, where the endocytosis, trafficking, and proteostasis of proteins is especially germane. At the presynaptic active zone, exocytosis, endocytosis, and recycling of neurotransmitter-containing vesicles is requisite for the rapid and continued release of neurotransmitter into the synapse. Further, at the postsynaptic site, exo- and endocytosis of transmembrane proteins, such as AMPA and NMDA receptors, is essential for synaptic plasticity, emphasizing the dynamic activity of this cellular system. This process is also highly specific—a classic study demonstrates that AMPA receptors are selectively targeted to either REs or lysosomes in accordance with the type of synaptic activity induced, which determines whether the receptor is recycled back to the synaptic surface or for degradation, respectively (Ehlers, 2000). Further, a recent detailed study shows that synaptic activity causes movement of lysosomes into the postsynapse, where they presumably regulate the proteostasis of proteins on demand (Goo et al., 2017). Thus, the precise endolysosomal trafficking of proteins that coordinates proteostasis of postsynaptic molecules is influenced by, and in turn influences, synaptic activity.

1.4.1. Synaptic receptor trafficking, proteostasis, and synaptic plasticity

A primary determinant of the postsynaptic sensitivity to afferent neurotransmitter release is the number of receptors at the postsynaptic membrane, which is regulated by their selective trafficking and membrane retention. The synaptic receptor composition is constitutively cycled,

such that the half-life of any given AMPA receptor at a typical synapse is on the order of several minutes, while keeping the total number of receptors consistent under basal conditions (Nishimune et al., 1998). Induction of synaptic plasticity drives this highly dynamic regulation to favor insertion (exocytosis) or removal (endocytosis) of AMPA receptors, thereby modifying the synaptic strength.

The dynamics of this process are influenced by posttranslational modifications. For instance, phosphorylation of GluA2 S880 is required for cerebellar LTD and important for LTD in the hippocampus. Phosphorylation at this site blocks interactions with the PSD-anchoring molecules GRIP1/2 and enhances interactions with PICK1, which promotes AMPA receptor endocytosis (Chung et al., 2000; Seidenman et al., 2003; Steinberg et al., 2006).

Among the best studied examples of how posttranslational modification of GluA subunits influences AMPA receptor trafficking is the phosphorylation of GluA1 at S845 and S831, which are both correlated with LTP. Phosphorylation of S845 limits the endocytosis of AMPA receptors and primes them for recruitment to the synapse during LTP and synaptic scaling but does not necessarily recruit them to the PSD directly (Diering et al., 2014; Ehlers, 2000; Kim and Ziff, 2014; Man et al., 2007; Oh et al., 2006). Phosphorylation at S831, on the other hand, is associated with AMPA receptors at the PSD (Diering et al., 2016), indicating a cooperative role for phosphorylation at these sites to promote AMPA receptor insertion during LTP (Diering and Huganir, 2018). These findings show that posttranslational modifications can shift the balance of AMPA receptor trafficking to reduce their removal for the synapse, which is a key event in their increase during plasticity.

One posttranslational modification that has heretofore been selectively left out of the discussion is protein palmitoylation. Protein palmitoylation is especially well-suited to influence

the dynamic trafficking of proteins through the endolysosomal system and plays an outsized role at the synapse.

1.5. Protein palmitoylation and depalmitoylation

Protein palmitoylation is the covalent linkage of the 16-carbon fatty acid, palmitate, to cysteine residues on target proteins (S-palmitoylation) via a thioester bond. Although this phenomenon has been known for several decades (Folch and Lees, 1951; Schmidt and Schlesinger, 1979; Schmidt et al., 1979), study of palmitoylation has emerged relatively recently and has proved its importance as a critical regulator of various cellular processes. This post-translational modification is a form of protein acylation, which adds a fatty acid to proteins and increases their hydrophobicity, facilitating their interaction with lipid membranes. In contrast to other modes of protein acylation (e.g., myristoylation, farnesylation), palmitoylation is generally reversible. This allows for phasic regulation and supports a wider functional repertoire for this modification. Indeed, palmitoylation enables proteins to dynamically interact with virtually all cellular membranous domains (Greaves and Chamberlain, 2007), playing critical roles in cellular signaling (Dunphy and Linder, 1998; Montersino and Thomas, 2015), protein-protein interactions (Hayashi et al., 2005; Jeyifous et al., 2016; Salaun et al., 2010), protein stability (Abrami et al., 2006; Percherancier et al., 2001; Sharma et al., 2008), and enzyme activity (Kostiuk et al., 2010).

Palmitoylation occurs preferentially on the C-termini of many transmembrane proteins, including various cellular receptor subunits (Blanc et al., 2015). In contrast, the palmitoylation of soluble proteins typically occurs at the extreme N-terminus (Collins et al., 2017), which in some cases is necessary for their phasic membrane shuttling and signaling activity (Rocks et al., 2005, 2010). Interestingly, a recent study demonstrates that many transmembrane proteins are palmitoylated on their extracellular face as well, opening further possibilities for palmitoylation-dependent regulation of protein trafficking (Gorenberg et al., 2020).

Protein palmitoylation is a reversible process. Thus, both the attachment and cleavage of palmitic acid are critical for regulating the amounts and localization of modified proteins. While the rate of palmitoylation and depalmitoylation can vary widely between protein type, regulated expression of each substrate requires a proper balance between the two processes. For example, the turnover of palmitate of the Ras family of GTPases is high, while caveolin-1 is irreversibly palmitoylated (Parat and Fox, 2001). Determining how protein depalmitoylation affects the function of individual proteins is a critical to understanding the role that protein palmitoylation plays in various contexts.

Given that S-palmitoylation is a flexible modification, its dynamics for each protein are defined by the enzymes that add and remove palmitate, the palmitoylation and depalmitoylation enzymes.

1.5.1. Palmitoylating and depalmitoylating enzymes

1.5.1.1. Palmitoyltransferases

Palmitoylation is mediated by palmitoyltransferases (PATs), enzymes encoded by the *ZDHHC* gene family that all contain a highly conserved DHHC (Asp-His-His-Cys) domain (Fukata et al., 2006; Lemonidis et al., 2015). There are 23 known zinc finger DHHC-type containing (ZDHHC) proteins. Most PATs are four-pass transmembrane proteins with the cytosolic-facing catalytic domain between transmembrane domain (TMD) 2 and 3 (Lemonidis et al., 2015; Tabaczar et al., 2017). Many PATs are residents of the endoplasmic reticulum or Golgi (Ohno et al., 2006) and, accordingly, these enzymes mediate palmitoylation-dependent trafficking of proteins between the ER, Golgi, and endolysosomal system (Rocks et al., 2010) . However, several members of the family (ZDHHC4, ZDHHC13, ZDHHC17, ZDHHC23, ZDHHC24) contain additional TMDs (while ZDHHC22 contains only 2 TMDs) or distinct functional domains (Tabaczar et al., 2017). Furthermore, a subset of PATs localizes to endosomal vesicles, the plasma membrane, and even the PSD, where they mediate local palmitoylation of target proteins (Brigidi et al., 2015; Howie et al., 2014; Noritake et al., 2009; Oku et al., 2013). This diversity indicates

that the ZDHHC enzymes, including those that mediate palmitoylation in the Golgi, have developed substrate specificity and distinct physiological roles (Lemonidis et al., 2014, 2015, 2017).

1.5.1.2. Depalmitoylases

To date, three major classes of depalmitoylating enzymes are described. All of them exist within the large and still growing superfamily of proteins known as α/β-hydrolase fold enzyme family (Hotelier et al., 2004). Namely, acyl-protein thioesterases (APTs), palmitoyl-protein thioesterases (PPTs), and select members of a larger subclass of proteins called α/β-hydrolase domain-containing 17 proteins (ABHD17s). These proteins exhibit distinct subcellular localizations, activities, and enzyme-substrate relationships. Thus, while there is likely to be some redundancy in their substrates, these protein families likely serve separate roles in their regulation of palmitoylated proteins.

The acyl-protein thioesterase (APT) family of depalmitoylating enzymes is made up of APT1 and APT2, which are expressed in virtually every organ, including the brain (Sugimoto et al., 1996; Toyoda et al., 1999). Following its isolation and cloning, APT1 was first functionally described for its role in depalmitoylating the G-protein coupled receptor (GPCR) component, $G\alpha_s$, and H-Ras (Duncan and Gilman, 1998). Other substrates of APT1 include endothelial nitric oxide synthase (eNOS) (Yeh et al., 1999), large conductance calcium- and voltage-activated potassium (BK) channels (Tian et al., 2012), the SNARE complex protein SNAP23 (Flaumenhaft et al., 2007; Sim et al., 2007), and the Fas cell surface death receptor (also known as CD95) (Berg et al., 2015). APT2 demonstrates depalmitoylase activity toward H-Ras in multiple cell lines (Pedro et al., 2017; Tomatis et al., 2010). APT2 also depalmitoylates Scribble, a critical regulator of epithelial cell polarization and tumor suppressor, the Src-family kinase Fyn (Hernandez et al., 2017; Yokoi et al., 2016), and the PAT zDHHC6 (Abrami et al., 2017).

Interestingly, the APTs are reversibly palmitoylated and this lability is important for regulating APT activity toward their substrates (Vartak et al., 2014). Specifically, it appears that APTs act in two interconvertible populations, depalmitoylating their substrates either in the Golgi or in the cytosol (especially signaling molecules) depending on whether they are palmitoylated or not, respectively.

The ABHD family of enzymes includes approximately 20 proteins which share the ABHD nomenclature but have varying functions. Of these, robust thioesterase activity has been demonstrated in the ABHD17 subclass of ABHD17A, ABHD17B, and ABHD17C. These proteins are ubiquitously expressed and demonstrate high expression in brain tissue. ABHD17s are palmitoylated proteins, and associate with the plasma membrane or endosomal membranes in the palmitoylated state (Lin and Conibear, 2015). ABHD17A-C enzymes were first identified for their depalmitoylation activity toward PSD-95 and N-Ras, as well as H-Ras, which was later corroborated in neurons (Lin and Conibear, 2015; Yokoi et al., 2016). Further, ABHD17s depalmitoylate microtubule associated protein 6 (MAP6) (Tortosa et al., 2017).

The finding that both APTs and ABHD17s are reversibly palmitoylated and, in select cases at least, can depalmitoylate PATs, indicates that the palmitoylation state of cellular substrates is regulated indirectly by the palmitoylation state of zDHHC enzymes and depalmitoylases themselves. This suggests a complex web of reciprocal interactions that governs protein palmitoylation and requires abundant additional research to decipher.

Two members of the PPT family have been identified—PPT1 and PPT2. PPT1 was identified as the first depalmitoylating enzyme by monitoring the enzymatic removal of [^{3}H]palmitate from H-Ras (Camp and Hofmann, 1993). Subsequently, both PPT1 and its homolog PPT2 were cloned and found to share nearly 30% identity (Camp et al., 1994; Soyombo and

Hofmann, 1997). Thus far, few proteins have been demonstrated experimentally to be genuine PPT1 substrates and no detailed work has been completed for PPT2.

PPT1 is primarily sorted to the lysosome through the classical mannose-6-phoshate pathway in non-neuronal cell types (see below), where it serves the role as one of approximately 60 lysosomal hydrolases (Verkruyse and Hofmann, 1996). These proteins are involved in protein degradation and PPT1 is no exception—PPT1 removes palmitic acid from modified cysteine residues prior to protein degradation. Interestingly, PPT1 may exhibit an auxiliary pH optimum near pH=7, distinguishing PPT1 from most lysosomal enzymes which act effectively within the limited, acidic pH of the lysosome (pH 4.5-5) (Camp and Hofmann, 1993; Cho and Dawson, 2000; Verkruyse and Hofmann, 1996). Further, PPT1 has been localized to all neuronal compartments, with high levels in the axon, indicating it may interact with a diverse range of substrates (Ahtiainen et al., 2003; Lehtovirta et al., 2001; Lyly et al., 2007).

PPT1 thus far has been shown to directly depalmitoylate only a few proteins. Early studies suggest that PPT1 depalmitoylates H-Ras (Camp and Hofmann, 1993; Cho and Dawson, 2000). Further, the F_1-complex of the mitochondrial ATP synthase is a bona fide PPT1 substrate and its depalmitoylation promotes proper localization of the complex (Lyly et al., 2008).

It should be noted that most studies on PATs and depalmitoylases have been performed in non-neuronal cell types and in overexpression systems, which might lead to poor approximations of their endogenous functions. Even more, due to the polarization and function specialize of neurons, it would not be surprising to find that the localization and role for some PATs is distinctive in these cells. Palmitoylation is only recently gaining recognition as a key regulator of synaptic protein function.

1.6. palmitoylation and depalmitoylation in neurons—focus on the synapse

While much progress has been made in understanding the regulation imparted by protein palmitoylation and depalmitoylation in peripheral cell types and cell lines, the neuronal proteome is abundant, diverse, and presents unique challenges for regulating palmitoylated proteins. Neurons are morphologically distinct cells with exceptionally long processes and profound functional polarization that represents a substantial challenge for integrating the endolysosomal system across the entire cell. Furthermore, synaptic transmission and plasticity rely heavily on the shuttling of proteins (e.g., presynaptic active zone mediators of vesicle fusion and postsynaptic receptors) between the cytosol, endolysosomal compartments, and plasma membrane. This functional specialization points to an outsized role for palmitoylation in the regulation of proteostasis at the synapse.

1.6.1. Palmitoylation in synaptic protein regulation

Emphasizing the role palmitoylation at the synapse, nearly half (~40%) of synaptic proteins have either an identified or predicted palmitoylation site, representing a significant enrichment compared to the whole proteome (Sanders et al., 2015). Included in the list of palmitoylated synaptic proteins are key molecules, including G-protein coupled receptors (e.g., mGluR5, $5HT_{1A}$), G-proteins (small GTPases), NCAMs, the signaling molecules Fyn kinase and NRas, GAP43, crucial synaptic scaffolds such as PSD95 and AKAP5, as well as all AMPA receptor subunits (GluA1-GluA4) and the NMDA receptor subunits GluN2A and GluN2B (Fukata and Fukata, 2010; Yokoi et al., 2016), among many others. These proteins are differentially regulated by palmitoylation depending on their functional properties (e.g., soluble signaling proteins vs. transmembrane proteins), the domain in which they are palmitoylated, the dynamics of their palmitoylation (fast vs. slow turnover), and the enzymes that act on them.

1.6.1.1. Palmitoylation in NMDA receptor regulation

The GluN2 subunits GluN2A and GluN2B were discovered to be palmitoylated by Kang and colleagues in 2008 (Kang et al., 2008). These subunits are palmitoylated at two distinct clusters in their C-terminus, the domain positioned intracellularly that has several binding partners at the PSD, including Fyn kinase and CaMK2. Specifically, palmitoylation occurs at two distinct regions, termed Cys cluster 1 and Cys cluster 2, which are located near the 4th transmembrane domain (TMD4) and in the middle of the C-terminal tail, respectively (Hayashi et al., 2009). Palmitoylation at Cys cluster 1 of both subunits suppresses the constitutive internalization of NMDA receptors by promoting their phosphorylation, thereby preventing clatherin-mediated endocytosis (see discussion in **Chapter 2**). Palmitoylation at Cys cluster 1, therefore, is important for the surface expression and the synaptic incorporation of NMDA receptors that they comprise (Hayashi et al., 2009; Mattison et al., 2012).

On the other hand, Cys cluster 2 palmitoylation and depalmitoylation regulates the trafficking of GluN2-NMDA receptors from the Golgi. Specifically, Hayashi *et al*., show that palmitoylation-deficient Cys cluster 2 GluN2 subunits are trafficked to the cellular surface and, in contrast, that overexpression of the Golgi-localized palmitoylation enzyme zDHHC3 results in the accumulation of GluN2 subunits in the Golgi. Therefore, depalmitoylation of GluN2 subunits in the Golgi might trigger surface delivery of GluN2-NMDA receptors (Hayashi et al., 2009). However, a functional study shows that this cell surface delivery might be restricted to perisynaptic sites (Mattison et al., 2012). These findings demonstrate clearly that GluN2 subunit palmitoylation regulates both the constitutive and activity-dependent trafficking of NMDA receptors.

1.6.1.2. Palmitoylation in AMPA receptor regulation

As compared to the GluN2 subunits, all GluA subunits are palmitoylated at two distinct sites on their intracellular face The first palmitoylated cysteine exists in the position just C-terminal to the second transmembrane domain (TMD2). Intriguingly, TMD2 forms the ion channel in the

assembled receptor and the conserved cysteine is only three amino acids from the Q/R editing site (residue 607 in GluA2). The second palmitoylation site is in the juxtamembrane domain just in the C-terminal tail just past TMD4.

Palmitoylation of GluA subunits at the TMD2 site, like GluN2 subunits, promotes their retention in the Golgi apparatus and thereby limits their trafficking to the surface. Indeed, overexpression of zDHHC3 leads to Golgi accumulation of GluA subunits (Hayashi et al., 2005). In contrast, palmitoylation at the TMD4 cysteine does not affect the steady-state surface expression of the GluA1 subunits. However, the TMD4 site is important for the activity-dependent trafficking of GluAs, as acute stimulation of TMD4 palmitoylation-deficient mutant GluAs blocks their internalization upon acute stimulation with AMPA or NDMA. This is due, in part, to the finding that TMD4 palmitoylation suppresses GluA association with the cytoskeletal protein 4.1N, which stabilizes AMPA receptors at the synaptic surface. Indeed, a more recent study using a TMD4 palmitoylation-deficient GluA1 (C811S) knock-in mouse extends these initial findings. GluA1 C811S hippocampal neurons show an exaggerated response to chemical LTP and are susceptible to seizure (via kindling paradigm). Together, these studies suggest that palmitoylation at this site negatively regulates the surface trafficking of GluA1 to dampen synaptic strength (Itoh et al., 2018). On the other hand, inducing receptor internalization acutely by glutamate treatment of neurons *in vitro* accelerates depalmitoylation of GluAs, indicating that the dynamics of palmitoylation (short-term vs. long-term) are crucial to the overall effect on surface receptor levels (Hayashi et al., 2005).

In addition to these intracellular sites, GluA1 contains a recently discovered palmitoylation site on its extracellular face that forms an intersubunit disulfide bond in the mature receptor (Gorenberg et al., 2020). However, the function of this site has not yet been studied systematically.

In sum, protein palmitoylation/depalmitoylation must be balanced to maintain homeostatic function of synaptic proteins and regulate plasticity. It follows that disruption of the genes involved in protein palmitoylation lead to neurological disorders.

1.6.2. Neurological diseases of disrupted palmitoylation and depalmitoylation

Several disorders are associated with mutations in the genes encoding palmitoylation enzymes. Mutations in the genes encoding *ZDHHC9* or *ZDHHC15* alone lead to intellectual disability (Mansouri et al., 2005; Raymond et al., 2007) and the phenotypic abnormalities observed in human patients were recapitulated in a mouse model of disease (Kouskou et al., 2018). The best-studied example to date involves *ZDHHC8*. Chromosomal microdeletion of the 22q11 locus or polymorphisms in the locus resident *ZDHHC8* incur risk to schizophrenia (Liu et al., 2002; Mukai et al., 2004). This deletion is among the most penetrant genetic risk factors for schizophrenia and zDHHC8 is likely a mechanistic driver of this increased disease risk (Mukai et al., 2004, 2015). As this pathway is critical for normal neurodevelopment (Ho et al., 2011; Mukai et al., 2008; Yoshii and Constantine-Paton, 2014), its disruption at any step may lead to the neuronal defects described in schizophrenia patients and increase risk to this and other psychiatric disorders (Nieto et al., 2013).

In addition to genetic mutations in PATs themselves, neurological disease processes are associated with disrupted palmitoylation of proteins. For instance, targeted mutation of cysteine 6, a palmitoylated residue on superoxide dismutase 1 (SOD1), reduces its activity similar to mutations in SOD1 associated with familial amyotrophic lateral sclerosis (ALS) (Antinone et al., 2013). In humans, mutation of this palmitoylation site results in rapidly progressing ALS, emphasizing the role for SOD1 palmitoylation in its proper function (Morita et al., 1996). Other examples include mutations disrupting putative palmitoylated cysteine residues of the Niemann-Pick C1 (*NPC1* gene) (Sanders et al., 2015) and the *LGI1* gene associated with autosomal dominant temporal lobe epilepsy (Gu et al., 2002).

Notably, the palmitoylation of amyloid precursor protein (APP) and β-Site APP cleaving enzyme 1 (BACE1) are implicated in Alzheimer's disease pathophysiology (Andrew et al., 2017; Bhattacharyya et al., 2013); however, also see (Vetrivel et al., 2009). Palmitoylation of APP increases the production of amyloid-β (Bhattacharyya et al., 2013), and a recent study shows that expression of palmitoylation-deficient BACE1 suppresses amyloid-β accumulation and improves memory performance in a severe Alzheimer's disease mouse model (Andrew et al., 2017). Disruptions in protein palmitoylation also appear to contribute to Huntington disease (HD) pathophysiology, as disease-causing expansions in the *HTT* gene fundamentally alter the proteins association with huntingtin interacting protein 14 (HIP14, zDHHC17) and HIP14-like (zDHHC13), which are both PATs. This leads to HTT hypopalmitoylation and severe alterations in its trafficking and function (Sutton et al., 2013; Yanai et al., 2006). Indeed, mutations in either HIP14 or HIP14-like recapitulate features of HD in mouse models of disease (Milnerwood et al., 2013; Sutton et al., 2013). Taken together, disruptions in protein palmitoylation, at various levels, are sufficient to cause severe neurological diseases, pointing to the critical function served by protein palmitoylation.

To date, no mutations in the depalmitoylases, apart from PPT1 (discussed below), are known to cause neurological disease. However, the APTs have been implicated in the pathogenesis of several cancers because they regulate Ras (Berchuck et al., 2005; Dekker et al., 2010; Hänel et al., 2018; Hernandez et al., 2017; Mohammed et al., 2018; Sadeghi et al., 2018; Stypulkowski et al., 2018).

The most severe disease cause by mutation of any palmitoylating or depalmitoylating enzyme arises from mutations in the gene encoding PPT1, *CLN1*. This is the topic of the next sections and the foundation for my thesis work.

1.7. Neuronal ceroid lipofuscinoses

PPT1 is the first depalmitoylating enzyme linked to a human genetic disorder (Vesa et al., 1995). Mutations in PPT1 cause a devastating pediatric neurodegenerative disease that is one in a larger class, called neuronal ceroid lipofuscinoses (NCLs)

The NCLs are a class of individually rare, primarily autosomal recessive, neurodegenerative diseases occurring in an estimated 2 to 4 of 100,000 live births in the US (NINDS; https://rarediseases.info.nih.gov/diseases/10739/neuronal-ceroid-lipofuscinosis). Collectively, NCLs represent the most prevalent class of hereditary pediatric neurodegenerative disease. NCLs are characterized by their histopathological hallmark, the lysosomal accumulation of proteolipid storage material called lipofuscin in all tissues, but particularly neurons. These inclusion bodies correspond to granular osmiophilic deposits (GRODs), also lysosomal accumulations, observed using electron microscopy (Nita et al., 2016). Therefore, NCLs are also classified as lysosomal storage disorders (LSDs).

Symptomatically, the NCLs are characterized by progressive, global neurodegeneration, visual failure (blindness), cognitive and motor deterioration, seizures, and premature death (Pagon et al., 2013). To date, mutations in 14 unique genes, *CLN1-14*, have been identified as the causes of NCL (Nita et al., 2016). The age of onset for NCLs exists on a continuum, depending on the affected gene and severity of mutation. For this reason, NCLs are colloquially classified into four major subtypes: 1) infantile, 2) late infantile, 3) juvenile, and 4) adult-onset; although, this conventional nomenclature has become somewhat obsolete, since mutations in distinct NCL genes can manifest the disease at overlapping ages (e.g., juvenile).

1.8. Infantile neuronal ceroid lipofuscinosis

Mutations in the *CLN1* gene, which encodes PPT1, cause the infantile form of NCL Infantile NCL, or CLN1, is a particularly devastating neurodegenerative disease with an onset

between 6-24 months. Following a seemingly typical period of initial growth and development, afflicted children present with regression of milestones, microcephaly, blindness, myoclonic jerks, motor disability, and epilepsy, progressing to death of the patient by five years (Nita et al., 2016). As with all NCLs, CLN1 is defined by the accumulation of lipofuscin, also called autofluorescent lipopigment (AL) or autofluorescent lysosomal storage material (ALSM), within the lysosomes of neurons. However, it is currently unclear whether the storage material is neurotoxic, benign, or an adaptive neuroprotective mechanism.

Mutations that underlie CLN1 cause either abolition of PPT1 enzymatic activity or loss of PPT1 protein expression. The severity of CLN1 phenotype is related to how robustly the specific mutation affects PPT1 enzyme activity. For example, while mutations causing classical infantile onset of disease generally show undetectable levels of enzyme activity in cell-based assays, mutations that cause later-onset CLN1 demonstrate residual enzyme activity, indicating a gene-dose effect on maintaining neuronal function (Das et al., 2001).

Disappointingly, there are no disease-modifying therapies for CLN1, so current treatment regiments are palliative (e.g. anticonvulsant medications) (Geraets et al., 2016). Approaches to treating CLN1 include substrate reduction therapies, enzyme-replacement therapy, gene therapy, pharmacological intervention focused on mimicking PPT1 activity. Substrate reduction therapy trials have been performed with limited success (Gavin et al., 2013; Levin et al., 2014). In preclinical models, PPT1 mimetic treatment partially reverses disease phenotype and extends the lifespan of PPT1-null animals (Bagh et al., 2017; Sarkar et al., 2013). Enzyme-replacement therapies using recombinant PPT1 and adeno-associated viral-delivery of PPT1 have also showed promise in mouse models of disease (Griffey et al., 2004; Hu et al., 2012; Roberts et al., 2012), with simultaneous intrathecal and intracranial administration conferring the greatest benefits (Shyng et al., 2017). Further, the FDA recently approved an adeno-associated virus-based gene therapy for CLN1, ABO-202, as an orphan drug, accelerating its testing in human

patients. These therapeutic strategies are discussed in more detail in **Chapter 4**. Due to the early onset and rapid degeneration in CLN1 patients, however, diagnosis is often not made until pathology is significant, while therapeutic efficacy is greatest with early treatment administration. This may represent a significant challenge to implementing a disease-modifying therapies. Another major limitation in designing and executing therapies for CLN1 is the lack of mechanistic insight of disease progression. Furthering this understanding starts with elucidating the primary functions of PPT1, which remain obscure.

In 2001, the *Ppt1*$^{-/-}$ model of CLN1 was generated, which largely recapitulates the human disease phenotype (Gupta et al., 2001). These animals present with myoclonic jerks beginning as early as 3 months of age, and generalized tonic-clonic seizures are observed upon handling them. In older animals, changes in gait and posture become obvious. When assessed for visual function using the visual cliff assay, an evaluation of proper depth perception, *Ppt1*$^{-/-}$ animals routinely fail. Importantly, by 7mo mortality of *Ppt1*$^{-/-}$ mice is 50%, and few animals live beyond 10 months. Histologically, *Ppt1*$^{-/-}$ mice demonstrate characteristic accumulation of lipofuscin, with widespread, robust AL is readily visible at 6 months of age. Further, these inclusions mimic the morphology/ultrastructure commonly observed in human CLN1 patients, indicating similar deposit material. Lastly, neuronal apoptosis in several brain regions is apparent by 6 months. Since, a body of work has described the accumulation of storage material, gliosis, neuronal apoptosis, and behavioral disruptions in similar disease models (Bouchelion et al., 2014; Miller et al., 2015).

A consistent finding in CLN1 mouse models is the early and robust appearance of gliosis, a signature of neuroinflammation, in brain regions that subsequently undergo neuron death. Kielar and colleagues (2007) performed a detailed analysis of gliosis in the forebrain of *Ppt1*$^{-/-}$ mice. Astrocytosis is robust in the thalamus by 3 months and is significant in the cortex by at the same time, while microgliosis is apparent by 5 months in the cortex (Kielar et al., 2007). In the cerebellum, astrocytosis appears as early as one month and is pronounced by 3 months, whereas

microglial activation is not detectable until 5 months—results similar to those in the forebrain. Interestingly, a recent *in vitro* study showed that *Ppt1*$^{-/-}$ astrocytes and microglia are activated under basal conditions and their function is compromised compared to those from wild-type (WT), indicating some substrates of Ppt1 may have a role in maintaining glial health (Lange et al., 2018).

Building on these findings, contemporary work has focused on the specific roles that PPT1 plays in the depalmitoylation of its substrates in neurons. Several groups have documented reduced presynaptic vesicle recycling in CLN1 models, resulting in reduced vesicle pool size and functional deficits in synaptic transmission (Kim et al., 2008; Virmani et al., 2005). Complementing these findings, PPT1-null *Drosophila* demonstrate disrupted endosomal trafficking and presynaptic function (Aby et al., 2013). Thus, a converging data indicate a prominent role for PPT1 at the presynapse that is disrupted in CLN1. It is plausible that dysregulated vesicle recycling and the consequent decrease in evoked synaptic transmission may lead to an axonal "dying back" pathology that contribute to other neurodegenerative disorders (Brady and Morfini, 2010; Kanaan et al., 2013). However, presynaptic deficits in vesicle pool size were observed in 6-month-old CLN1 mice, and not before (Kim et al., 2008). Beginning at 2 months, substantial ALSM accumulation, gliosis, neuronal apoptosis, cortical thinning, and behavioral dysfunction are already observed (Dearborn et al., 2015; Gupta et al., 2001; Hu et al., 2012; Sarkar et al., 2013; Shyng et al., 2017; Zhang et al., 2006). This indicates that while presynaptic dysfunction is a feature of CLN1, more work is required to identify proximal and distal causes of pathogenesis. Indeed, comparatively little function has been paid to the effects of PPT1 in postsynaptic function, which is arguably the major site of synaptic plasticity events.

1.9. Conclusion of introduction—Ppt1 function in postsynaptic plasticity

My thesis work has centered on the role of Ppt1 in postsynaptic plasticity, with a focus on two major themes: 1) NMDA receptor plasticity and 2) AMPA receptor plasticity. I studied each of

these with respect to the broader context of their roles in developmental plasticity, which I hypothesize is the central locus of molecular events that drive the progression of CLN1.

In **Chapter 2** of this thesis, I studied the role of Ppt1 in the regulation of a brain region-wide developmental event that is implicated in the closure of the visual critical period—the GluN2 subunit switch of NMDA receptors. In Chapter 3, I examined how Ppt1 regulates AMPA receptors during synaptic scaling, which is necessary to counterbalance Hebbian plasticity during development to appropriately wire neuronal circuitry. In the conclusion of this thesis (**Chapter 4**), I consider how disturbance in both molecular processes might contribute to irreversibly disrupt developmental neuronal plasticity and cause disease symptoms in CLN1 patients.

CHAPTER 1 CITED LITERATURE

Abraham, W.C., Jones, O.D., and Glanzman, D.L. (2019). Is plasticity of synapses the mechanism of long-term memory storage? Npj Sci Learn *4*, 9.

Abrami, L., Leppla, S.H., and Goot, F.G. van der (2006). Receptor palmitoylation and ubiquitination regulate anthrax toxin endocytosis. The Journal of Cell Biology *172*, 309–320.

Abrami, L., Dallavilla, T., Sandoz, P.A., Demir, M., Kunz, B., Savoglidis, G., Hatzimanikatis, V., and Goot, F.G. van der (2017). Identification and dynamics of the human ZDHHC16-ZDHHC6 palmitoylation cascade. ELife *6*.

Adesnik, H., and Nicoll, R.A. (2007). Conservation of Glutamate Receptor 2-Containing AMPA Receptors during Long-Term Potentiation. J Neurosci *27*, 4598–4602.

Ahtiainen, L., Diggelen, O.P., Jalanko, A., and Kopra, O. (2003). Palmitoyl protein thioesterase 1 is targeted to the axons in neurons. Journal of Comparative Neurology *455*.

Al-Hallaq, R.A., Conrads, T.P., Veenstra, T.D., and Wenthold, R.J. (2007). NMDA Di-Heteromeric Receptor Populations and Associated Proteins in Rat Hippocampus. J Neurosci *27*, 8334–8343.

Andrew, R.J., Fernandez, C.G., Stanley, M., Jiang, H., Nguyen, P., Rice, R.C., Buggia-Prévot, V., Rossi, P.D., Vetrivel, K.S., Lamb, R., et al. (2017). Lack of BACE1 S-palmitoylation reduces amyloid burden and mitigates memory deficits in transgenic mouse models of Alzheimer's disease. Proceedings of the National Academy of Sciences of the United States of America *114*, E9665–E9674.

Antinone, S.E., Ghadge, G.D., Lam, T.T., Wang, L., Roos, R.P., and Green, W.N. (2013). Palmitoylation of superoxide dismutase 1 (SOD1) is increased for familial amyotrophic lateral sclerosis-linked SOD1 mutants. The Journal of Biological Chemistry *288*, 21606–21617.

Bagh, M.B., Peng, S., Chandra, G., Zhang, Z., Singh, S.P., Pattabiraman, N., Liu, A., and Mukherjee, A.B. (2017). Misrouting of v-ATPase subunit V0a1 dysregulates lysosomal acidification in a neurodegenerative lysosomal storage disease model. Nature Communications *8*, 14612.

Barria, A., and Malinow, R. (2005). NMDA Receptor Subunit Composition Controls Synaptic Plasticity by Regulating Binding to CaMKII. Neuron *48*, 289–301.

Bellone, C., and Nicoll, R.A. (2007). Rapid Bidirectional Switching of Synaptic NMDA Receptors. Neuron *55*, 779–785.

Berchuck, A., Iversen, E.S., Lancaster, J.M., Pittman, J., Luo, J., Lee, P., Murphy, S., Dressman, H.K., Febbo, P.G., West, M., et al. (2005). Patterns of gene expression that characterize long-term survival in advanced stage serous ovarian cancers. Clinical Cancer Research : An Official Journal of the American Association for Cancer Research *11*, 3686–3696.

Berg, V., Rusch, M., Vartak, N., Jüngst, C., Schauss, A., Waldmann, H., Hedberg, C., Pallasch, C.P., Bastiaens, P.I., Hallek, M., et al. (2015). miRs-138 and -424 control palmitoylation-dependent CD95-mediated cell death by targeting acyl protein thioesterases 1 and 2 in CLL. Blood *125*, 2948–2957.

Bhattacharyya, R., Barren, C., and Kovacs, D.M. (2013). Palmitoylation of amyloid precursor protein regulates amyloidogenic processing in lipid rafts. The Journal of Neuroscience : The Official Journal of the Society for Neuroscience *33*, 11169–11183.

Blanc, M., David, F., Abrami, L., Migliozzi, D., Armand, F., Bürgi, J., and Goot, F.G.G. van der (2015). SwissPalm: Protein Palmitoylation database. F1000Research *4*, 261.

Bliss, T.V., and Lomo, T. (1973). Long-lasting potentiation of synaptic transmission in the dentate area of the anaesthetized rabbit following stimulation of the perforant path. J Physiology *232*, 331–356.

Bouchelion, A., Zhang, Z., Li, Y., Qian, H., and Mukherjee, A.B. (2014). Mice homozygous for c.451C>T mutation in Cln1 gene recapitulate INCL phenotype. Annals of Clinical and Translational Neurology *1*, 1006–1023.

Bourne, H.R., and Nicoll, R. (1993). Molecular machines integrate coincident synaptic signals. Cell *72*, 65–75.

Brigidi, G.S., Santyr, B., Shimell, J., Jovellar, B., and Bamji, S.X. (2015). Activity-regulated trafficking of the palmitoyl-acyl transferase DHHC5. Nat Commun *6*, 8200.

Burnashev, N., Monyer, H., Seeburg, P.H., and Sakmann, B. (1992). Divalent ion permeability of AMPA receptor channels is dominated by the edited form of a single subunit. Neuron *8*, 189–198.

Camp, L., and Hofmann, S. (1993). Purification and properties of a palmitoyl-protein thioesterase that cleaves palmitate from H-Ras. The Journal of Biological Chemistry *268*.

Camp, L., Verkruyse, L., Afendis, S., Slaughter, C., and Hofmann, S. (1994). Molecular cloning and expression of palmitoyl-protein thioesterase. The Journal of Biological Chemistry *269*.

Carmignoto, G., and Vicini, S. (1992). Activity-dependent decrease in NMDA receptor responses during development of the visual cortex. Science (New York, N.Y.) *258*.

Chazot, P.L., Coleman, S.K., Cik, M., and Stephenson, F.A. (1994). Molecular characterization of N-methyl-D-aspartate receptors expressed in mammalian cells yields evidence for the coexistence of three subunit types within a discrete receptor molecule. J Biol Chem *269*, 24403–24409.

Chen, L., Cooper, N.G.F., and Mower, G.D. (2000). Developmental changes in the expression of NMDA receptor subunits (NR1, NR2A, NR2B) in the cat visual cortex and the effects of dark rearing. Mol Brain Res *78*, 196–200.

Cho, S., and Dawson, G. (2000). Palmitoyl protein thioesterase 1 protects against apoptosis mediated by Ras-Akt-caspase pathway in neuroblastoma cells. Journal of Neurochemistry *74*, 1478–1488.

Chung, H.J., Xia, J., Scannevin, R.H., Zhang, X., and Huganir, R.L. (2000). Phosphorylation of the AMPA Receptor Subunit GluR2 Differentially Regulates Its Interaction with PDZ Domain-Containing Proteins. J Neurosci *20*, 7258–7267.

Citri, A., and Malenka, R.C. (2008). Synaptic Plasticity: Multiple Forms, Functions, and Mechanisms. Neuropsychopharmacol *33*, 18–41.

Collingridge, G.L., Kehl, S.J., and McLennan, H. (1983). Excitatory amino acids in synaptic transmission in the Schaffer collateral-commissural pathway of the rat hippocampus. J Physiology *334*, 33–46.

Collins, M.O., Woodley, K.T., and Choudhary, J.S. (2017). Global, site-specific analysis of neuronal protein S-acylation. Scientific Reports *7*, 4683.

Cull-Candy, S.G., and Farrant, M. (2021). Ca2+-permeable AMPA receptors and their auxiliary subunits in synaptic plasticity and disease. J Physiology *599*, 2655–2671.

Das, A.K., Lu, J.Y., and Hofmann, S.L. (2001). Biochemical analysis of mutations in palmitoyl-protein thioesterase causing infantile and late-onset forms of neuronal ceroid lipofuscinosis. Human Molecular Genetics *10*, 1431–1439.

Dekker, F.J., Rocks, O., Vartak, N., Menninger, S., Hedberg, C., Balamurugan, R., Wetzel, S., Renner, S., Gerauer, M., Schölermann, B., et al. (2010). Small-molecule inhibition of APT1 affects Ras localization and signaling. Nature Chemical Biology *6*, 449–456.

Diering, G.H., and Huganir, R.L. (2018). The AMPA Receptor Code of Synaptic Plasticity. Neuron *100*, 314–329.

Diering, G.H., Gustina, A.S., and Huganir, R.L. (2014). PKA-GluA1 coupling via AKAP5 controls AMPA receptor phosphorylation and cell-surface targeting during bidirectional homeostatic plasticity. Neuron *84*, 790–805.

Diering, G.H., Heo, S., Hussain, N.K., Liu, B., and Huganir, R.L. (2016). Extensive phosphorylation of AMPA receptors in neurons. Proc National Acad Sci *113*, E4920–E4927.

Dudek, S.M., and Bear, M.F. (1992). Homosynaptic long-term depression in area CA1 of hippocampus and effects of N-methyl-D-aspartate receptor blockade. Proc National Acad Sci *89*, 4363–4367.

Duncan, J.A., and Gilman, A.G. (1998). A cytoplasmic acyl-protein thioesterase that removes palmitate from G protein alpha subunits and p21(RAS). The Journal of Biological Chemistry *273*, 15830–15837.

Dunphy, J.T., and Linder, M.E. (1998). Signalling functions of protein palmitoylation. Biochimica et Biophysica Acta *1436*, 245–261.

Ehlers, M. (2000). Reinsertion or degradation of AMPA receptors determined by activity-dependent endocytic sorting. Neuron *28*.

Erisir, A., and Harris, J.L. (2003). Decline of the Critical Period of Visual Plasticity Is Concurrent with the Reduction of NR2B Subunit of the Synaptic NMDA Receptor in Layer 4. J Neurosci *23*, 5208–5218.

Fagiolini, M., Katagiri, H., Miyamoto, H., Mori, H., Grant, S.G.N., Mishina, M., and Hensch, T.K. (2003). Separable features of visual cortical plasticity revealed by N-methyl-d-aspartate receptor 2A signaling. Proc National Acad Sci *100*, 2854–2859.

Flaumenhaft, R., Rozenvayn, N., Feng, D., and Dvorak, A.M. (2007). SNAP-23 and syntaxin-2 localize to the extracellular surface of the platelet plasma membrane. Blood *110*, 1492–1501.

FOLCH, J., and LEES, M. (1951). Proteolipides, a new type of tissue lipoproteins; their isolation from brain. The Journal of Biological Chemistry *191*, 807–817.

Fukata, Y., and Fukata, M. (2010). Protein palmitoylation in neuronal development and synaptic plasticity. Nature Reviews Neuroscience *11*.

Fukata, Y., Iwanaga, T., and Fukata, M. (2006). Systematic screening for palmitoyl transferase activity of the DHHC protein family in mammalian cells. Methods *40*.

Gavin, M., Wen, G.Y., Messing, J., Adelman, S., Logush, A., Jenkins, E.C., Brown, W.T., and Velinov, M. (2013). Substrate Reduction Therapy in Four Patients with Milder CLN1 Mutations and Juvenile-Onset Batten Disease Using Cysteamine Bitartrate. JIMD Reports *11*, 87–92.

Geraets, R.D., Koh, S. y, Hastings, M.L., Kielian, T., Pearce, D.A., and Weimer, J.M. (2016). Moving towards effective therapeutic strategies for Neuronal Ceroid Lipofuscinosis. Orphanet Journal of Rare Diseases *11*, 40.

Goel, A., Jiang, B., Xu, L.W., Song, L., Kirkwood, A., and Lee, H.-K. (2006). Cross-modal regulation of synaptic AMPA receptors in primary sensory cortices by visual experience. Nat Neurosci *9*, 1001–1003.

Goel, A., Xu, L.W., Snyder, K.P., Song, L., Goenaga-Vazquez, Y., Megill, A., Takamiya, K., Huganir, R.L., and Lee, H.-K. (2011). Phosphorylation of AMPA receptors is required for sensory deprivation-induced homeostatic synaptic plasticity. Plos One *6*, e18264.

Goo, M.S., Sancho, L., Slepak, N., Boassa, D., Deerinck, T.J., Ellisman, M.H., Bloodgood, B.L., and Patrick, G.N. (2017). Activity-dependent trafficking of lysosomes in dendrites and dendritic spines. J Cell Biol *216*.

Gorenberg, E.L., Zhao, H.R., Bishai, J., Chou, V., Wirak, G.S., Lam, T.T., and Chandra, S.S. (2020). Identification of palmitoyl protein thioesterase 1 substrates defines roles for synaptic depalmitoylation. Biorxiv 2020.05.02.074302.

Granger, A.J., Shi, Y., Lu, W., Cerpas, M., and Nicoll, R.A. (2013). LTP requires a reserve pool of glutamate receptors independent of subunit type. Nature *493*, 495–500.

Gray, E.E., Fink, A.E., Sariñana, J., Vissel, B., and O'Dell, T.J. (2007). Long-Term Potentiation in the Hippocampal CA1 Region Does Not Require Insertion and Activation of GluR2-Lacking AMPA Receptors. J Neurophysiol *98*, 2488–2492.

Greaves, J., and Chamberlain, L.H. (2007). Palmitoylation-dependent protein sorting. The Journal of Cell Biology *176*, 249–254.

Griffey, M., Bible, E., Vogler, C., Levy, B., Gupta, P., Cooper, J., and Sands, M.S. (2004). Adeno-associated virus 2-mediated gene therapy decreases autofluorescent storage material and increases brain mass in a murine model of infantile neuronal ceroid lipofuscinosis. Neurobiology of Disease *16*, 360–369.

Gu, W., Brodtkorb, E., and Steinlein, O.K. (2002). LGI1 is mutated in familial temporal lobe epilepsy characterized by aphasic seizures. Annals of Neurology *52*, 364–367.

Guire, E.S., Oh, M.C., Soderling, T.R., and Derkach, V.A. (2008). Recruitment of Calcium-Permeable AMPA Receptors during Synaptic Potentiation Is Regulated by CaM-Kinase I. J Neurosci *28*, 6000–6009.

Gupta, P., Soyombo, A., Atashband, A., Wisniewski, K., Shelton, J., Richardson, J., Hammer, R., and Hofmann, S. (2001). Disruption of PPT1 or PPT2 causes neuronal ceroid lipofuscinosis in knockout mice. Proceedings of the National Academy of Sciences *98*.

Hänel, L., Gosau, T., Maar, H., Valentiner, U., Schumacher, U., Riecken, K., Windhorst, S., Hansen, N.-O., Heikaus, L., Wurlitzer, M., et al. (2018). Differential Proteome Analysis of Human Neuroblastoma Xenograft Primary Tumors and Matched Spontaneous Distant Metastases. Sci Rep-Uk *8*, 13986.

Hansen, K.B., Ogden, K.K., Yuan, H., and Traynelis, S.F. (2014). Distinct functional and pharmacological properties of Triheteromeric GluN1/GluN2A/GluN2B NMDA receptors. Neuron *81*, 1084–1096.

Hansen, K.B., Yi, F., Perszyk, R.E., Furukawa, H., Wollmuth, L.P., Gibb, A.J., and Traynelis, S.F. (2018). Structure, function, and allosteric modulation of NMDA receptors. J Gen Physiol *150*, 1081–1105.

Hayashi, T., Rumbaugh, G., and Huganir, R.L. (2005). Differential regulation of AMPA receptor subunit trafficking by palmitoylation of two distinct sites. Neuron *47*.

Hayashi, T., Thomas, G.M., and Huganir, R.L. (2009). Dual palmitoylation of NR2 subunits regulates NMDA receptor trafficking. Neuron *64*.

Hayashi, Y., Shi, S., Esteban, J., Piccini, A., Poncer, J., and Malinow, R. (2000). Driving AMPA receptors into synapses by LTP and CaMKII: requirement for GluR1 and PDZ domain interaction. Science (New York, N.Y.) *287*.

Hebb, D.O. (2002). The Organization of Behavior.

Henley, J.M., and Wilkinson, K.A. (2013). AMPA receptor trafficking and the mechanisms underlying synaptic plasticity and cognitive aging. Dialogues Clin Neurosci *15*, 11–27.

Hensch, T.K. (2004). CRITICAL PERIOD REGULATION. Annu Rev Neurosci *27*, 549–579.

Herculano-Houzel, S. (2012). The remarkable, yet not extraordinary, human brain as a scaled-up primate brain and its associated cost. Proceedings of the National Academy of Sciences *109*.

Hernandez, J.L., Davda, D., Kit, M.C.S., Majmudar, J.D., Won, S.J., Gang, M., Pasupuleti, S.C., Choi, A.I., Bartkowiak, C.M., and Martin, B.R. (2017). APT2 Inhibition Restores Scribble Localization and S-Palmitoylation in Snail-Transformed Cells. Cell Chemical Biology *24*, 87–97.

Ho, G.P.H., Selvakumar, B., Mukai, J., Hester, L.D., Wang, Y., Gogos, J.A., and Snyder, S.H. (2011). S-Nitrosylation and S-Palmitoylation Reciprocally Regulate Synaptic Targeting of PSD-95. Neuron *71*, 131–141.

Hotelier, T., Renault, L., Cousin, X., Negre, V., Marchot, P., and Chatonnet, A. (2004). ESTHER, the database of the alpha/beta-hydrolase fold superfamily of proteins. Nucleic Acids Research *32*, D145-7.

Howie, J., Reilly, L., Fraser, N.J., Walker, J.M.V., Wypijewski, K.J., Ashford, M.L.J., Calaghan, S.C., McClafferty, H., Tian, L., Shipston, M.J., et al. (2014). Substrate recognition by the cell surface palmitoyl transferase DHHC5. Proc National Acad Sci *111*, 17534–17539.

Hu, J., Lu, J.-Y.Y., Wong, A.M., Hynan, L.S., Birnbaum, S.G., Yilmaz, D.S., Streit, B.M., Lenartowicz, E.M., Thompson, T.C., Cooper, J.D., et al. (2012). Intravenous high-dose enzyme replacement therapy with recombinant palmitoyl-protein thioesterase reduces visceral lysosomal storage and modestly prolongs survival in a preclinical mouse model of infantile neuronal ceroid lipofuscinosis. Molecular Genetics and Metabolism *107*, 213–221.

HUBEL, D., and WIESEL, T. (1964). EFFECTS OF MONOCULAR DEPRIVATION IN KITTENS. Naunyn-Schmiedebergs Archiv Für Experimentelle Pathologie Und Pharmakologie *248*.

Hubel, D., and Wiesel, T. (1970). The period of susceptibility to the physiological effects of unilateral eye closure in kittens. The Journal of Physiology *206*.

Hubel, D., Wiesel, T., and LeVay, S. (1976). Functional architecture of area 17 in normal and monocularly deprived macaque monkeys. Cold Spring Harbor Symposia on Quantitative Biology *40*.

Huganir, R.L., and Nicoll, R.A. (2013). AMPARs and synaptic plasticity: the last 25 years. Neuron *80*, 704–717.

Ito, M., Sakurai, M., and Tongroach, P. (1982). Climbing fibre induced depression of both mossy fibre responsiveness and glutamate sensitivity of cerebellar Purkinje cells. J Physiology *324*, 113–134.

Itoh, M., Yamashita, M., Kaneko, M., Okuno, H., Abe, M., Yamazaki, M., Natsume, R., Yamada, D., Kaizuka, T., Suwa, R., et al. (2018). Deficiency of AMPAR-Palmitoylation Aggravates Seizure Susceptibility. The Journal of Neuroscience : The Official Journal of the Society for Neuroscience *38*, 10220–10235.

Jeyifous, O., Lin, E.I., Chen, X., Antinone, S.E., Mastro, R., Drisdel, R., Reese, T.S., and Green, W.N. (2016). Palmitoylation regulates glutamate receptor distributions in postsynaptic densities through control of PSD95 conformation and orientation. Proceedings of the National Academy of Sciences *113*.

Ju, W., Morishita, W., Tsui, J., Gaietta, G., Deerinck, T.J., Adams, S.R., Garner, C.C., Tsien, R.Y., Ellisman, M.H., and Malenka, R.C. (2004). Activity-dependent regulation of dendritic synthesis and trafficking of AMPA receptors. Nat Neurosci *7*, 244–253.

Kang, R., Wan, J., Arstikaitis, P., Takahashi, H., Huang, K., Bailey, A.O., Thompson, J.X., Roth, A.F., Drisdel, R.C., Mastro, R., et al. (2008). Neural palmitoyl-proteomics reveals dynamic synaptic palmitoylation. Nature *456*.

Kielar, C., Maddox, L., Bible, E., Pontikis, C.C., Macauley, S.L., Griffey, M.A., Wong, M., Sands, M.S., and Cooper, J.D. (2007). Successive neuron loss in the thalamus and cortex in a mouse model of infantile neuronal ceroid lipofuscinosis. Neurobiology of Disease *25*, 150–162.

Kim, S., and Ziff, E.B. (2014). Calcineurin Mediates Synaptic Scaling Via Synaptic Trafficking of Ca2+-Permeable AMPA Receptors. Plos Biol *12*, e1001900.

Kostiuk, M.A., Keller, B.O., and Berthiaume, L.G. (2010). Palmitoylation of ketogenic enzyme HMGCS2 enhances its interaction with PPARalpha and transcription at the Hmgcs2 PPRE. FASEB Journal : Official Publication of the Federation of American Societies for Experimental Biology *24*, 1914–1924.

Kouskou, M., Thomson, D.M., Brett, R.R., Wheeler, L., Tate, R.J., Pratt, J.A., and Chamberlain, L.H. (2018). Disruption of the Zdhhc9 intellectual disability gene leads to behavioural abnormalities in a mouse model. Experimental Neurology *308*, 35–46.

Lange, J., Haslett, L.J., Lloyd-Evans, E., Pocock, J.M., Sands, M.S., Williams, B.P., and Cooper, J.D. (2018). Compromised astrocyte function and survival negatively impact neurons in infantile neuronal ceroid lipofuscinosis. Acta Neuropathologica Communications *6*, 74.

Lee, H.-K. (2012). Ca2+-permeable AMPA receptors in homeostatic synaptic plasticity. Front Mol Neurosci *5*, 17.

Lee, H.-K.K., Takamiya, K., He, K., Song, L., and Huganir, R.L. (2010a). Specific roles of AMPA receptor subunit GluR1 (GluA1) phosphorylation sites in regulating synaptic plasticity in the CA1 region of hippocampus. Journal of Neurophysiology *103*, 479–489.

Lee, M.-C., Yasuda, R., and Ehlers, M.D. (2010b). Metaplasticity at Single Glutamatergic Synapses. Neuron *66*, 859–870.

Lehtovirta, M., Kyttälä, A., Eskelinen, E., Hess, M., Heinonen, O., and Jalanko, A. (2001). Palmitoyl protein thioesterase (PPT) localizes into synaptosomes and synaptic vesicles in neurons: implications for infantile neuronal ceroid lipofuscinosis (INCL). Human Molecular Genetics *10*.

Lemonidis, K., Gorleku, O.A., Sanchez-Perez, M.C., Grefen, C., and Chamberlain, L.H. (2014). The Golgi S-acylation machinery comprises zDHHC enzymes with major differences in substrate affinity and S-acylation activity. Molecular Biology of the Cell *25*, 3870–3883.

Lemonidis, K., Werno, M.W., Greaves, J., Diez-Ardanuy, C., Sanchez-Perez, M.C., Salaun, C., Thomson, D.M., and Chamberlain, L.H. (2015). The zDHHC family of S-acyltransferases. Biochemical Society Transactions *43*, 217–221.

Lemonidis, K., Salaun, C., Kouskou, M., Diez-Ardanuy, C., Chamberlain, L.H., and Greaves, J. (2017). Substrate selectivity in the zDHHC family of S-acyltransferases. Biochemical Society Transactions *45*, 751–758.

LeVay, S., Wiesel, T., and Hubel, D. (1980). The development of ocular dominance columns in normal and visually deprived monkeys. Journal of Comparative Neurology *191*.

Levin, S.W., Baker, E.H., Zein, W.M., Zhang, Z., Quezado, Z.M., Miao, N., Gropman, A., Griffin, K.J., Bianconi, S., Chandra, G., et al. (2014). Oral cysteamine bitartrate and N-acetylcysteine for patients with infantile neuronal ceroid lipofuscinosis: a pilot study. The Lancet Neurology *13*.

Lin, D.T., and Conibear, E. (2015). ABHD17 proteins are novel protein depalmitoylases that regulate N-Ras palmitate turnover and subcellular localization. ELife *4*, e11306.

Lisman, J. (1989). A mechanism for the Hebb and the anti-Hebb processes underlying learning and memory. Proc National Acad Sci *86*, 9574–9578.

Lissin, D.V., Gomperts, S.N., Carroll, R.C., Christine, C.W., Kalman, D., Kitamura, M., Hardy, S., Nicoll, R.A., Malenka, R.C., and Zastrow, M. von (1998). Activity differentially regulates the surface expression of synaptic AMPA and NMDA glutamate receptors. Proc National Acad Sci *95*, 7097–7102.

Liu, H., Abecasis, G.R., Heath, S.C., Knowles, A., Demars, S., Chen, Y.-J.J., Roos, J.L., Rapoport, J.L., Gogos, J.A., and Karayiorgou, M. (2002). Genetic variation in the 22q11 locus and susceptibility to schizophrenia. Proceedings of the National Academy of Sciences of the United States of America *99*, 16859–16864.

Lu, W., Shi, Y., Jackson, A.C., Bjorgan, K., During, M.J., Sprengel, R., Seeburg, P.H., and Nicoll, R.A. (2009). Subunit Composition of Synaptic AMPA Receptors Revealed by a Single-Cell Genetic Approach. Neuron *62*, 254–268.

Lyly, A., Schantz, C. von, Salonen, T., Kopra, O., Saarela, J., Jauhiainen, M., Kyttälä, A., and Jalanko, A. (2007). Glycosylation, transport, and complex formation of palmitoyl protein thioesterase 1 (PPT1)--distinct characteristics in neurons. BMC Cell Biology *8*, 22.

Lyly, A., Marjavaara, S.K., Kyttälä, A., Uusi-Rauva, K., Luiro, K., Kopra, O., Martinez, L.O., Tanhuanpää, K., Kalkkinen, N., Suomalainen, A., et al. (2008). Deficiency of the INCL protein Ppt1 results in changes in ectopic F1-ATP synthase and altered cholesterol metabolism. Human Molecular Genetics *17*, 1406–1417.

Lynch, G., Larson, J., Kelso, S., Barrionuevo, G., and Schottler, F. (1983). Intracellular injections of EGTA block induction of hippocampal long-term potentiation. Nature *305*, 719–721.

Malenka, R.C., Kauer, J.A., Perkel, D.J., Mauk, M.D., Kelly, P.T., Nicoll, R.A., and Waxham, M.N. (1989). An essential role for postsynaptic calmodulin and protein kinase activity in long-term potentiation. Nature *340*, 554–557.

Malinow, R., and Miller, J.P. (1986). Postsynaptic hyperpolarization during conditioning reversibly blocks induction of long-term potentiation. Nature *320*, 529–530.

Malinow, R., Schulman, H., and Tsien, R. (1989). Inhibition of postsynaptic PKC or CaMKII blocks induction but not expression of LTP. Science *245*, 862–866.

Man, H.-Y., Sekine-Aizawa, Y., and Huganir, R.L. (2007). Regulation of α-amino-3-hydroxy-5-methyl-4-isoxazolepropionic acid receptor trafficking through PKA phosphorylation of the Glu receptor 1 subunit. Proc National Acad Sci *104*, 3579–3584.

Mansouri, M.R., Marklund, L., Gustavsson, P., Davey, E., Carlsson, B., Larsson, C., White, I., Gustavson, K.-H.H., and Dahl, N. (2005). Loss of ZDHHC15 expression in a woman with a balanced translocation t(X;15)(q13.3;cen) and severe mental retardation. European Journal of Human Genetics : EJHG *13*, 970–977.

Martin, S.J., Grimwood, P.D., and Morris, R.G.M. (2000). Synaptic Plasticity and Memory: An Evaluation of the Hypothesis. Annu Rev Neurosci *23*, 649–711.

Mattison, H.A., Hayashi, T., and Barria, A. (2012). Palmitoylation at two cysteine clusters on the C-terminus of GluN2A and GluN2B differentially control synaptic targeting of NMDA receptors. PloS One *7*, e49089.

Mayer, M.L., Westbrook, G.L., and Guthrie, P.B. (1984). Voltage-dependent block by Mg2+ of NMDA responses in spinal cord neurones. Nature *309*, 261–263.

Miller, J.N., Kovács, A.D., and Pearce, D.A. (2015). The novel Cln1R151X mouse model of infantile neuronal ceroid lipofuscinosis (INCL) for testing nonsense suppression therapy. Hum Mol Genet *24*, 185–196.

Milnerwood, A.J., Parsons, M.P., Young, F.B., Singaraja, R.R., Franciosi, S., Volta, M., Bergeron, S., Hayden, M.R., and Raymond, L.A. (2013). Memory and synaptic deficits in Hip14/DHHC17 knockout mice. Proceedings of the National Academy of Sciences of the United States of America *110*, 20296–20301.

Mohammed, A., Zhang, C., Zhang, S., Shen, Q., Li, J., Tang, Z., and Liu, H. (2018). Inhibition of cell proliferation and migration in non-small cell lung cancer cells through the suppression of LYPLA1. Oncology Reports.

Montersino, A., and Thomas, G.M. (2015). Slippery signaling: Palmitoylation-dependent control of neuronal kinase localization and activity. Molecular Membrane Biology *32*, 179–188.

Monyer, H., Burnashev, N., Laurie, D., Sakmann, B., and Seeburg, P. (1994). Developmental and regional expression in the rat brain and functional properties of four NMDA receptors. Neuron *12*.

Morita, M., Aoki, M., Abe, K., Hasegawa, T., Sakuma, R., Onodera, Y., Ichikawa, N., Nishizawa, M., and Itoyama, Y. (1996). A novel two-base mutation in the Cu/Zn superoxide dismutase gene associated with familial amyotrophic lateral sclerosis in Japan. Neuroscience Letters *205*, 79–82.

Mukai, J., Liu, H., Burt, R.A., Swor, D.E., Lai, W.-S.S., Karayiorgou, M., and Gogos, J.A. (2004). Evidence that the gene encoding ZDHHC8 contributes to the risk of schizophrenia. Nature Genetics *36*, 725–731.

Mukai, J., Dhilla, A., Drew, L.J., Stark, K.L., Cao, L., MacDermott, A.B., Karayiorgou, M., and Gogos, J.A. (2008). Palmitoylation-dependent neurodevelopmental deficits in a mouse model of 22q11 microdeletion. Nature Neuroscience *11*, 1302–1310.

Mukai, J., Tamura, M., Fénelon, K., Rosen, A.M., Spellman, T.J., Kang, R., MacDermott, A.B., Karayiorgou, M., Gordon, J.A., and Gogos, J.A. (2015). Molecular substrates of altered axonal growth and brain connectivity in a mouse model of schizophrenia. Neuron *86*, 680–695.

Mulkey, R.M., Endo, S., Shenolikar, S., and Malenka, R.C. (1994). Involvement of a calcineurin/ inhibitor-1 phosphatase cascade in hippocampal long-term depression. Nature *369*, 486–488.

Nicoll, R.A., Kauer, J.A., and Malenka, R.C. (1988). The current excitement in long term potentiation. Neuron *1*, 97–103.

Nieto, R., Kukuljan, M., and Silva, H. (2013). BDNF and schizophrenia: from neurodevelopment to neuronal plasticity, learning, and memory. Frontiers in Psychiatry *4*, 45.

Nishimune, A., Isaac, J.T., Molnar, E., Noel, J., Nash, S.R., Tagaya, M., Collingridge, G.L., Nakanishi, S., and Henley, J.M. (1998). NSF binding to GluR2 regulates synaptic transmission. Neuron *21*, 87–97.

Nita, D.A., Mole, S.E., and Minassian, B.A. (2016). Neuronal ceroid lipofuscinoses. Epileptic Disorders *18*.

Noritake, J., Fukata, Y., Iwanaga, T., Hosomi, N., Tsutsumi, R., Matsuda, N., Tani, H., Iwanari, H., Mochizuki, Y., Kodama, T., et al. (2009). Mobile DHHC palmitoylating enzyme mediates activity-sensitive synaptic targeting of PSD-95. The Journal of Cell Biology *186*.

Nowak, L., Bregestovski, P., Ascher, P., Herbet, A., and Prochiantz, A. (1984). Magnesium gates glutamate-activated channels in mouse central neurones. Nature *307*, 462–465.

O'Brien, R.J., Kamboj, S., Ehlers, M.D., Rosen, K.R., Fischbach, G.D., and Huganir, R.L. (1998). Activity-dependent modulation of synaptic AMPA receptor accumulation. Neuron *21*, 1067–1078.

Oh, M.C., Derkach, V.A., Guire, E.S., and Soderling, T.R. (2006). Extrasynaptic Membrane Trafficking Regulated by GluR1 Serine 845 Phosphorylation Primes AMPA Receptors for Long-term Potentiation*. J Biol Chem *281*, 752–758.

Ohno, Y., Kihara, A., Sano, T., and Igarashi, Y. (2006). Intracellular localization and tissue-specific distribution of human and yeast DHHC cysteine-rich domain-containing proteins. Biochimica et Biophysica Acta *1761*, 474–483.

Oku, S., Takahashi, N., Fukata, Y., and Fukata, M. (2013). In silico screening for palmitoyl substrates reveals a role for DHHC1/3/10 (zDHHC1/3/11)-mediated neurochondrin palmitoylation in its targeting to Rab5-positive endosomes. The Journal of Biological Chemistry *288*, 19816–19829.

Pagon, R.A., Adam, M.P., Ardinger, H.H., Wallace, S.E., Amemiya, A., Bean, L.J., Bird, T.D., Ledbetter, N., Mefford, H.C., Smith, R.J., et al. (2013). Neuronal Ceroid-Lipofuscinoses.

Paoletti, P. (2011). Molecular basis of NMDA receptor functional diversity: NMDA receptor functional diversity. Eur J Neurosci *33*, 1351–1365.

Paoletti, P., Bellone, C., and Zhou, Q. (2013). NMDA receptor subunit diversity: impact on receptor properties, synaptic plasticity and disease. Nat Rev Neurosci *14*, 383–400.

Parat, M.O., and Fox, P.L. (2001). Palmitoylation of caveolin-1 in endothelial cells is post-translational but irreversible. The Journal of Biological Chemistry *276*, 15776–15782.

Pedro, M.P., Vilcaes, A.A., Gomez, G.A., and Daniotti, J.L. (2017). Individual S-acylated cysteines differentially contribute to H-Ras endomembrane trafficking and acylation/deacylation cycles. Molecular Biology of the Cell *28*, 962–974.

Percherancier, Y., Planchenault, T., Valenzuela-Fernandez, A., Virelizier, J.L., Arenzana-Seisdedos, F., and Bachelerie, F. (2001). Palmitoylation-dependent control of degradation, life span, and membrane expression of the CCR5 receptor. The Journal of Biological Chemistry *276*, 31936–31944.

Philpot, B., Sekhar, A., Shouval, H., and Bear, M. (2001). Visual experience and deprivation bidirectionally modify the composition and function of NMDA receptors in visual cortex. Neuron *29*.

Plant, K., Pelkey, K.A., Bortolotto, Z.A., Morita, D., Terashima, A., McBain, C.J., Collingridge, G.L., and Isaac, J.T. (2006). Transient incorporation of native GluR2-lacking AMPA receptors during hippocampal long-term potentiation. Nature Neuroscience *9*, 602–604.

Quinlan, E., Philpot, B., Huganir, R., and Bear, M. (1999). Rapid, experience-dependent expression of synaptic NMDA receptors in visual cortex in vivo. Nature Neuroscience *2*.

Rauner, C., and Köhr, G. (2011). Triheteromeric NR1/NR2A/NR2B Receptors Constitute the Major N-Methyl-d-aspartate Receptor Population in Adult Hippocampal Synapses. J Biol Chem *286*, 7558–7566.

Raymond, F.L., Tarpey, P.S., Edkins, S., Tofts, C., O'Meara, S., Teague, J., Butler, A., Stevens, C., Barthorpe, S., Buck, G., et al. (2007). Mutations in ZDHHC9, which encodes a palmitoyltransferase of NRAS and HRAS, cause X-linked mental retardation associated with a Marfanoid habitus. American Journal of Human Genetics *80*, 982–987.

Roberts, M.S., Macauley, S.L., Wong, A.M., Yilmas, D., Hohm, S., Cooper, J.D., and Sands, M.S. (2012). Combination small molecule PPT1 mimetic and CNS-directed gene therapy as a treatment for infantile neuronal ceroid lipofuscinosis. J Inherit Metab Dis *35*, 847–857.

Rocks, O., Peyker, A., Kahms, M., Verveer, P.J., Koerner, C., Lumbierres, M., Kuhlmann, J., Waldmann, H., Wittinghofer, A., and Bastiaens, P.I. (2005). An acylation cycle regulates localization and activity of palmitoylated Ras isoforms. Science (New York, N.Y.) *307*, 1746–1752.

Rocks, O., Gerauer, M., Vartak, N., Koch, S., Huang, Z.-P.P., Pechlivanis, M., Kuhlmann, J., Brunsveld, L., Chandra, A., Ellinger, B., et al. (2010). The palmitoylation machinery is a spatially organizing system for peripheral membrane proteins. Cell *141*, 458–471.

Sadeghi, R.S., Kulej, K., Kathayat, R.S., Garcia, B.A., Dickinson, B.C., Brady, D.C., and Witze, E.S. (2018). Wnt5a signaling induced phosphorylation increases APT1 activity and promotes melanoma metastatic behavior. ELife *7*.

Salaun, C., Greaves, J., and Chamberlain, L.H. (2010). The intracellular dynamic of protein palmitoylation. The Journal of Cell Biology *191*, 1229–1238.

Sanders, S.S., Martin, D.D., Butland, S.L., Lavallée-Adam, M., Calzolari, D., Kay, C., Yates, J.R., and Hayden, M.R. (2015). Curation of the Mammalian Palmitoylome Indicates a Pivotal Role for Palmitoylation in Diseases and Disorders of the Nervous System and Cancers. PLoS Computational Biology *11*, e1004405.

Sanderson, J.L., Gorski, J.A., and Dell'Acqua, M.L. (2016). NMDA Receptor-Dependent LTD Requires Transient Synaptic Incorporation of Ca2+-Permeable AMPARs Mediated by AKAP150-Anchored PKA and Calcineurin. Neuron *89*, 1000–1015.

Sanderson, J.L., Scott, J.D., and Dell'Acqua, M.L. (2018). Control of Homeostatic Synaptic Plasticity by AKAP-Anchored Kinase and Phosphatase Regulation of Ca 2+ -Permeable AMPA Receptors. J Neurosci *38*, 2863–2876.

Sans, N., Petralia, R., Wang, Y., Blahos, J., Hell, J., and Wenthold, R. (2000). A developmental change in NMDA receptor-associated proteins at hippocampal synapses. The Journal of Neuroscience : The Official Journal of the Society for Neuroscience *20*.

Sarkar, C., Chandra, G., Peng, S., Zhang, Z., Liu, A., and Mukherjee, A.B. (2013). Neuroprotection and lifespan extension in Ppt1(-/-) mice by NtBuHA: therapeutic implications for INCL. Nature Neuroscience *16*, 1608–1617.

Schmidt, M.F., and Schlesinger, M.J. (1979). Fatty acid binding to vesicular stomatitis virus glycoprotein: a new type of post-translational modification of the viral glycoprotein. Cell *17*, 813–819.

Schmidt, M.F., Bracha, M., and Schlesinger, M.J. (1979). Evidence for covalent attachment of fatty acids to Sindbis virus glycoproteins. Proceedings of the National Academy of Sciences of the United States of America *76*, 1687–1691.

Seidenman, K.J., Steinberg, J.P., Huganir, R., and Malinow, R. (2003). Glutamate Receptor Subunit 2 Serine 880 Phosphorylation Modulates Synaptic Transmission and Mediates Plasticity in CA1 Pyramidal Cells. J Neurosci *23*, 9220–9228.

Sharma, C., Yang, X.H., and Hemler, M.E. (2008). DHHC2 affects palmitoylation, stability, and functions of tetraspanins CD9 and CD151. Molecular Biology of the Cell *19*, 3415–3425.

Sheng, M., Cummings, J., Roldan, L.A., Jan, Y.N., and Jan, L.Y. (1994). Changing subunit composition of heteromeric NMDA receptors during development of rat cortex. Nature *368*, 144–147.

Shi, S.-H., Hayashi, Y., Petralia, R.S., Zaman, S.H., Wenthold, R.J., Svoboda, K., and Malinow, R. (1999). Rapid Spine Delivery and Redistribution of AMPA Receptors After Synaptic NMDA Receptor Activation. Science *284*, 1811–1816.

Shi, S.-H., Hayashi, Y., Esteban, J.A., and Malinow, R. (2001). Subunit-Specific Rules Governing AMPA Receptor Trafficking to Synapses in Hippocampal Pyramidal Neurons. Cell *105*, 331–343.

Shyng, C., Nelvagal, H.R., Dearborn, J.T., Tyynelä, J., Schmidt, R.E., Sands, M.S., and Cooper, J.D. (2017). Synergistic effects of treating the spinal cord and brain in CLN1 disease. Proceedings of the National Academy of Sciences of the United States of America *114*, E5920–E5929.

Sim, D.S., Dilks, J.R., and Flaumenhaft, R. (2007). Platelets possess and require an active protein palmitoylation pathway for agonist-mediated activation and in vivo thrombus formation. Arteriosclerosis, Thrombosis, and Vascular Biology *27*, 1478–1485.

Soyombo, A.A., and Hofmann, S.L. (1997). Molecular cloning and expression of palmitoyl-protein thioesterase 2 (PPT2), a homolog of lysosomal palmitoyl-protein thioesterase with a distinct substrate specificity. The Journal of Biological Chemistry *272*, 27456–27463.

Steinberg, J.P., Takamiya, K., Shen, Y., Xia, J., Rubio, M.E., Yu, S., Jin, W., Thomas, G.M., Linden, D.J., and Huganir, R.L. (2006). Targeted In Vivo Mutations of the AMPA Receptor Subunit GluR2 and Its Interacting Protein PICK1 Eliminate Cerebellar Long-Term Depression. Neuron *49*, 845–860.

Stocca, G., and Vicini, S. (1998). Increased contribution of NR2A subunit to synaptic NMDA receptors in developing rat cortical neurons. The Journal of Physiology *507 (Pt 1)*, 13–24.

Stypulkowski, E., Asangani, I.A., and Witze, E.S. (2018). The depalmitoylase APT1 directs the asymmetric partitioning of Notch and Wnt signaling during cell division. Science Signaling *11*.

Sugimoto, H., Hayashi, H., and Yamashita, S. (1996). Purification, cDNA cloning, and regulation of lysophospholipase from rat liver. The Journal of Biological Chemistry *271*, 7705–7711.

Sutton, L.M., Sanders, S.S., Butland, S.L., Singaraja, R.R., Franciosi, S., Southwell, A.L., Doty, C.N., Schmidt, M.E., Mui, K.K., Kovalik, V., et al. (2013). Hip14l-deficient mice develop neuropathological and behavioural features of Huntington disease. Human Molecular Genetics *22*, 452–465.

Tabaczar, S., Czogalla, A., Podkalicka, J., Biernatowska, A., and Sikorski, A.F. (2017). Protein palmitoylation: Palmitoyltransferases and their specificity. Experimental Biology and Medicine (Maywood, N.J.) *242*, 1150–1157.

Thiagarajan, T.C., Lindskog, M., and Tsien, R.W. (2005). Adaptation to Synaptic Inactivity in Hippocampal Neurons. Neuron *47*, 725–737.

Tian, L., McClafferty, H., Knaus, H.-G.G., Ruth, P., and Shipston, M.J. (2012). Distinct acyl protein transferases and thioesterases control surface expression of calcium-activated potassium channels. The Journal of Biological Chemistry *287*, 14718–14725.

Tomatis, V.M., Trenchi, A., Gomez, G.A., and Daniotti, J.L. (2010). Acyl-protein thioesterase 2 catalyzes the deacylation of peripheral membrane-associated GAP-43. PloS One *5*, e15045.

Tortosa, E., Adolfs, Y., Fukata, M., Pasterkamp, R.J., Kapitein, L.C., and Hoogenraad, C.C. (2017). Dynamic Palmitoylation Targets MAP6 to the Axon to Promote Microtubule Stabilization during Neuronal Polarization. Neuron *94*, 809-825.e7.

Toyoda, T., Sugimoto, H., and Yamashita, S. (1999). Sequence, expression in Escherichia coli, and characterization of lysophospholipase II. Biochimica et Biophysica Acta *1437*, 182–193.

Turrigiano, G.G. (2017). The dialectic of Hebb and homeostasis. Philosophical Transactions Royal Soc B Biological Sci *372*, 20160258.

Turrigiano, G.G., and Nelson, S.B. (2004). Homeostatic plasticity in the developing nervous system. Nature Reviews Neuroscience *5*.

Turrigiano, G., Leslie, K., Desai, N., Rutherford, L., and Nelson, S. (1998). Activity-dependent scaling of quantal amplitude in neocortical neurons. *391*.

Vartak, N., Papke, B., Grecco, H.E., Rossmannek, L., Waldmann, H., Hedberg, C., and Bastiaens, P.I. (2014). The autodepalmitoylating activity of APT maintains the spatial organization of palmitoylated membrane proteins. Biophysical Journal *106*, 93–105.

Verkruyse, L., and Hofmann, S. (1996). Lysosomal targeting of palmitoyl-protein thioesterase. The Journal of Biological Chemistry *271*.

Vesa, J., Hellsten, E., Verkruyse, L., Camp, L., Rapola, J., Santavuori, P., Hofmann, S., and Peltonen, L. (1995). Mutations in the palmitoyl protein thioesterase gene causing infantile neuronal ceroid lipofuscinosis. Nature *376*.

Vetrivel, K.S., Meckler, X., Chen, Y., Nguyen, P.D., Seidah, N.G., Vassar, R., Wong, P.C., Fukata, M., Kounnas, M.Z., and Thinakaran, G. (2009). Alzheimer disease Abeta production in the absence of S-palmitoylation-dependent targeting of BACE1 to lipid rafts. The Journal of Biological Chemistry *284*, 3793–3803.

Watt, A.J., Rossum, M.C.W. van, MacLeod, K.M., Nelson, S.B., and Turrigiano, G.G. (2000). Activity Coregulates Quantal AMPA and NMDA Currents at Neocortical Synapses. Neuron *26*, 659–670.

Watt, A.J., Sjöström, P.J., Häusser, M., Nelson, S.B., and Turrigiano, G.G. (2004). A proportional but slower NMDA potentiation follows AMPA potentiation in LTP. Nat Neurosci *7*, 518–524.

Wenthold, R., Petralia, R., J, I.B., and Niedzielski, A. (1996). Evidence for multiple AMPA receptor complexes in hippocampal CA1/CA2 neurons. J Neurosci *16*, 1982–1989.

Wigström, H., Gustafsson, B., Huang, Y.Y., and Abraham, W.C. (1986). Hippocampal long-term potentiation is induced by pairing single afferent volleys with intracellularly injected depolarizing current pulses. Acta Physiol Scand *126*, 317–319.

Williams, J.M., Guévremont, D., Mason-Parker, S.E., Luxmanan, C., Tate, W.P., and Abraham, W.C. (2007). Differential Trafficking of AMPA and NMDA Receptors during Long-Term Potentiation in Awake Adult Animals. J Neurosci *27*, 14171–14178.

Williams, K., Russell, S.L., Shen, Y.M., and Molinoff, P.B. (1993). Developmental switch in the expression of NMDA receptors occurs in vivo and in vitro. Neuron *10*, 267–278.

Xu, Z., Chen, R.-Q., Gu, Q.-H., Yan, J.-Z., Wang, S.-H., Liu, S.-Y., and Lu, W. (2009). Metaplastic Regulation of Long-Term Potentiation/Long-Term Depression Threshold by Activity-Dependent Changes of NR2A/NR2B Ratio. J Neurosci *29*, 8764–8773.

Yanai, A., Huang, K., Kang, R., Singaraja, R.R., Arstikaitis, P., Gan, L., Orban, P.C., Mullard, A., Cowan, C.M., Raymond, L.A., et al. (2006). Palmitoylation of huntingtin by HIP14 is essential for its trafficking and function. Nature Neuroscience *9*, 824–831.

Yashiro, K., and Philpot, B.D. (2008). Regulation of NMDA receptor subunit expression and its implications for LTD, LTP, and metaplasticity. Neuropharmacology *55*, 1081–1094.

Yeh, D.C., Duncan, J.A., Yamashita, S., and Michel, T. (1999). Depalmitoylation of endothelial nitric-oxide synthase by acyl-protein thioesterase 1 is potentiated by Ca(2+)-calmodulin. The Journal of Biological Chemistry *274*, 33148–33154.

Yokoi, N., Fukata, Y., Sekiya, A., Murakami, T., Kobayashi, K., and Fukata, M. (2016). Identification of PSD-95 Depalmitoylating Enzymes. The Journal of Neuroscience *36*.

Yoshii, A., and Constantine-Paton, M. (2014). Postsynaptic localization of PSD-95 is regulated by all three pathways downstream of TrkB signaling. Frontiers in Synaptic Neuroscience *6*, 6.

Yoshii, A., Sheng, M.H., and Constantine-Paton, M. (2003). Eye opening induces a rapid dendritic localization of PSD-95 in central visual neurons. Proceedings of the National Academy of Sciences *100*.

Zhou, Z., Liu, A., Xia, S., Leung, C., Qi, J., Meng, Y., Xie, W., Park, P., Collingridge, G.L., and Jia, Z. (2018). The C-terminal tails of endogenous GluA1 and GluA2 differentially contribute to hippocampal synaptic plasticity and learning. Nature Neuroscience *21*, 50–62.

Zundert, B. van, Yoshii, A., and Constantine-Paton, M. (2004). Receptor compartmentalization and trafficking at glutamate synapses: a developmental proposal. Trends in Neurosciences *27*.

2. DEVELOPMENTAL NMDA RECEPTOR DYSREGULATION IN THE INFANTILE NEURONAL CEROID LIPOFUSCINOSIS MOUSE MODEL

Chapter 2 is a reprinting in its entirety of my first author publication holding the identical title to that of this chapter, published in the journal *eLife* on April 4th, 2019 (previously published as Kevin P Koster, Walter Francesconi, Fulvia Berton, Sami Alahmadi, Roshan Srinivas, Akira Yoshii (2019) Developmental NMDA receptor dysregulation in the infantile neuronal ceroid lipofuscinosis mouse model, ELife 8.). Figures were renumbered to reflect that they are in Chapter 2, such that Figure 2 became Figure 2.2, and so on. Videos and references to the videos were also removed due to the thesis formatting. This publication is under a Creative Commons Attribution License. See **Appendix 1**.

2.1. Introduction

The neuronal ceroid lipofuscinoses (NCLs) are a class of individually rare, primarily autosomal recessive, neurodegenerative diseases occurring in an estimated 2 to 4 of 100,000 live births (Nita et al., 2016). Collectively, NCLs represent the most prevalent class of hereditary pediatric neurodegenerative disease (Haltia, 2006). The NCLs are characterized by progressive neurodegeneration, blindness, cognitive and motor deterioration, seizures, and premature death. The cardinal feature of all NCLs is the intracellular accumulation of proteolipid material, termed lipofuscin (Jalanko and Braulke, 2009; Nita et al., 2016). While lipofuscin accumulates in all cells of affected individuals, it deposits most robustly in neurons. This accumulation is concurrent with rapid and progressive neurodegeneration, particularly of thalamic and primary sensory cortical areas (Bible et al., 2004; Kielar et al., 2007). The NCLs are categorized into *CLN1-14* based on the age of onset and the causative gene mutated. The products of *CLN* genes are lysosomal and endosomal proteins, therefore NCLs are also classified as lysosomal storage disorders (LSDs)(Bennett and Hofmann, 1999; Jalanko and Braulke, 2009). The infantile form of disease, CLN1, presents as early as 6 months of age with progressive psychomotor deterioration, seizure, and death at approximately five years of age (Haltia, 2006; Jalanko and Braulke, 2009; Nita et al., 2016). CLN1 disease is caused by mutations in the gene *CLN1*, which encodes the enzyme palmitoyl-protein thioesterase 1 (PPT1)(Camp and Hofmann, 1993; Camp et al., 1994; Vesa et al., 1995; Jalanko and Braulke, 2009). PPT1 is a depalmitoylating enzyme responsible for the removal of palmitic acid from modified proteins (Camp and Hofmann, 1993; Lu and Hofmann, 2006).

Protein palmitoylation, the addition of a 16-carbon fatty acid (palmitic acid) to cysteine residues, is a crucial regulator of protein trafficking and function, particularly in neurons (Hayashi et al., 2005, 2009; Fukata et al., 2006; Kang et al., 2008; Fukata and Fukata, 2010; Han et al., 2015). This post-translational modification is mediated by palmitoyl acyltransferases (PATs) of

the DHHC enzyme family (Fukata et al., 2006; Fukata and Fukata, 2010). In contrast to other types of protein acylation, palmitoylation occurs via a reversible thioester bond (s-palmitoylation), permitting dynamic control over target protein interactions and function. Further, palmitoylated proteins require depalmitoylation prior to lysosomal degradation (Lu et al., 1996; Lu and Hofmann, 2006). Consequently, protein palmitoylation and depalmitoylation contribute significantly to mechanisms underlying synaptic plasticity and endosomal-lysosomal trafficking of proteins (Hayashi et al., 2005, 2009; Kang et al., 2008; Lin et al., 2009; Noritake et al., 2009; Fukata and Fukata, 2010; Mattison et al., 2012; Thomas et al., 2012, 2013; Fukata et al., 2013; Han et al., 2015). Indeed, PPT1 is a lysosome-targeted depalmitoylating enzyme that localizes to the axonal and synaptic compartments (Verkruyse and Hofmann, 1996; Ahtiainen et al., 2003; Kim et al., 2008). The synaptic association of PPT1 and prominence of palmitoylated synaptic proteins suggests that PPT1 influences synaptic functions through, at least, protein turnover. Many synaptic proteins undergo palmitoylation, including, but not limited to postsynaptic density protein 95 (PSD-95), all GluA subunits of AMPARs, and the GluN2A/2B subunits of NMDARs (Kang et al., 2008). However, the role of depalmitoylation in regulating synaptic protein function remains less clear.

N-methyl-D-aspartate receptors (NMDARs) are voltage-dependent, glutamate-gated ion channels consisting of two obligatory GluN1 subunits and two GluN2 subunits that undergo a developmental change (Cull-Candy et al., 2001; van Zundert et al., 2004; Lau and Zukin, 2007; Paoletti et al., 2013). NMDARs play a crucial role in synaptic transmission, postsynaptic signal integration, synaptic plasticity, and have been implicated in various neurodevelopmental and psychiatric disorders (Lau and Zukin, 2007; Lakhan et al., 2013; Paoletti et al., 2013; Yamamoto et al., 2015). NMDAR subunit composition, receptor localization, and downstream signaling mechanism undergo developmental regulation (Watanabe et al., 1992; Monyer et al., 1994; Sheng et al., 1994; Li et al., 1998; Stocca and Vicini, 1998; Tovar and Westbrook, 1999; Losi et

al., 2003; van Zundert et al., 2004; Paoletti et al., 2013; Wyllie et al., 2013). Specifically, GluN2B-containing NMDARs are expressed neonatally and display prolonged decay kinetics, which allows comparatively increased calcium influx thought to facilitate forms of synaptic plasticity critical for neurodevelopment (Sobczyk et al., 2005; Zhao et al., 2005, 2013; Zhang et al., 2008; Evans et al., 2012; Shipton and Paulsen, 2014). These GluN2B-containing receptors are supplanted at the synapse by diheteromeric GluN1/GluN2A NMDARs or triheteromeric (GluN1/GluN2A/GluN2B) receptors in response to experience-dependent neuronal activity (Quinlan et al., 1999b, 1999a; Tovar and Westbrook, 1999; Philpot et al., 2001; Liu et al., 2004; Paoletti et al., 2013; Tovar et al., 2013). This developmental switch of GluN2B- to GluN2A-containing NMDARs during brain maturation is mediated by the postsynaptic scaffolding receptors, SAP102 and PSD-95, respectively; SAP102-GluN2B-NMDAR complexes are replaced by PSD-95-GluN2A-NMDAR complexes in response to developmental, experience-dependent activity (Sans et al., 2000; van Zundert et al., 2004; Elias et al., 2008). While PSD-95, GluN2B, and GluN2A all undergo palmitoylation, how depalmitoylation regulates the turnover of these proteins, let alone during the GluN2B to GluN2A subunit switch, is unclear.

In the current study, we investigated the cellular and synaptic effects of PPT1-deficiency using the *Ppt1*$^{-/-}$ mouse model of CLN1 disease. We focused on the visual system in *Ppt1*$^{-/-}$ animals for two reasons. First, cortical blindness is a characteristic feature of CLN1 disease. Second, the rodent visual system is a well-studied model of cortical development and synaptic plasticity/maturation and it therefore serves as an optimal experimental model to examine the role of PPT1-mediated depalmitoylation during development. We found that lipofuscin accumulated in the *Ppt1*$^{-/-}$ visual cortex shortly after eye-opening at postnatal day (P) 14, a timing earlier than previously documented (Gupta et al., 2001). Using biochemistry and electrophysiology, we found impeded developmental NMDAR subunit switch from GluN2B to GluN2A in *Ppt1*$^{-/-}$ mice compared to wild-type (WT). This NMDAR disruption is associated with disrupted dendritic spine morphology

in vivo. To gain further mechanistic insight into neurodegeneration in CLN1, we used cultured cortical neurons and found that *Ppt1*$^{-/-}$ cells recapitulate the disrupted dendritic spine phenotype and GluN2B to GluN2A switch, leading to excessive extrasynaptic calcium transients and enhanced vulnerability to NMDA-mediated excitotoxicity. We directly examined protein palmitoylation state and found hyperpalmitoylation of GluN2B as well as Fyn kinase, which facilitates GluN2B surface retention, in *Ppt1*$^{-/-}$ neurons. Finally, we demonstrate that chronic treatment of *Ppt1*$^{-/-}$ neurons with palmitoylation inhibitors normalized GluN2B and Fyn kinase hyperpalmitoylation and rescued the enhanced susceptibility to excitotoxicity. Our results indicate that PPT1 plays a critical role in the developmental GluN2B to GluN2A subunit switch and synaptic maturation. Further, our results indicate that these dysregulated mechanisms contribute to CLN1 pathophysiology and may be shared features of common adult-onset neurodegenerative diseases.

2.2. Methods

2.2.1. Animals, group allocation, and data handling

All animal procedures were performed in accordance with the guidelines of the University of Illinois of Chicago Institutional Animal Care and Use Committee. *Ppt1*+/- (heterozygous) mice were obtained from Jackson Laboratory and maintained on 12h light/dark cycle with food and water ad libitum. Breeding of *Ppt1*+/- animals results in litters containing *Ppt1*$^{-/-}$, *Ppt1*+/-, and *Ppt1*+/+ (WT) animals. *Ppt1*$^{-/-}$ and WT littermate controls at specified developmental time points: P11, P14, P28, P33, P42, P60, P78, and P120 were genotyped in-house (Gupta et al., 2001) and used for experiments. Though we used the littermate control system, in which WT and *Ppt1*$^{-/-}$ mice from the same litters were compared, each n was treated independently in statistical testing (pair-wise tests were not used). Imaging data was acquired randomly for each experiment (no criteria for selecting cells, view fields, etc. except where anatomically necessary, e.g. Figure 2.1). All data was acquired and maintained without descriptive naming/labeling to ease randomization. Data was randomized by students within the lab prior to analysis by KPK.

2.2.2. Brain fractionation and immunoblotting

For collection of brain for biochemistry (immunoblot), *Ppt1*$^{-/-}$ and WT animals were decapitated following isoflurane anesthesia, then the brain was removed, and washed in ice cold PBS. The occipital cortex (visual cortex), hippocampus, and remaining cortex were separately collected on ice. Isolated visual cortices from *Ppt1*$^{-/-}$ and WT animals were homogenized in ice-cold synaptosome buffer (320mM sucrose, 1mM EDTA, 4mM HEPES, pH7.4 containing 1x protease inhibitor cocktail (Roche), 1x phosphatase inhibitor cocktail (Roche) and 1mM PMSF) using 30 strokes in a Dounce homogenizer. Aliquots for whole lysate (WL) were stored and the remaining sample was used for synaptosome preparation, performed as previously with slight modification. In brief, WLs were centrifuged at 1,000 x g to remove cellular debris, supernatant was then centrifuged at 12,000 x g for 15min to generate pellet P2. P2 was resuspended in

synaptosome buffer and spun at 18,000 x g for 15min to produce synaptosomal membrane fraction, LP1, which was used for downstream biochemical analyses (synaptosomes). For immunoblot, protein concentration of each sample was determined using BCA protein assay (Pierce). Samples were then measured to 20μg total protein in 2x Laemmli buffer containing 10% β-mercaptoethanol (Bio-rad), boiled at 70°C for 10min and loaded into 10% tris-glycine hand cast gels (Bio-rad), or 4-20% precast gels (Bio-rad) for electrophoresis (110V, 1.5-2h). Proteins were wet-transferred to PVDF membranes (Immobilon-P, Millipore), blocked in TBS, pH7.4 containing 5% non-fat milk and 0.1% Tween-20 (TBS-T+5% milk). Membranes were incubated in primary antibody solutions containing 2% BSA in TBS-T for 2h at RT or overnight at 4°C. Primary antibodies were used as follows: GluN2A (Cat: NB300-105, 1:1,000, Novus Biologicals), GluN2B (Cat: 75/097, 1:1,000, Neuromab), GluN1 (Cat: 75/272, 1:1000, Neuromab), PSD-95 (Cat: K28/74, 1:2,000, Neuromab), SAP102 (Cat: N19/2, 1:2,000, Neuromab), Fyn kinase (Cat: 4023, 1:1,000, Cell signaling), PPT1 (kindly provided by Dr. Sandra Hofmann, and β-actin-HRP (Cat: MA5-15739-HRP, 1:2,000, ThermoFisher). Membranes were then incubated with appropriate secondary, HRP-conjugated antibodies (Jackson ImmunoResearch) at either 1:5,000, 1:10,000, or 1:30,000 (PSD-95 only) for 1h at RT. Visualization and quantification was performed using Pierce SuperSignal ECL substrate and Odyssey-FC chemiluminescent imaging station (LI-COR). Signal density for each synaptic protein was measured using the LI-COR software, Image Studio Lite (version 5.2) and was normalized to the signal density for β-actin loading control for each lane. A total of four independent experiments was performed for both WL and LP1 analyses, with a minimum of two technical replicates for each experiment averaged together.

2.2.3. Histology and autofluorescent lipopigment quantification

Ppt1$^{-/-}$ and WT mice were anesthetized using isoflurane and transcardially perfused with ice cold PBS (pH 7.4, ~30ml/mouse) followed by 4% paraformaldehyde (PFA) in PBS (~15ml/mouse). Brains were removed and post-fixed for 48h at 4°C in 4% PFA and transferred to

PBS, pH7.4 containing 0.01% sodium azide for storage if necessary. Brains from *Ppt1*$^{-/-}$ and WT animals were incubated in 30% sucrose solution for 48h prior to sectioning using Vibratome 1000 in cold PBS. For imaging and quantification of AL, sagittal sections were cut at 100μm. Every third section was mounted on Superfrost Plus microscope slides (VWR) using Vectamount mounting media containing DAPI (Vector Laboratories, cat: H-5000). Interlaced/overlapping images of visual cortex area V1 from the cortical surface to subcortical white matter (or subiculum), which was localized using Paxino's mouse atlas (sagittal), were collected for 2-4 sections from each animal using a Zeiss LSM710 confocal laser scanning microscope at 40x magnification (excitation at 405nm to visualize DAPI and 561nm to visualize AL). All sections were imaged using identical capture conditions. Quantification of AL was performed by thresholding images in FIJI (NIH), generating a binary mask of AL-positive pixels (satisfied threshold) vs. background. The identical threshold was applied to each image (from cortical surface to subcortical white matter and across animals). Percent area occupied by AL puncta that satisfied the threshold was then calculated using the "analyze particles" tool in FIJI. This analysis was performed for 2-4 sections (total of ~10-20 images, as imaging an entire cortical column is typically 5 interlaced images) from each animal and averaged together to give a single value, representative of the total area occupied by AL in the cortical column imaged. Three to six animals per group were analyzed this way and averaged to give the mean area occupied by AL at each time point, for both genotypes (n=4-6 animals/group).

2.2.4. Electrophysiology

WT and *Ppt1*$^{-/-}$ animals at P42 were deeply anesthetized using isoflurane drop method and decapitated. Brains were resected in semi-frozen oxygenated (95% O2 and 5% CO2) artificial cerebrospinal fluid (aCSF, in mM: NaCl 85, sucrose 75, KCl 2.5, CaCl2 0.5, MgCl2 4, NaHCO3 24, NaH2PO4 1.25, D-glucose 25, pH 7.3), and 350μm sections containing visual cortex area V1 were sectioned using a Leica VT1200 S vibratome in semi-frozen aCSF. After recovery (1h) in

aCSF at 30°C, sections were transferred to the recording chamber, perfused at 2ml/min with aCSF at 30°C. Following localization of visual cortex area V1 using Paxinos mouse brain atlas, a stimulating electrode was placed in layer IV, and pyramidal neurons from layer II/III were blindly patched (patch solution in mM: CsOH monohydrate 130, D-Gluconic acid 130, EGTA 0.2, MgCl2 1, CsCl 6, Hepes 10, Na2-ATP 2.5, Na-GTP 0.5, Phoshocreatine 5, QX-314 3; pH 7.3, osmolarity 305 mOsm) and recorded in voltage clamp mode at +50mV (VH) to remove Mg2+ block from NMDARs. NMDA-EPSCs were pharmacologically isolated via addition of CNQX (10μM), (+)-Bicuculline (60 μM) and SCH 50911 to block AMPA, GABAA and GABAB receptors, respectively. Stimulation intensity was titrated to give a saturating postsynaptic response, and EPSCs were then recorded, averaging 5-10 sweeps. The decay phase of the averaged NMDAR-EPSCs were then fitted to a double exponential (Stocca and Vicini, 1998; Vicini et al., 1998). We calculated for each cell: the amplitude of the fast (Af) component (GluN2A-mediated), the amplitude of the slow (As) component (GluN2B-mediated), the contribution of the fast component Af/ Af+As to the overall decay phase, the τ fast (τf), the τ slow (τs) and the τweighted (τw) in WT and *Ppt1*$^{-/-}$ mice following this formula: $\tau w = \tau f x (Af/Af+As) + \tau s x (As/Af+As)$ (n=8/4 (cells/animals), WT; n=8/5 PPT-KO). For experiments in Figure 2.3E, baseline NMDAR-EPSCs were recorded as typical and compared to those following 30 minutes of bath-infused Ro 25-6981 (3μM).

2.2.5. In utero electroporation

In utero electroporation was performed as previously described (Yoshii et al., 2011). Timed-pregnant dams at E16.5 were deeply anesthetized via isoflurane (3% induction, 1-1.5% for maintenance of anesthesia during surgery) and laparotomized. The uterus was then externalized and up to ~1μl of solution containing GFP construct (2μg/μl) and fast green dye was delivered into the left lateral ventricle through the uterine wall using a micropipette. Using an ECM 830 Square Wave electroporator (Harvard Apparatus, Holliston MA), brains were electroporated with 5 pulses of 28V for 50msec at intervals of 950msec at such an angle to transfect neurons in

visual cortex. After recovery, pregnancies were monitored, and pups were delivered and nursed normally. Electroporated pups were genotyped, raised to P33, and sacrificed via transcardial perfusion as described above. Electroporated brains from WT and *Ppt1*$^{-/-}$ mice (procedure schematized in Figure 2.4A) were sectioned and sequentially mounted. Electroporated neurons in visual cortex (Figure 2.4B) were imaged to capture all apical neurites and 3D reconstructed images were analyzed in Imaris (Bitplane) for dendritic spine characteristics known to be associated with synaptic maturity (spine density, spine length, spine volume, and spine head volume). At least two z-stack images (typically >100 z-planes/image) were stitched together to capture the prominent apical neurites and extensions into the cortical surface for each cell. Each stitched image, equivalent to one cell, was considered one n.

2.2.6. Primary cortical neuron culture

For primary cortical neuron cultures, embryos from timed-pregnant, *Ppt1*-/+ dams were removed, decapitated, and cortices resected at embryonic day (E) 15.5. All dissection steps were performed in ice cold HBSS, pH7.4. Following cortical resection, tissue from each individually-genotyped embryo were digested in HBSS containing 20U/ml papain and DNAse (20min total, tubes flicked at 10min) before sequential trituration with 1ml (~15 strokes) and 200μl (~10 strokes) pipettes, generating a single-cell suspension. For live-cell imaging experiments, cells were counted then plated at 150,000-180,000 cells/well in 24-well plates containing poly-D-lysine/laminin-coated coverslips. For biochemical experiments, i.e. immunoblot, APEGS assay in vitro, cells were plated on poly-D-lysine/laminin-coated 6-well plates at 1,000,000 cells/well. Cells were plated and stored in plating medium (Neurobasal medium containing B27 supplement, L-glutamine and glutamate) for 3-5 DIV, before replacing half medium every 3 days with feeding medium (plating medium without glutamate). Cultures used in chronic palmitoylation inhibitor treatment were exposed to either DMSO (vehicle), 2-BP (1μm, Sigma, cat: 238422) or cerulenin (1μm, Cayman Chemicals, cat: 10005647) every 48 hours between DIV 12 and 18.

2.2.7. Primary cortical neuron harvest and immunoblotting

Primary cortical neurons from E15.5 WT and *Ppt1*$^{-/-}$ embryos were cultured for 7, 10, or 18 DIV prior to harvest for immunoblot or APEGS assay (only DIV18 used for APEGS). To harvest protein extracts, cells were washed 2x with ice-cold PBS before addition of lysis buffer containing 1% SDS and protease inhibitor cocktail, 500μl/well. Cells were incubated and swirled with lysis buffer for 5 minutes, scraped from the plate, triturated briefly, and collected in 1.5ml tubes. Lysates were centrifuged at 20,000g for 15min to remove debris, and the supernatant was collected for biochemical analysis. Immunoblotting analyses were performed as above. APEGS assay was carried out as described in the following section.

2.2.8. APEGS assay on primary cortical neuron lysates

The APEGS assay was performed as utilized in (Yokoi et al., 2016) and recommended by Dr. M. Fukata (personal communication, 06/2018). Briefly, cortical neuron lysates were brought to 150μg total protein in a final volume of 0.5ml buffer A (PBS containing 4% SDS, 5mM EDTA, protease inhibitors, remaining sample used in aliquots for “input”). Proteins were reduced by addition of 25mM Bond-Breaker™ TCEP (0.5M stock solution, ThermoFisher) and incubation at 55°C for 1h. Next, to block free thiols, freshly prepared N-ethylmaleimide (NEM) was added to lysates (to 50mM) and the mixture was rotated end-over-end for 3h at RT. Following 2x chloroform-methanol precipitation (at which point, protein precipitates were often stored overnight at -20°C), lysates were divided into +hydroxylamine (HA) and –HA groups for each sample, which were exposed to 3 volumes of HA-containing buffer (1M HA, to expose palmitoylated cysteine residues) or Tris-buffer control (-HA, see Figure 2.10), respectively, for 1h at 37°C. Following chloroform-methanol precipitation, lysates were solubilized and exposed to 10mM TCEP and 20mM mPEG-5k (Laysan Bio Inc., cat# MPEG-MAL-5000-1g) for 1h at RT with shaking (thereby replacing palmitic acid with mPEG-5K on exposed cysteine residues). Following the final chloroform-methanol precipitation, samples were solubilized in a small volume (60μl) of PBS

containing 1% SDS and protein concentration was measured by BCA assay (Pierce). Samples were then brought to 10μg protein in laemmli buffer with 2% β-mercaptoethanol for immunoblot analyses as above. Quantification of palmitoylated vs. non-palmitoylated protein was carried out as above, with the added consideration that palmitoylated protein was taken as the sum of all (typically two-three distinct bands, see Figure 2.11) bands demonstrating the APEGS-dependent molecular weight shift compared to the –HA control lane. Non-palmitoylated protein was quantified from the band size-matched to the –HA control sample. The ratio was taken as the palmitoylated protein divided by non-palmitoylated protein, all divided by β-actin control from the same lane.

2.2.9. Transfection, dendritic spine and calcium imaging analyses

For analysis of dendritic spine morphology, WT and *Ppt1*$^{-/-}$ neurons were transfected between DIV6-8 with GFP using Lipofectamine® 2000 (ThermoFisher) according to manufacturer protocol with a slight modification. Briefly, GFP DNA construct (~2μg/μl, added at ~1μg/well) was mixed with Lipofectamine-containing Neurobasal medium, incubated for 30min to complex DNA-Lipofectamine, equilibrated to 37^{0}C, and added to the cells 250μl/well for 1-1.5h. Following incubation, complete medium was returned to the cells. Neurons were then imaged at DIV15 and DIV20 for dendritic spine morphology using a Zeiss LSM 710 confocal microscope equipped with a heated stage at 63x magnification. GFP-positive neurons were imaged at 0.2μm Z-plane interval (typically 25 Z-planes/image). Three to seven overlapping Z-stacks were stitched to visualize an entire neuron. Z-stack images were collapsed into a single plane and dendritic spines were analyzed using semi-automated image processing software, Imaris (Bitplane). The same dendrite and dendritic spine processing parameters were used for each image. For DIV15: n=4-5 neurons/group, 3-independent experiments, WT=21,514 spines; *Ppt1*$^{-/-}$=18,013 spines. For DIV20: n=3 neurons/group, 2-independent experiments, WT=11,335 spines; *Ppt1*$^{-/-}$=9,958 spines.

To directly image calcium signals in WT and *Ppt1*$^{-/-}$ neurons, cells were transfected as above using the construct encoding GCaMP3 (see Acknowledgments) at DIV8. A subset of cells (Figure 2.10) were treated with 2-BP (1μM) or cerulenin (1μM) from DIV12-18. Cells were grown to DIV18 then imaged at room temperature in Tyrode's solution (imaging medium, 139mM NaCl, 3mM KCl, 17mM NaHCO3, 12mM glucose, and 3mM CaCl2) for a maximum of 15min using a Mako G-507B camera mounted onto a Leica inverted microscope. Videos were acquired at ~7 frames per second using StreamPix software (NorPix). A maximum of 5min per neuron was recorded (thus, minimum 3 neurons per coverslip were acquired). N=3-6 neurons/group, three independent experiments. For treatment with Ro 25-6981, neurons were imaged at baseline for 2-2.5min before adding Ro 25-6981 (1μM) directly to the imaging medium. Neurons were then imaged for an additional 2.5min.

To analyze the area under the curve (AUC) and width (diffusion distance) of calcium transients, 500-600 frames from the middle of each video (average frame count for whole videos= ~2200 frames) for WT, *Ppt1*$^{-/-}$, and *Ppt1*$^{-/-}$ palmitoylation inhibitor-treated (treatment performed as in 'Primary cortical neuron culture section; DIV12-18, every other day, 1μM) neurons were analyzed using FIJI (NIH). Dendritic segments, excluding primary dendrites, were traced using a segmented line ROI with pixel width of 50, which reliably encompassed the dendritic segment and accompanying dendritic spines. Next, the following macro derived from the ImageJ forum (http://forum.imagej.net/t/how-to-obtain-xy-values-from-repeated-profile-plot/1398) was run on each individual ROI:

```
macro "Stack profile Plot" {
   collectedValues="";
   ymin = 0;
   ymax = 255;
   saveSettings();
   if (nSlices==1)
     exit("Stack required");
   run("Profile Plot Options...",
```

```
  "width=400 height=200 minimum="+ymin+" maximum="+ymax+" fixed");
setBatchMode(true);
stack1 = getImageID;
stack2 = 0;
n = nSlices;
for (i=1; i<=n; i++) {
   showProgress(i, n);
   selectImage(stack1);
   setSlice(i);
   run("Clear Results");
    profile = getProfile();
   for (j=0; j<profile.length; j++) {
      collectedValues=collectedValues+profile[j] + "\t";
   }
   collectedValues=collectedValues+"\n";

   run("Plot Profile");
   run("Copy");
   w = getWidth; h = getHeight;
   close();
   if (stack2==0) {
      newImage("Plots", "8-bit", w, h, 1);
      stack2 = getImageID;
   } else {
      selectImage(stack2);
      run("Add Slice");
   }
   run("Paste");
}
f = File.open("C:/“cell#, ROI #”.xls");
print(f, collectedValues);
setSlice(1);
setBatchMode(false);
restoreSettings();
}
```

This gives the fluorescence intensity at each pixel along the ROI across the time/frame dimension. The background fluorescence for each ROI was then subtracted by averaging the fluorescence across the ROI in an inactive state (no calcium transients), giving the measure $\Delta F/F0$ when examined across time/frame. For each ROI (up to 1265 pixels in length), each calcium transient at individual synaptic sites (dendritic spines or dendritic shafts) was averaged. Those averages were then compiled to give the average transient signal, which was then used to analyze the AUC and calcium diffusion distance (n=3 neurons/group/experiment, 3 distinct cultures: WT=55 ROIs, 185 synaptic sites, 1630 transients; *Ppt1*$^{-/-}$=38 ROIs, 131 synaptic sites, 1281

transients; *Ppt1*$^{-/-}$ + 2-BP= 28 ROIs, 82 synaptic sites, 420 transients; *Ppt1*$^{-/-}$ + cerulenin= 24 ROIs, 82 synaptic sites, 540 transients). For Ro 25-6981-treated neurons, the same protocol was followed with the exception that calcium transients at an individual synaptic site were split into "before application" and "after application" groups.

To analyze synaptic synchrony, $\Delta F/F_0$ measurements for 20 randomly-chosen sites of synaptic activity per neuron were correlated across the time dimension (500 frames of each video). A correlation matrix was generated to determine the average correlation of each synaptic site with all other chosen sites. The average values for each synaptic site, for 5 neurons/group are plotted in Figure 2.7.

2.2.10. NMDA toxicity assays

To measure cell viability following exposure of WT and *Ppt1*$^{-/-}$ neurons to NMDA and glycine, neurons were plated as above and grown to DIV18. For experiments presented in Figure 2.8, feeding medium was removed from neurons, stored at 37°C, and replaced with B27-free Neurobasal medium with or without NMDA/glycine at the following concentrations: 10/1μM, 100/10μM, or 300/30μM (ratio maintained at 10:1). Cells were incubated for 2h at 37°C in treatment medium. Following incubation, treatment medium was removed and replaced with the original feeding medium. Cells were then incubated an additional 22h before addition of PrestoBlue® cell viability reagent (ThermoFisher). At 24h, fluorescence intensity of each well was measured using a Beckman Coulter DTX 800 Multimode Detector. Cell viability for each treatment condition was calculated and expressed as percentage of vehicle-treated control wells (no pretreatment, no NMDA application). Experiments in Figure 2.9 were performed similarly except that cultures were pretreated with either DMSO (vehicle), 2-BP (1μM, Sigma, cat: 238422) or cerulenin (1μM, Cayman Chemicals, cat: 10005647) every 48 hours between DIV 11 and 18.

2.2.11. AL accumulation in vitro, palmitoylation inhibitor treatment, imaging and analysis

WT and *Ppt1*$^{-/-}$ neurons were cultured as above. To examine AL deposition, neurons were grown to DIV18-20, fixed in 4% PFA for 10min at RT, and stored in PBS for up to 72 hours prior to immunocytochemistry. To examine AL accumulation alone, cells were immunostained for the microtubule associated protein, MAP2 (Millipore Sigma, cat: AB5622) and mounted in DAPI-containing mounting medium. To assess AL localization, DIV18-DIV20 neurons were immunostained for MAP2 and LAMP-2 (Abcam, cat: ab13524). Neurons were then imaged at random using a Zeiss LSM 710 confocal microscope at 63x magnification. Z-stacks (0.4μm Z-plane interval, 12-22 Z-planes/image) were taken at 512 x 512 pixel density. 7-10 neurons/group for three independent experiments.

To semi-automatically analyze the percentage of AL-containing cells, the cytosolic area covered by AL deposits, and the cytosolic area covered by lysosomes, images immunostained for MAP2 and LAMP-2 were processed in FIJI. Each channel of the image: LAMP-2 (488nm), MAP2 (633nm), DAPI (405nm), AL (561nm) was thresholded separately as to display only the lysosomes, cell soma, the nucleus, and AL deposits, respectively. Thresholds were kept identical between images. Next, the areas of these compartments/deposits were measured using the "analyze particles" tool restricted to an ROI tracing the cell soma. Lysosomes needed to have a circularity of >0.5 to avoid counting small clusters of lysosomes as a single unit (Bandyopadhyay et al., 2014; Grossi et al., 2016). To measure AL deposits, the same approach was used with the additional constraint: AL deposits were required to have a circularity >0.4 and comprise more than 8 adjacent pixels. Cytosolic area was calculated by measuring MAP2 signal area and subtracting the area occupied by DAPI stain.

For line scan analysis of the representative, vehicle treated WT and *Ppt1*$^{-/-}$ images in Figure 2.9.1, images were loaded in Fiji and channels split individually. Next, line scans of the cell

soma across areas encompassing somatic lysosomes and, in the case of *Ppt1*$^{-/-}$ neurons, AL deposits, were drawn manually as a line ROI. The 'plot profile' tool was then used to obtain the grey scale values for the fluorescence intensity of each channel across the same ROI. These values were then plotted either individually (as in B and E) or plotted with LAMP2 and AL signals overlapping (as in C and F).

2.2.12. Immunocytochemistry

Coverslips were stained in runs so that all experimental and control groups were immunostained simultaneously. Coverslips were washed 3x with TBS, permeabilized for 20min at RT with TBS containing 0.5% Triton X-100 and blocked for 1h at RT in TBS containing 0.1% Triton X-100 and 5% BSA. Then, primary antibody (MAP2 or LAMP-2) at 1:400 dilution was added to coverslips in TBS containing 0.1% Triton X-100 and 1% BSA and incubated for 2h at RT or overnight at 4^0C. Following 4X washes with TBS containing 0.1% Triton X-100, cells were incubated with 1:400 secondary, fluorophore-linked antibody (either Alexa Fluor 488, cat. #: A-11034, A-11006; or Alexa Fluor 633, ThermoFisher, cat. #: A-21070) in TBS containing 0.1% Triton x-100 and 1% BSA. These steps are repeated for double immunostained cells. For LAMP-2/MAP2 double immunostaining, saponin was used in place of Triton X-100 at the same concentrations. Coverslips are then mounted on SuperFrost Plus slides in DAPI Vectamount medium.

TABLE 1. Key resources table #1

Reagent type (species) or resource	Designation	Source or reference	Identifiers	Additional information
strain, strain background (M*us musculus*)	B6;129-Ppt1^{tm1Hof}/J	Jax stock #: 004313	Gupta, PNAS, 2001; RRID:MGI:004313	
antibody	Rabbit polyclonal anti-GluN2A	Novus Biologicals	Cat: NB300-105; RRID:AB_10001400	(1:1000)
antibody	Mouse monoclonal anti-GluN2B	UC Davis/NIH NeuroMab Facility	Cat: 75/097; RRID:AB_10673405	(1:1000)
antibody	Mouse monoclonal anti-GluN1	UC Davis/NIH NeuroMab Facility	Cat: 75/272; RRID:AB_11000180	(1:1000)
antibody	Mouse monoclonal anti-PSD-95	UC Davis/NIH NeuroMab Facility	Cat: K28/74; RRID:AB_2315909	(1:2000)
antibody	Mouse monoclonal anti-SAP102	UC Davis/NIH NeuroMab Facility	Cat: N19/2; RRID:AB_2261666	(1:2000)
antibody	Rabbit polyclonal anti-Fyn	Cell Signaling	Cat: 4032	(1:1000)
antibody	Rabbit polyclonal anti-PPT1	Gift from Sandra Hofmann		(1:500); Dr. Hofmann
antibody	Mouse monoclonal anti-β-actin-HRP	ThermoFisher Scientific	Cat: MA5-15739-HRP; RRID:AB_2537667	(1:2000)
antibody	Rabbit polyclonal anti-MAP2	Millipore Sigma	Cat: AB5622; RRID:AB_91939	(1:400)
antibody	Rat monoclonal anti-LAMP2	abcam	Cat: ab13524; RRID:AB_2134736	(1:400)
recombinant DNA reagent	pEF-GFP	Addgene	Plasmid: 11154	Drs. Matsuda and Cepko
recombinant DNA reagent	G-CaMP3	Addgene	Plasmid: 22692	Dr. Looger
commercial assay or kit	PrestoBlue cell viability assay	ThermoFisher Scientific	Cat: A13261	

chemical compound, drug	2-bromopalmitate	Sigma	Cat: 238422	Treatment: 1μM
chemical compound, drug	cerulenin	Cayman Chemicals	Cat: 10005647	Treatment: 1μM
software, algorithm	Fiji			

2.3. Results

To understand synaptic dysregulation in CLN1 disease, we utilized the visual cortex of *Ppt1*$^{-/-}$ animals as a model system. The rodent visual cortex undergoes timed, experience-dependent plasticity, which has been well-characterized at the systemic, cellular, and molecular levels (Bear et al., 1990; Gordon and Stryker, 1996; Hensch et al., 1998; Quinlan et al., 1999a; Fagiolini and Hensch, 2000; Mataga et al., 2001, 2004; Philpot et al., 2001; Desai et al., 2002; Yoshii et al., 2003; Hensch, 2005; Cooke and Bear, 2010). We examined WT and *Ppt1*$^{-/-}$ littermates at the following ages: P11, P14, P28, P33, P42, P60, P78, P120, which correspond to particular developmental events in visual cortex. In mice, P11 and P14 are prior to and just after eye opening (EO) respectively. Further, the critical period in the visual cortex peaks at P28 and closes from P33 to P42. Postnatal day 60, P78, and P120 were selected as adult time points. We determined whether experience-dependent synaptic maturation is altered during the progression of CLN1 pathology.

2.3.1. Lipofuscin deposits immediately following eye opening in visual cortex of *Ppt1*$^{-/-}$ mice

Although it remains controversial whether lipofuscin is toxic to neurons or an adaptive, neuroprotective mechanism, its accumulation correlates with disease progression. Therefore, we examined lipofuscin deposition in the visual cortex as a marker of pathology onset and progression. Lipofuscin aggregates are readily detectable as autofluorescent lipopigments (ALs) without staining under a confocal microscope. To examine the temporal and spatial accumulation of ALs in *Ppt1*$^{-/-}$ mice, we performed quantitative histology on the visual cortex (area V1) of WT and *Ppt1*$^{-/-}$ mice during early development. Visual cortical sections were imaged at the above-mentioned developmental time points and ALs were quantified in a laminar-specific manner. We found that ALs are detectable first at P14 in *Ppt1*$^{-/-}$ visual cortex, earlier than previously reported at three or six months (**Figure 2.1A-C**)(Gupta et al., 2001; Blom et al., 2013). Further, AL

accumulated rapidly through the critical period (Berardi et al., 2000; Hensch, 2005; Maffei and Turrigiano, 2008) and plateaued by adulthood (P60) (**Figure 2.1A-C**). This result suggests that neuronal AL load is saturable, and that this saturation occurs early on in disease, as *Ppt1*$^{-/-}$ animals do not perish until around 10 months of age.

Whether lipofuscin accumulation is directly neurotoxic or not, profiling the temporospatial and sub-regional pattern of AL deposition will be valuable for assessing therapeutic interventions in future studies. The pattern of deposition revealed herein suggests a correlation between systemic neuronal activation and AL accumulation., as we found that AL deposition started immediately following EO, the onset of patterned visual activity, and accumulated rapidly during development (**Figure 2.1A, C, Table 2**). These findings suggest that neuronal activity or experience-dependent plasticity may be linked to lipofuscin deposition.

Figure 2.1. ALs deposit immediately following eye opening in visual cortex of *Ppt1*$^{-/-}$ mice.

(A) Representative composite confocal images through area V1 of visual cortex in WT (top) and *Ppt1*$^{-/-}$ mice (bottom) during development and into adulthood. DAPI nuclear stain (blue, 405nm excitation) and AL signals (red, 561nm excitation) are visualized. Cortical layers are marked (left). Scale=50μm. Note that scale bars for P11 and P14 images are enlarged to account for reduced cortical thickness at these ages. **(B)** Quantification of the mean percent area occupied by ALs through all cortical layers (see methods). *Ppt1*$^{-/-}$ and WT were compared (n=4-6 animals/group) at each age using t-test and the significance was indicated as follows: *p<0.05, **p<0.01, and ***p<0.001. Differences between two consecutive ages (e.g. *Ppt1*$^{-/-}$ P14 vs. P11) is denoted: * p<0.05 and ** p<0.01 where indicated. Error bars represent s.e.m. **(C)** Cortical layer-specific quantification of area occupied by ALs separated by each cortical layer (x-axis) and age (z-axis). Averaged values, s.e.m., and n for each condition are represented in **Table 2**.

Figure 2.1. ALs deposit immediately following eye opening in visual cortex of *Ppt1*$^{-/-}$ mice.

TABLE 2. Autofluorescent lipopigment accumulation values and sample information

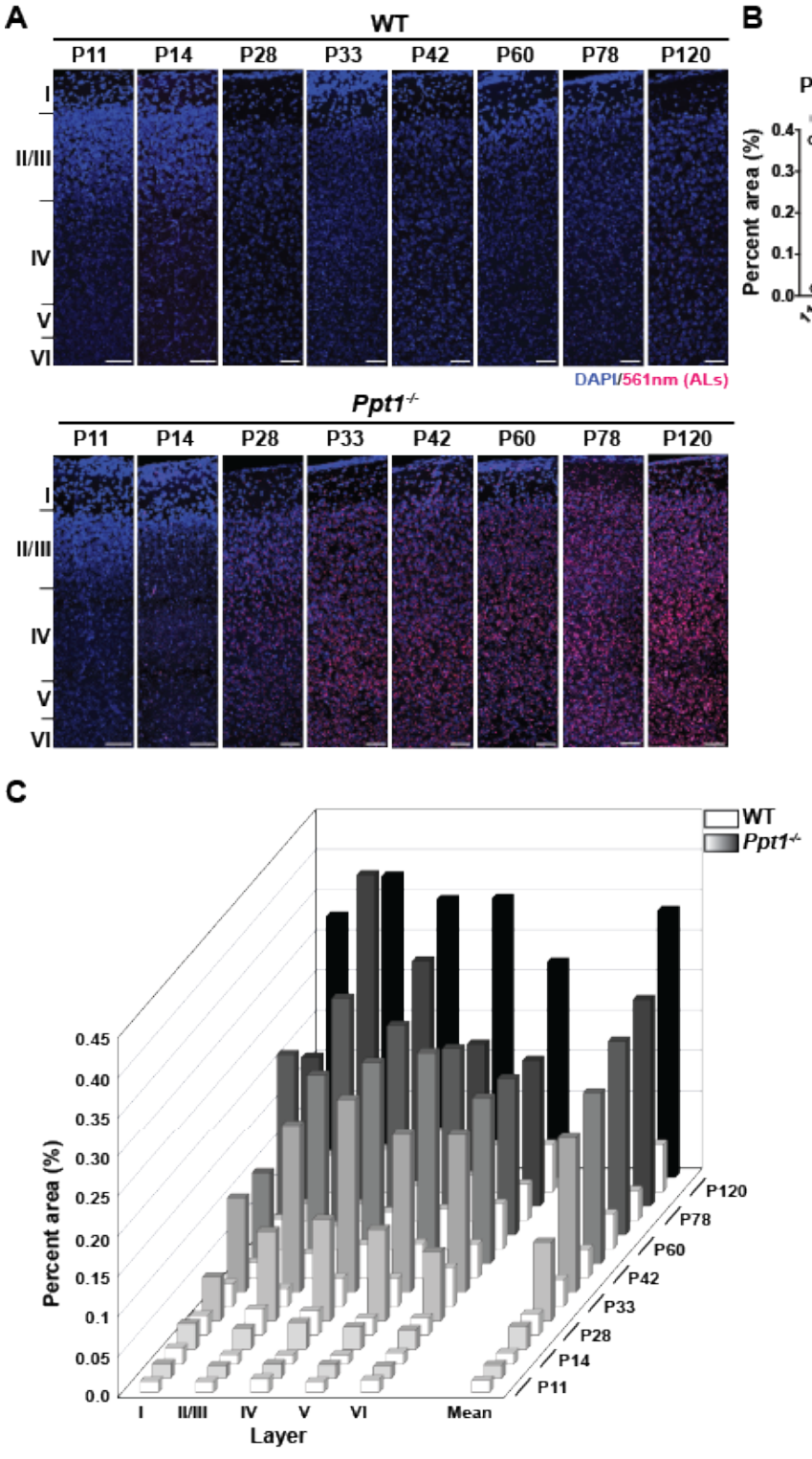

	Layer	WT			Mutant		
		Mean	SEM	n	Mean	SEM	n
P11	1	0.014726	0.051334	4	0.018432	0.020171	5
	2/3	0.014029	0.002		0.015746	0.001837	
	4	0.017716	0.005554		0.018337	0.003265	
	5	0.013956	0.003186		0.017544	0.002825	
	6	0.016376	0.004648		0.015585	0.009563	
P14	1	0.020027	0.003256	3	0.032299	0.003201	6
	2/3	0.012068	0.003681		0.026184	0.003002	
	4	0.011678	0.001782		0.03401	0.004257	
	5	0.011427	0.003523		0.028279	0.003798	
	6	0.014201	0.004393		0.024822	0.008465	
P28	1	0.025066	0.030382	4	0.054899	0.050557	5
	2/3	0.032533	0.008919		0.111296	0.020856	
	4	0.030768	0.01448		0.125996	0.021164	
	5	0.021373	0.004357		0.113626	0.017283	
	6	0.021647	0.007201		0.086127	0.013937	
P33	1	0.028305	0.073043	5	0.117601	0.023632	6
	2/3	0.022777	0.008171		0.21026	0.013193	
	4	0.035548	0.011861		0.242556	0.034924	
	5	0.035123	0.010396		0.197036	0.074042	
	6	0.048262	0.010111		0.19617	0.024701	
P42	1	0.019019	0.060801	4	0.113172	0.012468	5
	2/3	0.030153	0.011804		0.237298	0.021055	
	4	0.041546	0.011364		0.253448	0.029969	
	5	0.042801	0.009777		0.265477	0.041234	
	6	0.041961	0.00768		0.209104	0.035667	
P60	1	0.037639	0.008034	4	0.227769	0.053888	6
	2/3	0.029154	0.009176		0.297558	0.059318	
	4	0.046682	0.014308		0.263665	0.052311	
	5	0.049726	0.007089		0.234832	0.038626	
	6	0.056535	0.011388		0.197509	0.041092	
P78	1	0.020962	0.005615	3	0.188845	0.002442	3
	2/3	0.020522	0.001178		0.415522	0.007618	
	4	0.043183	0.012138		0.308193	0.037127	
	5	0.055858	0.004104		0.205356	0.055491	
	6	0.045009	0.004334		0.184726	0.003858	
P120	1	0.046265	0.023688	3	0.32851	0.141037	3
	2/3	0.053516	0.029019		0.378299	0.065604	
	4	0.077311	0.038016		0.349415	0.062099	
	5	0.058412	0.038213		0.35062	0.059149	
	6	0.059228	0.040012		0.271503	0.068553	

2.3.2. NMDAR subunit composition is biased toward immaturity in *Ppt1*$^{-/-}$ visual cortex

To examine the role of PPT1 in excitatory synapse function, we focused on the NMDAR subunits, GluN2B and GluN2A, which are both palmitoylated (Hayashi et al., 2009). Developmental GluN2B to GluN2A subunit change (Paoletti et al., 2013) is critical for NMDAR function and maturation, which facilitates refinement of neural circuits and a higher tolerance to glutamate-mediated excitotoxicity (Hardingham and Bading, 2002, 2010; Hardingham et al., 2002). Furthermore, previous work shows evidence for NMDA-induced excitotoxicity in the pathogenesis of CLN1 (Finn et al., 2012). We biochemically analyzed WT and *Ppt1*$^{-/-}$ visual cortices from P11 to P60, and measured levels of GluN2B and GluN2A subunits in whole lysates and synaptosomes of WT and *Ppt1*$^{-/-}$ visual cortices. Whereas GluN2B levels were comparable between WT and *Ppt1*$^{-/-}$ at all ages, GluN2A levels in synaptosomes were significantly lower in *Ppt1*$^{-/-}$ than WT (**Figure 2.2A**). This decrease was present at time points during, and just following, the critical period in visual cortical development (P33, P42, and P60). When analyzed as a ratio of GluN2A/GluN2B, a robust and persistent decrease is observed in *Ppt1*$^{-/-}$ visual cortex (**Figure 2.2B**). GluN1 levels were unchanged between WT and *Ppt1*$^{-/-}$ in synaptosomes (**Figure 2.2C**), indicating the selective obstruction of GluN2A incorporation into NMDARs.

The developmental shift from GluN2B-containing NMDARs to synaptic GluN2A-containing NMDARs is mediated by the postsynaptic scaffolding proteins, SAP102 and PSD-95 (Townsend et al., 2003; van Zundert et al., 2004; Elias et al., 2008). SAP102 preferentially interacts with GluN2B-containing NMDARs, which are enriched neonatally (Sans et al., 2000; van Zundert et al., 2004; Zheng et al., 2010; Chen et al., 2011). In contrast, PSD-95 has greater affinity to GluN2A-containing NMDARs, particularly in the mature brain (Sans et al., 2000; van Zundert et al., 2004; Dongen, 2009; Yan et al., 2014). Thus, we examined the expression of these scaffolding proteins in WT and *Ppt1*$^{-/-}$ visual cortex. Similar to the results obtained for GluN2B and GluN2A,

while SAP102 levels remained unchanged, we observed a decrease in PSD-95 levels at P33-P60, the same developmental time points where GluN2A expression was reduced (**Figure 2.2D**). Together, these results suggest reduced incorporation and scaffolding of GluN2A-containing NMDARs in *Ppt1*$^{-/-}$ synapses, indicating immature or dysfunctional synaptic composition.

Next, we measured PPT1 protein level across the same time points in WT animals to examine whether the expression profile of PPT1, and thus presumably its cellular activity, temporally correlated with the observed reductions in mature synaptic components in *Ppt1*$^{-/-}$ animals. Indeed, PPT1 expression in synaptosomes is low at P11 and P14 and increases with age, reaching peak levels between P33 and P60 (**Figure 2.2E**). This expression profile correlates with the time course of AL accumulation (**Figure 2.1B and C**) and fits with the notion that PPT1 activity at the synapse plays a role in neurodevelopmental processes.

To examine whether the reduction in GluN2A is due to selective exclusion from the postsynaptic site or alterations in the total protein amount, we also measured NMDAR subunit levels in whole lysates. These findings closely match our findings in synaptosomes. Namely, GluN2A levels showed reductions in *Ppt1*$^{-/-}$ lysates beginning at the same time point (P33) (**Figure 2.2.1A**), while GluN2B levels were stable (**Figure 2.2.1B**). The GluN2A/2B ratios in *Ppt1*$^{-/-}$ whole lysates were also lower than those in WT lysates and the reduction was comparable to that observed in synaptosomes (**Figure 2.2.1C**). GluN1 levels, however, were unaltered between genotypes (**Figure 2.2.1D**), again indicating a selective reduction in the expression of GluN2A. Interestingly, while PPT1 levels in whole lysates were, similarly to synaptosomes, low at P11 and P14, expression subsequently peaked at P28 and P33 before declining at P60 (**Figure 2.2.1E**). Together, these results indicate a selective decrease in the total amount of mature synaptic components in *Ppt1*$^{-/-}$ brains that temporally correlates with the cellular PPT1 expression profile in developing WT neurons, suggesting that synaptosomal reductions in GluN2A and PSD-95 may

result from altered transcription or translation of these proteins instead of direct depalmitoylation by PPT1.

Figure 2.2. NMDAR subunit composition is biased toward immaturity in *Ppt1*$^{-/-}$ visual cortex.

(A) Representative immunoblots from synaptosomes of GluN2 subunits, GluN2A and GluN2B across age (P11-P60) and genotype as indicated (top) and quantification of band density (bottom) normalized to β-actin loading control within lane. **(B)** Representative immunoblots from synaptosomes of GluN2A and GluN2B (top) and quantification of the ratio of GluN2A/GluN2B band density within animal normalized to β-actin loading control within lane (bottom). **(C)** Representative immunoblot of GluN1 from synaptosomes across age and genotype as indicated (top) and quantification of band density (bottom) normalized to β-actin loading control within lane. **(D)** Representative immunoblots from synaptosomes of the scaffolding molecules PSD-95 and SAP102 across age and genotype as indicated (top) and quantification of band density (bottom) normalized to β-actin loading control within lane. **(E)** Representative immunoblot from synaptosomes of PPT1 across age and genotype as indicated (top) and protein expression level (bottom) normalized to β-actin. For experiments in Figure 2.2A-D, *Ppt1*$^{-/-}$ and WT were compared (n=4 independent experiments/animals with 2 repetitions/group) at each age using t-test and the significance was indicated as follows: *$p<0.05$, and **$p<0.01$. In Figure 2.2E, WT expression levels at each age were compared (n=4 independent experiments/animals with 2 repetitions/group) by ANOVA followed by Tukey's post-hoc test. Significance between ages is indicated: *$p<0.05$. Error bars represent s.e.m.

Figure 2.2. NMDAR subunit composition is biased toward immaturity in *Ppt1*$^{-/-}$ visual cortex

Figure 2.2.1.

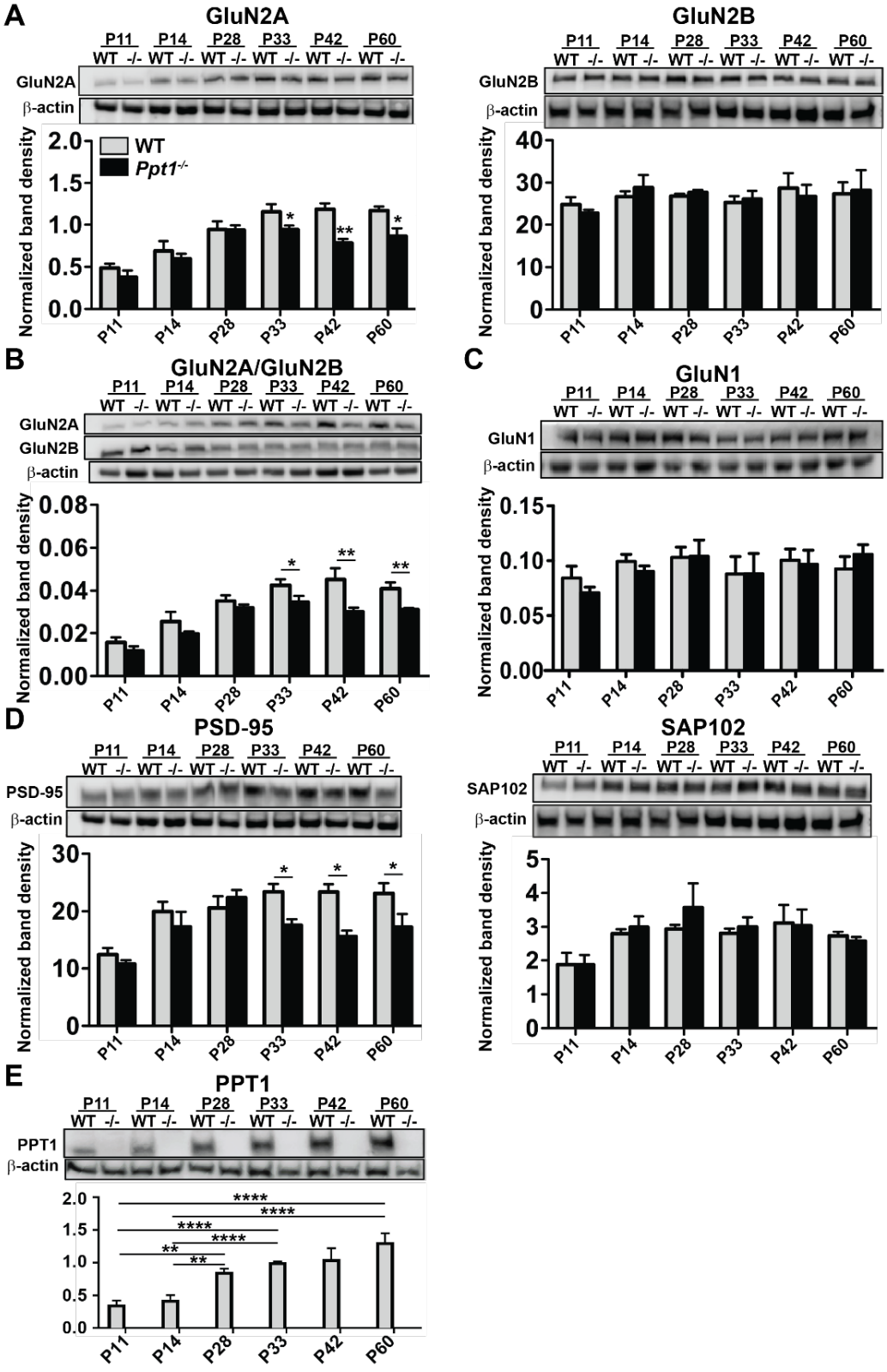

(A) Representative immunoblots of the GluN2A in whole lysates across age and genotype as indicated (top) and quantification of band density (bottom) normalized to β-actin loading control within lane. **(B)** Representative immunoblots of the GluN2B in whole lysates across age and genotype as indicated (top) and quantification of band density (bottom) normalized to β-actin loading control within lane. **(C)** Representative immunoblots of GluN2A and GluN2B (top) from whole lysates across age and genotype and quantification of the ratio of GluN2A/GluN2B band density within animal (bottom). **(D)** Representative immunoblots of GluN1 in whole lysates across age and genotype as indicated (top) and quantification of band density (bottom) normalized to β-actin loading control within lane. **(E)** Representative immunoblot from whole lysates of PPT1 across age and genotype as indicated (top) and protein expression level (bottom) normalized to β-actin. For experiments in Figure 2.2.1A-C, *Ppt1*$^{-/-}$ and WT were compared (n=4 independent experiments/animals with 2 repetitions/group) at each age using t-test and the significance is indicated: *p<0.05. In Figure 2.2D, WT expression levels at each age were compared (n=4 independent experiments/animals with 2 repetitions/group) by ANOVA followed by Tukey's post-hoc test. Significance between ages is indicated: *p<0.05, **p<0.01, ***p<0.001, ****p<0.0001. Error bars represent s.e.m.

Figure 2.2.1.

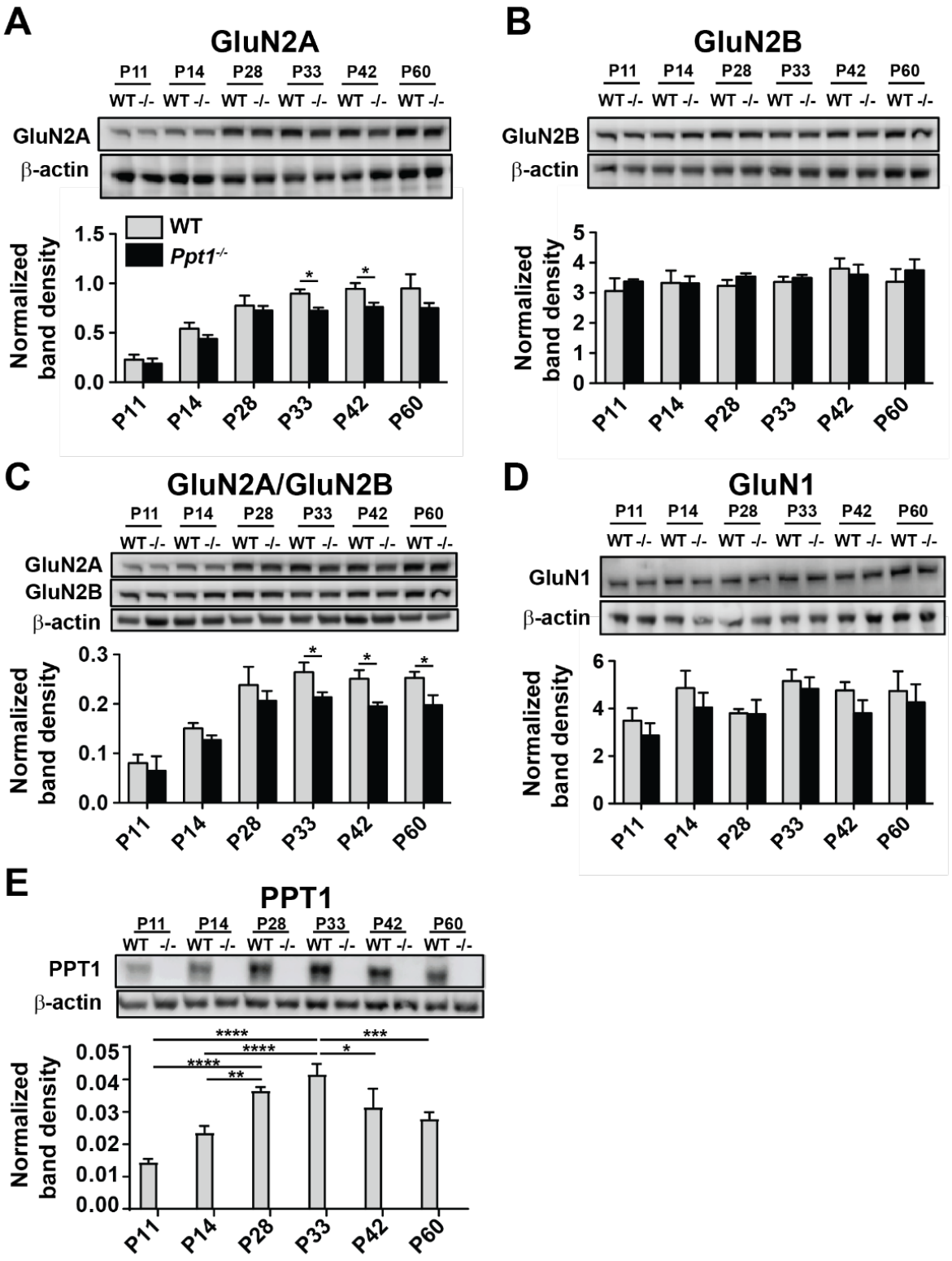
A
GluN2A
P11 P14 P28 P33 P42 P60
WT -/- WT -/- WT -/- WT -/- WT -/- WT -/-
GluN2A
β-actin
Normalized band density
WT
Ppt1-/-
B
GluN2B
GluN2B
β-actin
C
GluN2A/GluN2B
GluN2A
GluN2B
β-actin
D
GluN1
GluN1
β-actin
E
PPT1
PPT1
β-actin

2.3.3. NMDAR-mediated EPSCs are altered in *Ppt1*$^{-/-}$ visual cortex

Next, we sought to correlate our biochemical findings with electrophysiological changes in NMDAR functionality (**Figure 2.2**). While human CLN1 patients present with retinal degeneration and the *Ppt1*$^{-/-}$ mouse model of CLN1 phenocopies the human disease, the electroretinogram (ERG) is effectively unaltered at 4 months in the mouse model (Lei et al., 2006), allowing for detailed study of the electrophysiological changes in the visual cortex associated with early disease states. We recorded evoked, NMDAR-mediated excitatory postsynaptic currents (EPSCs) in layer II/III cortical neurons in visual cortical slices of WT and *Ppt1*$^{-/-}$ mice at P42. The NMDA-EPSCs were pharmacologically isolated (see Methods section) and were recorded in whole cell patch mode clamped at +50mV. As GluN2A- and GluN2B-containing NMDARs exhibit differential receptor kinetics, with GluN2A displaying fast (~50ms) and GluN2B displaying slow decay kinetics (~300ms), their relative contribution is reliably interpolated by fitting the EPSC decay phase with a double exponential function (Stocca and Vicini, 1998; Vicini et al., 1998). From the fitting of absolute amplitude-normalized, WT and *Ppt1*$^{-/-}$ NMDAR-EPSCs (**Figure 2.3A**), we measured the following parameters: the ratios of the amplitudes (A) of the fast, A_f/ A_f+A_s, and slow, A_s/ A_f+A_s components, and the weighted decay time constants (τ_w). *Ppt1*$^{-/-}$ mice showed significantly decreased ratio of A_f/A_f+A_s as compared to WT, while A_s/A_f+A_s was increased (**Figure 2.3B**). Further, *Ppt1*$^{-/-}$ neurons showed a significant increase in weighted decay time τ_w as compared to WT (**Figure 2.3C**). Remarkably, the rise time (time to peak amplitude) of *Ppt1*$^{-/-}$ NMDAR-EPSCs was slightly but significantly longer than WT (**Figure 2.3D**), suggesting that the response involves the receptors more distant from the presynaptic release site. Indeed, previous studies documented similar observations and postulated that a longer rise time is characteristic of GluN2B-containing NMDARs that are preferentially localized on the extrasynaptic membrane (Townsend et al., 2003; van Zundert et al., 2004; Sanz-Clemente et al., 2013).

Next, we treated cortical slices with Ro 25-6981, a potent and selective inhibitor of GluN2B-containing NMDARs (Fischer et al., 1997) and asked if functional GluN2B-containing NMDARs are overrepresented in *Ppt1*$^{-/-}$ neurons. We recorded NMDA-EPSCs at baseline and during bath infusion of Ro 25-6981 (30 minutes, 3μM), then compared the percent inhibition (τ_w percent of baseline) between WT and *Ppt1*$^{-/-}$ groups. Ro 25-6981 treatment significantly decreased the τ_w of NMDA EPSCs from the baseline in both WT and *Ppt1*$^{-/-}$ cells at P42 (**Figure 2.3E**). To our surprise, no significant effects were present between the two genotypes after Ro 25-6981 treatment by two-way ANOVA, suggesting that NMDARs are inhibited to the same degree in WT and *Ppt1*$^{-/-}$ cortices.

At first glance, the above result did not fulfill the anticipation that NMDA-EPSCs in *Ppt1*$^{-/-}$ neurons would respond to Ro 25-6981 treatment to a greater degree than in WT, due to an overrepresentation of GluN2B-containing receptors. However, cortical neurons predominantly express NMDARs consisting of two GluN1, one GluN2A and one GluN2B subunits (Sheng et al., 1994; Luo et al., 1997; Tovar and Westbrook, 1999). These triheteromeric NMDARs display prolonged decay kinetics compared to GluN2A-diheteromeric NMDARs, while being largely insensitive to GluN2B-specific antagonists. Indeed, the fast component of the amplitude is reduced in *Ppt1*$^{-/-}$ neurons (**Figure 2.3B**), indicating a functional decrease in the contribution of GluN2A to NMDAR-mediated EPSCs in these cells. Moreover, analysis of the weighted decay time constant (**Figure 2.3C**) suggests a larger contribution of GluN2B to the overall NMDAR-EPSC in *Ppt1*$^{-/-}$ cells (Stocca and Vicini, 1998; Vicini et al., 1998). Thus, our findings suggest an enhanced incorporation of triheteromeric NMDARs at *Ppt1*$^{-/-}$ synapse, and corroborate our biochemical findings (see **Discussion**). Collectively, our data indicate a functionally immature NMDAR phenotype in *Ppt1*$^{-/-}$ layer II/III visual cortical neurons.

Figure 2.3. NMDAR-mediated EPSCs are altered in *Ppt1*$^{-/-}$ visual cortex.

(A) Representative traces of amplitude-scaled NMDAR-EPSCs recorded from pyramidal neurons in layer II/III of the visual cortex (V1) of WT and *Ppt1*$^{-/-}$ mice. Black and red arrows above traces indicate EPSC rise time for WT and *Ppt1*$^{-/-}$ responses, respectively. Red arrow below traces indicates onset of evoked stimulus. Neurons were voltage clamped at +50mV and NMDAR-EPSCs evoked in layer IV. Neurons were voltage clamped at +50mV and NMDAR-EPSCs evoked in layer IV. **(B)** Quantification of the ratio of the amplitude (A) of the fast component, A_f/A_f+A_s, and A_s/A_f+A_s derived from fitting the decay phase of the evoked NMDAR-EPSCs with the double exponential function: $Y(\tau) = A_{f*}e^{-\tau/\tau_{fast}} + A_{s*}e^{-\tau/\tau_{slow}}$. **(C)** Quantification of the weighted decay constant, τ_w derived from fitting the decay phase of the amplitude-scaled evoked NMDAR-EPSCs with the double exponential function: $Y(\tau) = A_{f*}e^{-\tau/\tau_{fast}} + A_{s*}e^{-\tau/\tau_{slow}}$. **(D)** Quantification of the NMDAR-EPSC time to peak amplitude. **(E)** Percent change in τ_w following bath application of Ro 25-6981 (3μM, 30 min) for each cell in WT and *Ppt1*$^{-/-}$ neurons. For experiments in Figure 2.3A-D, *Ppt1*$^{-/-}$ and WT were compared (n=8 cells, 4 mice (WT); n=8 cells, 5 mice (*Ppt1*$^{-/-}$)) using t-test and the significance was indicated as follows: *p<0.05, and **p<0.01. For experiments in Figure 2.3E, the change in τ_w from baseline induced by Ro 25-6981 were compared in WT and *Ppt1*$^{-/-}$ neurons (n=7 cells, 4 mice (WT); n=6 cells, 4 mice (*Ppt1*$^{-/-}$)) using repeated measures two-way ANOVA followed by Tukey's post-hoc test and significance was indicated as follows: *p<0.05, and **p<0.01 vs. baseline. Error bars represent s.e.m.

Figure 2.3. NMDAR-mediated EPSCs are altered in *Ppt1*$^{-/-}$ visual cortex.

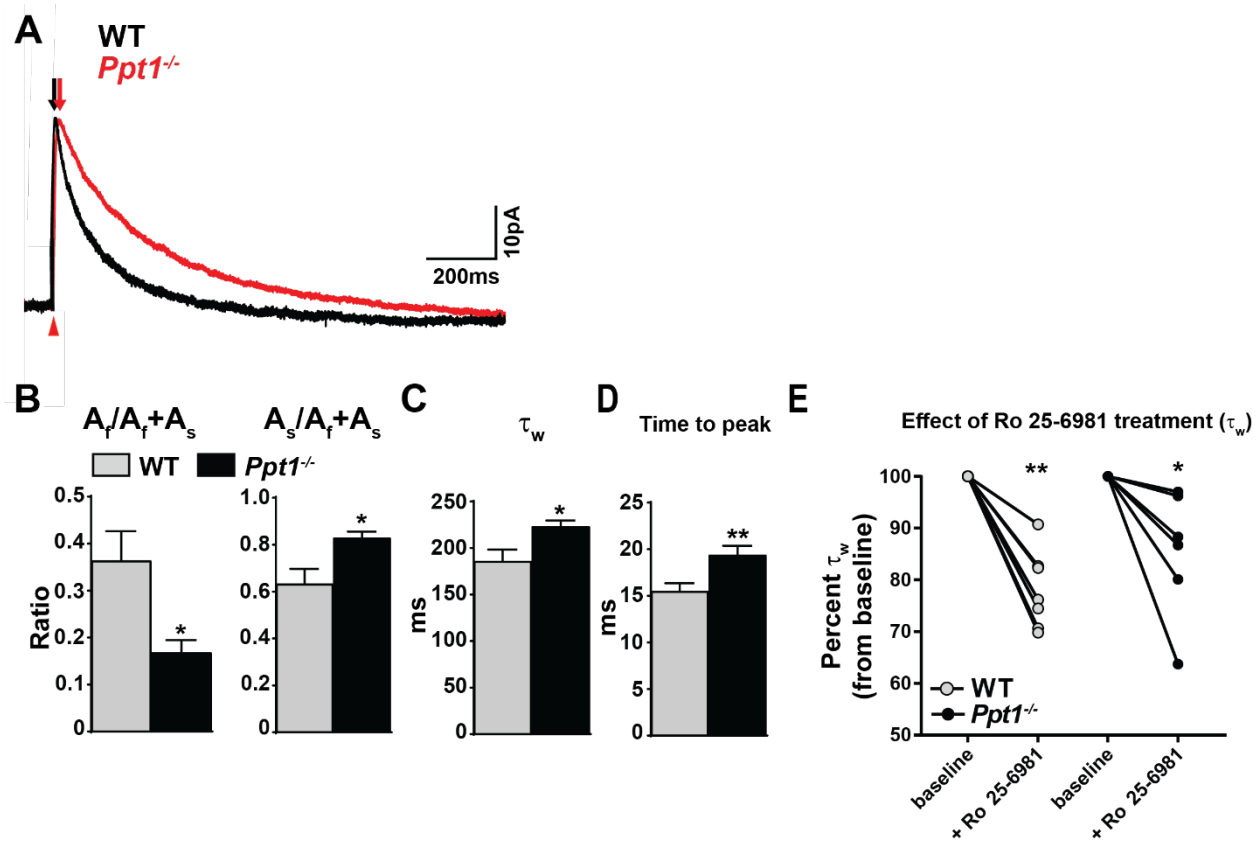

2.3.4. Dendritic spine morphology is immature in *Ppt1*$^{-/-}$ visual cortex

The morphology of dendritic spines is dynamic and synaptic activity directly alters spine morphology during synaptic plasticity (Engert and Bonhoeffer, 1999; Parnass et al., 2000; Yuste and Bonhoeffer, 2001; Matsuzaki et al., 2004). During visual cortical development that is concomitant with the GluN2B to GluN2A switch, dendritic spine morphology undergoes robust structural plasticity at excitatory synapses. Dendritic spines contribute to experience-dependent synaptic plasticity via the generation, maturation, and long-term stabilization of spines, ultimately giving rise to established synaptic circuits. Typically, by P33, dendritic spines begin to demonstrate a reduction in turnover and an increase in mushroom-type spines, indicating synaptic maturity. Importantly, dendritic spines are morphologically disrupted in many neurodevelopmental disorders, typically skewing towards an immature phenotype (Purpura, 1979; Irwin et al., 2001; Penzes et al., 2011).

We hypothesized that dendritic spine morphology is immature or disrupted in *Ppt1*$^{-/-}$ neurons, particularly given that GluN2A subunit incorporation is disrupted *in vivo*. Thus, we used *in utero* electroporation to sparsely label layer II/III cortical neurons in the visual cortex using a GFP construct (Matsuda and Cepko, 2004). GFP-expressing cells from WT and *Ppt1*$^{-/-}$ animals were imaged for detailed analysis of dendritic spine morphology (spine length, spine volume, and spine head volume) at P33, a time point when dendritic spine morphology is typically considered mature and GluN2A is reduced at *Ppt1*$^{-/-}$ synapses.

We analyzed dendritic spine characteristics of GFP-expressing cells (procedure schematized in **Figure 2.4A**) from WT and *Ppt1*$^{-/-}$ visual cortex (**Figure 2.4B**) using the Imaris software (Bitplane). While WT neurons exhibited mushroom-type spine morphology with high-volume spine heads (**Figure 2.4C**, arrows), *Ppt1*$^{-/-}$ neurons showed longer, filopodial protrusions or stubby spines (**Figure 2.4C**, arrowheads). Quantification of spine length and spine volume demonstrated that *Ppt1*$^{-/-}$ spines were longer and less voluminous compared to WT (**Figure 2.4D-**

E). Further, the volume of dendritic spine heads was reduced in *Ppt1*$^{-/-}$ neurons (**Figure 2.4E**, inset). Interestingly, dendritic spine density was significantly increased in *Ppt1*$^{-/-}$ neurons, signifying dysregulated synapse formation or refinement in the *Ppt1*$^{-/-}$ brain (**Figure 2.4F**). These data indicate that dendritic spine morphology is disrupted in the developing CLN1 visual cortex, corresponding with the finding that NMDAR composition is immature at P33 and suggesting a reduced ability to compartmentalize calcium and other localized biochemical signals in CLN1.

Figure 2.4. Dendritic spine morphology is immature in *Ppt1*$^{-/-}$ layer II/III visual cortical neurons.

(A) Schematic of *in utero* electroporation procedure and timeline (bottom) **(B)** coronal diagram from Paxinos' mouse brain atlas demonstrating areas of visual cortex (left) and representative low-magnification (10x) confocal image of a successfully transfected group of layer II/III neurons in visual cortex (right). Scale bar=100μm. **(C)** Representative confocal images of GFP-transfected dendritic segments from WT and *Ppt1*$^{-/-}$ neurons at P33. Arrows mark mature, mushroom-type spines; arrowheads mark thin, filopodial spines or stubby, headless spines. Scale bar=10μm. **(D)** Semi-automated quantification of dendritic spine length in WT and *Ppt1*$^{-/-}$ visual cortical neurons at P33. **(E)** Semi-automated quantification of dendritic spine volume and spine head volume (inset) in WT and *Ppt1*$^{-/-}$ visual cortical neurons at P33. **(F)** Semi-automated quantification of dendritic spine density per 10μm of dendrite in WT and *Ppt1*$^{-/-}$ visual cortical neurons at P33. For experiments in Figure 2.4, WT and *Ppt1*$^{-/-}$ were compared (n=3-4 cells/animal, 3 animals/group) using t-test and the significance was indicated as follows: *p<0.05, **p<0.01, ***p<0.001,, *Ppt1*$^{-/-}$ vs. WT. Error bars represent s.e.m.

Figure 2.4. Dendritic spine morphology is immature in *Ppt1*$^{-/-}$ layer II/III visual cortical neurons.

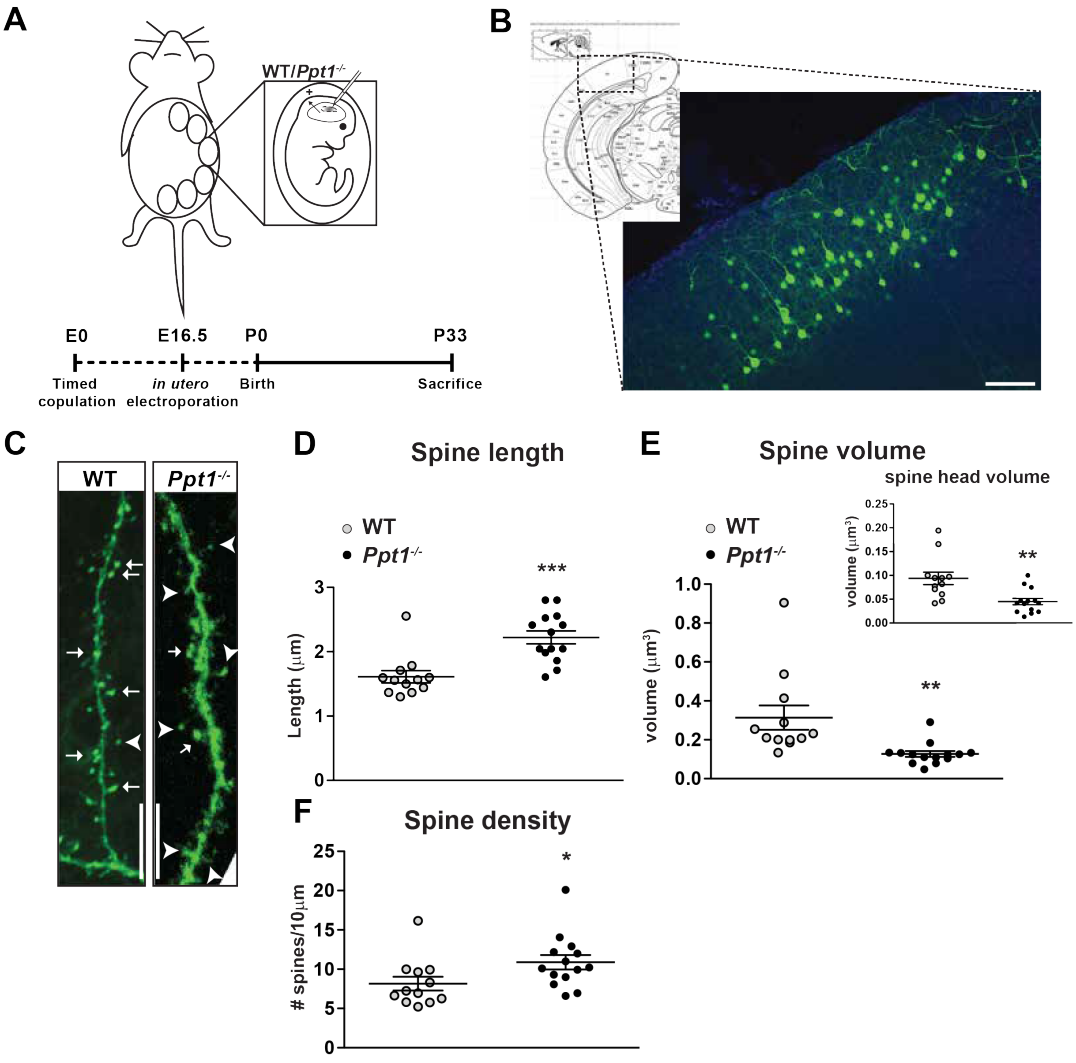

2.3.5. NMDAR subunit composition and dendritic spine morphology are also immature in *Ppt1*$^{-/-}$ primary cortical neurons

The GluN2B to GluN2A switch and maturation of dendritic spine characteristics in WT primary neurons has been previously demonstrated (Williams et al., 1993; Zhong et al., 1994; Papa et al., 1995). We established that the developmental switch from GluN2B- to GluN2A-containing NMDARs and dendritic spine morphology are impaired in the *Ppt1*$^{-/-}$ mouse brain. To understand these mechanisms more comprehensively and examine protein palmitoylation more directly, we used dissociated neuronal cultures. First, we analyzed these developmental events in WT and *Ppt1*$^{-/-}$ primary cortical neurons to determine whether the biochemical and structural features of disease are recapitulated *in vitro*.

We collected lysates from cultured cortical neurons for 7, 10, or 18 days *in vitro* (DIV 7, 10, or 18) harvested and performed immunoblot analyses for markers of immature (GluN2B) or mature (GluN2A, PSD-95) excitatory synapses. Expression of GluN2B clearly preceded that of mature synaptic markers, peaking in both WT and *Ppt1*$^{-/-}$ neurons at DIV10 and decreasing slightly thereafter (**Figure 2.5A**). In contrast, levels of both GluN2A and PSD-95 remained low until DIV18, at which point expression was robust (**Figure 2.5B, C**). Importantly, GluN2A, PSD-95, and GluN2A/GluN2B ratio levels showed reductions in *Ppt1*$^{-/-}$ neurons compared to WT at DIV18, indicating that the biochemical phenotype is recapitulated to an extent *in vitro* (**Figure 2.5B-D**).

Figure 2.5. GluN2B to GluN2A NMDAR switch and *Ppt1*$^{-/-}$-induced synaptic deficits are recapitulated in primary cortical neurons.

(A) Representative immunoblot (top) and quantification of GluN2B levels in WT and *Ppt1*$^{-/-}$ neurons at DIV7, 10, and 18. **(B)** Representative immunoblot (top) and quantification of GluN2A levels (bottom) in WT and *Ppt1*$^{-/-}$ neurons at DIV7, 10, and 18. **(C)** Representative immunoblot (top) and quantification of PSD-95 levels (bottom) in WT and *Ppt1*$^{-/-}$ neurons at DIV7, 10, and 18. **(D)** Representative immunoblot (top) and quantification of the GluN2A/2B ratio (bottom) in WT and *Ppt1*$^{-/-}$ neurons at DIV7, 10, and 18. For all experiments in Figure 2.5, *Ppt1*$^{-/-}$ and WT were compared (n=2 independent experiments with 2 repetitions/group) at each time point using t-test and the significance indicated as follows: *p<0.05 where indicated. Error bars represent s.e.m.

Figure 2.5. GluN2B to GluN2A NMDAR switch and *Ppt1*$^{-/-}$-induced synaptic deficits are recapitulated in primary cortical neurons.

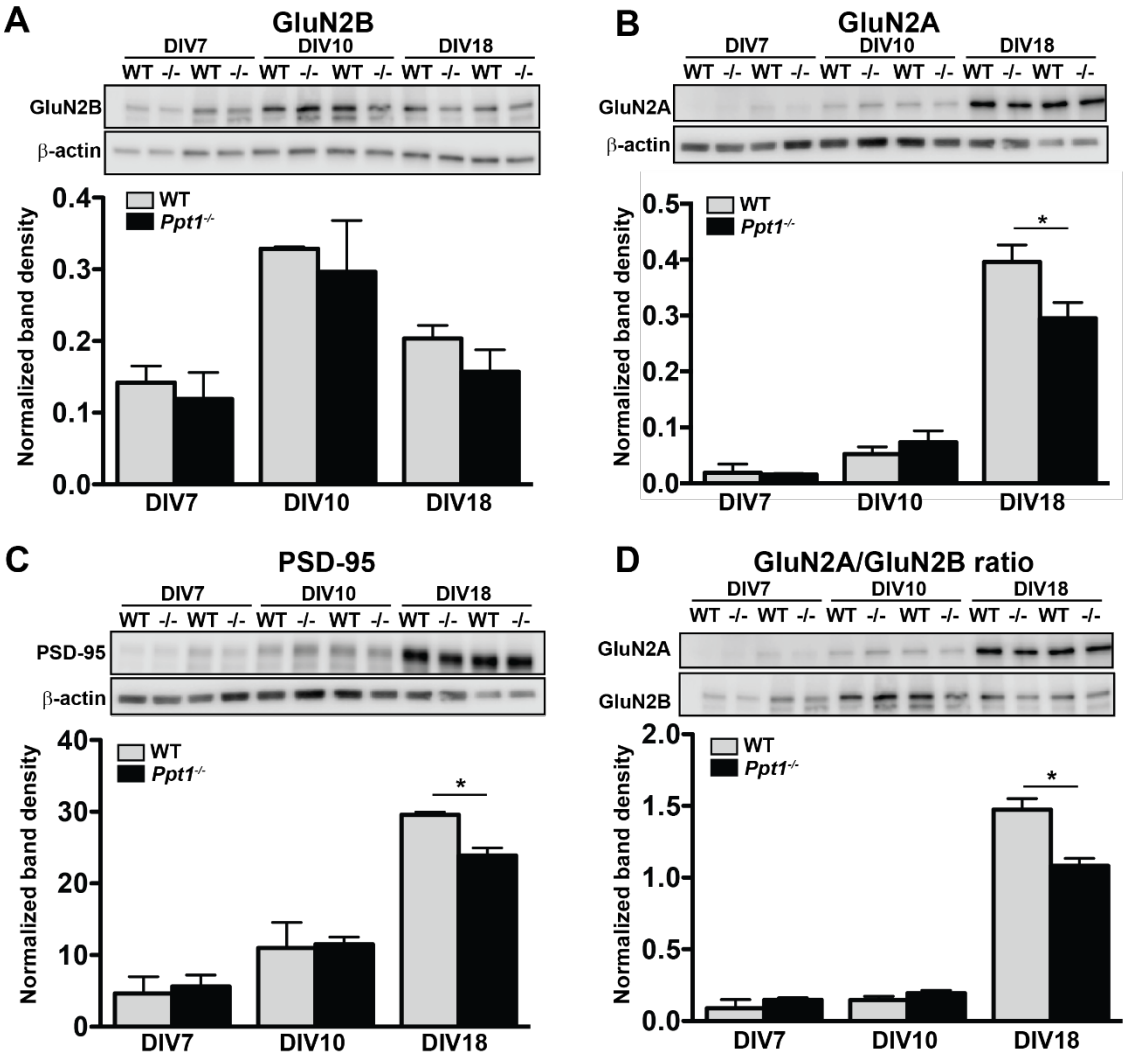

To analyze dendritic spine morphology, primary cortical neurons from fetal WT and *Ppt1*$^{-/-}$ mice were transfected with the GFP construct as above (Matsuda and Cepko, 2004) and were cultured until DIV 15 or 20 when live cell imaging was performed (**Figure 2.6A**). We measured dendritic spine length and volume in transfected cells using the Imaris software (Bitplane). At both DIV 15 and 20, we observed a significant alterations in the dendritic spine length (**Figure 2.6B-E**).The distribution of spine length in *Ppt1*$^{-/-}$ neurons at DIV15 significantly shifted toward longer protrusions as compared to WT cells (**Figure 2.6B**). The averaged spine length demonstrate a robust increase in *Ppt1*$^{-/-}$ neurons compared to WT cells (**Figure 2.6C**). A similar change was also present at DIV20 (**Figure 2.6D-E**). Next, we analyzed differences in dendritic spine volume (**Figure 2.6F-I**). *Ppt1*$^{-/-}$ neurons exhibit a significant reduction in the percentage of spines with volumes greater than ~0.2μm^3 at both DIV15 (**Figure 2.6F**) and DIV20 (**Figure 2.6H**). The averaged spine volume was also reduced in *Ppt1*$^{-/-}$ neurons at both DIV15 (**Figure 2.6G**) and DIV20 (**Figure 2.6I**). As observed *in vivo*, *Ppt1*$^{-/-}$ neurons showed an increase in the dendritic spine density at DIV15 (**Figure 2.6J**) and DIV20 (**Figure 2.6K**), again suggesting aberrant synapse formation, a failure of synaptic pruning, or both in *Ppt1*$^{-/-}$ neurons. Together, these data demonstrate that *Ppt1*$^{-/-}$ neurons in culture give rise to morphologically immature dendritic spines and corroborate our *in vivo* findings.

Figure 2.6. Dendritic spine morphology is immature in *Ppt1*$^{-/-}$ neurons *in vitro*.

(A) Representative composite confocal images of live DIV15 (left) and DIV20 (right) GFP-transfected, cultured WT and *Ppt1*$^{-/-}$ neurons. Insets represent dendrite segments within dotted line. Scale bar=10μm. **(B)** Quantification of dendritic spine length in WT and *Ppt1*$^{-/-}$ neurons at DIV15. Spine length is binned into 19 discrete groups from 0 - >4μm. **(C)** Mean length of all spines in cultured WT and *Ppt1*$^{-/-}$ neurons at DIV15. **(D)** Quantification of dendritic spine length in WT and *Ppt1*$^{-/-}$ neurons at DIV20. Spine length is binned into 19 discrete groups from 0 - >4μm. **(E)** Mean length of all spines in cultured WT and *Ppt1*$^{-/-}$ neurons at DIV20. **(F)** Semi-automated quantification of dendritic spine volume in WT and *Ppt1*$^{-/-}$ cultured neurons at DIV15. Spine volume is binned into 27 discrete groups form 0 - >1μm^3. **(G)** Mean volume of all spines in cultured WT and *Ppt1*$^{-/-}$ neurons at DIV15. **(H)** Semi-automated quantification of dendritic spine volume in WT and *Ppt1*$^{-/-}$ cultured neurons at DIV20. Spine volume is binned into 27 discrete groups form 0 - >1μm^3. **(I)** Mean volume of all spines in cultured WT and *Ppt1*$^{-/-}$ neurons at DIV20. **(J)** Semi-automated quantification of dendritic spine density per 10μm of dendrite in WT and *Ppt1*$^{-/-}$ cultured neurons at DIV15. **(K)** Semi-automated quantification of dendritic spine density per 10μm of dendrite in WT and *Ppt1*$^{-/-}$ cultured neurons at DIV20. For experiments in Figure 2.6, *Ppt1*$^{-/-}$ and WT were compared (For DIV15: n=4-5 neurons/group, 3-independent experiments, WT=21,514 spines; *Ppt1*$^{-/-}$=18,013 spines. For DIV20: n=3 neurons/group, 2-independent experiments, WT=11,335 spines; *Ppt1*$^{-/-}$=9,958 spines) using t-test (within bin in the case of distribution graphs) and the significance was indicated as follows: *p<0.05, **p<0.05, ***p<0.001 where indicated. Error bars represent s.e.m.

Figure 2.6. Dendritic spine morphology is immature in *Ppt1*$^{-/-}$ neurons *in vitro*.

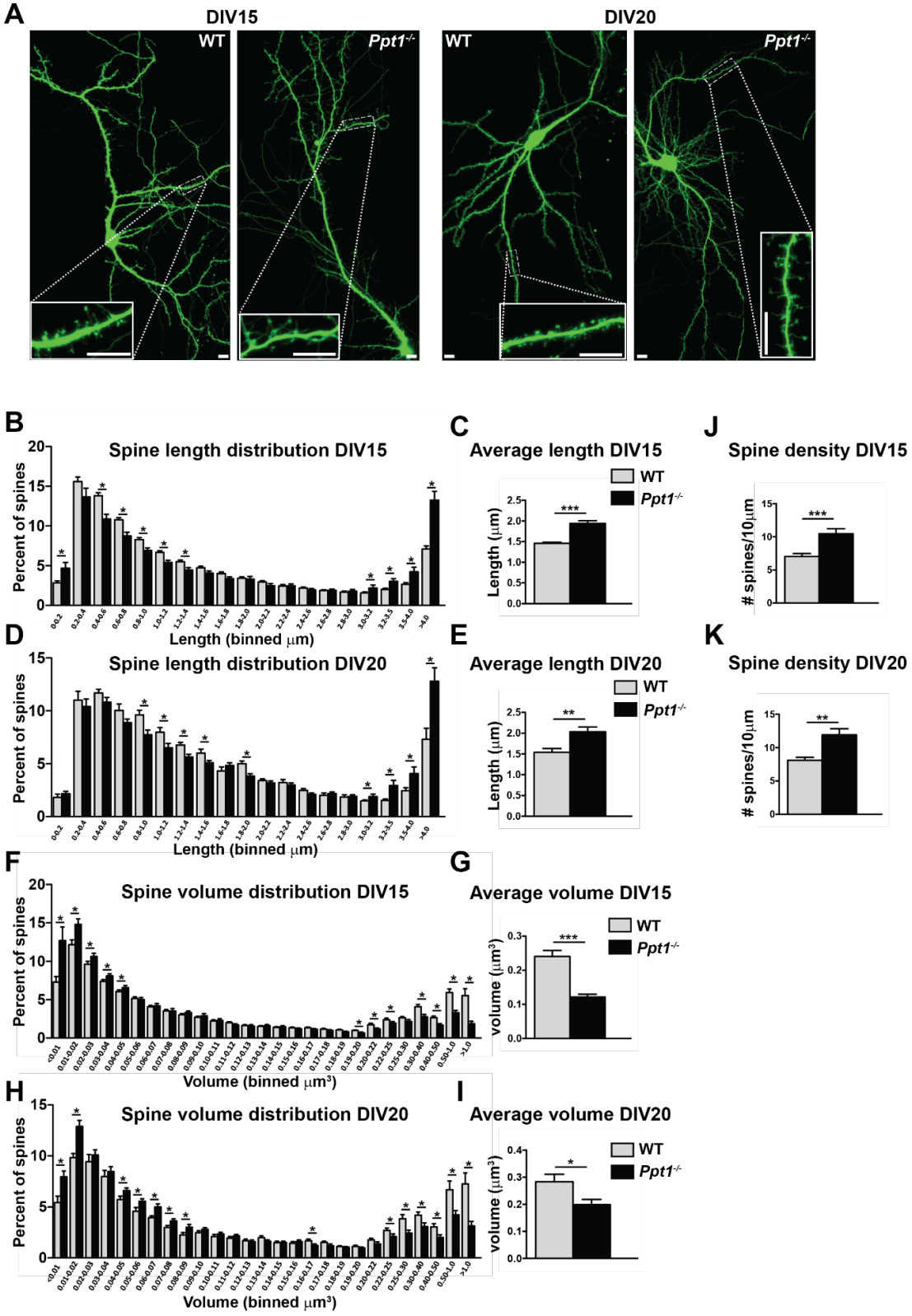
A
DIV15
WT
Ppt1-/-
DIV20
WT
Ppt1-/-
B
Spine length distribution DIV15
Percent of spines
Length (binned μm)
C
Average length DIV15
WT
Ppt1-/-
Length (μm)
***
J
Spine density DIV15
spines/10μm
***
D
Spine length distribution DIV20
Percent of spines
Length (binned μm)
E
Average length DIV20
WT
Ppt1-/-
Length (μm)
**
K
Spine density DIV20
spines/10μm
**
F
Spine volume distribution DIV15
Percent of spines
Volume (binned μm³)
G
Average volume DIV15
WT
Ppt1-/-
volume (μm³)
***
H
Spine volume distribution DIV20
Percent of spines
Volume (binned μm³)
I
Average volume DIV20
WT
Ppt1-/-
volume (μm³)
*

2.3.6. Calcium imaging reveals extrasynaptic calcium dynamics in *Ppt1*$^{-/-}$ neurons

Intracellular calcium dynamics, compartmentalization, and signaling play a critical role in synaptic transmission and plasticity. These properties are altered by glutamate receptor composition and location (Lau and Zukin, 2007; Hardingham and Bading, 2010; Paoletti et al., 2013). GluN2B-containing NMDARs maintain a prolonged open conformation compared to GluN2A-containing receptors, allowing increased calcium entry per synaptic event (Sobczyk et al., 2005). Moreover, previous studies indicate that GluN2A-containing NMDARs are generally inserted in the PSD whereas GluN2B-containing NMDARs are localized extrasynaptically and associated with SAP102 (Tovar and Westbrook, 1999; Townsend et al., 2003; van Zundert et al., 2004; Washbourne et al., 2004; Groc et al., 2007; Elias et al., 2008; Martel et al., 2009). To determine more directly the effects of our biochemical and electrophysiological findings on calcium dynamics, we analyzed calcium signals in WT and *Ppt1*$^{-/-}$ neurons transfected with the genetically encoded calcium sensor, GCaMP3 (Tian et al., 2009).

While WT neurons exhibited primarily compartmentalized calcium signals that were restricted to a spine (**Figure 2.7A-C, left**), *Ppt1*$^{-/-}$ neurons demonstrated diffuse calcium influxes that spread through the dendritic shaft (**Figure 2.7A-C, right**). These extrasynaptic transients appear rarely in WT cells (**Figure 2.7**). To analyze the calcium dynamics in more detail, measurements of $\Delta F/F_0$ were made for each dendritic segment, from each cell over the course of the captured videos (see **Methods**). Multiple transients from the same synaptic site are shown as a heat map of $\Delta F/F_0$ measurements and they are largely consistent across time in both WT and *Ppt1*$^{-/-}$ neurons (**Figure 2.7B**). Further, plotting of the averaged $\Delta F/F_0$ transients at an individual synaptic site demonstrates that local fluorescence increases in WT cells are confined to a short distance from the peak $\Delta F/F_0$ at synaptic sites (**Figure 2.7B and C, left**), while those of *Ppt1*$^{-/-}$ neurons diffuse longer distances within the dendrite (**Figure 2.7B and C, right**). To quantitatively compare these properties, we performed measurements of area under the curve (AUC) and

calcium diffusion distance (see shaded region in **Figure 2.7C**) for each synaptic site from WT and *Ppt1*$^{-/-}$ neurons. These analyses revealed a robust increase in both the AUC (**Figure 2.7D**) and the calcium diffusion distance (**Figure 2.7E**) in *Ppt1*$^{-/-}$ neurons compared to WT. Furthermore, performing correlation analysis of calcium events across time (see **Methods**) within a given neuron demonstrates that calcium influxes are more synchronous (increased correlation coefficient) in *Ppt1*$^{-/-}$ neurons compared to WT (**Figure 2.7F**). This result may involve mechanisms underlying synaptic cluster plasticity, including synaptic integration via translational activation influenced by excessive Ca^{2+} entry (Govindarajan et al., 2006), enhanced biochemical crosstalk between synapses by, for example, small GTPases (which are generally palmitoylated proteins) (Harvey et al., 2008), or direct cooperative multi-synaptic Ca^{2+} signaling (Weber et al., 2016) in *Ppt1*$^{-/-}$ neurons. Together, these data indicate that calcium entry and dispersion are enhanced at *Ppt1*$^{-/-}$ synapses *in vitro.*

These data are in line with our biochemical and electrophysiological findings and suggest that GluN2B-containing NMDARs mediate the observed calcium signals. To further test this possibility, we next treated WT and *Ppt1*$^{-/-}$ neurons with Ro 25-6981 (1μM, added in imaging medium following 2.5min imaging at baseline) and performed calcium imaging. Ro 25-6981 had virtually no effect on calcium signals recorded from WT cells (**Figure 2.7G-I**). In contrast, *Ppt1*$^{-/-}$ neurons treated with Ro 25-6981 showed a reduction in dendritic calcium influxes within shafts, while few residual, compartmentalized transients persisted (**Figure 2.7G-I**). Quantitatively, both AUC (**Figure 2.7H**) and calcium diffusion (**Figure 2.7I**) distance were rescued to WT levels following Ro 25-6981 treatment of *Ppt1*$^{-/-}$ neurons. Together, these data suggest that *Ppt1*$^{-/-}$ neurons have extrasynaptic calcium signaling compared to WT that is sensitive to GluN2B-NMDAR blockade.

Figure 2.7. Calcium imaging reveals extrasynaptic calcium dynamics in *Ppt1*$^{-/-}$ neurons.

DIV16-18, WT and *Ppt1*$^{-/-}$ cortical neurons transfected with GCaMP3 and imaged in the absence of Mg^{2+} for 5 minutes. **(A)** Single frames from videos of WT (left) and *Ppt1*$^{-/-}$ (right) cultured neurons. Dendritic segments within the dotted-lines represent zoomed-in images of a single spine (left, WT) or dendritic shaft segment (right, *Ppt1*$^{-/-}$) at baseline (top) and active (bottom) states. Scale=10μm. **(B)** Representative heat maps of $\Delta F/F_0$ values at one synaptic site from WT (left) and *Ppt1*$^{-/-}$ (right) dendrite segments during a portion the imaging session (350 frames, 50 seconds). **(C)** Representative averaged $\Delta F/F_0$ responses at one synaptic site from WT (left) and *Ppt1*$^{-/-}$ (right) neurons. Area under the curve represents calcium influx and is shaded in red. **(D)** Quantification of calcium transient area under the curve WT and *Ppt1*$^{-/-}$ neurons. **(E)** Quantification of calcium transient diffusion distance from WT and *Ppt1*$^{-/-}$ neurons. (**F**) Quantification of average correlation coefficient (synaptic synchrony) across time between sites of synaptic activity in WT and *Ppt1*$^{-/-}$ neurons. **(G)** Representative heat maps of $\Delta F/F_0$ values at one synaptic site from WT (left) and *Ppt1*$^{-/-}$ (right) dendrite segments before (top) and after (bottom) treatment with Ro 25-6981 (130 frames, 18 seconds). (**H**) Quantification of calcium transient area under the curve WT and *Ppt1*$^{-/-}$ neurons before and after treatment with Ro 25-6981. **(I)** Quantification of calcium transient diffusion distance from WT and *Ppt1*$^{-/-}$ neurons before and after treatment with Ro 25-6981. For experiments in Figure 2.7D-E, *Ppt1*$^{-/-}$ and WT were compared (n=185 synaptic sites (WT), n=131 synaptic sites (*Ppt1*$^{-/-}$), 3 neurons/group, 3 individual experiments) by t-test and the significance was indicated as follows: ***p<0.001 vs. WT by t-test. For experiments in Figure 2.7F, *Ppt1*$^{-/-}$ and WT were compared (n=100 synaptic sites (WT), n=100 synaptic sites (*Ppt1*$^{-/-}$); 3 neurons/group, 2 individual experiments) by t-test and the significance was indicated as follows: ***p<0.001 vs. WT by t-test. For experiments in Figure 2.7H-I, *Ppt1*$^{-/-}$ and WT were compared (n=25 synaptic sites (WT), n=28 synaptic sites (*Ppt1*$^{-/-}$); 3 neurons/group, 2 individual experiments) by t-test and the significance was indicated as follows: ***p<0.001 vs. WT by t-test. 65 pixels is representative of 10μm. Error bars represent s.e.m.

Figure 2.7. Calcium imaging reveals extrasynaptic calcium dynamics in *Ppt1*$^{-/-}$ neurons.

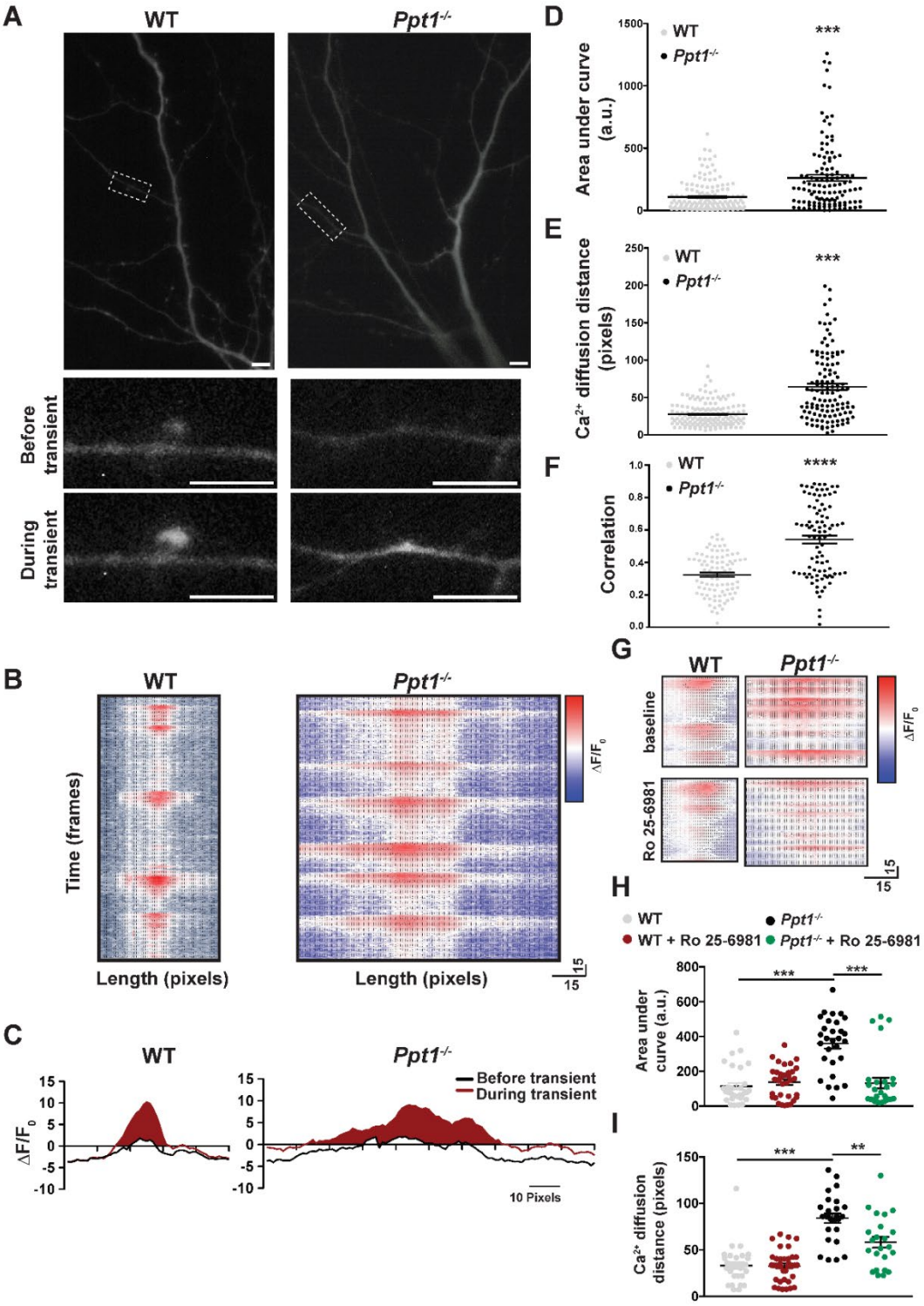

2.3.7. *Ppt1*$^{-/-}$ cultured neurons show enhanced vulnerability to NMDA-mediated excitotoxicity

GluN2B-predominant NMDARs are implicated in enhanced neuronal susceptibility to NMDA-mediated neuronal death (Martel et al., 2009, 2012). Our results from biochemical, electrophysiological, and live-imaging analyses indicate decreased GluN2A/2B ratio suggesting an intriguing possibility that *Ppt1*$^{-/-}$ neurons are more vulnerable to excitotoxicity (Finn et al., 2012). Therefore, we treated WT and *Ppt1*$^{-/-}$ cultured neurons with NMDA (varying doses, 10-300μm) and glycine (1-30μm, always in 1:10 ratio with NMDA) for 2 hours and assayed cell viability 24 hours later using the PrestoBlue® reagent (ThermoFisher Scientific) (**Figure 2.8A**). As expected, both WT and *Ppt1*$^{-/-}$ neurons demonstrated dose-dependent reductions in cell viability in response to increasing concentrations of NMDA/glycine (**Figure 2.8B**). Importantly, *Ppt1*$^{-/-}$ neurons were more vulnerable to NMDA insult, as exposure to 10μM NMDA was sufficient to reduce cell viability significantly in *Ppt1*$^{-/-}$ neurons but not WT cells (WT = 93 ± 4.1%; *Ppt1*$^{-/-}$ = 76 ± 3.5%; **p*= 0.046; **Figure 2.8B**). Further, at 100μM NMDA, WT neuron viability decreased by 35%, while *Ppt1*$^{-/-}$ neuron viability was reduced significantly further, by 58% (WT = 65 ± 1.8%; *Ppt1*$^{-/-}$ = 42 ± 4.5%; ***p*= 0.0043; **Figure 2.8B**). At 300μM NMDA treatment this effect plateaued, as cell viability between WT and *Ppt1*$^{-/-}$ neurons was comparable (**Figure 2.8B**). These results indicate *Ppt1*$^{-/-}$ neurons are more vulnerable to excitotoxicity and are consistent with our calcium imaging data that demonstrated the predominance of extrasynaptic, GluN2B-mediated NMDAR activity.

Figure 2.8. *Ppt1*$^{-/-}$ cultured neurons show enhanced vulnerability to NMDA-mediated excitotoxicity.

(A) Schematic of cellular toxicity experimental design. Briefly, neurons were grown to DIV11, treated with vehicle of palmitoylation inhibitors for 7d (every 48h) and neuronal viability was measured by PrestoBlue® cellular viability assay following exposure (2h exposure, 22h incubation in medium) to NMDA and glycine. **(B)** Quantification of cellular viability in WT and *Ppt1*$^{-/-}$ neurons at DIV19 treated with increasing concentrations of NMDA and glycine (10/1, 100/10, and 300/30μM). *Ppt1*$^{-/-}$ and WT were compared (n=4 independent experiments, in duplicate) by two-way ANOVA followed by Tukey's post hoc test and significance was indicated as follows: *p<0.05 and ***p<0.001 where indicated. Error bars represent s.e.m.

Figure 2.8. *Ppt1*$^{-/-}$ cultured neurons show enhanced vulnerability to NMDA-mediated excitotoxicity.

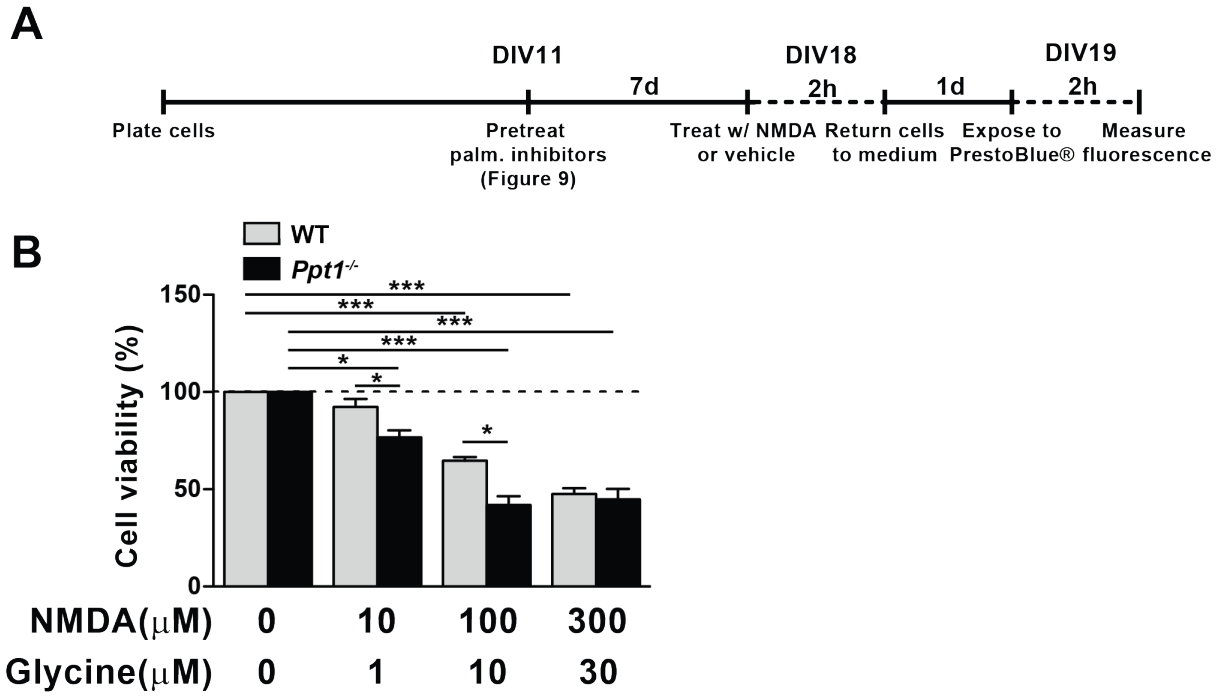

2.3.8. Palmitoylation inhibitors rescue enhanced vulnerability to NMDA-mediated excitotoxicity in *Ppt1*$^{-/-}$ cultured neurons

We next asked whether this enhanced vulnerability to excitotoxicity results from hyperpalmitoylation of neuronal substrates, and if it can be corrected by balancing the level of synaptic protein palmitoylation/depalmitoylation. First, we found that 77% of cultured *Ppt1*$^{-/-}$ neurons accumulate ALs spontaneously at DIV18-20 (**Figure 2.9A and B**). In agreement, an immunostaining for lysosomal-associated membrane protein-2 (LAMP-2) showed colocalization of the lysosomal marker with ALs in *Ppt1*$^{-/-}$ but not WT neurons (vehicle treatment in **Figure 2.9B**, **Figure 2.9.1**). Further, lysosomes appeared swollen in vehicle-treated *Ppt1*$^{-/-}$ neurons (see arrows in **Figure 2.9B, Figure 2.9.1D-F**). Treatment with the palmitoylation inhibitors, 2-bromopalmitate (2-BP, 1μM, 7-day treatment) and cerulenin (1μM, 7-day treatment) reduced the percentage of AL-positive neurons (**Figure 2.9C**) and the area occupied with ALs per neuron (**Figure 9D**). Further, the mean lysosomal size also normalized in *Ppt1*$^{-/-}$ neurons when these cells were treated with 2-BP or cerulenin (**Figure 2.9E**).

To examine the efficacy of these compounds in preventing NMDA-mediated toxicity, we pretreated a subset of neurons with the same palmitoylation inhibitors, 2-BP (1μM, DIV12-18) and cerulenin (1μM, DIV12-18) prior to treatment with NMDA and glycine. Notably, pretreatment with both 2-BP and cerulenin improved cell viability of *Ppt1*$^{-/-}$ neurons to that of WT following excitotoxicity induction, while the chronic low-dose treatment alone had no effect on neuronal viability (**Figure 2.9F**). These results indicate at least two features of *Ppt1*$^{-/-}$ neurons, accumulation of proteolipid materials and a higher vulnerability to excitotoxicity, can be mitigated by correcting a balance between palmitoylation and depalmitoylation.

Figure 2.9. Palmitoylation inhibitors rescue enhanced vulnerability to NMDA-mediated excitotoxicity in *Ppt1*$^{-/-}$ cultured neurons.

(A) 3D reconstructions of a WT and *Ppt1*$^{-/-}$ neuron at DIV20. Arrows point to AL deposits. Scale bar=5μm **(B)** Representative collapsed z-stacks of WT and *Ppt1*$^{-/-}$ DIV20 neurons, demonstrating accumulations of ALs (arrows) within the soma, particularly within LAMP2-positive vesicles, of *Ppt1*$^{-/-}$ neurons. Note the enlarged lysosomes in *Ppt1*$^{-/-}$, vehicle-treated neurons (see Figure 9-figure supplement 1). Scale bar=10μm **(C)** Quantification of the percentage of AL-containing neurons at DIV20 with or without the palmitoylation inhibitors, 2-bromopalmitate (2-BP, 1μM) and cerulenin (1μM), treatment for 6d. **(D)** The percentage of soma area occupied by ALs with or without the palmitoylation inhibitors, 2-BP (1μM) and cerulenin (1μM), treatment for 6d. **(E)** Quantification of the percentage of soma area occupied by lysosomes (LAMP-2-positive vesicles) with and without palmitoylation inhibitor, 2-BP (1μM) and cerulenin (1μM), treatment for 6d. WT, *Ppt1*$^{-/-}$, and drug treatment conditions were compared (7-10 neurons/group/experiment, n=3 independent experiments) by two-way ANOVA followed by Tukey's post-hoc test and significance indicated as follows: *p<0.05, ***p<0.001 where indicated. **(F)** Quantification of cellular viability in DIV18-20 WT and *Ppt1*$^{-/-}$ neurons treated with NMDA and glycine (100/10μM) with or without pretreatment with vehicle (DMSO) only, 2-BP (1μM) or cerulenin (1μM). Values for treatment with 2-BP (1μM) or cerulenin (1μM) in the absence of NMDA and glycine are also shown. WT, *Ppt1*$^{-/-}$, and drug treatment conditions were compared (n=4 independent experiments, in duplicate) by two-way ANOVA followed by Tukey's post-hoc test and significance indicated as follows: **p<0.01, ***p<0.001 where indicated. Error bars represent s.e.m.

Figure 2.9. Palmitoylation inhibitors rescue enhanced vulnerability to NMDA-mediated excitotoxicity in *Ppt1*$^{-/-}$ cultured neurons.

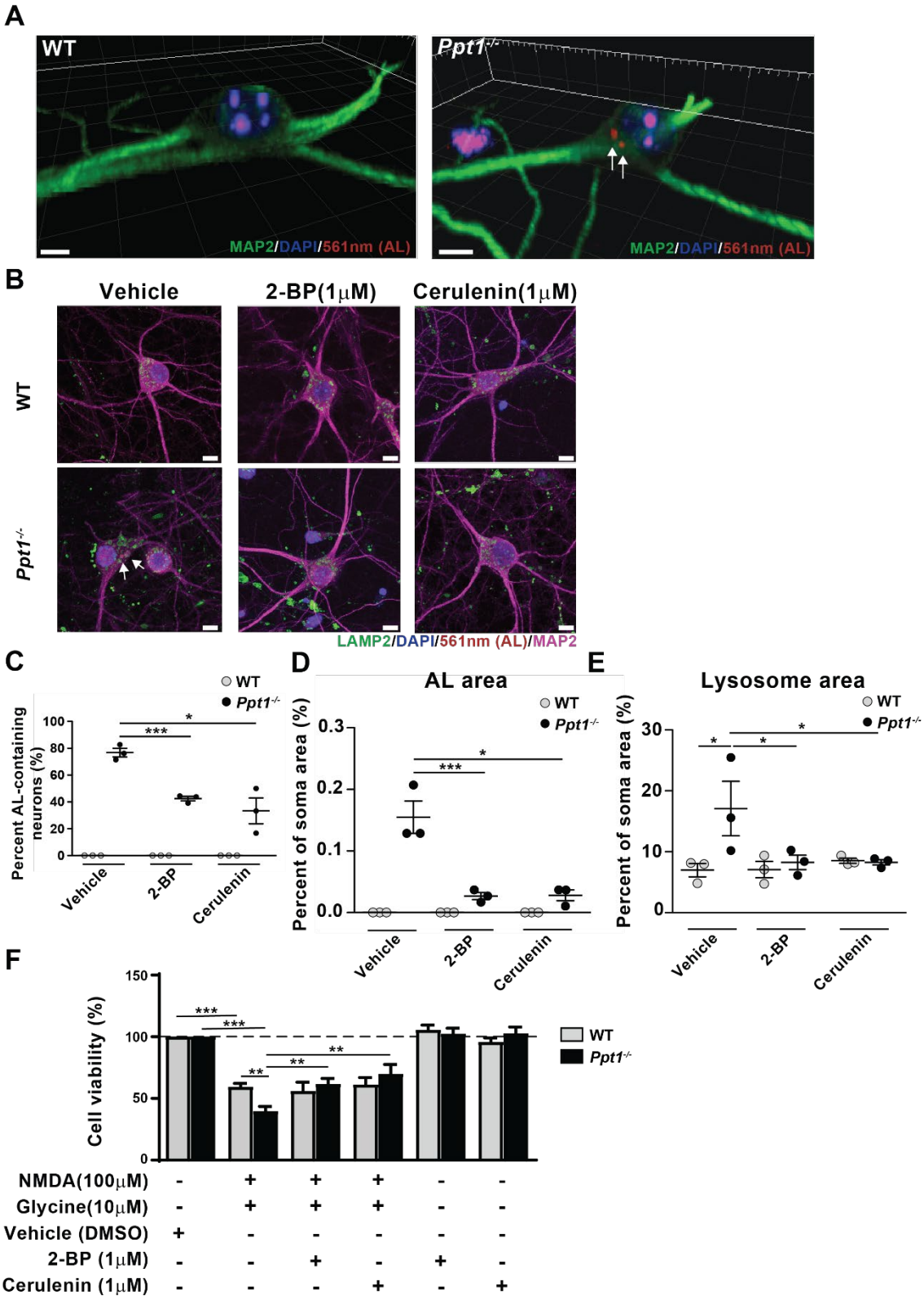

Figure 2.9.1.

(A) Single channel greyscale images of the WT, vehicle-treated representative composite image from Figure 9B displaying LAMP2, 561nm (AL), MAP2, and DAPI signals individually. Red lines in images correspond to line scans in (B). Scale bar=10μm. **(B)** Fluorescence intensity plots (grey value plots) of the line scans through the WT, vehicle-treated soma for each channel. Note: black bars above the LAMP2 signal plot denote the diameter in pixels of each lysosome captured by the line scan for that cell. **(C)** *Left*, magnified composite image of the WT, vehicle-treated soma demonstrating the location of the line scan. *Right*, line scans for the LAMP2 and 561nm (AL) channels plotted together. Note the lack of signal in the 561nm (AL) channel in the WT cell. Scale bar=10μm. **(D)** Single channel greyscale images of the *Ppt1*$^{-/-}$, vehicle-treated representative composite image from Figure 9B displaying LAMP2, 561nm (AL), MAP2, and DAPI signals individually. Red lines in images correspond to line scans in (E). Scale bar=10μm. **(E)** Fluorescence intensity plots (grey value plots) of the line scans through the *Ppt1*$^{-/-}$, vehicle-treated soma for each channel. Note: black bars above the LAMP2 signal plot denote the diameter in pixels of each lysosome captured by the line scan for that cell. **(F)** *Left*, magnified composite image of the *Ppt1*$^{-/-}$, vehicle-treated soma demonstrating the location of the line scan. *Right*, line scans for the LAMP2 and 561nm (AL) channels plotted together. Arrows denote AL deposits (increases in 561nm (AL) fluorescence) within the enlarged lysosomes (see black bars above LAMP2 line scan) of the *Ppt1*$^{-/-}$, vehicle-treated cell. Scale bar=10μm.

Figure 2.9.1.

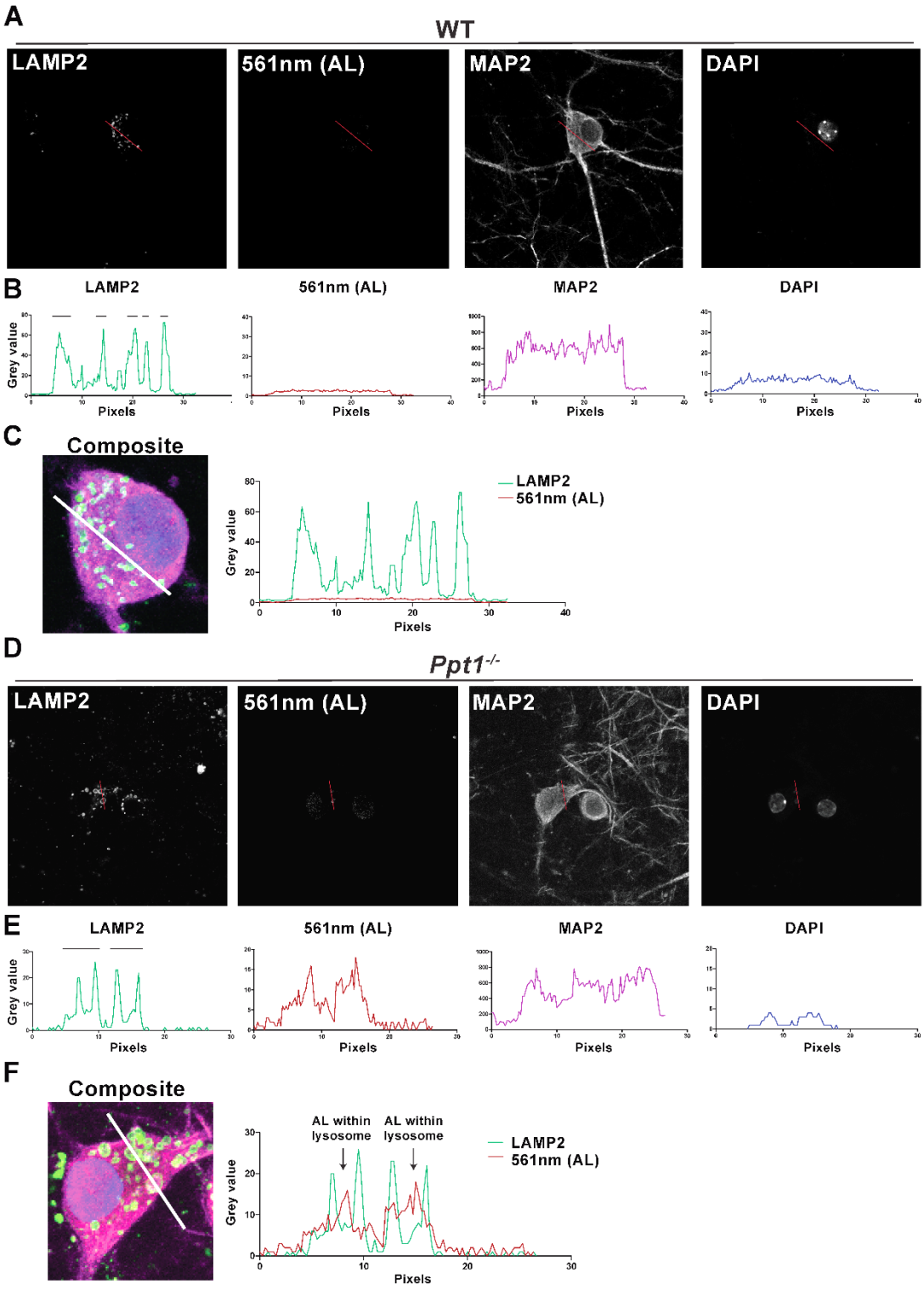
A
WT
LAMP2
561nm (AL)
MAP2
DAPI
B
LAMP2
561nm (AL)
MAP2
DAPI
Grey value
Pixels
C
Composite
LAMP2
561nm (AL)
Grey value
Pixels
D
Ppt1-/-
LAMP2
561nm (AL)
MAP2
DAPI
E
LAMP2
561nm (AL)
MAP2
DAPI
Grey value
Pixels
F
Composite
AL within lysosome
AL within lysosome
LAMP2
561nm (AL)
Grey value
Pixels

2.3.9. Palmitoylation inhibitor treatment improves pathological calcium dynamics in *Ppt1*$^{-/-}$ neurons

To determine whether palmitoylation inhibitor treatment had a functional effect on the calcium dynamics in *Ppt1*$^{-/-}$ neurons, we treated a subset of *Ppt1*$^{-/-}$ cells from DIV12-18 with 2-BP (1μM) or cerulenin (1μM) before imaging under the same conditions described for **Figure 2.7**. Notably, treatment with both 2-BP and cerulenin decreased the AUCs of specified synapses compared to untreated *Ppt1*$^{-/-}$ cells, nearly to WT levels (**Figure 2.10A**), indicating more compartmentalized calcium influx. In fact, the morphology of treated *Ppt1*$^{-/-}$ neurites appeared more mature. However, the AUC of cerulenin-treated *Ppt1*$^{-/-}$ neurons was still significantly increased compared to WT, indicating a partial rescue of phenotype (**Figure 2.10A**). We also observed similar changes for the calcium diffusion distance at synaptic sites, as groups followed the order: *Ppt1*$^{-/-}$ > *Ppt1*$^{-/-}$ + cerulenin ≥ *Ppt1*$^{-/-}$ + 2-BP = WT. These results further confirm the efficacy of palmitoylation inhibitor treatment (**Figure 2.10B**). Further, calcium transient frequency was higher in *Ppt1*$^{-/-}$ cells than in WT but was lowest in *Ppt1*$^{-/-}$ neurons treated with 2-BP or cerulenin (**Figure 2.10C and D**). It is plausible that chronic palmitoylation inhibitor treatment caused dissipation of synaptic proteins, including NMDARs (El-Husseini et al., 2002; Li et al., 2003), thereby reducing transient frequency.

Figure 2.10. Palmitoylation inhibitor treatment partially reverses pathological calcium dynamics in *Ppt1*$^{-/-}$ neurons.

A subset of *Ppt1*$^{-/-}$ cells treated with the palmitoylation inhibitors, 2-BP (1μM) or cerulenin (1μM) from DIV12-18 were transfected with GCaMP3 and imaged in the absence of Mg^{2+} for 5 minutes. Sites of calcium influx (spontaneous synaptic activity, $\Delta F/F_0$) were analyzed. These data were compared to WT and *Ppt1*$^{-/-}$ groups from **Figure 2.7**. **(A)** Quantification of calcium transient area under the curve (AUC) in WT, *Ppt1*$^{-/-}$, *Ppt1*$^{-/-}$ + 2-BP, and *Ppt1*$^{-/-}$ + cerulenin treated groups. **(B)** Quantification of calcium transient diffusion distance from WT, *Ppt1*$^{-/-}$, *Ppt1*$^{-/-}$ + 2-BP, and *Ppt1*$^{-/-}$ + cerulenin treated groups. (**C**) Quantification of calcium transient frequency (# transients/500 frames) for each synaptic site between WT, *Ppt1*$^{-/-}$, *Ppt1*$^{-/-}$ + 2-BP, and *Ppt1*$^{-/-}$ + cerulenin treated groups. **(D)** Representative kymographs displaying the calcium influx ($\Delta F/F_0$) at one synaptic site (pixels, X-axis) over the course of 500 frames (arrow represents direction of time in frames) from WT (left), *Ppt1*$^{-/-}$ (middle), and *Ppt1*$^{-/-}$ + palmitoylation inhibitor treatment groups. For experiments in Figure 2.10A-C, WT, *Ppt1*$^{-/-}$, *Ppt1*$^{-/-}$ + 2-BP, and *Ppt1*$^{-/-}$ + cerulenin groups were compared (n=185 synaptic sites (WT), n=131 synaptic sites (*Ppt1*$^{-/-}$), n=85 synaptic sites (*Ppt1*$^{-/-}$ + 2-BP), n=82 synaptic sites (*Ppt1*$^{-/-}$ + cerulenin); 3-4 neurons/group; 3 individual experiments) by one-way ANOVA followed by Tukey's post-hoc test and the significance was indicated as follows: *p<0.05,**p<0.01 ****p<0.0001 where indicated. Dots represent values for individual synaptic sites. Error bars represent s.e.m.

Figure 2.10. Palmitoylation inhibitor treatment partially reverses pathological calcium dynamics in *Ppt1*$^{-/-}$ neurons.

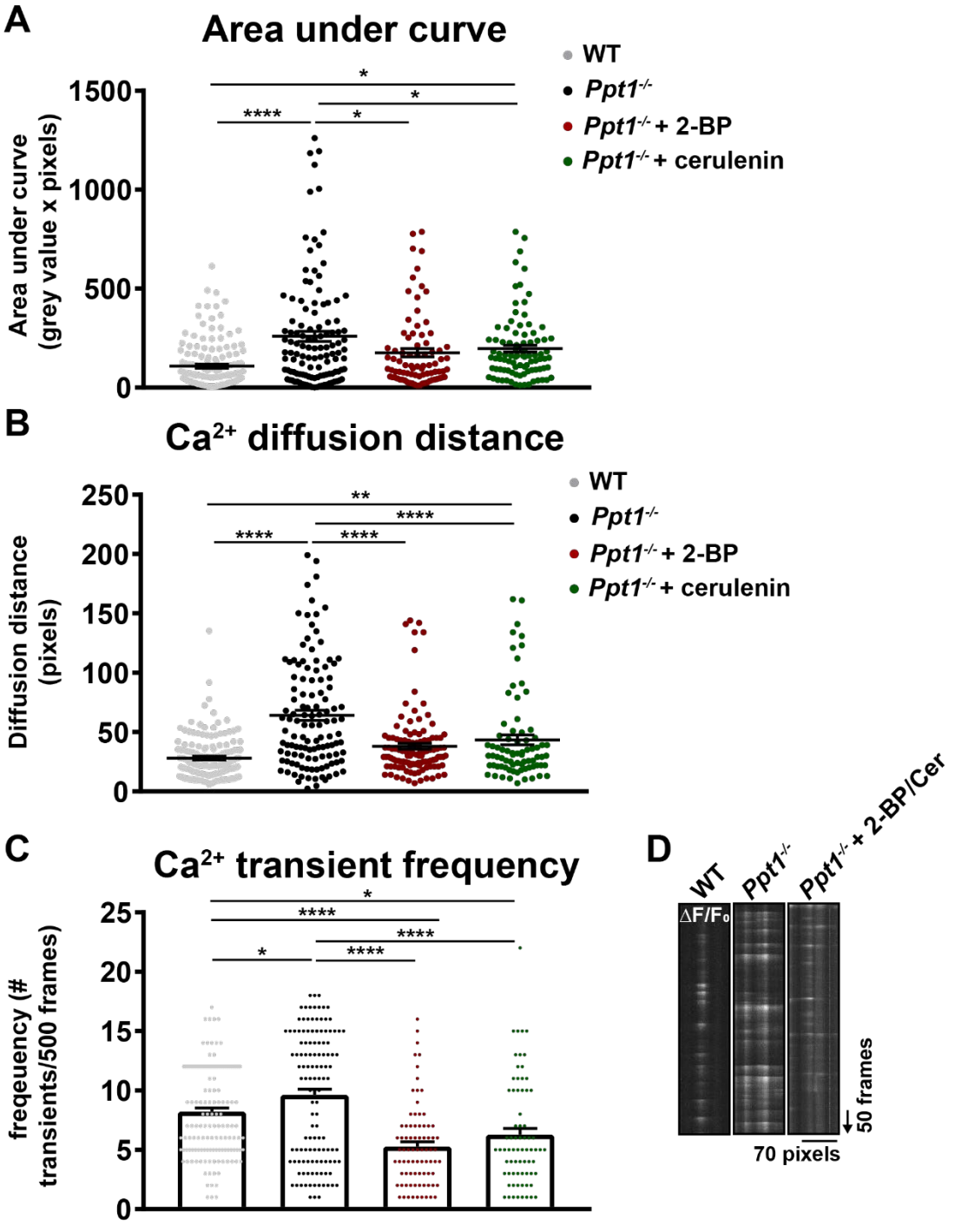

2.3.10. Palmitoylation inhibitors rescue Fyn kinase and GluN2B hyperpalmitoylation in *Ppt1*$^{-/-}$ neurons

Finally, we directly examined the palmitoylation state of neuronal proteins to gain insight into the mechanisms by which hyperpalmitoylation of neuronal substrates may lead to NMDA-mediated excitotoxicity in *Ppt1*$^{-/-}$ neurons. We also asked whether palmitoylation inhibitors can correct these abnormalities. We employed a modified acyl-biotin exchange procedure (Drisdel and Green, 2004), termed the APEGS assay (acyl-PEGyl exchange gel-shift)(Yokoi et al., 2016). The APEGS assay effectively tags the palmitoylation sites of neuronal substrates with a 5kDa polyethylene glycol (PEG) polymer, causing a molecular weight-dependent gel shift in immunoblot analyses. Thus, we quantitatively analyzed the palmitoylated fraction of synaptic proteins and palmitoylated signaling molecules that may influence NMDAR function.

To test the feasibility of the APEGS assay in our primary cortical neuronal cultures, we collected lysates at DIV18 from WT, *Ppt1*$^{-/-}$, and palmitoylation inhibitor-treated (2-BP or cerulenin, DIV12-18, 1μm) neurons and examined two palmitoylated proteins, PSD-95 and Fyn, which have been successfully quantified using this method (Yokoi et al., 2016).

We examined the palmitoylation state of PSD-95 at baseline and in response to palmitoylation inhibitor treatment (**Figure 2.11A**). As we found in our initial immunoblotting analyses of the homogenates derived from cortical tissues (**Figure 2.2)** and neuronal cultures **(Figure 2.5**), *Ppt1*$^{-/-}$ neurons had lower amounts of total PSD-95 protein than WT, as evidenced by decreased overall band density (**Figure 2.11B**). Remarkably, the palmitoylation states of PSD-95 were comparable between *Ppt1*$^{-/-}$ and WT neurons (**Figure 2.11C**), suggesting that PSD-95 may not be a PPT1 substrate. This finding is consistent with previous results showing that PSD-95 is depalmitoylated by ABHD17 but not PPT1 (Yokoi et al., 2016). Further, in line with previous data (El-Husseini et al., 2002; Fukata et al., 2004), 2-BP treatment decreased the relative palmitoylation level (ratio of palm/non-palm) of PSD-95 by nearly 50% in WT neurons (**Figure**

2.11C). However, we did not observe this effect in *Ppt1*$^{-/-}$ neurons. Also, cerulenin treatment had no consistent effects on PSD-95 levels or palmitoylation state in WT or *Ppt1*$^{-/-}$ cells (**Figure 2.11B and C**). However, the specificity of palmitoylation inhibitors is incompletely understood and compensatory mechanisms may restore PSD-95 palmitoylation due to chronic low-dose inhibitor treatment.

We performed the same analysis on another well-studied palmitoylated protein, Fyn kinase (**Figure 2.11D**). Fyn is a prominent member of the Src family kinases that phosphorylates and thereby stabilizes GluN2B at the synaptic surface (Prybylowski et al., 2005; Trepanier et al., 2012). Further, Fyn palmitoylation is important for its localization to the plasma membrane, where it may interact with GluN2B (Sato et al., 2009). Hence, Fyn hyperpalmitoylation can be a mechanism by which GluN2B retention may be enhanced in *Ppt1*$^{-/-}$ neurons. Indeed, total levels of Fyn were increased in *Ppt1*$^{-/-}$ neurons compared to WT, and were significantly suppressed by 2-BP and cerulenin treatment in both WT and *Ppt1*$^{-/-}$ neurons (**Figure 2.11E**). 2-BP and cerulenin treatments also significantly reduced the ratio of palmitoylated/non-palmitoylated Fyn in WT and *Ppt1*$^{-/-}$ neurons (**Figure 2.11F**). These findings imply that palmitoylation of Fyn regulates its stability and that Fyn hyperpalmitoylation may play a vital role in the stagnation of GluN2B to GluN2A subunit switch (**Figure 2.11E and F**).

Next, we examined the palmitoylation state of GluN2B (**Figure 2.11G**). First, total GluN2B levels were comparable between WT and *Ppt1*$^{-/-}$, vehicle-treated neurons at DIV18 (**Figure 2.11G and H**). While 2-BP had no effect on total GluN2B levels in WT neurons, 2-BP treatment decreased total GluN2B in *Ppt1*$^{-/-}$ neurons compared to vehicle-treated cells (**Figure 2.11H**). Cerulenin had the same effect (**Figure 2.11H**). Importantly, both 2-BP and cerulenin corrected the ratio of palmitoylated/non-palmitoylated GluN2B in *Ppt1*$^{-/-}$ neurons, with values approaching those of vehicle-treated WT cells (**Figure 2.11I**). No effect was observed in WT neurons treated with cerulenin. The latter results indicate that GluN2B palmitoylation state is less sensitive to

chronic, low-dose palmitoylation inhibitor treatment than Fyn palmitoylation state. One possibility, therefore, is that enhanced surface retention of GluN2B-containing NMDARs in *Ppt1*$^{-/-}$ neurons results from Fyn hyperpalmitoylation. Alternatively, hyperpalmitoylation of GluN2B may directly lead to enhanced surface retention of GluN2B-containing NMDARs in *Ppt1*$^{-/-}$ neurons (Mattison et al., 2012). Nevertheless, these data are in line with **Figure 2.10C**, which shows the frequency of calcium influxes in *Ppt1*$^{-/-}$ neurons is robustly decreased by treatment with 2-BP or cerulenin.

Finally, we examined the palmitoylation state of GluN2A at baseline and in response to palmitoylation inhibitor treatment (**Figure 2.11J)**. As we found in our biochemical analyses of the cortical homogenates (**Figure 2.2 and 2.5**), total levels of GluN2A were decreased in *Ppt1*$^{-/-}$ neurons compared to WT, as evidenced by decreased overall band density (**Figure 2.11J and K**). The palmitoylation state (ratio of palm/non-palm) of GluN2A, however, was unchanged between WT and *Ppt1*$^{-/-}$ at baseline (**Figure 2.11L**), suggesting that PPT1 is not directly involved in the palmitoylation state of GluN2A. Interestingly, chronic treatment with 2-BP and cerulenin had dissimilar effects on GluN2A levels and palmitoylation state in WT and *Ppt1*$^{-/-}$ neurons. In WT cells, 2-BP had no effect on GluN2A levels or palmitoylation state (**Figure 2.11K and L)**, indicating that the chronic low-dose treatment does not intervene the GluN2A depalmitoylation in WT neurons. In contrast, 2-BP treatment in *Ppt1*$^{-/-}$ neurons robustly increased both the total level and palmitoylation state of GluN2A, resulting in the nearly equal representation of two distinct GluN2A palmitoylated species (**Figure 2.11K and L**). Differing from 2-BP, cerulenin treatment modestly decreased total GluN2A levels and GluN2A palmitoylation state in WT cells (**Figure 2.11K and L)**. In contrast, cerulenin treatment of *Ppt1*$^{-/-}$ cells increased the total GluN2A protein level (**Figure 2.11K and L**), albeit not nearly as robustly as 2-BP. Overall, these results illustrate complex and potentially indirect effects of palmitoylation inhibitor treatment on the palmitoylation state of GluN2A in *Ppt1*$^{-/-}$ neurons. While there may be other possibilities, the data suggest that 2-BP treatment may have corrected a defect in palmitoylation in *Ppt1*$^{-/-}$ neurons (e.g. Fyn

hyperpalmitoylation), thereby initiating or facilitating the GluN2B to GluN2A switch. Nevertheless, the increase in GluN2A levels and palmitoylation in *Ppt1*$^{-/-}$ cells may ultimately account for the beneficial effects of inhibitor treatment in our complementary analyses (**Figure 2.9 and 2.10**).

In aggregate, these data point to hyperpalmitoylation of Fyn and GluN2B as mechanisms by which chronic low-dose palmitoylation inhibitor treatment may decrease the synaptic stabilization of GluN2B. This in thereby reducing calcium load in *Ppt1*$^{-/-}$ neurons and mitigating the enhanced susceptibility to excitotoxicity. Further, these data imply that the progression of CLN1 may be mediated by the palmitoylation of Fyn kinase, which is also being targeted for the treatment of Alzheimer's disease (Kaufman et al., 2015; Nygaard et al., 2015).

Figure 2.11. Hyperpalmitoylation of Fyn kinase and GluN2B is reversed in *Ppt1*$^{-/-}$ primary cortical neurons by palmitoylation inhibitor treatment.

(A) Representative post-APEGS immunoblot of PSD-95 with β-actin loading control. **(B)** Quantification of total PSD-95 levels following chronic (7d) treatment with vehicle or the palmitoylation inhibitors, 2-BP (1μM) or cerulenin (1μM) where indicated. **(C)** Quantification of the ratio of palmitoylated/non-palmitoylated PSD-95 levels following chronic (7d) treatment with vehicle or the palmitoylation inhibitors, 2-BP (1μM) or cerulenin (1μM) where indicated. **(D)** Representative post-APEGS immunoblot of Fyn kinase with β-actin loading control and minus hydroxylamine (-HA) control. **(E)** Quantification of total Fyn kinase levels following chronic (7d) treatment with vehicle or the palmitoylation inhibitors, 2-BP (1μM) or cerulenin (1μM) where indicated. **(F)** Quantification of the ratio of palmitoylated/non-palmitoylated Fyn kinase levels following chronic (7d) treatment with vehicle or the palmitoylation inhibitors, 2-BP (1μM) or cerulenin (1μM) where indicated. **(G)** Representative post-APEGS immunoblot of GluN2B with β-actin loading control and minus hydroxylamine (-HA) control. **(H)** Quantification of total GluN2B levels following chronic (7d) treatment with vehicle or the palmitoylation inhibitors, 2-BP (1μM) or cerulenin (1μM) where indicated. **(I)** Quantification of the ratio of palmitoylated/non-palmitoylated GluN2B levels following chronic (7d) treatment with vehicle or the palmitoylation inhibitors, 2-BP (1μM) or cerulenin (1μM) where indicated. **(J)** Representative post-APEGS immunoblot of GluN2A with β-actin loading control. **(K)** Quantification of total GluN2A levels following chronic (7d) treatment with vehicle or the palmitoylation inhibitors, 2-BP (1μM) or cerulenin (1μM) where indicated. **(L)** Quantification of the ratio of palmitoylated/non-palmitoylated GluN2A levels following chronic (7d) treatment with vehicle or the palmitoylation inhibitors, 2-BP (1μM) or cerulenin (1μM) where indicated. DMSO was used for vehicle treatment. For experiments in Figure 2.11 A and D, WT, *Ppt1*$^{-/-}$, WT + 2-BP, WT + cerulenin, *Ppt1*$^{-/-}$ + 2-BP, and *Ppt1*$^{-/-}$ + cerulenin treatment groups were compared (n=4 independent experiments) by two-way ANOVA followed by Tukey's post-hoc test and significance indicated as follows: *p<0.05, **p<0.01, ****p<0.0001 where indicated. For experiments in Figure 2.11B and C, WT, *Ppt1*$^{-/-}$, WT + 2-BP, WT + cerulenin, *Ppt1*$^{-/-}$ + 2-BP, and *Ppt1*$^{-/-}$ + cerulenin were compared (n=2-4 independent experiments) at each time point using two-way ANOVA followed by Tukey's post-hoc test and the significance was indicated as follows: *p<0.05, **p<0.01, ***p<0.001 where indicated. Error bars represent s.e.m.

Figure 2.11. Hyperpalmitoylation of Fyn kinase and GluN2B is reversed in *Ppt1*$^{-/-}$ primary cortical neurons by palmitoylation inhibitor treatment.

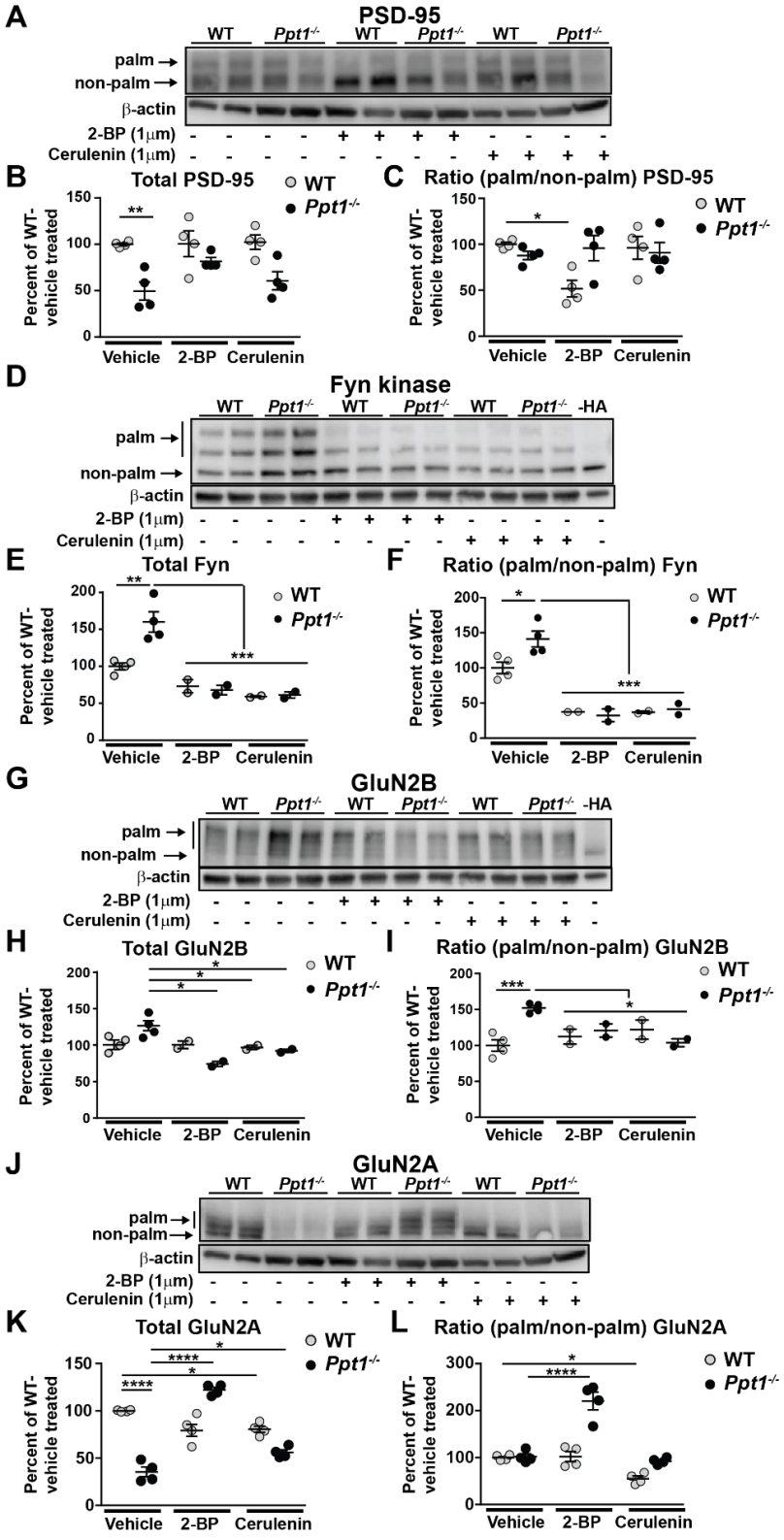

2.4. Discussion

Since the development of the first *Ppt1*$^{-/-}$ mouse and knock-in mouse model of CLN1, much progress has been made in understanding the temporal, regional, and cell-type specific effects of lipofuscin accumulation and neuronal degeneration, particularly in late stage disease (Gupta et al., 2001; Bible et al., 2004; Kielar et al., 2007; Bouchelion et al., 2014). In addition, comprehensive data characterizing the behavioral dysfunction of the *Ppt1*$^{-/-}$ mouse has recapitulated clinical symptoms of the disease (Dearborn et al., 2015). Recent data demonstrate that PPT1 localizes to synaptic compartments and influences presynaptic localization and mobility of prominent presynaptic proteins, including SNAP25 (Kim et al., 2008). These findings correlate with histological and electrophysiological findings in cultured *Ppt1*$^{-/-}$ neurons, demonstrating a depletion of presynaptic vesicle pool size (Virmani et al., 2005). Moreover, presynaptic protein localization and function are altered in CLN1 models and in human tissue (Kanaani et al., 2004; Kim et al., 2008; Aby et al., 2013).

In the current study, we have identified a role for PPT1 in postsynaptic maturation in the *Ppt1*$^{-/-}$ mouse model of CLN1. Our principal finding demonstrates a role for PPT1 in the regulation of NMDAR composition and function that leaves *Ppt1*$^{-/-}$ neurons vulnerable to excitotoxic insult, which is alleviated by chronic low-dose palmitoylation inhibitor treatment. Together, these data implicate dysregulated GluN2 subunit switch as a major pathogenic mechanism in CLN1.

2.4.1. Stagnation of GluN2B to GluN2A subunit switch in the *Ppt1*$^{-/-}$ mouse visual cortex

During early postnatal development, NMDARs switch their subunit composition from primarily containing GluN2B subunits to predominantly containing GluN2A subunits (Carmignoto and Vicini, 1992; Sheng et al., 1994; Stocca and Vicini, 1998). The increased contribution of GluN2A subunits is accompanied by several distinctive changes in NMDAR-mediated synaptic currents, including a shortening of the decay time (Carmignoto and Vicini, 1992). In the rodent

visual cortex, developmental decrease of the NMDAR-EPSC decay time and the corresponding switch from GluN2B- to GluN2A-diheteromeric receptors occurs between the second and fourth postnatal weeks (Carmignoto and Vicini, 1992; Quinlan et al., 1999a, 1999b; Philpot et al., 2001). The GluN2 subunit switch is not absolute, and GluN2B subunits remains expressed in many regions of the adult brain. Consequently, synaptic NMDARs are predominantly diheteromeric GluN1/GluN2A and triheteromeric GluN1/GluN2A/GluN2B receptors (Luo et al., 1997; Tovar and Westbrook, 1999; Tovar et al., 2013), while extrasynaptic sites are enriched in GluN2B-containing receptors (Carmignoto and Vicini, 1992; Rumbaugh and Vicini, 1999; Tovar and Westbrook, 1999).

Our biochemical analyses show reductions in the protein amount of GluN2A subunit and their preferential synaptic scaffold, PSD-95, in the *Ppt1*$^{-/-}$ mouse visual cortex at distinct developmental time points (P33-P60). These alterations correlate with the prolongation of the evoked NMDAR-EPSC decay time in *Ppt1*$^{-/-}$ layer II/III cortical neurons. One may anticipate the prolonged decay time in *Ppt1*$^{-/-}$ neurons is more sensitive to a GluN2B-specific inhibitor. However, both WT and *Ppt1*$^{-/-}$ neurons equally responded to Ro 25-6981 (**Figure 2.3E**). Importantly, triheteromeric NMDARs have intermediate decay kinetics (between purely GluN2A- or GluN2B-containing diheteromeric receptors) and are relatively insensitive to GluN2B-specific inhibitors (Stroebel et al., 2018). Still, the GluN2B subunit may dominate specific features of these triheteromeric NMDARs such as their recycling rate or activation during synaptic plasticity (Tang et al., 2010; Delaney et al., 2013). We demonstrate that GluN2B is hyperpalmitoylated in *Ppt1*$^{-/-}$ neurons (**Figure 2.11C**). Therefore, the dysregulated GluN2 subunit switch in *Ppt1*$^{-/-}$ neurons may be explained by the growing presence of the triheteromeric receptors at P42 (and anticipate the same results between P33-P60) in the cortex (Luo et al., 1997). Specifically, we propose that increased palmitoylation of GluN2B subunits leads to more stable assembly of triheteromeric receptors and their accumulation at postsynaptic sites.

However, the presence of triheteromeric receptors does not fully explain the Ca^{2+} imaging data demonstrating that Ro 25-6981 treatment sufficiently inhibits extrasynaptic Ca^{2+} influx *in vitro* (**Figure 2.7**), which is likely mediated by diheteromeric GluN2B-NMDARs. In rat hippocampal neurons, though the ifenprodil-sensitive component of synaptic and extrasynaptic NMDAR populations declines with maturation, the majority of extrasynaptic NMDARs remain sensitive to ifenprodil (diheteromeric GluN2B-NMDARs) even into synaptic maturity (DIV13-19)(Thomas et al., 2006). This sustained extrasynaptic population of diheteromeric GluN2B-NMDARs would be represented in our *in vitro* imaging experiments (in Mg^{2+} free solution) and be blocked by bath application of Ro 25-6981, constraining the remaining activity to synaptic NMDARs that more closely resemble WT neurons (**Figure 2.7**). Another explanation is that immature spine structure may have altered the dendritic distribution of GluN2B-containing diheteromeric receptors in *Ppt1*$^{-/-}$ neurons, limiting the representation of these Ro 25-6981-sensitive NMDARs evoked by single pulse of synaptic activation as in **Figure 2.3E**. These differences in experimental preparation (dissociated neurons vs. slice and electrophysiology vs. Ca^{2+} imaging) may therefore contribute to the observed variation in Ro 25-6981 efficacy *in vivo* and *in vitro*.

2.4.2. Candidate PPT1 substrates that regulate the GluN2B to GluN2A subunit switch

Initially, we predicted synaptic markers, particularly PSD-95, would be hyperpalmitoylated and overrepresented at postsynaptic sites, since their synaptic distribution depends on the balance between palmitoylation and depalmitoylation (Craven et al., 1998; El-Husseini et al., 2000; Jeyifous et al., 2016). As PSD-95 facilitates the GluN2 subunit switch and preferentially interacts with GluN2A, we also hypothesized an increase in the GluN2A subunit. However, our biochemical data indicate reductions in the total amount as well as the synaptic incorporation of GluN2A and PSD-95 in the PPT1-deficient brain (**Figure 2.2.1**). Interestingly, a recent study suggests that PSD-95 is depalmitoylated by ABHD17 family enzymes, not PPT1 (Yokoi et al.,

2016). Our results support this notion, as PSD-95 palmitoylation state is comparable between WT and *Ppt1*$^{-/-}$ neurons (**Figure 11B**). These findings illustrate that depalmitoylases demonstrate substrate specificity which may be important for the regulation of coordinated, long-term changes at the synapse.

Our biochemical analyses demonstrate that the GluN2B to GluN2A switch is disrupted both *in vivo* (**Figure 2.2A-D**) and *in vitro* (**Figure 2.5A-D**) in *Ppt1*$^{-/-}$ neurons and that PPT1 expression in the WT visual cortex correlates tightly with the timing of this disruption (**Figure 2.2E**). Further, both electrophysiological (**Figure 2.3**) and calcium imaging data (**Figure 2.7**) indicate that *Ppt1*$^{-/-}$ neurons have more GluN2B-predominant extrasynaptic NMDARs. Finally, we demonstrate that GluN2B is hyperpalmitoylated in *Ppt1*$^{-/-}$ *in vitro* (**Figure 2.11C**). These findings raise the possibility that GluN2B is a PPT1 substrate and thus, lack of PPT1-mediated GluN2B depalmitoylation partly drives disease symptoms. Indeed, protein palmitoylation generally enhances the half-life of proteins (Linder and Deschenes, 2007) and, in the case of GluN2B, specifically enhances its phosphorylation and consequent surface retention (Hayashi et al., 2009). Thus, GluN2B hyperpalmitoylation alone may alter NMDAR function enough to drive some of the functional deficits described in *Ppt1*$^{-/-}$ neurons herein.

Alternatively, the lack of PPT1 function may indirectly set the stage for an overrepresentation of GluN2B at excitatory synapses and consequent pathogenic activity. A primary candidate for such an indirect mechanism involves Src family kinase Fyn, which regulates GluN2B protein conformation, surface retention, and fine-scale synaptic localization (Prybylowski et al., 2005; Nakazawa et al., 2006; Mattison et al., 2012). Fyn is palmitoylated and their subcellular localization is palmitoylation-dependent (Koegl et al., 1994). Further, Fyn kinase is developmentally regulated (Umemori et al., 1992; Inomata et al., 1994) and a major palmitoylated downstream kinase of reelin signaling (see below) that phosphorylates GluN2B, affecting its surface stabilization (Alland et al., 1994; Koegl et al., 1994; Prybylowski et al., 2005; Kang et al.,

2008). Crucially, palmitoylation of GluN2B enhances Fyn-mediated phosphorylation at Tyr1472 and thereby inhibits its internalization (Hayashi et al., 2009). Thus, Fyn hyperactivation may be responsible for the dysregulation of GluN2B to GluN2A switch in *Ppt1*$^{-/-}$ neurons. Specifically, hyperpalmitoylated Fyn kinase may lead to enhanced phosphorylation and surface retention of GluN2B-containing NMDARs, limiting access to alternative depalmitoylating enzymes which may act in recycling endosomes or other cellular compartments, resulting in GluN2B hyperpalmitoylation. Indeed, the palmitoylation state of Fyn is more sensitive to palmitoylation inhibitors (**Figure 2.11B**) than GluN2B (**Figure 2.11C**). Notably, 2BP-treated *Ppt1*$^{-/-}$ neurons exhibit an increase in GluN2A palmitoylation state (**Figure 2.11D**). While the reason for change is not entirely clear, one possibility is that the palmitoylation state of Fyn is more sensitive to the chronic low-dose inhibition than that of GluN2 subunits. In this scenario, suppression of Fyn palmitoylation attenuates its function, thereby exaggerating the GluN2 subunit switch in *Ppt1*$^{-/-}$ neurons.

There are several other mechanisms underlying this GluN2 subunit switch that may be affected by lack of PPT1. These signaling pathways include reelin, Wnt-5a, and mGluR5 (Groc et al., 2007; Cerpa et al., 2011; Matta et al., 2011). The accumulation of reelin at excitatory synapses during development, for example, mobilizes GluN2B-containing NMDARs and enhances the synaptic contribution of GluN2A-containing NMDARs (Groc et al., 2007; Iafrati et al., 2014). Similarly, evoked activation of mGluR5 at hippocampal synapses is necessary for incorporation of GluN2A-containing NMDARs, and mGluR5-null mice demonstrate deficient GluN2B to GluN2A switching (Matta et al., 2011). Importantly, Wnt-5a, mGluR5, and Fyn kinase (downstream of reelin signaling) are directly regulated by palmitoylation state (Kurayoshi et al., 2007; Yokoi et al., 2016), suggesting that disruptions in protein depalmitoylation may lead to impaired synaptic maturation through several pathways. Further study is needed to elucidate precisely how PPT1 influences the GluN2B to GluN2A switch and if Fyn is indeed a key mediator. Nevertheless, we

have shown that the lack of functional PPT1 results in aberrant surface retention of GluN2B-containing NMDAR complexes, either directly or indirectly, thereby impeding the developmental switch to GluN2A-containing receptors.

2.4.3. Excitotoxicity and NMDAR regulation

Patients afflicted with later-onset NCLs typically exhibit an enlarged VEP prior to degeneration, concurrent with seizure (Pampiglione and Harden, 1977; Haltia, 2006; Pagon et al., 2013). This phenomenon has not been directly observed in CLN1, though this may be due to the rapid degeneration and advanced pathology at time of diagnosis for these patients. Nevertheless, it is conceivable that disrupted GluN2 subunit switch contributes to hyperexcitability in CLN1 and thereby accelerates cell death, leading to the rapid degeneration of neuronal circuits. Indeed, recent evidence link GluN2 subunit composition and NMDAR localization to opposing downstream transcriptional programs (Martel et al., 2009, 2012; Hardingham and Bading, 2010). Specifically, GluN2A-containing NMDARs in the postsynaptic density activate cyclic-AMP response element binding protein (CREB) and other transcription factors associated with cell-survival and learning. In contrast, extrasynaptic, GluN2B-containing NMDARs preferentially trigger pro-apoptotic signaling pathways and cause inhibition of CREB (Hardingham and Bading, 2002; Hardingham et al., 2002). Though this system is likely more intricate than described here (Thomas et al., 2006), these previous studies are consistent with our observations that *Ppt1*$^{-/-}$ neurons are biased toward extrasynaptic calcium transients (**Figure 2.7**) and that they are more susceptible to excitotoxicity (**Figures 2.8 and 2.9**). These data are also in agreement with previous studies demonstrating markedly enhanced NMDA-mediated toxicity in *Ppt1*$^{-/-}$ neurons and improved behavioral phenotype of *Ppt1*$^{-/-}$ mice treated with the NMDAR antagonist, memantine (Finn et al., 2013). Furthermore, the most significant outcome of this study is that palmitoylation inhibitors mitigated the pro-apoptotic predisposition of *Ppt1*$^{-/-}$ neurons *in vitro* (**Figure 2.9**).

The incorporation of GluN2A into NMDARs is experience-dependent (Quinlan et al., 1999b, 1999a). Therefore, an intriguing possibility is that *Ppt1*$^{-/-}$ neurons in sensory cortices are unable to tolerate normal sensory experiences, in part because this experience-dependent GluN2 subunit switch is disrupted. Indeed, PPT1-defeciency results in selective degeneration of thalamic nuclei and primary sensory cortices (Bible et al., 2004; Kielar et al., 2007). Further, PPT1 expression, as we demonstrate herein (**Figure 2.2E, Figure 2.2.1E**), is developmentally-regulated in WT rodents and may regulate this switching phenomenon (Suopanki et al., 1999a, 1999b). Together, we argue that intact PPT1 plays a critical role in regulating NMDAR functional properties in response to external stimuli, thereby facilitating synaptic maturation and preventing excitotoxicity. Whether manipulating neuronal activity or experience-dependent synaptic plasticity ameliorates disease progression remains unknown and is a focus of ongoing experiments.

2.4.4. Dendritic spine immaturity induced by lack of PPT1

The current study demonstrates that dendritic spines in *Ppt1*$^{-/-}$ neurons are longer and thinner. We also show that dendritic spine density is increased in *Ppt1*$^{-/-}$ neurons as compared to WT (**Figures 2.4, 2.6**). These features are both generally indications of dendritic spine immaturity. During neurodevelopment, rapid spinogenesis involves filopodial formation followed by molecular and structural changes that lead to dendritic spine maturation in the adult brain. These processes are regulated by various palmitoylated proteins including the ones we have examined in this study. It is established that Src family kinase activity, including Fyn, mediates biochemical changes that lead to filopodia and dendritic spine formation in neurons (Morita et al., 2006; Webb et al., 2007; Babus et al., 2011; Formoso et al., 2015). GluN2B activity also enhances filopodial formation in hippocampal neurons, and application of GluN2B-specific blockers inhibits this effect (Henle et al., 2012). Further, GluN2B hyperpalmitoylation at specific sites stabilizes GluN2B-containing receptors at the cell surface (Mattison et al., 2012). Thus, it is plausible that hyperpalmitoylation of GluN2B in *Ppt1*$^{-/-}$ cells increases filopodial formation through enhanced

expression of surface NMDARs, resulting in an increased spine density (**Figure 2.4 and 2.6**). However, whether hyperpalmitoylation of GluN2B and Fyn are directly responsible for the altered spine morphology in *Ppt1*$^{-/-}$ neurons awaits further studies. Regardless, the immature dendritic morphology of *Ppt1*$^{-/-}$ neurons correlates with stagnation of the developmental switch of GluN2 subunit. However, there are also other palmitoylated proteins that may account for aberrant spine formation in *Ppt1*$^{-/-}$ neurons. Increased spine density in *Ppt1*$^{-/-}$ neurons suggests that filopodial organizer proteins may be substrates of PPT1 or are indirectly affected by the enzyme. Several neuronal proteins readily induce filopodial formation in a palmitoylation-dependent manner in cultured neurons (Patterson and Skene, 1994; Gauthier-Campbell et al., 2004). For example, palmitoylation of the growth-associated protein-43 (GAP-43) regulates filopodial formation (Kutzleb et al., 1998; Gauthier-Campbell et al., 2004; Arstikaitis et al., 2008), and its protein amount increases in the *Ppt1*$^{-/-}$ brain beginning at 1 month (Zhang et al., 2006). Cdc42 is another palmitoylated protein that may accelerate neurite formation in *Ppt1*$^{-/-}$ neurons (Gauthier-Campbell et al., 2004; Kang et al., 2008). Hyperactivity of these palmitoylated proteins may accelerate actin dynamics, and lead to excessive filopodial formation in *Ppt1*$^{-/-}$ neurons (Patterson and Skene, 1999).

Filopodial formation is generally followed by spine maturation, which is facilitated by the palmitoylation and localization of PSD-95 at the postsynaptic membrane (Craven et al., 1998; El-Husseini et al., 2000a; Yoshii et al., 2011; Jeyifous et al., 2016). Synaptosomes derived from *Ppt1*$^{-/-}$ mouse cortices show reductions in PSD-95 protein levels (**Figure 2.2**). This finding is consistent with the decrease in mature dendritic spine characteristics in *Ppt1*$^{-/-}$ neurons *in vitro* and *in vivo* (**Figure 2.4 and 2.6**). However, the lack of PPT1 function had no direct effect on PSD-95 palmitoylation state (**Figure 2.11A**). Thus, we argue that the perturbed GluN2B to GluN2A switch is primarily responsible for excessive filopodial formation in *Ppt1*$^{-/-}$ neurons. While underrepresented PSD-95 expression correlates with impaired spine maturation, this is likely a

secondary effect. Further study is warranted to identify the PPT1 substrates that directly regulate spinogenesis.

2.4.5. Implications for other neurodegenerative diseases

While substantial progress has been made in our understanding of adult-onset neurodegenerative diseases including Alzheimer's disease and Parkinson's disease, effective, disease-modifying therapeutics are yet to be developed for most of these disorders. In part, this is likely due to the genetic complexity and heterogeneity of these diseases as well as lifestyle and environmental factors limiting the translational success of seemingly promising therapeutic strategies. Recently, studies in monogenic diseases have attracted attention because they share common pathological hallmarks with adult-onset neurodegenerative diseases, including lipofuscin. This approach has turned out to be valuable to decipher underlying disease mechanisms in Parkinson's disease, for instance (Peltonen et al., 2006; Neudorfer et al., 1996; Tayebi et al., 2001; Sidransky et al., 2009; Sidransky and Lopez, 2012).

Our data indicate a significant dysregulation of NMDAR composition and function in the *Ppt1*$^{-/-}$ cortex associated with GluN2B and Fyn hyperpalmitoylation. Importantly, GluN2B has already been implicated in psychiatric and neurodegenerative disorders, including Alzheimer's disease (Paoletti et al., 2013; Yamamoto et al., 2015). Furthermore, Fyn is currently being investigated in clinical trials for Alzheimer's disease (Nygaard et al., 2014, 2015; Kaufman et al., 2015). Hence, our findings in CLN1 corroborate evidence in adult-onset neurodegenerative disorders and converge on disruption of Fyn kinase, GluN2B, or both as a shared feature of neurodegeneration. GluN2B and Fyn function therefore represent promising therapeutic targets for CLN1 and beyond.

The enrichment and importance of palmitoylation at the synapse imply that additional mechanisms linking dysregulated protein palmitoylation to neurological diseases will likely be

revealed. For instance, AMPAR and GABAR subunits undergo palmitoylation (Hayashi et al., 2005; Fang et al., 2006) and recent work demonstrates that deficient AMPAR palmitoylation facilitates seizure activity *in vivo* (Itoh et al., 2018). Further, preliminary results from our lab show developmental hyperpalmitoylation of at least one AMPAR subunit in *Ppt1*$^{-/-}$ animals (Koster, unpublished findings). Hence, the regulation of these receptors may also be involved in the pathogenesis of CLN1 or other diseases with perturbations in the balance between palmitoylation and depalmitoylation. Importantly, the palmitoylation of amyloid precursor protein (APP) and huntingtin are implicated in Alzheimer's disease and Huntington's disease pathogenesis, respectively (Huang et al., 2004; Smith et al., 2005; Zheng and Koo, 2006; Bhattacharyya et al., 2013). Thus, our results extend a growing body of evidence implicating protein palmitoylation in neurological diseases and warrant further investigation of protein depalmitoylation as a therapeutic target.

CHAPTER 2 CITED LITERATURE

Aby E, Gumps K, Roth A, Sigmon S, Jenkins SE, Kim JJ, Kramer NJ, Parfitt KD, Korey CA (2013) Mutations in palmitoyl-protein thioesterase 1 alter exocytosis and endocytosis at synapses in Drosophila larvae. Fly 7:267–279.

Ahtiainen L, Diggelen OP, Jalanko A, Kopra O (2003) Palmitoyl protein thioesterase 1 is targeted to the axons in neurons. The Journal of comparative neurology 455:368–377.

Alland L, Peseckis S, Atherton R, Berthiaume L, Resh (1994) Dual myristylation and palmitylation of Src family member p59fyn affects subcellular localization. The Journal of biological chemistry 269:16701–16705.

Aoki C, Fujisawa S, Mahadomrongkul V, Shah PJ, Nader K, Erisir A (2003) NMDA receptor blockade in intact adult cortex increases trafficking of NR2A subunits into spines, postsynaptic densities, and axon terminals. Brain research 963:139–149.

Arstikaitis P, Gauthier-Campbell C, Herrera R, Huang K, Levinson JN, Murphy TH, Kilimann MW, Sala C, Colicos MA, El-Husseini A (2008) Paralemmin-1, a modulator of filopodia induction is required for spine maturation. Molecular biology of the cell 19:2026–2038.

Arstikaitis P, Gauthier-Campbell C, Huang K, El-Husseini A, Murphy TH (2011) Proteins that promote filopodia stability, but not number, lead to more axonal-dendritic contacts. PloS one 6:e16998.

Babus LW, Little EM, Keenoy KE, Minami S, Chen E, ng J, Caviness J, Koo S-YY, Pak DT, Rebeck G, Turner R, Hoe H-SS (2011) Decreased dendritic spine density and abnormal spine morphology in Fyn knockout mice. Brain research 1415:96–102.

Bandyopadhyay D, Cyphersmith A, Zapata JA, Kim Y, Payne CK (2014) Lysosome transport as a function of lysosome diameter. PloS one 9:e86847.

Bear M, Kleinschmidt A, Gu Q, Singer W (1990) Disruption of experience-dependent synaptic modifications in striate cortex by infusion of an NMDA receptor antagonist. The Journal of neuroscience: 10:909–925.

Bennett M, Hofmann S (1999) The neuronal ceroid-lipofuscinoses (Batten disease): a new class of lysosomal storage diseases. Journal of inherited metabolic disease 22:535–544.

Berardi N, Pizzorusso T, Maffei L (2000) Critical periods during sensory development. Current opinion in neurobiology 10:138–145.

Bhattacharyya R, Barren C, Kovacs DM (2013) Palmitoylation of amyloid precursor protein regulates amyloidogenic processing in lipid rafts. The Journal of neuroscience: 33:11169–11183.

Bible E, Gupta P, Hofmann SL, Cooper JD (2004) Regional and cellular neuropathology in the

palmitoyl protein thioesterase-1 null mutant mouse model of infantile neuronal ceroid lipofuscinosis. Neurobiology of disease 16:346–359.

Blom T, Schmiedt M-LL, Wong AM, Kyttälä A, Soronen J, Jauhiainen M, Tyynelä J, Cooper JD, Jalanko A (2013) Exacerbated neuronal ceroid lipofuscinosis phenotype in Cln1/5 double-knockout mice. Disease models & mechanisms 6:342–357.

Bouchelion A, Zhang Z, Li Y, Qian H, Mukherjee AB (2014) Mice homozygous for c.451C>T mutation in Cln1 gene recapitulate INCL phenotype. Annals of clinical and translational neurology 1:1006–1023.

Camp L, Hofmann S (1993) Purification and properties of a palmitoyl-protein thioesterase that cleaves palmitate from H-Ras. The Journal of biological chemistry 268:22566–22574.

Camp L, Verkruyse L, Afendis S, Slaughter C, Hofmann S (1994) Molecular cloning and expression of palmitoyl-protein thioesterase. The Journal of biological chemistry 269:23212–23219.

Carmignoto G, Vicini S (1992) Activity-dependent decrease in NMDA receptor responses during development of the visual cortex. Science (New York, NY) 258:1007–1011.

Cerpa W, Gambrill A, Inestrosa NC, Barria A (2011) Regulation of NMDA-Receptor Synaptic Transmission by Wnt Signaling. The Journal of Neuroscience 31:9466–9471.

Chen B-SS, Thomas EV, Sanz-Clemente A, Roche KW (2011) NMDA receptor-dependent regulation of dendritic spine morphology by SAP102 splice variants. The Journal of neuroscience: 31:89–96.

Cooke SF, Bear MF (2010) Visual experience induces long-term potentiation in the primary visual cortex. The Journal of neuroscience: 30:16304–16313.

Craven SE, El-Husseini AE, Bredt DS (1998) Synaptic Targeting of the Postsynaptic Density Protein PSD-95 Mediated by Lipid and Protein Motifs. Neuron 22:497–509.

Cull-Candy S, Brickley S, Farrant M (2001) NMDA receptor subunits: diversity, development and disease. Current opinion in neurobiology 11:327–335.

Dearborn JT, Harmon SK, Fowler SC, O'Malley KL, Taylor GT, Sands MS, Wozniak DF (2015) Comprehensive functional characterization of murine infantile Batten disease including Parkinson-like behavior and dopaminergic markers. Scientific reports 5:12752.

de Armentia M, Sah P (2003) Development and subunit composition of synaptic NMDA receptors in the amygdala: NR2B synapses in the adult central amygdala. The Journal of neuroscience: 23:6876–6883.

Delaney AJ, Sedlak PL, Autuori E, Power JM, Sah P (2013) Synaptic NMDA receptors in

basolateral amygdala principal neurons are triheteromeric proteins: physiological role of GluN2B subunits. Journal of neurophysiology 109:1391–1402.

Desai NS, Cudmore RH, Nelson SB, Turrigiano GG (2002) Critical periods for experience-dependent synaptic scaling in visual cortex. Nature neuroscience 5:783–789.

Dongen AM (2009) Biology of the NMDA Receptor. CRC Press/Taylor & Francis.

Dong YN, Waxman EA, Lynch DR (2004) Interactions of postsynaptic density-95 and the NMDA receptor 2 subunit control calpain-mediated cleavage of the NMDA receptor. The Journal of neuroscience: 24:11035–11045.

Drisdel RC, Green WN (2004) Labeling and quantifying sites of protein palmitoylation. BioTechniques 36:276–285.

El-Husseini AE, Craven SE, Chetkovich DM, Firestein BL, Schnell E, Aoki C, Bredt DS (2000a) Dual Palmitoylation of Psd-95 Mediates Its Vesiculotubular Sorting, Postsynaptic Targeting, and Ion Channel Clustering. The Journal of Cell Biology 148:159–172.

El-Husseini A, Schnell E, Chetkovich D, Nicoll R, Bredt D (2000b) PSD-95 involvement in maturation of excitatory synapses. Science (New York, NY) 290:1364–1368.

El-Husseini A, Schnell E, Dakoji S, Sweeney N, Zhou Q, Prange O, Gauthier-Campbell C, Aguilera-Moreno A, Nicoll RA, Bredt DS (2002) Synaptic strength regulated by palmitate cycling on PSD-95. Cell 108:849–863.

Elias G, Elias L, Apostolides P, Kriegstein A, Nicoll R (2008) Differential trafficking of AMPA and NMDA receptors by SAP102 and PSD-95 underlies synapse development. Proceedings of the National Academy of Sciences of the United States of America 105:20953–20958.

Engert F, Bonhoeffer T (1999) Dendritic spine changes associated with hippocampal long-term synaptic plasticity. Nature 399:66–70.

Evans RC, Morera-Herreras T, Cui Y, Du K, Sheehan T, Kotaleski JH, Venance L, Blackwell KT (2012) The effects of NMDA subunit composition on calcium influx and spike timing-dependent plasticity in striatal medium spiny neurons. PLoS computational biology 8:e1002493.

Fagiolini M, Hensch T (2000) Inhibitory threshold for critical-period activation in primary visual cortex. Nature 404:183–186.

Fang C, Deng L, Keller CA, Fukata M, Fukata Y, Chen G, Lüscher B (2006) GODZ-mediated palmitoylation of GABA(A) receptors is required for normal assembly and function of GABAergic inhibitory synapses. The Journal of neuroscience: 26:12758–12768.

Finn R, Kovács AD, Pearce DA (2012) Altered glutamate receptor function in the cerebellum of the Ppt1−/− mouse, a murine model of infantile neuronal ceroid lipofuscinosis. Journal of

Neuroscience Research 90:367–375.

Finn R, Kovács AD, Pearce DA (2013) Treatment of the Ppt1(-/-) mouse model of infantile neuronal ceroid lipofuscinosis with the N-methyl-D-aspartate (NMDA) receptor antagonist memantine. Journal of child neurology 28:1159–1168.

Fischer G, Mutel V, Trube G, Malherbe P, Kew J, Mohacsi E, Heitz M, Kemp J (1997) Ro 25-6981, a highly potent and selective blocker of N-methyl-D-aspartate receptors containing the NR2B subunit. Characterization in vitro. The Journal of pharmacology and experimental therapeutics 283:1285–1292.

Formoso K, Billi SC, Frasch AC, Scorticati C (2015) Tyrosine 251 at the C-terminus of neuronal glycoprotein M6a is critical for neurite outgrowth. Journal of neuroscience research 93:215–229.

Fox K, Henley J, Isaac J (1999) Experience-dependent development of NMDA receptor transmission. Nature neuroscience 2:297–299.

Fukata Y, Dimitrov A, Boncompain G, Vielemeyer O, Perez F, Fukata M (2013) Local palmitoylation cycles define activity-regulated postsynaptic subdomains. The Journal of cell biology 202:145–161.

Fukata Y, Fukata M (2010) Protein palmitoylation in neuronal development and synaptic plasticity. Nature reviews Neuroscience 11:161–175.

Fukata Y, Iwanaga T, Fukata M (2006) Systematic screening for palmitoyl transferase activity of the DHHC protein family in mammalian cells. Methods (San Diego, Calif) 40:177–182.

Gauthier-Campbell C, Bredt DS, Murphy TH, El-Husseini A (2004) Regulation of dendritic branching and filopodia formation in hippocampal neurons by specific acylated protein motifs. Molecular biology of the cell 15:2205–2217.

Gavin M, Wen G, Messing J, Adelman S, Logush A, Jenkins E, Brown W, Velinov M (2013) Substrate Reduction Therapy in Four Patients with Milder CLN1 Mutations and Juvenile-Onset Batten Disease Using Cysteamine Bitartrate. JIMD reports 11:87–92.

Gokhale A, Mullin AP, Zlatic SA, Easley CA, Merritt ME, Raj N, Larimore J, Gordon DE, Peden AA, Sanyal S, Faundez V (2015) The N-ethylmaleimide-sensitive factor and dysbindin interact to modulate synaptic plasticity. The Journal of neuroscience: 35:7643–7653.

Goo MS, Sancho L, Slepak N, Boassa D, Deerinck TJ, Ellisman MH, Bloodgood BL, Patrick GN (2017) Activity-dependent trafficking of lysosomes in dendrites and dendritic spines. The Journal of cell biology 216:2499–2513.

Gordon J, Stryker M (1996) Experience-dependent plasticity of binocular responses in the primary visual cortex of the mouse. The Journal of neuroscience: 16:3274–3286.

Govindarajan A, Kelleher RJ, Tonegawa S (2006) A clustered plasticity model of long-term memory engrams. Nature reviews Neuroscience 7:575–583.

Groc L, Choquet D, Stephenson AF, Verrier D, Manzoni OJ, Chavis P (2007) NMDA Receptor Surface Trafficking and Synaptic Subunit Composition Are Developmentally Regulated by the Extracellular Matrix Protein Reelin. The Journal of Neuroscience 27:10165–10175.

Grossi M, Morgunova M, Cheung S, Scholz D, Conroy E, Terrile M, Panarella A, Simpson JC, Gallagher WM, O'Shea DF (2016) Lysosome triggered near-infrared fluorescence imaging of cellular trafficking processes in real time. Nature communications 7:10855.

Gupta P, Soyombo A, Atashband A, Wisniewski K, Shelton J, Richardson J, Hammer R, Hofmann S (2001) Disruption of PPT1 or PPT2 causes neuronal ceroid lipofuscinosis in knockout mice. Proceedings of the National Academy of Sciences of the United States of America 98:13566–13571.

Haltia M (2006) The neuronal ceroid-lipofuscinoses: from past to present. Biochimica et biophysica acta 1762:850–856.

Han J, Wu P, Wang F, Chen J (2015) S-palmitoylation regulates AMPA receptors trafficking and function: a novel insight into synaptic regulation and therapeutics. Acta pharmaceutica Sinica B 5:1–7.

Hardingham GE, Bading H (2002) Coupling of extrasynaptic NMDA receptors to a CREB shut-off pathway is developmentally regulated. Biochimica et biophysica acta 1600:148–153.

Hardingham GE, Bading H (2010) Synaptic versus extrasynaptic NMDA receptor signalling: implications for neurodegenerative disorders. Nature reviews Neuroscience 11:682–696.

Hardingham G, Fukunaga Y, Bading H (2002) Extrasynaptic NMDARs oppose synaptic NMDARs by triggering CREB shut-off and cell death pathways. Nature neuroscience 5:405–414.

Harvey CD, Yasuda R, Zhong H, Svoboda K (2008) The spread of Ras activity triggered by activation of a single dendritic spine. Science (New York, NY) 321:136–140.

Hayashi T, Rumbaugh G, Huganir RL (2005) Differential regulation of AMPA receptor subunit trafficking by palmitoylation of two distinct sites. Neuron 47:709–723.

Hayashi T, Thomas GM, Huganir RL (2009) Dual palmitoylation of NR2 subunits regulates NMDA receptor trafficking. Neuron 64:213–226.

Henle F, Dehmel M, Leemhuis J, Fischer C, Meyer DK (2012) Role of GluN2A and GluN2B subunits in the formation of filopodia and secondary dendrites in cultured hippocampal neurons. Naunyn-Schmiedeberg's archives of pharmacology 385:171–180.

Hensch T, Fagiolini M, Mataga N, Stryker M, Baekkeskov S, Kash S (1998) Local GABA circuit control of experience-dependent plasticity in developing visual cortex. Science (New York, NY) 282:1504–1508.

Hensch TK (2005) Critical period plasticity in local cortical circuits. Nature reviews Neuroscience 6:877–888.

Huang K, Yanai A, Kang R, Arstikaitis P, Singaraja RR, Metzler M, Mullard A, Haigh B, Gauthier-Campbell C, Gutekunst C-AA, Hayden MR, El-Husseini A (2004) Huntingtin-interacting protein HIP14 is a palmitoyl transferase involved in palmitoylation and trafficking of multiple neuronal proteins. Neuron 44:977–986.

Iafrati J, Orejarena M, Lassalle O, Bouamrane L, Gonzalez-Campo C, Chavis P (2014) Reelin, an extracellular matrix protein linked to early onset psychiatric diseases, drives postnatal development of the prefrontal cortex via GluN2B-NMDARs and the mTOR pathway. Molecular Psychiatry 19:mp201366.

Inomata M, Takayama Y, Kiyama H, Nada S, Okada M, Nakagawa H (1994) Regulation of Src family kinases in the developing rat brain: correlation with their regulator kinase, Csk. Journal of biochemistry 116:386–392.

Irwin S, Patel B, Idupulapati M, Harris J, Crisostomo R, Larsen B, Kooy F, Willems P, Cras P, Kozlowski P, Swain R, Weiler I, Greenough W (2001) Abnormal dendritic spine characteristics in the temporal and visual cortices of patients with fragile-X syndrome: a quantitative examination. American journal of medical genetics 98:161–167.

Itoh M, Yamashita M, Kaneko M, Okuno H, Abe M, Yamazaki M, Natsume R, Yamada D, Kaizuka T, Suwa R, Sakimura K, Sekiguchi M, Wada K, Hoshino M, Mishina M, Hayashi T (2018) Deficiency of AMPAR-Palmitoylation Aggravates Seizure Susceptibility. The Journal of neuroscience: 38:10220–10235.

Jalanko A, Braulke T (2009) Neuronal ceroid lipofuscinoses. Biochimica et biophysica acta 1793:697–709.

Jeyifous O, Lin EI, Chen X, Antinone SE, Mastro R, Drisdel R, Reese TS, Green WN (2016) Palmitoylation regulates glutamate receptor distributions in postsynaptic densities through control of PSD95 conformation and orientation. Proceedings of the National Academy of Sciences 113:E8482–E8491.

Kanaani J, Diacovo MJ, El-Husseini A, Bredt DS, Baekkeskov S (2004) Palmitoylation controls trafficking of GAD65 from Golgi membranes to axon-specific endosomes and a Rab5a-dependent pathway to presynaptic clusters. Journal of cell science 117:2001–2013.

Kang R, Wan J, Arstikaitis P, Takahashi H, Huang K, Bailey AO, Thompson JX, Roth AF, Drisdel RC, Mastro R, Green WN, Yates JR, Davis NG, El-Husseini A (2008) Neural palmitoyl-proteomics reveals dynamic synaptic palmitoylation. Nature 456:904–909.

Kaufman AC, Salazar SV, Haas LT, Yang J, Kostylev MA, Jeng AT, Robinson SA, Gunther EC, van Dyck CH, Nygaard HB, Strittmatter SM (2015) Fyn inhibition rescues established memory and synapse loss in Alzheimer mice. Annals of Neurology 77:953–971.

Kielar C, Maddox L, Bible E, Pontikis CC, Macauley SL, Griffey MA, Wong M, Sands MS, Cooper JD (2007) Successive neuron loss in the thalamus and cortex in a mouse model of infantile neuronal ceroid lipofuscinosis. Neurobiology of disease 25:150–162.

Kim S-JJ, Zhang Z, Sarkar C, Tsai P-CC, Lee Y-CC, Dye L, Mukherjee AB (2008) Palmitoyl protein thioesterase-1 deficiency impairs synaptic vesicle recycling at nerve terminals, contributing to neuropathology in humans and mice. The Journal of clinical investigation 118:3075–3086.

Koegl M, Zlatkine P, Ley S, Courtneidge S, Magee A (1994) Palmitoylation of multiple Src-family kinases at a homologous N-terminal motif. The Biochemical journal 303 (Pt 3):749–753.

Kurayoshi M, Yamamoto H, Izumi S, Kikuchi A (2007) Post-translational palmitoylation and glycosylation of Wnt-5a are necessary for its signalling. Biochemical Journal 402:515–523.

Kutzleb C, Sanders G, Yamamoto R, Wang X, Lichte B, Petrasch-Parwez E, Kilimann M (1998) Paralemmin, a prenyl-palmitoyl-anchored phosphoprotein abundant in neurons and implicated in plasma membrane dynamics and cell process formation. The Journal of cell biology 143:795–813.

Lakhan SE, Caro M, Hadzimichalis N (2013) NMDA Receptor Activity in Neuropsychiatric Disorders. Frontiers in psychiatry 4:52.

Lau C, Zukin R (2007) NMDA receptor trafficking in synaptic plasticity and neuropsychiatric disorders. Nature reviews Neuroscience 8:413–426.

Lei B, Tullis GE, Kirk MD, Zhang K, Katz ML (2006) Ocular phenotype in a mouse gene knockout model for infantile neuronal ceroid lipofuscinosis. Journal of neuroscience research 84:1139–1149.

Levin SW, Baker EH, Zein WM, Zhang Z, Quezado ZM, Miao N, Gropman A, Griffin KJ, Bianconi S, Chandra G, Khan OI, Caruso RC, Liu A, Mukherjee AB (2014) Oral cysteamine bitartrate and N-acetylcysteine for patients with infantile neuronal ceroid lipofuscinosis: a pilot study. The Lancet Neurology 13:777–787.

Li B, Otsu Y, Murphy TH, Raymond LA (2003) Developmental decrease in NMDA receptor desensitization associated with shift to synapse and interaction with postsynaptic density-95. The Journal of neuroscience: 23:11244–11254.

Li J, Wang Y, Wolfe B, Krueger K, Corsi L, Stocca G, Vicini S (1998) Developmental changes in localization of NMDA receptor subunits in primary cultures of cortical neurons. The European

journal of neuroscience 10:1704–1715.

Lin D-TT, Makino Y, Sharma K, Hayashi T, Neve R, Takamiya K, Huganir RL (2009) Regulation of AMPA receptor extrasynaptic insertion by 4.1N, phosphorylation and palmitoylation. Nature neuroscience 12:879–887.

Linder ME, Deschenes RJ (2007) Palmitoylation: policing protein stability and traffic. Nature reviews Molecular cell biology 8:74–84.

Liu X-BB, Murray KD, Jones EG (2004) Switching of NMDA receptor 2A and 2B subunits at thalamic and cortical synapses during early postnatal development. The Journal of neuroscience: 24:8885–8895.

Losi G, Prybylowski K, Fu Z, Luo J, Wenthold RJ, Vicini S (2003) PSD-95 regulates NMDA receptors in developing cerebellar granule neurons of the rat. The Journal of physiology 548:21–29.

Lu J, Verkruyse L, Hofmann S (1996) Lipid thioesters derived from acylated proteins accumulate in infantile neuronal ceroid lipofuscinosis: correction of the defect in lymphoblasts by recombinant palmitoyl-protein thioesterase. Proceedings of the National Academy of Sciences of the United States of America 93:10046–10050.

Lu J-YY, Hofmann SL (2006) Thematic review series: lipid posttranslational modifications. Lysosomal metabolism of lipid-modified proteins. Journal of lipid research 47:1352–1357.

Luo J, Wang Y, Yasuda R, Dunah A, Wolfe B (1997) The majority of N-methyl-D-aspartate receptor complexes in adult rat cerebral cortex contain at least three different subunits (NR1/NR2A/NR2B). Molecular pharmacology 51:79–86.

Maffei A, Turrigiano G (2008) The age of plasticity: developmental regulation of synaptic plasticity in neocortical microcircuits. Progress in brain research 169:211–223.

Martel M-AA, Ryan TJ, Bell KF, Fowler JH, McMahon A, Al-Mubarak B, Komiyama NH, Horsburgh K, Kind PC, Grant SG, Wyllie DJ, Hardingham GE (2012) The subtype of GluN2 C-terminal domain determines the response to excitotoxic insults. Neuron 74:543–556.

Martel M-AA, Wyllie D, Hardingham G (2009) In developing hippocampal neurons, NR2B-containing N-methyl-D-aspartate receptors (NMDARs) can mediate signaling to neuronal survival and synaptic potentiation, as well as neuronal death. Neuroscience 158:334–343.

Mataga N, Fujishima S, Condie B, Hensch T (2001) Experience-dependent plasticity of mouse visual cortex in the absence of the neuronal activity-dependent marker egr1/zif268. The Journal of neuroscience: 21:9724–9732.

Mataga N, Mizuguchi Y, Hensch TK (2004) Experience-dependent pruning of dendritic spines in visual cortex by tissue plasminogen activator. Neuron 44:1031–1041.

Matsuda T, Cepko CL (2004) Electroporation and RNA interference in the rodent retina in vivo and in vitro. Proceedings of the National Academy of Sciences 101:16–22.

Matsuzaki M, Honkura N, Ellis-Davies GC, Kasai H (2004) Structural basis of long-term potentiation in single dendritic spines. Nature 429:761–766.

Matta JA, Ashby MC, Sanz-Clemente A, Roche KW, Isaac JT (2011) mGluR5 and NMDA receptors drive the experience- and activity-dependent NMDA receptor NR2B to NR2A subunit switch. Neuron 70:339–351.

Mattison HA, Hayashi T, Barria A (2012) Palmitoylation at two cysteine clusters on the C-terminus of GluN2A and GluN2B differentially control synaptic targeting of NMDA receptors. PloS one 7:e49089.

Monyer H, Burnashev N, Laurie D, Sakmann B, Seeburg P (1994) Developmental and regional expression in the rat brain and functional properties of four NMDA receptors. Neuron 12:529–540.

Morita A, Yamashita N, Sasaki Y, Uchida Y, Nakajima O, Nakamura F, Yagi T, Taniguchi M, Usui H, Katoh-Semba R, Takei K, Goshima Y (2006) Regulation of dendritic branching and spine maturation by semaphorin3A-Fyn signaling. The Journal of neuroscience: 26:2971–2980.

Nakazawa T, Komai S, Watabe AM, Kiyama Y, Fukaya M, Arima-Yoshida F, Horai R, Sudo K, Ebine K, Delawary M, Goto J, Umemori H, Tezuka T, Iwakura Y, Watanabe M, Yamamoto T, Manabe T (2006) NR2B tyrosine phosphorylation modulates fear learning as well as amygdaloid synaptic plasticity. The EMBO journal 25:2867–2877.

Neudorfer O, Giladi N, Elstein D, Abrahamov A, Turezkite T, Aghai E, Reches A, Bembi B, Zimran A (1996) Occurrence of Parkinson's syndrome in type I Gaucher disease. QJM : monthly journal of the Association of Physicians 89:691–694.

Nita DA, Mole SE, Minassian BA (2016) Neuronal ceroid lipofuscinoses. Epileptic disorders: international epilepsy journal with videotape 18:73–88.

Noritake J, Fukata Y, Iwanaga T, Hosomi N, Tsutsumi R, Matsuda N, Tani H, Iwanari H, Mochizuki Y, Kodama T, Matsuura Y, Bredt DS, Hamakubo T, Fukata M (2009) Mobile DHHC palmitoylating enzyme mediates activity-sensitive synaptic targeting of PSD-95. The Journal of cell biology 186:147–160.

Nygaard HB, van Dyck CH, rittmatter S (2014) Fyn kinase inhibition as a novel therapy for Alzheimer's disease. Alzheimer's research & therapy 6:8.

Nygaard HB, Wagner AF, Bowen GS, Good SP, MacAvoy MG, Strittmatter KA, Kaufman AC, Rosenberg BJ, Sekine-Konno T, Varma P, Chen K, Koleske AJ, Reiman EM, rittmatter S, van Dyck CH (2015) A phase Ib multiple ascending dose study of the safety, tolerability, and central

nervous system availability of AZD0530 (saracatinib) in Alzheimer's disease. Alzheimer's research & therapy 7:35.

Pagon RA, Adam MP, Ardinger HH, Wallace SE, Amemiya A, Bean LJ, Bird TD, Ledbetter N, Mefford HC, Smith RJ, Stephens K (2013) Neuronal Ceroid-Lipofuscinoses. University of Washington, Seattle.

Pampiglione G, Harden A (1977) So-called neuronal ceroid lipofuscinosis. Neurophysiological studies in 60 children. Journal of neurology, neurosurgery, and psychiatry 40:323–330.

Paoletti P, Bellone C, Zhou Q (2013) NMDA receptor subunit diversity: impact on receptor properties, synaptic plasticity and disease. Nature reviews Neuroscience 14:383–400.

Papa M, Bundman M, Greenberger V, gal (1995) Morphological analysis of dendritic spine development in primary cultures of hippocampal neurons. The Journal of neuroscience: 15:1–11.

Parnass Z, Tashiro A, Yuste R (2000) Analysis of spine morphological plasticity in developing hippocampal pyramidal neurons. Hippocampus 10:561–568.

Patterson S, Skene J (1994) Novel inhibitory action of tunicamycin homologues suggests a role for dynamic protein fatty acylation in growth cone-mediated neurite extension. The Journal of cell biology 124:521–536.

Patterson S, Skene J (1999) A shift in protein S-palmitoylation, with persistence of growth-associated substrates, marks a critical period for synaptic plasticity in developing brain. Journal of neurobiology 39:423–437.

Penzes P, Cahill ME, Jones KA, VanLeeuwen J-EE, Woolfrey KM (2011) Dendritic spine pathology in neuropsychiatric disorders. Nature neuroscience 14:285–293.

Philpot B, Sekhar A, Shouval H, Bear M (2001) Visual experience and deprivation bidirectionally modify the composition and function of NMDA receptors in visual cortex. Neuron 29:157–169.

Prybylowski K, Chang K, Sans N, Kan L, Vicini S, Wenthold RJ (2005) The synaptic localization of NR2B-containing NMDA receptors is controlled by interactions with PDZ proteins and AP-2. Neuron 47:845–857.

Purpura D (1979) Pathobiology of cortical neurons in metabolic and unclassified amentias. Research publications - Association for Research in Nervous and Mental Disease 57:43–68.

Quinlan EM, Olstein DH, Bear MF (1999a) Bidirectional, experience-dependent regulation of N-methyl-d-aspartate receptor subunit composition in the rat visual cortex during postnatal development. Proceedings of the National Academy of Sciences 96:12876–12880.

Quinlan E, Philpot B, Huganir R, Bear M (1999b) Rapid, experience-dependent expression of synaptic NMDA receptors in visual cortex in vivo. Nature neuroscience 2:352–357.

Rumbaugh G, Vicini S (1999) Distinct synaptic and extrasynaptic NMDA receptors in developing cerebellar granule neurons. The Journal of neuroscience: 19:10603–10610.

Sans N, Petralia R, Wang Y, Blahos J, Hell J, Wenthold R (2000) A developmental change in NMDA receptor-associated proteins at hippocampal synapses. The Journal of neuroscience: 20:1260–1271.

Sanz-Clemente A, Nicoll RA, Roche KW (2013) Diversity in NMDA receptor composition: many regulators, many consequences. The Neuroscientist: a review journal bringing neurobiology, neurology and psychiatry 19:62–75.

Sato I, Obata Y, Kasahara K, Nakayama Y, Fukumoto Y, Yamasaki T, Yokoyama KK, Saito T, Yamaguchi N (2009) Differential trafficking of Src, Lyn, Yes and Fyn is specified by the state of palmitoylation in the SH4 domain. Journal of cell science 122:965–975.

Shehata M, Matsumura H, Okubo-Suzuki R, Ohkawa N, Inokuchi K (2012) Neuronal stimulation induces autophagy in hippocampal neurons that is involved in AMPA receptor degradation after chemical long-term depression. The Journal of neuroscience: 32:10413–10422.

Sheng M, Cummings J, Roldan L, Jan Y, Jan L (1994) Changing subunit composition of heteromeric NMDA receptors during development of rat cortex. Nature 368:144–147.

Shipton OA, Paulsen O (2014) GluN2A and GluN2B subunit-containing NMDA receptors in hippocampal plasticity. Philosophical transactions of the Royal Society of London Series B, Biological sciences 369:20130163.

Sidransky E et al. (2009) Multicenter analysis of glucocerebrosidase mutations in Parkinson's disease. The New England journal of medicine 361:1651–1661.

Sidransky E, Lopez G (2012) The link between the GBA gene and parkinsonism. The Lancet Neurology 11:986–998.

Smith R, Brundin P, Li J-Y (2005) Synaptic dysfunction in Huntington's disease: a new perspective. Cellular and Molecular Life Sciences 62:1901–1912.

Sobczyk A, Scheuss V, Svoboda K (2005) NMDA receptor subunit-dependent [Ca2+] signaling in individual hippocampal dendritic spines. The Journal of neuroscience: 25:6037–6046.

Stocca G, Vicini S (1998) Increased contribution of NR2A subunit to synaptic NMDA receptors in developing rat cortical neurons. The Journal of physiology 507 (Pt 1):13–24.

Stroebel D, Casado M, Paoletti P (2018) Triheteromeric NMDA receptors: from structure to synaptic physiology. Current opinion in physiology 2:1–12.

Suopanki J, Tyynelä J, Baumann M, Haltia M (1999a) The expression of palmitoyl-protein thioesterase is developmentally regulated in neural tissues but not in nonneural tissues. Molecular genetics and metabolism 66:290–293.

Suopanki J, Tyynelä J, Baumann M, Haltia M (1999b) Palmitoyl-protein thioesterase, an enzyme implicated in neurodegeneration, is localized in neurons and is developmentally regulated in rat brain. Neuroscience letters 265:53–56.

Tang TT, Badger JD, Roche PA, Roche KW (2010) Novel approach to probe subunit-specific contributions to N-methyl-D-aspartate (NMDA) receptor trafficking reveals a dominant role for NR2B in receptor recycling. The Journal of biological chemistry 285:20975–20981.

Tayebi N, Callahan M, Madike V, Stubblefield B, Orvisky E, Krasnewich D, Fillano J, Sidransky E (2001) Gaucher disease and parkinsonism: a phenotypic and genotypic characterization. Molecular genetics and metabolism 73:313–321.

Thomas CG, Miller AJ, Westbrook GL (2006) Synaptic and extrasynaptic NMDA receptor NR2 subunits in cultured hippocampal neurons. Journal of neurophysiology 95:1727–1734.

Thomas GM, Hayashi T, Chiu S-LL, Chen C-MM, Huganir RL (2012) Palmitoylation by DHHC5/8 targets GRIP1 to dendritic endosomes to regulate AMPA-R trafficking. Neuron 73:482–496.

Thomas GM, Hayashi T, Huganir RL, Linden DJ (2013) DHHC8-dependent PICK1 palmitoylation is required for induction of cerebellar long-term synaptic depression. The Journal of neuroscience: 33:15401–15407.

Tian L, Hires AS, Mao T, Huber D, Chiappe EM, ekanth Chalasani H, Petreanu L, Akerboom J, McKinney SA, Schreiter ER, Bargmann CI, Jayaraman V, Svoboda K, Looger LL (2009) Imaging neural activity in worms, flies and mice with improved GCaMP calcium indicators. Nature Methods 6:nmeth.1398.

Tovar KR, McGinley MJ, Westbrook GL (2013) Triheteromeric NMDA receptors at hippocampal synapses. The Journal of neuroscience: 33:9150–9160.

Tovar K, Westbrook G (1999) The incorporation of NMDA receptors with a distinct subunit composition at nascent hippocampal synapses in vitro. The Journal of neuroscience: 19:4180–4188.

Townsend M, Yoshii A, Mishina M, Constantine-Paton M (2003) Developmental loss of miniature N-methyl-d-aspartate receptor currents in NR2A knockout mice. Proceedings of the National Academy of Sciences 100:1340–1345.

Trepanier CH, Jackson MF, MacDonald JF (2012) Regulation of NMDA receptors by the tyrosine kinase Fyn. The FEBS journal 279:12–19.

Umemori H, Wanaka A, Kato H, Takeuchi M, Tohyama M, Yamamoto T (1992) Specific expressions of Fyn and Lyn, lymphocyte antigen receptor-associated tyrosine kinases, in the central nervous system. Brain research Molecular brain research 16:303–310.

van Zundert B, Yoshii A, Constantine-Paton M (2004) Receptor compartmentalization and trafficking at glutamate synapses: a developmental proposal. Trends in neurosciences 27:428–437.

Verkruyse L, Hofmann S (1996) Lysosomal targeting of palmitoyl-protein thioesterase. The Journal of biological chemistry 271:15831–15836.

Vesa J, Hellsten E, Verkruyse L, Camp L, Rapola J, Santavuori P, Hofmann S, Peltonen L (1995) Mutations in the palmitoyl protein thioesterase gene causing infantile neuronal ceroid lipofuscinosis. Nature 376:584–587.

Vicini S, Wang J, Li J, Zhu W, Wang Y, Luo J, Wolfe B, Grayson D (1998) Functional and pharmacological differences between recombinant N-methyl-D-aspartate receptors. Journal of neurophysiology 79:555–566.

Virmani T, Gupta P, Liu X, Kavalali ET, Hofmann SL (2005) Progressively reduced synaptic vesicle pool size in cultured neurons derived from neuronal ceroid lipofuscinosis-1 knockout mice. Neurobiology of disease 20:314–323.

von Engelhardt J, Doganci B, Seeburg PH, Monyer H (2009) Synaptic NR2A- but not NR2B-Containing NMDA Receptors Increase with Blockade of Ionotropic Glutamate Receptors. Frontiers in molecular neuroscience 2:19.

Wang H, Stradtman GG, Wang X-JJ, Gao W-JJ (2008) A specialized NMDA receptor function in layer 5 recurrent microcircuitry of the adult rat prefrontal cortex. Proceedings of the National Academy of Sciences of the United States of America 105:16791–16796.

Washbourne P, Liu X-BB, Jones EG, McAllister A (2004) Cycling of NMDA receptors during trafficking in neurons before synapse formation. The Journal of neuroscience: 24:8253–8264.

Watanabe M, Inoue Y, Sakimura K, Mishina M (1992) Developmental changes in distribution of NMDA receptor channel subunit mRNAs. Neuroreport 3:1138–1140.

Webb DJ, Zhang H, Majumdar D, Horwitz AF (2007) alpha5 integrin signaling regulates the formation of spines and synapses in hippocampal neurons. The Journal of biological chemistry 282:6929–6935.

Weber JP, Andrásfalvy BK, Polito M, Magó Á, Ujfalussy BB, Makara JK (2016) Location-dependent synaptic plasticity rules by dendritic spine cooperativity. Nature communications 7:11380.

Williams K, Russell S, en Y, Molinoff P (1993) Developmental switch in the expression of

NMDA receptors occurs in vivo and in vitro. Neuron 10:267–278.

Wyllie D, Livesey M, Hardingham G (2013) Influence of GluN2 subunit identity on NMDA receptor function. Neuropharmacology 74:4–17.

Yamamoto H, Hagino Y, Kasai S, Ikeda K (2015) Specific Roles of NMDA Receptor Subunits in Mental Disorders. Current molecular medicine 15:193–205.

Yan Y-GG, Zhang J, Xu S-JJ, Luo J-HH, Qiu S, Wang W (2014) Clustering of surface NMDA receptors is mainly mediated by the C-terminus of GluN2A in cultured rat hippocampal neurons. Neuroscience bulletin 30:655–666.

Yokoi N, Fukata Y, Sekiya A, Murakami T, Kobayashi K, Fukata M (2016) Identification of PSD-95 Depalmitoylating Enzymes. The Journal of neuroscience: 36:6431–6444.

Yoshii A, Murata Y, Kim J, Zhang C, okat K, Constantine-Paton M (2011) TrkB and protein kinase Mζ regulate synaptic localization of PSD-95 in developing cortex. The Journal of neuroscience: 31:11894–11904.

Yoshii A, Sheng MH, Constantine-Paton M (2003) Eye opening induces a rapid dendritic localization of PSD-95 in central visual neurons. Proceedings of the National Academy of Sciences of the United States of America 100:1334–1339.

Yuste R, Bonhoeffer T (2001) Morphological changes in dendritic spines associated with long-term synaptic plasticity. Annual review of neuroscience 24:1071–1089.

Zhang X-HH, Liu F, Chen Q, Zhang C-LL, Zhuo M, Xiong Z-QQ, Li B-MM (2008) Conditioning-strength dependent involvement of NMDA NR2B subtype receptor in the basolateral nucleus of amygdala in acquisition of auditory fear memory. Neuropharmacology 55:238–246.

Zhang Z, Lee Y-CC, Kim S-JJ, Choi MS, Tsai P-CC, Xu Y, Xiao Y-JJ, Zhang P, Heffer A, Mukherjee AB (2006) Palmitoyl-protein thioesterase-1 deficiency mediates the activation of the unfolded protein response and neuronal apoptosis in INCL. Human molecular genetics 15:337–346.

Zhao D, Liu D, Chen X, Wang K, Zhang A, Kang J, Zhou Q, Duan T (2013) Prenatal stress disturbs hippocampal KIF17 and NR2B in spatial cognition in male offspring. Journal of neuroscience research 91:535–544.

Zhao M-GG, Toyoda H, Lee Y-SS, Wu L-JJ, Ko SW, Zhang X-HH, Jia Y, Shum F, Xu H, Li B-MM, Kaang B-KK, Zhuo M (2005) Roles of NMDA NR2B subtype receptor in prefrontal long-term potentiation and contextual fear memory. Neuron 47:859–872.

Zheng C-YY, Petralia RS, Wang Y-XX, Kachar B, Wenthold RJ (2010) SAP102 is a highly mobile MAGUK in spines. The Journal of neuroscience: 30:4757–4766.

Zheng H, Koo EH (2006) The amyloid precursor protein: beyond amyloid. Molecular neurodegeneration 1:5.

Zhong J, Russell S, Pritchett D, Molinoff P, Williams K (1994) Expression of mRNAs encoding subunits of the N-methyl-D-aspartate receptor in cultured cortical neurons. Molecular pharmacology 45:846–853.

Zhu Y-CC, Li D, Wang L, Lu B, Zheng J, Zhao S-LL, Zeng R, Xiong Z-QQ (2013) Palmitoylation-dependent CDKL5-PSD-95 interaction regulates synaptic targeting of CDKL5 and dendritic spine development. Proceedings of the National Academy of Sciences of the United States of America 110:9118–9123.

APPENDIX 1

Chapter 2 is comprised of published material from my article, Koster et al. (2019). This article is published in the journal, eLife, and is therefore distributed under the terms of a Creative Commons Attribution License that permits unrestricted use and redistribution provided that the original author and source are credited. We have cited the original work herein and are therefore compliant. A screenshot of the eLife policy is shared below (https://elifesciences.org/terms).

License to Use Journal Articles and Related Content

Unless otherwise indicated, the articles and journal content published by eLife on the eLife Sites are licensed under a Creative Commons Attribution license (also known as a CC-BY license). This means that you are free to use, reproduce and distribute the articles and related content (unless otherwise noted), for commercial and noncommercial purposes, subject to citation of the original source in accordance with the CC-BY license.

3. LOSS OF DEPALMITOYLATION EXAGGERATES HOMEOSTATIC PLASTICITY AND LEADS TO NEUROINFLAMMATION IN INFANTILE NEURONAL CEROID LIPOFUSCINOSIS

3.1. Introduction

Protein homeostasis, or proteostasis, is a fundamental molecular mechanism whereby quality, quantity, and distribution of proteins are rigorously controlled through synthesis, folding, trafficking, and degradation. Proteostasis is germane to neurodegeneration and lysosomal storage diseases, as well as cancer, diabetes, and normal aging. This dynamic proteomic regulation depends on the balance between supply and breakdown of proteins. Several pathways carry out protein degradation, including the unfolded protein response, ubiquitination-mediated proteasomal degradation, autophagy, and lysosomal degradation. The lysosome in particular plays a critical role in digesting proteins modified with glycosyl or lipid chains. Accordingly, there are over 50 lysosomal storage disorders, and most of them are associated with mutations in lysosomal enzymes to detach the modification.

Infantile neuronal ceroid lipofuscinosis (CLN1) is a devastating pediatric neurodegenerative disease and is classified as a lysosomal storage disorder (Nita et al., 2016). Children afflicted by CLN1 show no detectable pathology or symptoms during the first 6 to 12 months of life. Following this seemingly typical developmental period, CLN1 patients present with a deceleration of head growth (microcephaly), loss of vision, motor deterioration, and epilepsy that constitute a severe developmental regression and result in premature death by age 5 (Haltia, 2003; Nita et al., 2016). CLN1 is caused by mutations in the gene *CLN1*, which encodes the enzyme palmitoyl-protein-thioesterase (PPT1) (Vesa et al., 1995).

Ppt1 is a depalmitoylating enzyme, which removes the 16-carbon fatty acid, palmitate, from postranslationally palmitoylated proteins, thereby regulating their trafficking, localization, and turnover. Appreciation for the functional importance of protein palmitoylation at the synapse has increased substantially in recent years (Fukata and Fukata, 2010). Early studies of Ppt1 function demonstrated its activity toward soluble signaling molecules, such as H-Ras (Camp and Hofmann, 1993), and demonstrated in non-neuronal cell types that it is localized to the lysosome

(Verkruyse and Hofmann, 1996). Indeed, loss of PPT1 in CLN1 disease results in an accumulation of autofluorescent lysosomal storage material (ALSM) frequently known as lipofuscin. Vesa and colleagues first suggested that Ppt1 is also secreted (Vesa et al., 1995), however, and recent studies showed that Ppt1 localizes beyond the lysosome to the broader endolysosomal compartment in neurons, potentially synaptic vesicles (Ahtiainen et al., 2003, 2006; Lehtovirta et al., 2001; Lyly et al., 2007), and is secreted to the synaptic cleft (Gorenberg et al., 2020). It is becoming clear that synaptic proteins, especially transmembrane proteins, make up a large proportion of Ppt1 substrates. A recent study probing for substrates of Ppt1 using a stringent proteomic screen showed that roughly 10% of the synaptic palmitome, representing over 100 proteins, is depalmitoylated by Ppt1. Interestingly, this study identified the α-amino-3-hydroxy-5-methyl-4-isoxazolepropionic acid receptor (AMPAR) subunit GluA1 as a substrate (Gorenberg et al., 2020).

Given the emerging evidence for Ppt1 as a synaptic enzyme, defining its role in synaptic plasticity is important for understanding the pathophysiology of CLN1 disease and has broader implications for cortical circuit development. Two major forms of synaptic plasticity, Hebbian and homeostatic, govern brain circuit formation and function (Keck et al., 2017; Turrigiano, 2017). Hebbian plasticity is a conceptual framework where synapses that fire together, wire together (Katz and Shatz, 1996), such that local synaptic strength is either strengthened or weakened depending on the frequency or intensity of the incoming stimulus. A high frequency stimulus induces synaptic strengthening in a process called long-term potentiation (LTP), while low frequency stimuli triggers synapse weakening termed long-term depression (LTD). Synaptic scaling is a form of homeostatic plasticity by which a neuronal network compensates for changes in chronic afferent activity levels by increasing or decreasing the number of receptors on the synaptic surface (O'Brien et al., 1998; Turrigiano et al., 1998). Detailed analyses have revealed that synaptic scaling "up" (upscaling), which is an increase in the number of synaptic AMPARs in

response to chronic activity blockade, is largely constituted by increases in calcium-permeable AMPARs (CP-AMPARs)(Ju et al., 2004; Thiagarajan et al., 2005), (Lee, 2012), typically composed of GluA1 homomers (Burnashev et al., 1992; Wenthold et al., 1996). Importantly, synaptic scaling is known to be disrupted in neurodevelopmental and neurodegenerative diseases, such as Rett syndrome and Alzheimer disease (Blackman et al., 2012; Gilbert et al., 2017; Pratt et al., 2011; Qiu et al., 2012; Styr and Slutsky, 2018). Moreover, CP-AMPARs are also implicated in epilepsy, stroke, and motor neuron disease.

One study shows that loss of Ppt1 suppresses LTP in *ex vivo* hippocampal slice recordings (Sapir et al., 2019). However, the link between lysosomal depalmitoylation and homeostatic plasticity mechanisms has not been studied. We hypothesized that proteostasis of palmitoylated synaptic proteins governs homeostatic plasticity. Therefore, we sought to determine if synaptic scaling (Turrigiano and Nelson, 2004; Turrigiano et al., 1998) is dysregulated in *Ppt1*$^{-/-}$ mice and if the abnormal response contributes to CLN1 pathology.

Here, we describe the mechanism by which synaptic scaling is disrupted in *Ppt1*$^{-/-}$ neurons. In particular, we find that synaptic upscaling of CP-AMPARs is exaggerated in *Ppt1*$^{-/-}$ neurons as a result of an overload of the palmitoylated GluA1 fraction. Further, we show that dark rearing *Ppt1*$^{-/-}$ mice, an *in vivo* model of synaptic upscaling in the visual cortex, accelerates neuroinflammation and brain atrophy. Notably, A-kinase anchor protein 5 (Akap5) and its associated signaling pathways contribute to CLN1 pathology through the hyperactivation of nuclear factor activated in T-cells (NFATc3) and neuroinflammation, representing a link between aberrant synaptic plasticity and an inflammatory cascade in CLN1 and opening a new set of therapeutic targets. Together, these data indicate that Ppt1 regulates proteostasis of CP-AMPARs through depalmitoylation and plays a critical role in controlling homeostatic plasticity. Further, our findings show that loss of Ppt1 function underlies hypersynchrony and neurodegeneration of cortical circuitry.

3.2. Methods

3.2.1. Animals, group allocation, and data handling

All animal procedures were performed in accordance with the guidelines of the University of Illinois of Chicago Institutional Animal Care and Use Committee. *Ppt1*$^{+/-}$ (heterozygous) mice were obtained from Jackson Laboratory and maintained on 12h light/dark cycle with food and water *ad libitum.* Breeding of *Ppt1*$^{+/-}$ animals results in litters containing *Ppt1*$^{-/-}$, *Ppt1*$^{+/-}$, and *Ppt1*$^{+/+}$ (WT) animals. *Ppt1*$^{-/-}$ and WT littermate controls were genotyped in-house (Gupta et al., 2001) and used for experiments at specified developmental time points: P11, P14, P28, P33, P42, P60, P78, and P120. Though we used the littermate control system, in which WT and *Ppt1*$^{-/-}$ mice from the same litters were compared, each cohort size (n) was treated independently in statistical testing for *in vivo* comparisons (pair-wise tests were not used). In contrast, *in vitro* and imaging data were treated as paired analyses, since each culture was often collected, processed, or immunostained at distinct times (rather than multiple n being processed simultaneously). Imaging data was acquired randomly for each experiment (no criteria for selecting cells, view fields, etc. except where anatomically necessary). All data was acquired and maintained without descriptive naming/labeling to ease randomization. Data was either analyzed by lab members blinded to condition or randomized by students prior to analysis by KPK, with the exception that 2-photon data was not randomized before analysis; however, these calcium data are extracted in a fully automated manner by the EZ calcium Matlab plugin to minimize observer bias (see below).

3.2.2. Brain fractionation, biochemical assays from tissue samples, and immunoblotting

For collection of brain for biochemistry (immunoblot), *Ppt1*$^{-/-}$ and WT animals were decapitated following isoflurane anesthesia, then the brain was removed, and washed in ice-cold PBS. The occipital cortex (visual cortex), hippocampus, and remaining cortex were dissected and separately collected on an ice block. Isolated visual cortices from *Ppt1*$^{-/-}$ and WT animals were

homogenized in ice-cold synaptosome buffer (320mM sucrose, 1mM EDTA, 4mM HEPES, pH7.4 containing 1x protease inhibitor cocktail (Roche), 1x phosphatase inhibitor cocktail (Roche) and 1mM PMSF) using 30 strokes in a Dounce homogenizer. Aliquots for whole lysate (WL) were stored and the remaining sample was used for synaptosome preparation, performed as previously with slight modification. In brief, WLs were centrifuged at 1,000 x g to remove cellular debris, supernatant was then centrifuged at 12,000 x g for 15min to generate pellet P2. P2 fraction was resuspended in synaptosome buffer and spun at 18,000 x g for 15min to produce synaptosomal membrane fraction, LP1, which was used for downstream biochemical analyses (synaptosomes). For immunoblot, protein concentration of each sample was determined using BCA protein assay (Pierce). Samples were then measured to 20mg total protein in 2x Laemmli buffer containing 10% b-mercaptoethanol (Bio-rad), heated at 70°C for 10min and loaded into 4-20% precast gels (Bio-rad) for electrophoresis (130V, 1.5-2h). Proteins were wet-transferred to PVDF membranes (Immobilon-P, Millipore), blocked in TBS, pH7.4 containing 5% non-fat milk and 0.1% Tween-20 (TBS-T+5% milk). Membranes were incubated in primary antibody solutions containing 2% BSA in TBS-T for 2h at room temperature (RT) or overnight at 4°C. Primary antibodies were used according to the **Table 3**. Membranes were then incubated with appropriate secondary, HRP-conjugated antibodies (Jackson ImmunoResearch) at either 1: 1,000 or 1:5,000 for 1h at RT before washing three times with TBS-T. Visualization and quantification was performed using Pierce SuperSignal ECL substrate and Odyssey-FC chemiluminescent imaging station (LI-COR). Signal density for each synaptic protein was measured using the LI-COR software, Image Studio Lite (version 5.2) and was normalized to the signal density for β-actin loading control for each lane.

3.2.3. APEGS assay from visual cortices

The APEGS assay was performed as described by Kanadome and colleagues (Kanadome et al., 2019), following the guidelines for tissue samples. Visual cortices first

underwent the synaptosome preparation protocol as above, except that homogenate buffer used was as directed by the APEGS protocol (20mM Tris-HCl, 2mM EDTA, 0.32M sucrose, pH 8.0). Whole lysates and synaptosomes were then brought to 300μg total protein in a final volume of 0.5ml buffer B (PBS containing 4% SDS, 5mM EDTA, 8.9M urea, and protease inhibitors). The remaining sample was used for inputs. 300μg protein was reduced by addition of 25mM Bond-Breaker™ TCEP (0.5M stock solution, ThermoFisher) and incubation at RT for 1h. Next, to block free thiols, freshly prepared N-ethylmaleimide (NEM) in 100% ethanol was added to lysates (to 50mM) and the mixture was rotated end-over-end for 3h at RT. Following 2x chloroform-methanol precipitation (at which point, protein precipitates were often stored overnight at -20°C), lysates were divided into +hydroxylamine (HA) and –HA groups for each sample, which were exposed to 3 volumes of HA-containing buffer (1M HA, to expose palmitoylated cysteine residues) or Tris-buffer control (-HA), respectively, for 1h at 37°C. Following chloroform-methanol precipitation, the samples were solubilized and exposed to 10mM TCEP and 20mM mPEG-5k (Laysan Bio Inc., cat# MPEG-MAL-5000-1g) for 1h at RT with shaking (thereby replacing palmitic acid with mPEG-5K on exposed cysteine residues). Following the final chloroform-methanol precipitation, samples were solubilized in a small volume (70μl) of PBS containing 1% SDS and protein concentration was measured by BCA assay (Pierce). Samples were then brought to 20μg protein in laemmli buffer with 2% β-mercaptoethanol for immunoblot analyses as above. Quantification of palmitoylated vs. non-palmitoylated protein was carried out as for standard immunoblot analysis, with the additional consideration that signal from palmitoylated bands demonstrating the APEGS-dependent molecular weight shift was divided by the signal from the non-palmitoylated band, the location of which was verified by matching to the –HA control sample. This ratio was divided by β-actin control from the same lane for normalization.

3.2.4. Acyl-biotin exchange (ABE) assay for palmitoyl-proteomics

WT and *Ppt1*$^{-/-}$ occipital cortices from P42 were used for palmitoyl-proteomic analysis

(Drisdel and Green, 2004a). Lysates and synaptosomes were collected as described above. The palmitoyl-proteomic protocol was then carried out according to Wan et al., (2007) with slight modifications (Wan et al., 2007). First, a BCA assay was performed prior to beginning the assay in order to start with equal (600μg) protein content for each sample. Blocking (NEM), hydroxylamine, and biotinylation (HPDP-biotin) steps were all performed as recommended in the protocol. The elution protocol was also followed, with the exception that instead of streptavidin resin, magnetic streptavidin coated beads (Dynabeads™, ThermoFisher) were used (100μl beads/sample). The final eluent was frozen at -80ºC and prepared for mass spectrometry (see below). Due to the small starting material (occipital cortex only), a persistent modification is that the whole procedure was scaled down to be performed in 2mL tubes, including chloroform-methanol precipitations, which were carried out with the following volumes: 150μl sample, 600μl methanol, 150μl chloroform, and 450μl water. This limited protein loss, which was evident in trial runs using 15ml conical tubes.

3.2.5. Mass spectrometry

Eluents from the ABE assay described above were processed for quantitative, label-free proteomics. Samples were dried for approximately 30 minutes and digested using S-trap Micro Spin Column Digestion protocol (Protifi, Huntington, NY) with minor changes. 30 µL of 10% sodium dodecyl sulfate (SDS) 100 mM triethylammonium bicarbonate (TEAB) with Pierce protease inhibitor cocktail (ThermoFisher Scientific, Waltham, MA) and phosphatase inhibitors (10 mM sodium pyrophosphate, 1 mM PMSF, 1 mM sodium orthovanidate, and 1 mM β-glycerolphosphate). Proteins were reduced with 20 mM final concentration of dithiothreitol (DDT) at 95 °C for 10 minutes, followed by alkylation in the dark, at room temperature, with 40 mM of iodoacetamide. Next, phosphoric acid was added for a final concentration of 1.2%. Samples were briefly vortexed to mix before 300 µL of S-trap binding buffer (90% MeOH, 100 mM TEAB) was added. Samples were vortex again prior to loading onto the S-Trap Micro Spin Columns (Protifi,

Cat: C02-micro-10). After four washes with 150 µL of S-trap binding buffer with centrifugation at 1,000 xg, 40 µL of 50 mM TEAB containing 0.75 µg of trypsin was added and incubated overnight at 37 °C.

Peptides were eluted with 40 µL of each of the following solutions: 50 mM TEAB, 0.2 % formic acid (FA), and 50% acetonitrile (ACN) 0.1% FA. Spin column was spun at 4,000 xg in after adding each solution. Pooled elution was dried down prior to resuspension in 100 µL of 3% ACN 0.1% FA.

LC-MS Analysis

3 µL of resuspended samples were injected for LC-MS/MS analysis, similar to a previously mentioned method (Nguyen et al., 2019). Briefly, peptides were loaded onto a Thermo NanoViper trap column (75 µm x 20 mm, 3 µm C18, 100 Å) (Thermo Fisher Scientific, Bremen, Germany) using an Agilent 1260 Infinity nanoLC system (Agilent Technologies, Santa Clara, CA) and washed for 10 minutes with 0.1% FA at 2 µL/min. Peptides were separated with a 120-minute gradient (from 5-60% ACN with 0.1% FA), at 0.25 µL/min flowrate, on an Agilent Zorbax 300SB-C18 column (75 µm x 150 mm, 3.5 µm, 300 Å). Data collection was done using data-dependent acquisition (DDA) analysis by a Thermo Q Exactive mass spectrometer (Thermo Fisher Scientific, Bremen, Germany). Settings for the mass spectrometer are as followed: capillary temperature at 250 °C, spray voltage 1.5 kV, MS1 scan at 70,000 resolution, scanning from 375-1600 m/z, automatic gain control (AGC) target 1E6 for a maximum injection time (IT) of 100 ms. Ten most abundant peaks within an MS1 spectrum were isolated for MS/MS, with an isolation width at 1.5 m/z and dynamic active exclusion set for 20 s. MS/MS spectra were collected at 17,500 resolution, for a maximum of 50 ms or a minimum of 1E5 ions. Normalized collision energy (NCE) was set at 27%. Masses with charges of 1 and larger than 6 were excluded from MS/MS analysis.

Database Searching and Analysis

Raw files were searched with Proteome Discoverer 2.3 (Thermo Fisher Scientific,

Waltham, MA) using the Sequest HT search engine against the UniProt *Mus musculus* database (22,286 gene sequence; downloaded April 27, 2017). Mass error tolerance was set to 10 ppm for precursors, cleaved by trypsin, allowing a maximum of two missed cleavages, with sequence lengths between 6 and 144 amino acids. Fragment masses were searched with a tolerance of ± 0.02 Da. Dynamic modifications included oxidation (M), deamidation (N, R, Q), and acetylation (N-terminus). Carbamidomethylation was set as a static modification (C). Both peptides and PSMs were set to a target false discovery rate (FDR) ≤ 0.01 for matches with high confidence. Label-free quantification (LFQ) was done using precursor ion intensity. Samples were normalized using the average intensity of all peptides. Top 5 most abundant peptides were used for protein abundance calculation. T-test were used to determine the p-values between the two conditions.

3.2.6. Pathway and network analysis for palmitoyl-proteomics

SynGO and STRING analysis

Datasets filtered for 2 unique peptides were further narrowed by filtering for proteins showing an increase in their abundance ratio (*Ppt1*$^{-/-}$/WT) of >1.2 fold. These filtered gene lists for whole lysates and synaptosomes were input separately into the SynGO online tool (Koopmans et al., 2019). The genes encompassed in the top significant biological process (BP) SynGO-term for lysates and synaptosomes were then input into STRING, the online protein-protein interaction database. A K-means cluster analysis was performed to detect clusters of functionally related proteins and for clarity of visualization.

3.2.7. Transcardial perfusion, immunohistochemistry, and image analysis

Ppt1$^{-/-}$ and WT mice were anesthetized using isoflurane and transcardially perfused with ice cold PBS (pH 7.4, ~30ml/mouse) followed by 4% paraformaldehyde (PFA) in PBS (~15ml/mouse). Brains were removed and post-fixed overnight at 4°C in 4% PFA and transferred to PBS, pH7.4 containing 0.01% sodium azide for storage if necessary. Brains from *Ppt1*$^{-/-}$ and WT animals were incubated in 30% sucrose solution for 48h prior to sectioning at either 50 or

100μm in cold PBS using a Vibratome 1000 (Technical Products International, St. Louis, MO). Serial sections were stored free floating in cryoprotectant solution (30% glycerol, 30% ethylene glycol in PBS) at -20°C until analysis of ALSM or immunohistochemistry was performed.

For ALSM analysis (as in Koster et al., 2019), 3-4 mid-sagittal sections were mounted on Superfrost Plus microscope slides (VWR) using Vectamount mounting media containing DAPI (Vector Laboratories, cat: H-5000). Images were acquired for at least 2 sections from each animal using a Zeiss LSM710 confocal laser scanning microscope at 40x magnification (excitation at 405nm to visualize DAPI and 561nm to visualize ALSM). All sections were imaged using identical capture conditions. Quantification of ALSM was performed by thresholding images in FIJI (NIH), generating a binary mask of ALSM-positive pixels (satisfied threshold) vs. background. The identical threshold was applied to each image (from cortical surface to subcortical white matter and across animals). Percent area occupied by ALSM puncta that satisfied the threshold was then calculated using the “analyze particles” tool in FIJI. This analysis was performed for 2-4 sections (total of ~10-20 images, as imaging an entire cortical column is typically 5 interlaced images) from each animal and averaged together to give a single value, representative of the total area occupied by ALSM in the cortical column imaged. Three to six animals per group were analyzed this way and averaged to give the mean area occupied by ALSM at each time point, for both genotypes (n=4-6 animals/group).

For immunohistochemistry, 3-4 slices medial sections were first incubated in TBS for 10 min before undergoing permeabilization (TBS + 0.5% Triton X-100) for 30 minutes at RT. Next, samples underwent antigen retrieval by heating in tris-EDTA (pH 9.0) at 95°C for 30 minutes before being equilibrated to room temperature in tris-EDTA solution for 40 minutes. Tissue was then blocked (TBS + 0.1% Triton X-100, 4% BSA, and 5% normal goat serum) for 2 hours at RT before being incubated in rabbit anti-Iba1 (1:1,000, in TBS + 0.1% Triton X-100 + 2% BSA) for 48 hours. After washing 4 times, 10 minutes each, tissue was incubated in Alexa Fluor 488 goat anti-

rabbit (1:1,000; ThermoFisher) overnight at RT. The tissue was then washed (4x, 10 minutes) and mounted onto Superfrost Plus microscope slides (VWR) using Vectamount mounting media containing DAPI (Vector Laboratories, cat: H-5000).

Microglial images were acquired with a Zeiss LSM710 confocal microscope either at 10x (low magnification images) or 63x for Scholl analysis. 63x images were acquired as 30-60 plane Z-stacks (Z-interval = 2μm) in random fashion (the only criterion is that at least one full microglia had to be centered in the stack) at the border of layer 2/3 and 4 in the visual cortex. 3-4 images were taken from 2 tissue sections for each animal. Images were analyzed using the Scholl analysis tool in Fiji by lab members blinded to the condition. Briefly, the image was collapsed into a maximum-intensity projection to ensure all microglia processes were captured and individual microglia were outlined with a freehand ROI. The surrounding area was removed ("clear outside" function in Fiji) and the image was then thresholded to generate a mask of all microglia processes and an ROI was created at the center of the cell soma. Scholl analysis was performed according to these parameters: start radius (from the center of cell soma ROI) = 5μm, step size = 2μm, end radius = 70μm. The number of intersections at each 2μm step was averaged for all microglia from each animal and counted as one n.

3.2.8. Electrophysiology

WT and *Ppt1*$^{-/-}$ animals at P15 or P28-32 were deeply anesthetized using isoflurane drop method and decapitated. All recordings were conducted from layer 2/3 pyramidal neurons of monocular visual cortex (350-μm-thick coronal slices) at 33–35°C using a cesium-based internal solution containing 0.1% Neurobiotin (Vector Laboratories) and the following (in mM): 140 CsCl, 10 HEPES, 2 $MgCl_2$, 5 NaATP, 0.6 NaGTP, and 3 QX-314, pH 7.23–7.28, 280–282 mOsm. The recording artificial cerebral spinal fluid contained the following (in mM): 122.5 NaCl, 3.5 KCl, 25 $NaHCO_3$, 1 NaH_2PO_4, 2.5 $CaCl_2$, 1 $MgCl_2$, 20 glucose, and 1 ascorbic acid, pH 7.40–7.43, 295–305 mOsm. Both spontaneous glutamatergic and GABAergic synaptic events were assessed by

recording the frequency of postsynaptic currents (PSC) at the −60 mV (PSC−60mV) and +15 mV (PSC+15mV) holding potentials, respectively. Only neurons with at least 15 min of stable baseline activity were included for analyses. The frequency of PSC−60mV and PSC+15mV events from at least two noncontiguous epochs of 60 s each was compared.

3.2.9. Stereotaxic viral injection

Injection into neonatal mice was performed according to He et al., (2018). P0 or P1 pups underwent hypothermia-induced anesthesia (incubation on an ice block for 5-10min) before being placed in the mouse stereotaxic frame (on a second ice block) equipped with specialized ear bars for holding pups (RWD Life Science Inc). AAV.CamKII.GCaMP6f.WPRE.SV40 (AAV9) (Addgene) and pAAV-hSyn-mCherry (AAV2) were pre-mixed in 1:1 ratio before being backloaded into a Neuros syringe (33 gauge, Hamilton). Alternatively, a Nanoject 3 automatic injector (Drummond Scientific Company; Broomall, PA) was used with a finely pulled borosilicate capillary micropipette. 200nL of the mixture was injected at a 15° angle approximately 150μm below the dura surface to transfect a large population of layer 2/3 excitatory cortical neurons with the viral particles. The needle was left in place for 1 minute, then lifted by a minimal distance and left in place for an additional 30 seconds before being slowly removed to avoid reflux of solution along the needle track. Pups were immediately placed on a heating pad and monitored until they regained consciousness.

3.2.10. Cranial window implantation

Cranial window implantation was performed as previously described with some modification (Holtmaat et al., 2009). Virus injected animals were anesthetized via isoflurane inhalation (4% induction, 1-1.5% maintenance) and placed in a stereotaxic frame (RWD Life Science Inc.). All procedures were performed under sterile conditions. Buprenorphine-SR (1mg/kg, subcutaneous), meloxicam (2mg/kg, subcutaneous), and dexamethasone (2mg/kg, subcutaneous) were administered preoperatively. Hair from the scalp was removed using

commercially available Nair by applying it with a cotton swab, waiting for 3 minutes, and removing the hair with several clean cotton swabs. The scalp was then cleaned by sequential application of betadine-iodine (3x, allowing to dry in between each fresh application) and alcohol using alcohol pads (2x). Once the scalp was clean, an approximately 1cm incision was made along the posterior aspect of the midline and the margins of the incision were expanded to visualize the skull covering the left visual cortex by gently pushing aside the scalp tissue with sterile, fine tipped cotton swabs. Once the incision was large enough and centered on the left visual cortex, the connective tissue beneath the scalp were removed from the skull by applying of ~25ul epinephrine-lidocaine (via insulin syringe) and rubbing with sterile cotton swabs. The margins of the incision were also simultaneously dried with the swab. Once the margins of the tissue were dried, a layer of cyanoacrylate was applied to the edges and cured using minimal application of Zip Kicker cyanoacrylate catalyst (Zap). Next, the position of the headplate (CP-1, Narishige) was marked by positioning it so that the center was atop the visual cortex and marking its location with a fine tip marker. A layer of cyanoacrylate was then applied over the entire surface of exposed skull, leaving sufficient area (~6mm) so that glue does not cover the eventual drilling site, and the headplate was quickly secured with the glue to the desired position. After at least 5 minutes, allowing for the glue to cure, a 4-5mm circular piece of skull was removed by drilling around the circle circumference using a dental drill (Marathon) and frequent soaking with sterile PBS to soften the skull. Once the drill site was thin enough, fine forceps were used to lift the medial edge and the 5mm bone fragment was removed completely. The exposed brain tissue was covered with PBS-soaked sterile gelfoam (Surgifoam) to clear away any blood, which was minimal. Lastly, a 5mm coverslip was glued to the top of the burr hole on the headplate. Animals were then immediately moved to a heating pad and monitored until they regained consciousness. Animals typically recovered fully within 15 minutes and showed little impact of the headplate implantation on normal functions such as eating and drinking (without any weight loss).

3.2.11. Primary cortical neuron culture

For primary cortical neuron cultures, embryos from timed-pregnant, *Ppt1*$^{-/+}$ dams were removed, decapitated, and cortices resected at embryonic day (E) 15.5. All dissection steps were performed in ice cold HBSS, pH7.4. Following cortical resection, tissue from each individually genotyped embryo were digested in HBSS containing 20U/ml papain and DNAse at 37°C (20min total, tubes flicked at 10min) before sequential trituration with 1ml (~15 strokes) and 200μl (~10 strokes) pipettes, generating a single-cell suspension. For live-cell imaging experiments, cells were counted then plated at 150,000-180,000 cells/well in 24-well plates containing poly-D-lysine/laminin-coated coverslips. For biochemical experiments, i.e. immunoblot, APEGS assay *in vitro,* cells were plated on poly-D-lysine/laminin-coated 6-well plates at 1,000,000 cells/well. Cells were plated and incubated at 37°C in plating medium (Neurobasal medium containing B27 supplement, L-glutamine and glutamate) for 3-5 DIV, before replacing half medium every 3 days with feeding medium (plating medium without glutamate). For synaptic scaling experiments, neurons were treated with either bicuclline (20μM, solubilized in DMSO, Tocris) or TTX-citrate (1μM, solubilized in sterile water, Tocris) for 48 hours where indicated.

3.2.12. Primary cortical neuron harvest and immunoblotting

Primary cortical neurons from E15.5 WT and *Ppt1*$^{-/-}$ embryos were cultured for 7, 10, or 18 DIV prior to harvest for immunoblot or APEGS assay (only DIV18 used for APEGS). To harvest protein extracts for APEGS, cells were placed on ice, washed 2x with ice-cold PBS before addition of 400μl per well of PBS with 4% SDS and protease inhibitor cocktail (as in Yokoi et al., 2016). Cells were incubated and swirled with lysis buffer for 5 minutes, scraped from the plate, triturated briefly, and collected in 1.5ml tubes. Lysates were centrifuged at 20,000g for 15min to remove debris, and the supernatant was collected for biochemical analysis. Immunoblotting analyses were performed as above. APEGS assay *in vitro* was carried out as described in the following section.

3.2.13. APEGS assay on primary cortical neuron lysates

The APEGS assay was performed as described by Kanadome et al., (2019) and in Koster et al., (2019). The protocol is nearly identical to the description above for *in vivo* samples, with slight modifications as recommended in the protocol by Kanadome et al. (2019). Specifically, the cortical neuron lysates were brought to 300μg total protein in a final volume of 0.5ml buffer A (PBS containing 4% SDS, 5mM EDTA, protease inhibitors; instead of buffer B). Further, the initial protein reduction by TCEP incubation was performed at 55°C for 1h (rather than at RT). Following the final chloroform-methanol precipitation, samples were solubilized in 60μl of PBS containing 1% SDS and protein concentration was measured by BCA assay (Pierce). Samples were then brought to 10μg protein in laemmli buffer with 2% β-mercaptoethanol for immunoblot analyses as above. Quantification of palmitoylated versus non-palmitoylated protein was carried out as described for *in vivo* samples.

3.2.14. Biotinylation

Surface biotinlyation assay was performed as in Ehlers, 2000 and Yoshii et al., 2013 with some modifications. Briefly, neuron cultures in 6-well plates were cooled on ice to stop membrane trafficking in cold DPBS plus 1 mm $MgCl_2$ and 2.5 mm $CaCl_2$, then treated with 1.5 mg/ml sulfo-NHS-biotin in DPBS for 30 min to label surface receptors. Unbound biotin was quenched with cold DPBS plus 1 mm $MgCl_2$, 2.5 mm $CaCl_2$, and 50 mM glycine (rinse, 2 × 3 min). Neurons were then lysed for 5 min in SDS-RIPA buffer (Cell Signaling) with protease inhibitor cocktail (Roche), scraped and the lysed solution was centrifuged at 16,000 × g for 15 min at 4°C. Protein concentration of the supernatant was determined and 400 μg of protein was adjusted to a volume of 1ml with 0.1% SDS-RIPA buffer. Biotinylated GluA1 receptor subunits were precipitated with 75μl streptavidin coated magnetic bead (Thermo Scientific) slurry either for 3 hours at RT or overnight at 4°C with end over end rotation. Beads were then washed with the SDS-RIPA buffer twice before brief centrifugation. Pulled down subunits were eluted into Laemmli sample buffer +

2% b-mercaptoethanol by boiling for 6 min and the magnetic beads were removed from solution. Samples were then loaded onto 4-20% Bio-Rad gradient gels as above for immunoblot analysis.

3.2.15. Transfection, *in vitro* calcium imaging, FRAP, and GFP-NFAT nuclear translocation analyses

To image calcium signals in WT and *Ppt1*$^{-/-}$ cultured neurons, cells were transfected at DIV10 with GCaMP3 (see **Acknowledgements**) using Lipofectamine® 2000 (ThermoFisher) according to manufacturer protocol with a slight modification. GCaMP3 DNA construct (~2μg/μl, added at ~1μg/well) was mixed with Lipofectamine-containing Neurobasal medium, incubated for 30min to complex DNA-Lipofectamine, equilibrated to 37^{0}C, and added to the cells 250μl/well for 1h. Following incubation, complete medium was returned to the cells.

Cells were grown to DIV16-18 and a subset of cells were treated with TTX (1mM) for 48 hours to induce synaptic upscaling. Neurons were imaged with constant perfusion (~2.5ml/min) of Tyrode's solution without magnesium (imaging medium: 139mM NaCl, 3mM KCl, 17mM $NaHCO_3$, 12mM glucose, and 3mM $CaCl_2$) using a LSM710 confocal microscope equipped with heated stage. 16-bit videos were acquired at a resolution of 512 x 512 at ~5 frames per second at 10x magnification (with 3x digital zoom). Baseline acquisition, NASPM perfusion (1 or 10μm), and washout periods were 4 min, 4, min, and 8 minutes, respectively; this corresponds to 1000 video frames, 1000 video frames, and 2000 video frames, respectively. For analysis, since NASPM persists in the bath for some time after infusion, the final 1000 frames (3000-4000) were always used for the washout period (i.e. frames 2000-3000 were excluded from analysis as a transition period between NASPM and washout, since washing is not complete during that time). All active synapses were encompassed with a minimal-sized circular (spines) or rectangular (shaft) ROI manually for each video by lab members blinded to condition and genotype. A typical video resulted in 120-200 ROIs (synapses). The "multi measure" tool was applied to each ROI to generate a $\Delta F/F_0$ trace for each synapse. The raw fluorescence data for each synapse was then

normalized to its own baseline and split into 1000 frame portions corresponding to baseline, NASPM, and washout conditions. The number of active frames for each period were counted by summing the frames reaching a threshold plus 3 x standard deviation (SD) for each synapse. A synapse was considered to be inhibited by NASPM if it met the following criteria: 1) The synapse had to be active, i.e. show at least 6 active frames (+3 x SD) during the baseline period, 2) the synapse showed a reduction in active frames in the NASPM period by more than 80%, and 3) the synapse recovered by showing at least 5 active frames in the washout period. The total activity plots (counted active frames) are plotted in **Figure 3.4C**, while the proportion of inhibited synapses (synapses which met the above criteria) is plotted in **Figure 3.4D.**

For FRAP analyses, WT and *Ppt1*$^{-/-}$ cortical neurons were transfected with SEP-GluA1 (Kopec et al., 2006) at DIV10 as described above. Neurons at DIV16 were imaged in Tyrode's solution (in mM: 135 NaCl, 5 KCl, 2 CaCl2, 1 MgCl2, 25 HEPES, and 10 glucose, pH 7.4) using a Zeiss LSM880 in Airyscan mode. Five to six spines were randomly selected for each neuron to bleach during the imaging program. Images were acquired every 15 seconds for 5 frames to establish baseline fluorescence before bleaching at maximum laser intensity. Images were then acquired every 15 seconds thereafter for 10 minutes to analyze fluorescence recovery at bleached spines. The Zen Definite Focus function (Zen Black, Zeiss) was utilized to correct potential drifting of the imaging plane. To analyze FRAP of SEP-GluA1, manual ROIs were drawn over the bleached spines and one to two control (unbleached) spines for each cell and the $\Delta F/F_0$ was extracted using the multi measure tool. Baseline fluorescence (average of first 5 frames) was set to 100%, and the following frames were compared to that baseline, generating the FRAP curves in **Figure 3.3**. FRAP curves were fit using a non-linear regression in Graphpad Prism 9.0 using the LOWESS function. The immobile fraction was calculated by subtracting the average of the fluorescence recovery value for the final 5 frames for each spine from 100%. All spines for each cell were averaged to create one n. cells were taken from two independent cultures.

Analysis of NFATc3 nuclear translocation following culture-wide depolarization was performed as in Murphy et al., 2014 with minor modification. Neurons were transfected at DIV 12 with roughly 1:1 mixture of CAG-mCherry and mouse GFP-NFATc3 (pCMV-SGFP2-mNFATc3.dna), 1mg DNA per coverslip using Lipofectamine® 2000 (ThermoFisher) as above. A subset of neurons was treated with TTX (1μM) for 48 hours leading up to the assay to induce synaptic scaling. The assay was then performed as schematized in **Figure 3.10A**. Solutions were composed as follows: Tyrode + TTX (in mM: 135 NaCl, 5 KCl, 2 CaCl2, 1 MgCl2, 25 HEPES, and 10 glucose, pH 7.4 plus 1mM TTX), Depolarization solution was isotonic, but with 50mM KCl (85mM NaCl) and without TTX, and recovery solution was standard Tyrode without TTX. Cells were incubated at 37ºC in between steps. For every coverslip of depolarized (KCl) neurons, a control with no depolarization (sham, Tyrode solution + TTX) and depolarization with NASPM (KCl + 10 μmNASPM) condition were performed in parallel. Following fixation at the end of the assay, cells were immunostained with anti-GFP 488 antibody (ThermoFisher) following the protocol above to amplify the GFP-NFAT signal. GFP-NFAT nucleus/soma ratio was analyzed by manually tracing the nucleus, based on the DAPI staining signal, and soma as independent ROIs and dividing the integrated fluorescence value (measured by multi measure tool in Fiji) for nucleus by that for the soma.

3.2.16. Immunocytochemistry

All experimental and control groups were immunostained simultaneously to match exact staining conditions. Neurons were first immunostained for surface AMPA receptors (GluA1 subunit) before permeabilization for staining of intracellular antigens (MAP2). Coverslips were washed 3x with TBS and blocked for 1h at RT in TBS containing 5% BSA. Then, primary antibody (GluA1 or MAP2, see **Table 3**) at 1:400 dilution was added to coverslips in TBS containing 1% BSA and incubated for 2h at RT or overnight at 4^0C. Following 4X washes with TBS cells were incubated with 1:400 secondary, fluorophore-linked antibody (Alexa Fluor 488, cat. #: A-11034,

A-11006) in TBS containing 1% BSA. These steps were repeated to immunolabel MAP2 (1:400, see **Table 3** for primary and secondary antibody information), with the addition of 0.1% Triton x-100 in all solutions. Coverslips are then mounted on SuperFrost Plus slides in DAPI Vectamount medium.

TABLE 3. Key resources table #2

Reagent type (species) or resource	Designation	Source or reference	Identifiers	Additional information
strain, strain background (M*us musculus*)	B6;129-Ppt1^{tm1Hof}/J	Jax stock #: 004313	Gupta, PNAS, 2001; RRID: MGI:004313	
antibody	Mouse monoclonal anti-GluA1	Millipore Sigma	Cat: MAB2263; RRID: AB_11212678	1:500 for biotinylation,1:1000 for all else
antibody	Mouse monoclonal anti-GluA2	UC Davis/NIH NeuroMab Facility	Cat: 75-002; RRID: AB_2232661	1:500 for biotinylation,1:1000 for all else
antibody	Rabbit polyclonal anti-Akap79/150	Gift from Mark Dell'Acqua	RRID: AB_2532138	1:1000
antibody	Rabbit polyclonal anti-PPT1	Gift from Sandra Hofmann		1:500
antibody	Mouse monoclonal anti-β-actin	ThermoFisher Scientific	Cat: A2228; RRID: AB_476697	1:2000
antibody	Donkey anti-Rabbit IgG Secondary Antibody, HRP	ThermoFisher Scientific	Cat: SA1-200; RRID: AB_325994	1:1000 for biotinylation; 1:5000 or 1:10000 for all else
antibody	Rabbit polyclonal anti-MAP2	Millipore Sigma	Cat: AB5622; RRID: AB_91939	1:400
antibody	Peroxidase AffiniPure Goat Anti-Mouse HRP	Jackson ImmunoResearch	Cat: 115-035-146; RRID_AB_2307392	1:1000 for biotinylation; 1:5000 or 1:10000 for all else
antibody	Rabbit polyclonal anti-Iba1	Fujifilm/Wako	Cat# 019-1974; RRID: AB_839504	1:1000
antibody	GFP Polyclonal Antibody, Alexa Fluor 488	ThermoFisher Scientific	Cat: A-21311; RRID: AB_221477	1:1000
antibody	Mouse monoclonal anti-transferrin	ThermoFisher Scientific	Cat# A-11130; RRID:AB_2534136)	1:500
antibody	Mouse monoclonal anti-GluN2B	UC Davis/NIH NeuroMab Facility	Cat: 75/097; RRID:AB_10673405	(1:1000)
recombinant DNA reagent	pEF-GFP	Addgene	Plasmid: 11154	Drs. Matsuda and Cepko

recombinant DNA reagent	G-CaMP3	Addgene	Plasmid: 22692	Dr. Looger
recombinant DNA reagent	GFP-mNFATc3	Gift from Mark Dell'Acqua		Mouse NFATc3 with GFP tag
commercial assay or kit	Dynabeads™ M-280 Streptavidin	ThermoFisher Scientific	Cat: 11205D	
Virus	pENN.AAV.CamKII.GCaMP6f.WPRE.SV40 (AAV9)	Addgene	item #100834-AAV9	Injected 200nL of undiluted virus, 10^{14} viral genomes/μl
Virus	pAAV-hSyn-mCherry (AAV2)	Addgene	item #114472-AAV2	Injected 200nL of undiluted virus, 10^{14} viral genomes/μl (mixed 1:1 with GCaMP virus)
chemical compound, drug	Naspm trihydrochloride	Tocris	Cat: 2766	Treatment: 1 or 10μM
chemical compound, drug	Tetrodotoxin-citrate (TTX)	Tocris	Cat: 1069	Treatment: 1μM
chemical compound, drug	(+)-Bicuculline	Tocris	Cat: 0130	Treatment: 20μM
chemical compound, drug	mPEG-Maleimide, MW 5,000	Laysan Bio Inc.	MPEG-MAL-5000-1g	
software, algorithm	Fiji			
software, algorithm	Matlab 2020a	Mathworks		EZcalcium (Cantu et al., 2020)
software, algorithm	Prism 9.0.1	Graphpad		

3.3. Results

3.3.1. Excitatory synapse formation is impaired in *Ppt1*$^{-/-}$ visual cortex

To examine the role of Ppt1 in the developmental regulation of AMPA receptors (AMPARs), we first performed immunoblotting for the GluA1 and GluA2 subunits in both whole lysates and synaptosomal fractions from WT and *Ppt1*$^{-/-}$ visual cortices. Total levels of GluA1 and GluA2 individually were unchanged throughout development (postnatal day, P11, 14, 28, 33, 42, 60), both in whole lysates (**Figure 3.1A, B**) and synaptosomes (**Figure 3.1C, D**).

To compare the functionality of synaptic AMPARs between the visual cortex of WT and *Ppt1*$^{-/-}$ mice, we next analyzed the frequency and amplitude of spontaneous excitatory postsynaptic potentials (sEPSPs) in layer 2/3 visual cortical neurons using *ex vivo* patch-clamp electrophysiology (**Figure 3.1E**). We found that compared to WT neurons, *Ppt1*$^{-/-}$ cells showed no change in their frequency or amplitude at P15 (data not shown). By P28, however, *Ppt1*$^{-/-}$ neurons demonstrated a significant decrease in sEPSC frequency (**Figures 3.1F**), which indicates a reduction in the number of synapses impinging on layer 2/3 neurons. These data suggest that the experience-dependent delivery or surface retention of AMPARs typical of excitatory synapse maturation in the visual cortex is impaired in the *Ppt1*$^{-/-}$ visual cortex.

Figure 3.1. Developmental AMPA receptor transmission is decreased in *Ppt1*$^{-/-}$ visual cortex.

(A) Quantification of total GluA1 levels in lysates from WT and *Ppt1*$^{-/-}$ visual cortices via immunoblots for ages postnatal day (P) 11-60. *Ppt1*$^{-/-}$ data are normalized to the WT mean value at each age and comparisons were made within age. N=2-4, Data represent mean ± SEM.

(B) Quantification of total GluA2 levels in lysates from WT and *Ppt1*$^{-/-}$ visual cortices via immunoblots for ages postnatal day (P) 11-60. *Ppt1*$^{-/-}$ data are normalized to the WT mean value at each age and comparisons were made within age. N=2-4, Data represent mean ± SEM.

(C) Quantification of GluA1 levels in synaptosomes from WT and *Ppt1*$^{-/-}$ visual cortices via immunoblots for ages postnatal day (P) 11-60. *Ppt1*$^{-/-}$ data are normalized to the WT mean value at each age and comparisons were made within age. N=2-4, Data represent mean ± SEM.

(D) Quantification of GluA2 levels in synaptosomes from WT and *Ppt1*$^{-/-}$ visual cortices via immunoblots for ages postnatal day (P) 11-60. *Ppt1*$^{-/-}$ data are normalized to the WT mean value at each age and comparisons were made within age. N=2-4, Data represent mean ± SEM.

(E) Schematic of the electrophysiological recording configuration.

(F) Representative voltage-clamp recordings of spontaneous EPSPs (sEPSPs) from layer 2/3 visual cortical neurons in WT (top) and *Ppt1*$^{-/-}$ (bottom) mice at P28. ****P<0.0001.

Figure 3.1. Developmental AMPA receptor transmission is decreased in *Ppt1*$^{-/-}$ visual cortex.

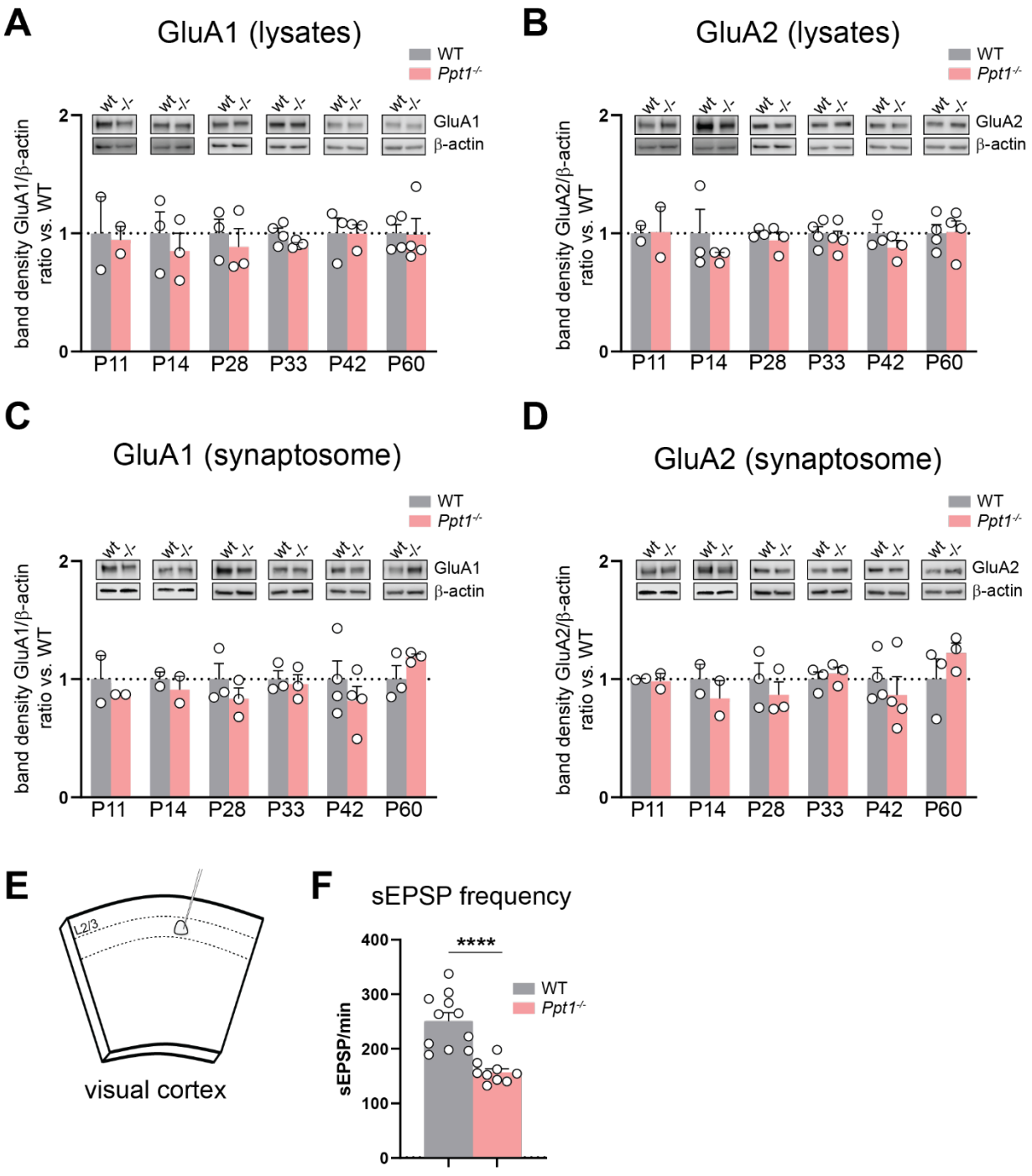

3.3.2. Synaptic upscaling of GluA1 is exaggerated in *Ppt1*$^{-/-}$ neurons *in vitro*

Given the reduction of AMPAR sEPSPs in the visual cortex of *Ppt1*$^{-/-}$ mice but no detectable change in synaptosomal GluA levels, we hypothesized that the reduced number of functional synapses are strengthened by synaptic scaling. Synaptic scaling is a dendrite- (Barnes et al., 2017) or neuron-wide mechanism of plasticity that compensates for chronic changes in activity by sensitizing or desensitizing synapses in compensatory fashion (O'Brien et al., 1998; Turrigiano, 1999; Turrigiano et al., 1998). Specifically, in response to chronic activity blockade (on the order of days), AMPARs are inserted into the membrane while, in response to a chronic increase in afferent activity, AMPARs are endocytosed (O'Brien et al., 1998; Turrigiano et al., 1998). Several studies show GluA1-containing AMPARs mediate synaptic scaling (Goel et al., 2006; Ju et al., 2004; Shepherd et al., 2006; Thiagarajan et al., 2005) and recent evidence points to a role for Ppt1 in depalmitoylating this AMPAR subunit (Gorenberg et al., 2020).

To determine whether Ppt1 regulates synaptic scaling, we modeled this form of plasticity *in vitro* by incubating WT or *Ppt1*$^{-/-}$ primary cortical neurons in either bicuculline (20μM in DMSO) to induce downscaling, TTX (1μM in water) to induce upscaling, or vehicle control (VC, DMSO to a final concentration of 0.1%) for 48 hours, as previously reported (Diering et al., 2014; Sanderson et al., 2018; Shepherd et al., 2006; Turrigiano et al., 1998).

First, we performed a surface biotinylation assay to examine the surface expression of GluA1 after scaling down (Bic), up (TTX), or vehicle control treatment (VC). As demonstrated in previous studies (Diering et al., 2014; Shepherd et al., 2006), bicuculline treatment of WT cells decreased surface expression of GluA1; however, there was no effect of bicuculline in *Ppt1*$^{-/-}$ neurons (**Figure 3.2A, B**). Interestingly, while TTX treatment induced synaptic upscaling in both WT and *Ppt1*$^{-/-}$ neurons, upscaling was exaggerated in *Ppt1*$^{-/-}$ cells, as demonstrated by significantly greater surface levels of GluA1 (**Figure 3.2A, B**). Immunoblots of inputs from the

same cell lysates showed an increase in total GluA1 levels to an equal degree in both WT and *Ppt1*$^{-/-}$ neurons during upscaling (**Figure 3.2C, D**). However, while we observed a significant decrease of GluA2 in WT downscaled cells, there was not an increase in the total levels of GluA2 in either WT or *Ppt1*$^{-/-}$ neurons under these conditions (**Figure 3.2E**). Collectively, these data indicating that posttranslational or trafficking mechanism is responsible for the exaggerated GluA1 surface expression.

Next, we employed the same scaling assay to visualize GluA1 surface expression using fluorescent immunolabeling under non-permeabilizing conditions. Again, bicuculline treatment did not induce a statistically detectable scaling down of GluA1 puncta (percent area/20μm of dendrite) in *Ppt1*$^{-/-}$ neurons but did so in WT cells (**Figure 3.2F**). Similar to our biochemical findings, TTX treatment induced upscaling in both WT and *Ppt1*$^{-/-}$ cells, but the increase was greater in *Ppt1*$^{-/-}$ neurons, as we observed by increased GluA1 puncta count and percent area covered along the dendrite (**Figure 3.2F-H**). These data indicate that *Ppt1*$^{-/-}$ neurons *in vitro* exhibit amplified synaptic upscaling.

To examine whether surface AMPAR subunit mobility is impaired, we employed fluorescence recovery after photobleaching (FRAP) analysis by overexpressing the superecliptic (SEP) GluA1 subunit in WT and *Ppt1*$^{-/-}$ neurons and photobleaching individual dendritic spines (**Figure 3.3A**). SEP-GluA1 is useful to visualize receptors on the cell surface , because fluorescent signals are quenched in acidic environment within endosomes. These analyses revealed a significantly slower recovery of photobleached SEP-GluA1 signal at individual synapses (**Figure 3.3B, C**), resulting in an increased immobile fraction of GluA1 in *Ppt1*$^{-/-}$ neurons (**Figure 3.3D**). Thus, this amplified upscaling is induced partly by a reduced surface mobility of GluA1 in the synaptic membrane of *Ppt1*$^{-/-}$ neurons.

Figure 3.2. Synaptic scaling is exaggerated in primary cortical *Ppt1*$^{-/-}$ neurons.

(A) Representative immunoblot of surface GluA1 and transferrin control following surface biotinylation assay in DIV16 cortical neuron cultures. Cells were treated with bicuculline (20μM), vehicle (DMSO, final concentration 0.1%), or TTX (1μM) for 48h.

(B) Quantification of the surface GluA1 levels in WT and *Ppt1*$^{-/-}$ treated and untreated cortical neurons, normalized to transferrin for each experiment and expressed as percent change vs. vehicle condition. N=6 independent cultures. Data represent mean ± SEM. *p<0.05, **p<0.01.

(C) Representative immunoblots of GluA1, GluA2, and β-actin loading control for input samples (lysates). N=6 cultures.

(D) Quantification of input GluA1 levels in WT and *Ppt1*$^{-/-}$ treated and untreated cortical neurons, normalized to β-actin for each experiment and expressed as percent change vs. vehicle condition. N=6 independent cultures. Data represent mean ± SEM. *p<0.05, **p<0.01.

(E) Quantification of input GluA2 levels in WT and *Ppt1*$^{-/-}$ treated and untreated cortical neurons, normalized to β-actin for each experiment and expressed as percent change vs. vehicle condition. N=6 independent cultures. Data represent mean ± SEM.

(F) Representative images of surface immunolabeled GluA1 in DIV16 WT and *Ppt1*$^{-/-}$ cortical neurons, treated with bicuculline (20μM), vehicle control (DMSO, final concentration 0.1%), or TTX (1μM) for 48h. Scale bars for low magnification images = 20μm, for high magnification = 5μm.

(G) Quantification of the number of surface immunolabeled GluA1 puncta over 20μm of dendrite at 50-100mm from the soma. N = 2-5 cultures/group (number of cultures and total number of cells analyzed are listed for each group on the graph). Data are normalized to the WT vehicle control (VC) condition. Data represent mean ± SEM. *p<0.05, **p<0.01, **** indicates p<0.0001.

(H) Quantification of the percent area covered by surface immunolabeled GluA1 puncta over 20μm of dendrite at 50-100μm from the soma. N = 2-5 cultures/group (number of cultures and total number of cells analyzed are listed for each group on the graph). Data are normalized to the WT vehicle control condition. Data represent mean ± SEM. *p<0.05, ***p<0.001, **** indicates p<0.0001.

Figure 3.2. Synaptic scaling is exaggerated in primary cortical *Ppt1*$^{-/-}$ neurons.

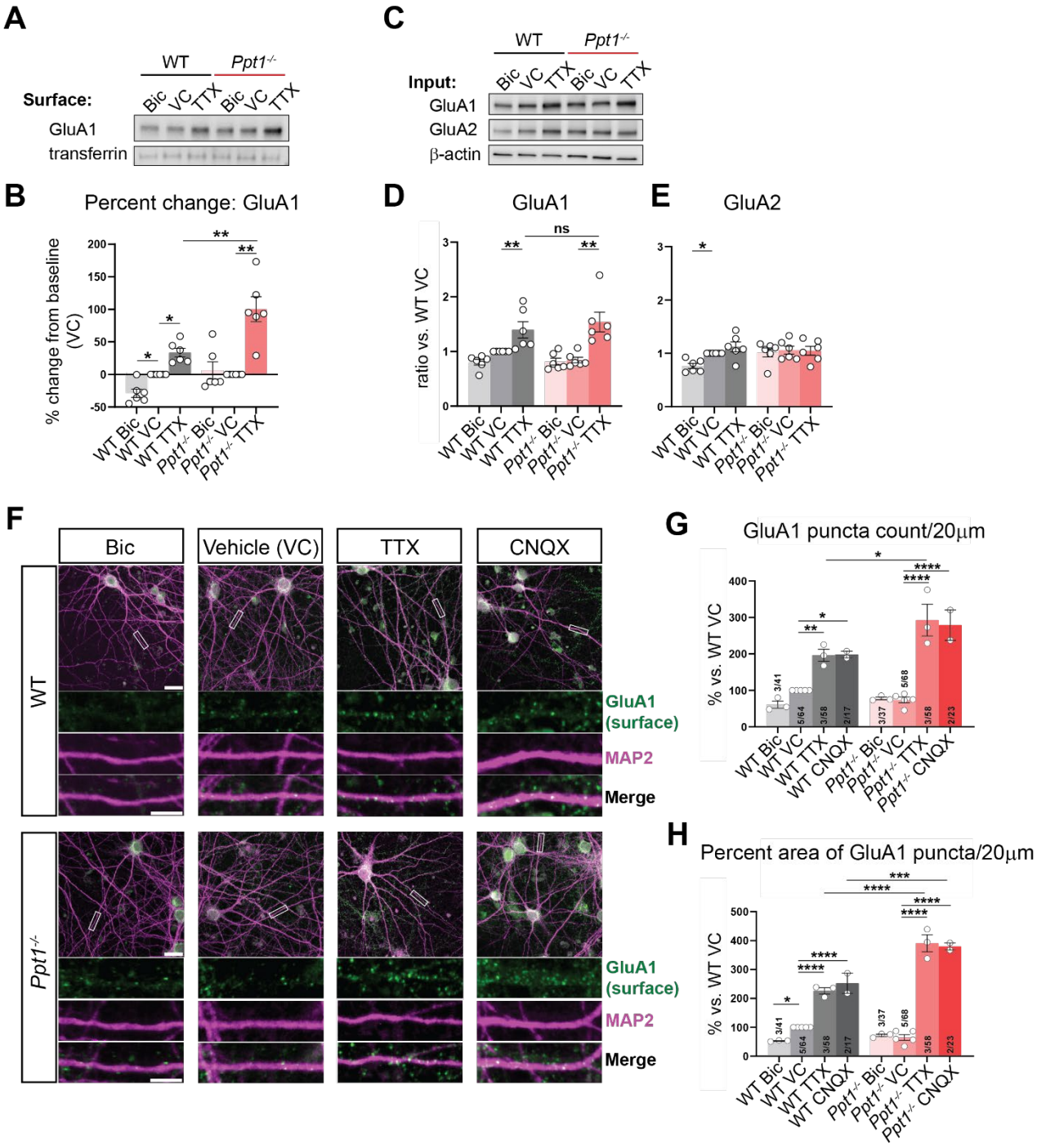

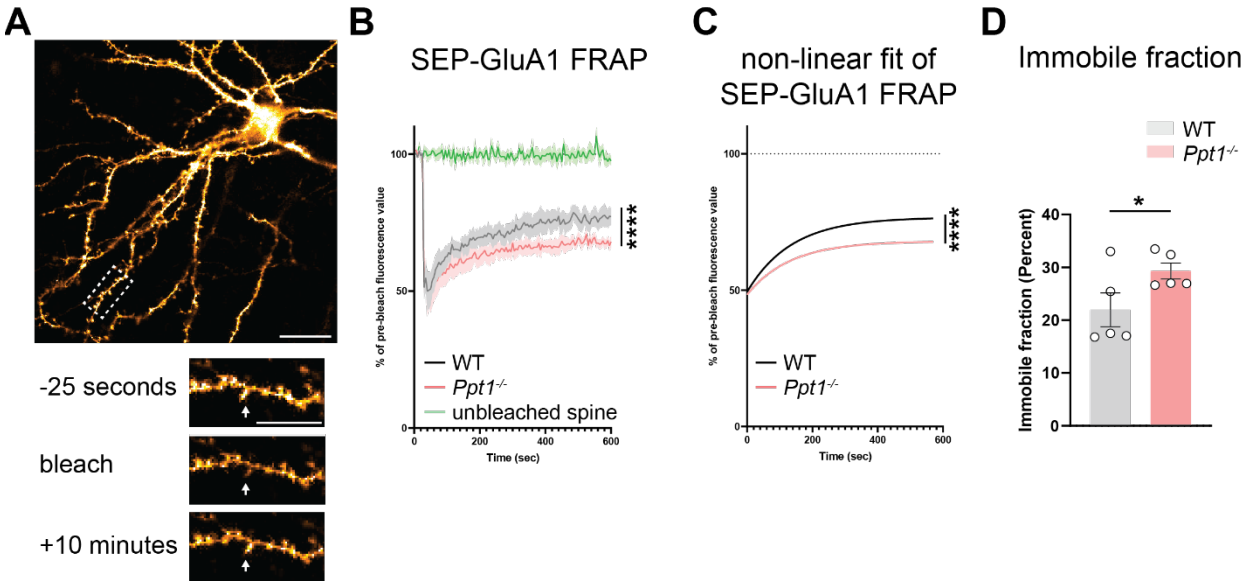

Figure 3.3. Membrane mobility of SEP-GluA1 is reduced in *Ppt1*$^{-/-}$ neurons.

(A) Representative image of a SEP-GluA1 transfected neuron (top) and a 20μm segment of dendrite before, just after, and 10minafter bleaching of an individual spine (arrow, bottom). Scale=20μm for low magnification images (top), 10μm for high magnification images (bottom).

(B) Time-dependent recovery of SEP-GluA1 fluorescence after photobleaching (FRAP) in WT and *Ppt1*$^{-/-}$ primary cortical neurons. Average of n=5 cells across 2 independent cultures, 5-6 bleached spines per cell.

(C) Non-linear fit of (single phase decay) of SEP-GluA1 fluorescence after photobleaching (FRAP) in WT and *Ppt1*$^{-/-}$ primary cortical neurons. **** p<0.0001.

(D) Quantification of the immobile fraction (percent unrecovered compared to pre-bleach fluorescence) of SEP-GluA1 fluorescence after photobleaching (FRAP) for each cell. N=5 cells across 2 independent cultures, 5-6 spines per cell. *p<0.05.

3.3.3. CP-AMPARs are responsible for exaggerated upscaling in *Ppt1*$^{-/-}$ neurons

Given previous studies showing the contribution of CP-AMPARs to synaptic scaling, we aimed to directly discern the activity of this receptor subtype from calcium-impermeable, GluA1/GluA2 AMPARs in overly upscaled synapses in *Ppt1*$^{-/-}$ cells. To this end, we performed calcium imaging in WT and *Ppt1*$^{-/-}$ primary cortical neurons. We transfected WT and *Ppt1*$^{-/-}$ cells with GCaMP3 and exposed them to TTX or vehicle for 48h, then performed a live-cell calcium imaging assay while perfusing the CP-AMPAR specific blocker NASPM (1 or 10μM, where indicated) into the bath (**Figure 3.4A**). We manually selected all active synapses in each video and extracted their $\Delta F/F_0$ traces (**Figure 3.4B**). First, similar to our earlier analyses (**Figure 3.2**), we did not see a difference in the number of calcium transients between WT and *Ppt1*$^{-/-}$ vehicle-treated neurons (**Figure 3.4C**). However, while TTX treatment increased the number of synaptic calcium transients in both WT and *Ppt1*$^{-/-}$ cells, upscaled *Ppt1*$^{-/-}$ neurons exhibited the highest number of baseline calcium transients on average (**Figure 3.4C**). Importantly, while the proportion of NASPM-sensitive synapses was also similar with vehicle treatment between WT and *Ppt1*$^{-/-}$ neurons, upscaled *Ppt1*$^{-/-}$ neurons demonstrated significantly more NASPM-sensitive synapses, at both 1μM and 10μM doses, than all other groups (**Figure 3.4D**). These data indicate that *Ppt1*$^{-/-}$ neurons upregulated CP-AMPARs to a greater extent following synaptic upscaling compared to WT cells. Further, the data demonstrate that the activity-dependent trafficking of CP-AMPARs is dysregulated in *Ppt1*$^{-/-}$ neurons.

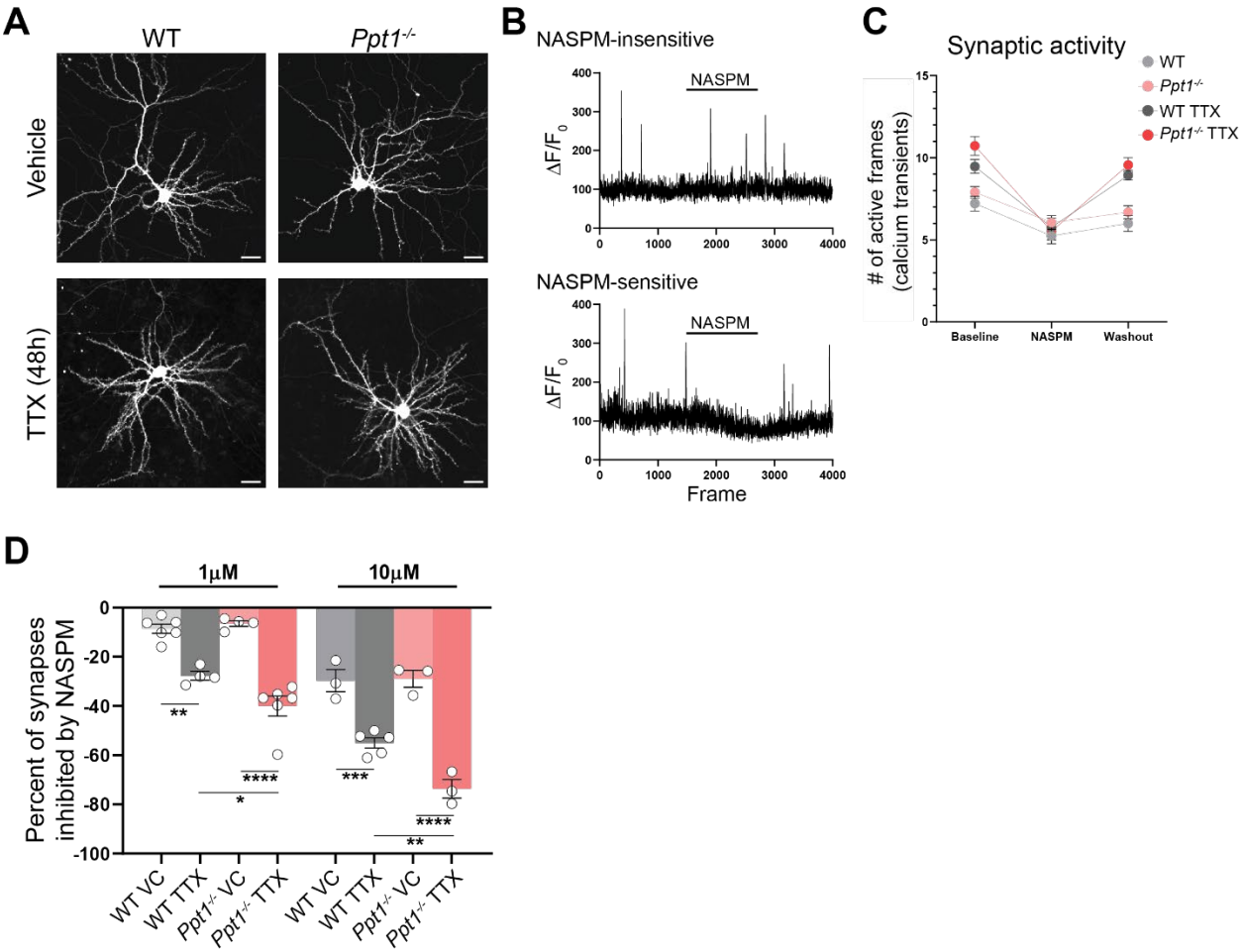

Figure 3.4. Exaggerated synaptic scaling leads to synaptic incorporation of calcium-permeable AMPARs.

(A) Representative calcium imaging (GCaMP) video still frames of vehicle control or TTX-treated (1μm, 48h) WT and *Ppt1*$^{-/-}$ cortical neurons.

(B) Representative $\Delta F/F_0$ traces for one synapse that is NASPM-insensitive and one that is NASPM-sensitive.

(C) Quantification of the average synaptic activity (number of frames >3SDs from baseline) for all synapses in one representative cell from each condition prior to, during, and following NASPM (1μM) bath infusion.

(D) Quantification of the proportion of NASPM-sensitive synapses in WT, TTX-treated WT, *Ppt1*$^{-/-}$, and TTX-treated *Ppt1*$^{-/-}$ cortical neurons expressed as the percentage of synapses inhibited during NASPM infusion. N=3-5 cells/group, cells taken from at least 2 independent cultures. Data represent mean ± SEM. *p<0.05, **p<0.01, ***p<0.001, **** indicates p<0.0001.

3.3.4. Exaggerated synaptic upscaling in *Ppt1*$^{-/-}$ neurons correlates with an overload of palmitoylated GluA1

A recent study showed that the AMPAR subunit GluA1 is a substrate of Ppt1 using quantitative palmitoyl-proteomics (Gorenberg et al., 2020). To examine whether palmitoylation of GluA1 is accountable for the enhanced incorporation or activity of CP-AMPARs in *Ppt1*$^{-/-}$ neurons during synaptic scaling, we performed the Acyl-PEGyl Exchange Gel-Shift (APEGS) assay in WT and *Ppt1*$^{-/-}$ neurons following scaling down (bicuculline), upscaling (TTX), or vehicle control. We measured the density of palmitoylated GluA1 (upper band in immunoblot) to the non-palmitoylated fraction (lower band in immunoblot) to calculate the palmitoylated ratio. While we did not detect any significant change in GluA1 palmitoylation in WT cells following scaling, similar to a previous report (Yang et al., 2009), we observed a significant increase in the palmitoylated GluA1 ratio in upscaled *Ppt1*$^{-/-}$ neurons (**Figure 3.5A, B**). In contrast, we did not see a significant change in GluA2 palmitoylation in either genotype (**Figure 3.5A, B**). Interestingly, Ppt1 levels exhibit a scaling-dependent effect in WT cells—Ppt1 levels are increased by upscaling (TTX) (**Figure 3.5A, C**), suggesting that activity-dependent expression of Ppt1 during synaptic scaling in WT neurons prevents GluA1 subunits from uncontrolled palmitoylation and accumulation at the synapse. Further, the exaggerated increase in CP-AMPARs in *Ppt1*$^{-/-}$ cortical neurons may be attributable to aberrant GluA1 palmitoylation that occurs with loss of normal Ppt1 function. However, given the distinct effects of GluA1 palmitoylation at each of its currently recognized three sites on AMPA receptor trafficking, further study is required to determine the specific role of increased palmitoylation on GluA1 during scaling in *Ppt1*$^{-/-}$ cells.

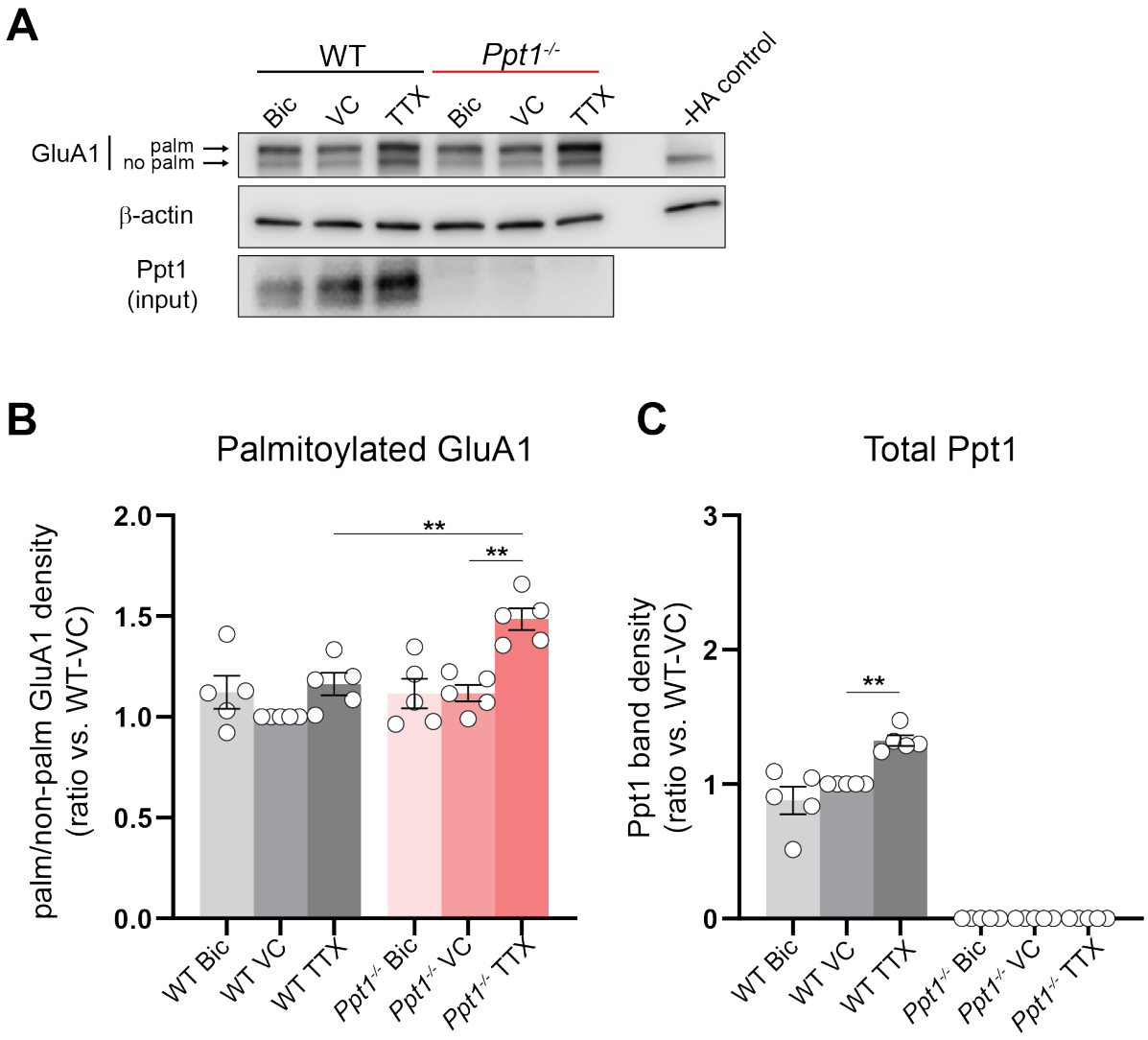

Figure 3.5. Exaggerated synaptic scaling in *Ppt1*$^{-/-}$ cortical neurons is associated with increased GluA1 palmitoylation.

(A) Representative immunoblot of APEGS assay-processed cortical neurons lysates probing for GluA1, GluA2, and β-actin. Representative blot for Ppt1 (input) also shown. Neurons were treated with bicuculline (20μM), vehicle control (DMSO, final concentration 0.1%), or TTX (1μM) for 48h prior to APEGS assay.

(B) Quantification of the ratio of palmitoylated vs. non-palmitoylated GluA1 levels, normalized to β-actin loading control. N=5 independent cultures. Data represent mean ± SEM. **p<0.01.

(C) Quantification of the Ppt1 levels, normalized to β-actin loading control. N=5 independent cultures. Data represent mean ± SEM. **p<0.01.

3.3.5. *In vivo* two-photon calcium imaging reveals increased cortical synchrony in *Ppt1*$^{-/-}$ visual cortex

To determine the circuit-level effects of dysregulated neural activity in *Ppt1*$^{-/-}$ mice, we employed *in vivo* two-photon calcium imaging in awake mice at four to five weeks of age, at the same time point we observe a decrease in excitatory synapse number (sEPSC frequency, **Figure 3.1**). We transfected layer 2/3 visual cortical neurons with the calcium indicator, GCaMP6f and fluorescent cell marker, mCherry, in neonates (see **Table 3**) implanted a cranial window over the left V1 of injected animals between P21-27, and imaged visual cortical calcium activity at P28-P35 (recovery period from surgery was a minimum of 7 days.

We monitored visual cortical neuron activity for 5-minute epochs in WT and *Ppt1*$^{-/-}$ mice and extracted the $\Delta F/F_0$ trace for each active neuron in each video (**Figure 3.6A, B**). Spontaneous activity in WT and *Ppt1*$^{-/-}$ visual cortical neurons showed no significant difference in the total number of active neurons or the average activity of individual neurons per field of view. However, analyzing the pair wise co-activity of all neurons in the videos revealed that compared to WT, the calcium activity of *Ppt1*$^{-/-}$ visual cortical neurons demonstrated a significantly increased correlation (Fisher corrected Pearson's r) on average (**Figure 3.6C, D**). This was not due to strong correlations between a few cortical cells driving up the average in *Ppt1*$^{-/-}$ mice, as the maximum correlation of any two cells across all videos for each animal was not different between WT and *Ppt1*$^{-/-}$ (data not shown). These data indicate that although the number of AMPAR-containing excitatory synapses are decreased in *Ppt1*$^{-/-}$ mice at P28 (**Figure 3.1**), the preserved connectivity and neuronal activity drive hypersynchrony of spontaneous activity in the *Ppt1*$^{-/-}$ visual cortex.

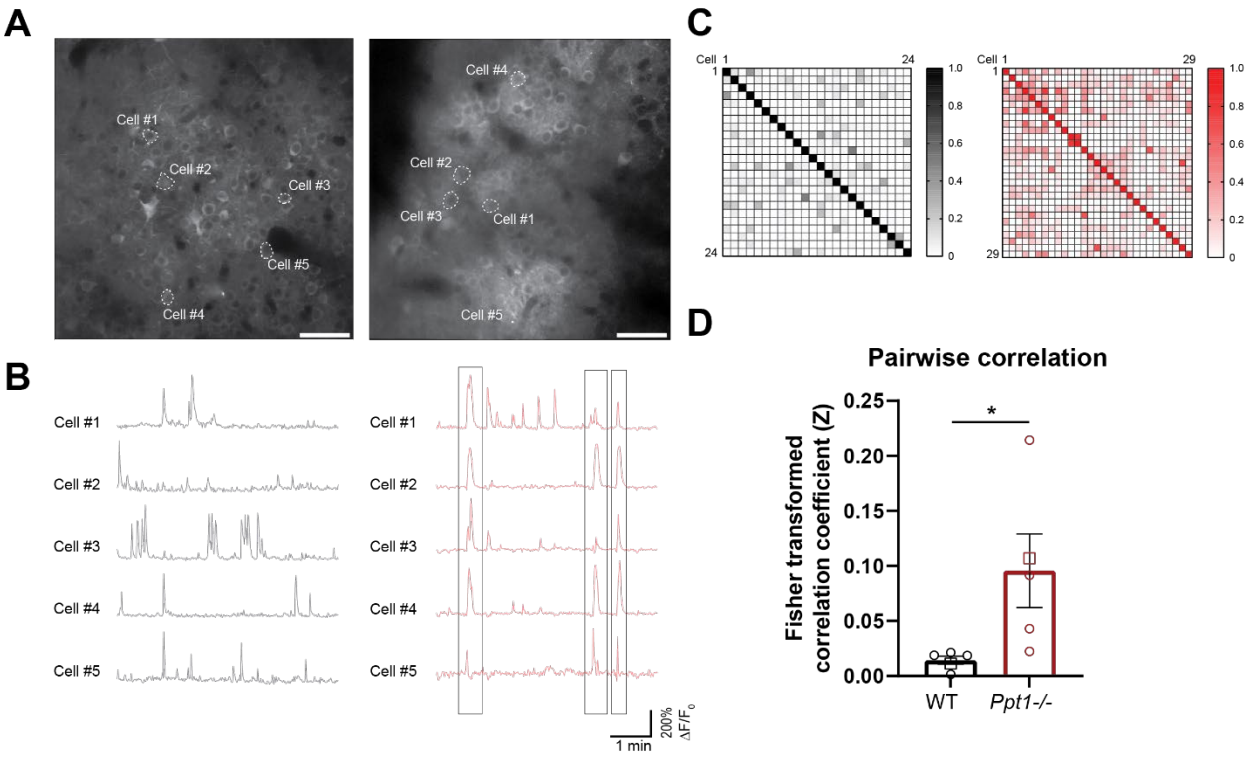

Figure 3.6. *in vivo* 2-photon calcium imaging reveals hypersynchrony of layer 2/3 visual cortical neurons in *Ppt1*$^{-/-}$ mice.

(A) Representative calcium imaging video still frames of layer 2/3 cortical neuronal somata from a WT and *Ppt1*$^{-/-}$ mouse. Scale bar = 50μm.

(B) Representative $\Delta F/F_0$ traces for selected cells in each video. Note the coactivity of multiple cells in the *Ppt1*$^{-/-}$ brain demarked by grey boxes.

(C) Correlation matrices of the deconvolved coactivity (Persons r correlation values) of all cells in in the representative videos.

(D) Averaged cross-cell correlation value (Fisher transformed) for all videos, from all animals. Each point represents the average for one mouse. Square points denote the representative correlation matrices from (D).

3.3.6. Dark rearing *Ppt1*$^{-/-}$ mice exacerbates disease pathology in the visual cortex

Synaptic scaling is a crucial mechanism guiding circuit formation in the developing brain and the consequences of its disruption may contribute to the progression of CLN1 disease. Next, we aimed to induce synaptic scaling of CP-AMPARs *in vivo* by manipulating visual experience. In particular, rearing rodents in complete darkness stimulates increased mini excitatory postsynaptic current (mEPSC) amplitude, an increase in the amount of postsynaptic GluA1 content, and an increased inward rectification of AMPAR-dependent currents in visual cortical neurons, hallmarks of synaptic upscaling of CP-AMPARs (Desai et al., 2002; Goel and Lee, 2007; Goel et al., 2006, 2011). Our results led us to the hypothesis that Ppt1, either directly through the depalmitoylation of GluA1 (Gorenberg et al., 2020) or indirectly through the palmitoylation of other synaptic molecules, which regulates AMPAR trafficking in response to early visual experience and CP-AMPARs would be overly incorporated in *Ppt1*$^{-/-}$ visual cortical synapses following dark rearing. Therefore, we reared groups of WT and *Ppt1*$^{-/-}$ mice in complete darkness (dark reared, DR) beginning at 10-12 days postnatal, before pups open their eye, to determine if loss of Ppt1 would occlude or amplify the lack of synapse maturation characteristic of this intervention (Desai et al., 2002).

Interestingly, dark rearing simultaneously exacerbated disease symptoms in the visual cortex of *Ppt1*$^{-/-}$ mice. The hallmark of CLN1, ALSM, was increased in the visual cortex (**Figure 3.7A, B**), cortical thickness was decreased (**Figure 3.7C**), and mortality occurred significantly earlier as a result of severe seizures in *Ppt1*$^{-/-}$ animals (**Figure 3.7D**). Together, these data demonstrate that loss of Ppt1 causes an exaggerated synaptic scaling response *in vivo* induced by visual sensory deprivation that accelerated cortical atrophy and death, implicating CP-AMPARs in CLN1 disease progression.

Figure 3.7. Dark rearing *Ppt1*$^{-/-}$ animals exacerbates disease pathology.

(A) Representative sagittal sections of medial visual cortex from WT, DR-WT, *Ppt1*$^{-/-}$, and DR-*Ppt1*$^{-/-}$ showing the accumulation of autofluorescent lipopigment with age (postnatal ages 28-78). Scale bar = 50μm.

(B) Quantification of the percent area covered by autofluorescent lipopigment. N=3-5 animals/group. *p<0.05, **p<0.01, ***p<0.001 by two-way ANOVA followed by Tukey's post hoc test.

(C) Quantification of cortical thickness across age in WT, DR-WT, *Ppt1*$^{-/-}$, and DR-*Ppt1*$^{-/-}$ mice. N=3-5 animals/group. *p<0.05, **p<0.01, ***p<0.001, ****p<0.0001 by two-way ANOVA followed by Tukey's post hoc test.

(D) Kaplan-Meier plot of mortality in *Ppt1*$^{-/-}$ and DR-*Ppt1*$^{-/-}$ mice. N=6 *Ppt1*$^{-/-}$, 10 for DR-*Ppt1*$^{-/-}$. ***P<0.001 by log-rank (Mantel-Cox) test.

Figure 3.7. Dark rearing *Ppt1*$^{-/-}$ animals exacerbates disease pathology.

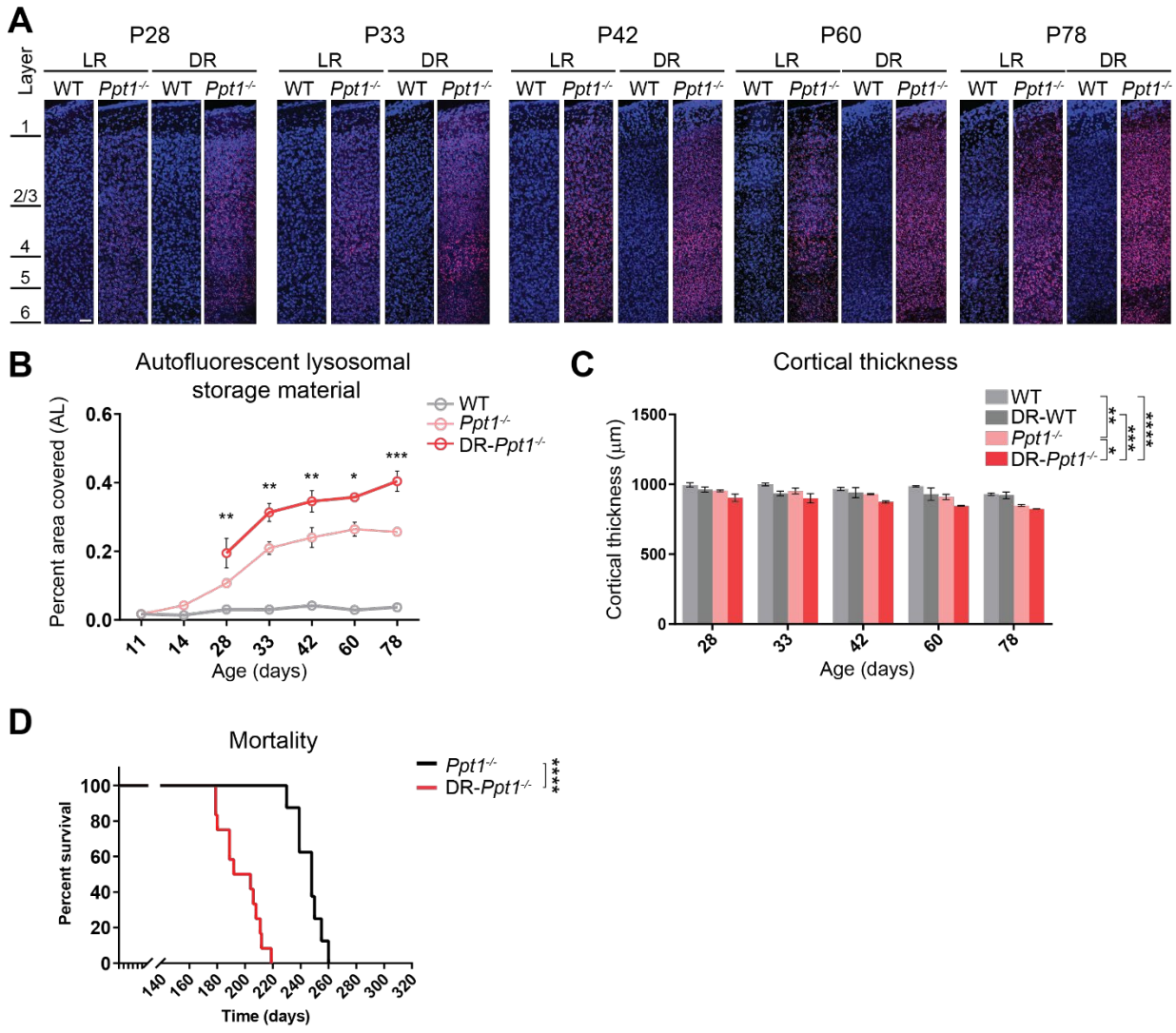

3.3.7. Palmitoyl proteomics points to hyperpalmitoylation of Akap5

To better understand the molecular pathways that underlie dysregulated synaptic upscaling in *Ppt1*$^{-/-}$ neurons, we employed palmitoyl-proteomics using the acyl-biotin exchange method (Drisdel and Green, 2004b; Roth et al., 2006) to visual cortical lysates and synaptosomes (Wan et al., 2007). This analysis detected 512 palmitoylated proteins in whole lysates and 596 in synaptosomes from WT and *Ppt1*$^{-/-}$ visual cortices at P42 (**Figure 3.8A, B**). In whole lysates, we did not detect any significant changes in the abundance ratio (*Ppt1*$^{-/-}$/WT) for any proteins (**Figure 3.8A**). In synaptosomes, we detected significantly increased palmitoylation levels of only two proteins, acid ceramidase and cathepsin D, demonstrating that these proteins are consistently overrepresented in the CLN1 brain across several studies (**Figure 3.8B**) (Atiskova et al., 2019; Chandra et al., 2015; Gorenberg et al., 2020; Sleat et al., 2017). Despite only a few proteins showing statistically significant excessive palmitoylation, we found that the majority of the identified proteins showed modest overpalmitoylation in the *Ppt1*$^{-/-}$ brain, particularly in synaptosomes. Specifically, in *Ppt1*$^{-/-}$ whole lysates, 144 proteins (28.1%) show a >1.2-fold increase in the abundance ratio compared to WT, vs 13 (2.5%) showing a <0.80-fold change (**Figure 3.8C**). The trend is more robust in *Ppt1*$^{-/-}$ synaptosomes, with 380 proteins (63.8%) demonstrating a >1.2-fold change increase, while only 31 proteins (5.2%) show a <0.80-fold change reduction (**Figure 3.8D**). While individual synaptic proteins do not demonstrate statistically significant changes in their palmitoylation by ~1.5 months, these data suggested a bulk increase of the palmitoylation level of synaptic proteins with loss of Ppt1 function.

To identify the features of synaptic proteins that are overrepresented in the palmitoyl fraction of *Ppt1*$^{-/-}$ visual cortices, we input our gene lists for whole lysates and synaptosomes separately into the online synaptic protein ontology database, SynGO (Koopmans et al., 2019). For both datasets, SynGO analysis demonstrated a robust enrichment for synaptic proteins compared to a whole-brain proteomic background dataset (**Figure 3.8E, F**), emphasizing the role

for palmitoylation at the synapse. The top ten enriched SynGO terms demonstrated substantial overlap between whole lysates and synaptosomes, which is expected given the enrichment for palmitoylated proteins (acyl-biotin exchange) in both populations. “Process in the synapse,” “process in the presynapse,” “synaptic vesicle cycle,” “synapse organization,” and “process in the postsynapse,” represent the top five enriched terms in synaptosomes **(Figure 3.8G**), which also appeared in the top ten enriched terms for whole lysates.

To highlight specific pathways that might be dysregulated by lack of Ppt1, we performed a network analysis on all genes annotated with the top SynGO term “process in the synapse” using the online protein-protein interaction database, STRING (https://string-db.org, see **Methods**). As expected from the SynGO analysis, the networks in lysates and synaptosomes (**Figure 3.8H**) demonstrated substantial overlap (networks for lysates not shown). We noticed a particular cluster that appeared in synaptosomes (as well as in lysates, with some variation), consisting of *Akap5*, the cAMP-dependent protein kinase subunits *Prkacb*, *Prkar1b*, and *Prkar2b*, the protein kinase C subunits *Prkcb*, and *Prkcg*, and the calcineurin subunit *Ppp3ca* (**Figure 3.8H**).

The *Akap5* gene encodes the A-kinase anchoring protein 5 (Akap5), a postsynaptic scaffolding protein that anchors protein kinase A, protein kinase C, and calcineurin to the postsynaptic density via its interactions with MAGUK scaffolding proteins such as Sap97, or PSD-95 (Colledge et al., 2000; Robertson et al., 2009), which we also identified in our experiment; however, PSD-95 did not show >1.2-fold increase in either fraction, which is consistent with our previous observations (Koster et al., 2019) and the finding that PSD-95 is not a Ppt1 substrate (Yokoi et al., 2016). Due to its close interaction with glutamate receptors, Akap5 creates a signaling microdomain that links neurotransmitter receptor activity to signaling cascades, translating neuronal activity to long-lasting changes in the postsynaptic neuron (Sanderson and Dell’Acqua, 2011). Critically, Akap5 indirectly regulates CP-AMPAR incorporation during synaptic

scaling and, furthermore, the palmitoylation state of Akap5 is specifically implicated in the regulation of CP-AMPARs during LTP and is induced by seizure *in vivo* (Keith et al., 2012; Purkey et al., 2018; Sanderson et al., 2018). We validated that Akap5 is indeed excessively palmitoylated in the *Ppt1*$^{-/-}$ mice by APEGS assay in visual cortical synaptosomes (**Figure 3.8I**), although we generally do not detect changes in the total level of Akap5 in lysates or synaptosomes (**Figure 3.9A, B**). Adding to our previous *in vitro* findings (Koster et al., 2019), we also observe an increase in GluN2B palmitoylation at this time point (**Figure 3.9C**). In contrast, there was no significant increase in GluA1 or GluA2 palmitoylation in *Ppt1*$^{-/-}$ animals at this age (**Figure 3.9C**).

Figure 3.8. Palmitoyl-proteomics points to excessive palmitoylation of Akap5 and associated signaling proteins in the *Ppt1*$^{-/-}$ visual cortex.

(A) Volcano plot showing the log2 fold change in palmitoyl-protein expression from whole lysates of WT and *Ppt1*$^{-/-}$ visual cortex. N=6 visual cortices/group.
(B) Volcano plot showing the log2 fold change in palmitoyl-protein expression from synaptosomes of WT and *Ppt1*$^{-/-}$ visual cortex. N=6 visual cortices/group.
(C) Breakdown of the proportion of proteins exhibiting a 1.2-fold (red), 0.8-fold (blue), or no change in the abundance ratio *Ppt1*$^{-/-}$/WT (changes not necessarily significant) from visual cortical lysates (left) and synaptosomes (right).
(D) SynGO biological process (BP) gene count enrichment annotation of genes showing >1.2-fold increase in the palmitoyl-proteome of visual cortical whole lysates from *Ppt1*$^{-/-}$ mice.
(E) SynGO biological process (BP) gene count enrichment annotation of genes showing >1.2-fold increase in the palmitoyl-proteome of visual cortical synaptosomes from *Ppt1*$^{-/-}$ mice.
(F) Top 10 BP SynGO terms showing significant enrichment in visual cortical synaptosomes.
(G) Network analysis of synaptosome palmitoyl-proteome of genes annotated with the biological process SynGO term “process at the synapse.” Red circle denotes Akap5 pathway.
(H) Representative immunoblot of APEGS-processed synaptosomes probing for Akap5 from WT and *Ppt1*$^{-/-}$ visual cortices. N=3/group. *$p<0.05$ by t-test.

Figure 3.8. Palmitoyl-proteomics points to excessive palmitoylation of Akap5 and associated signaling proteins in the *Ppt1*$^{-/-}$ visual cortex.

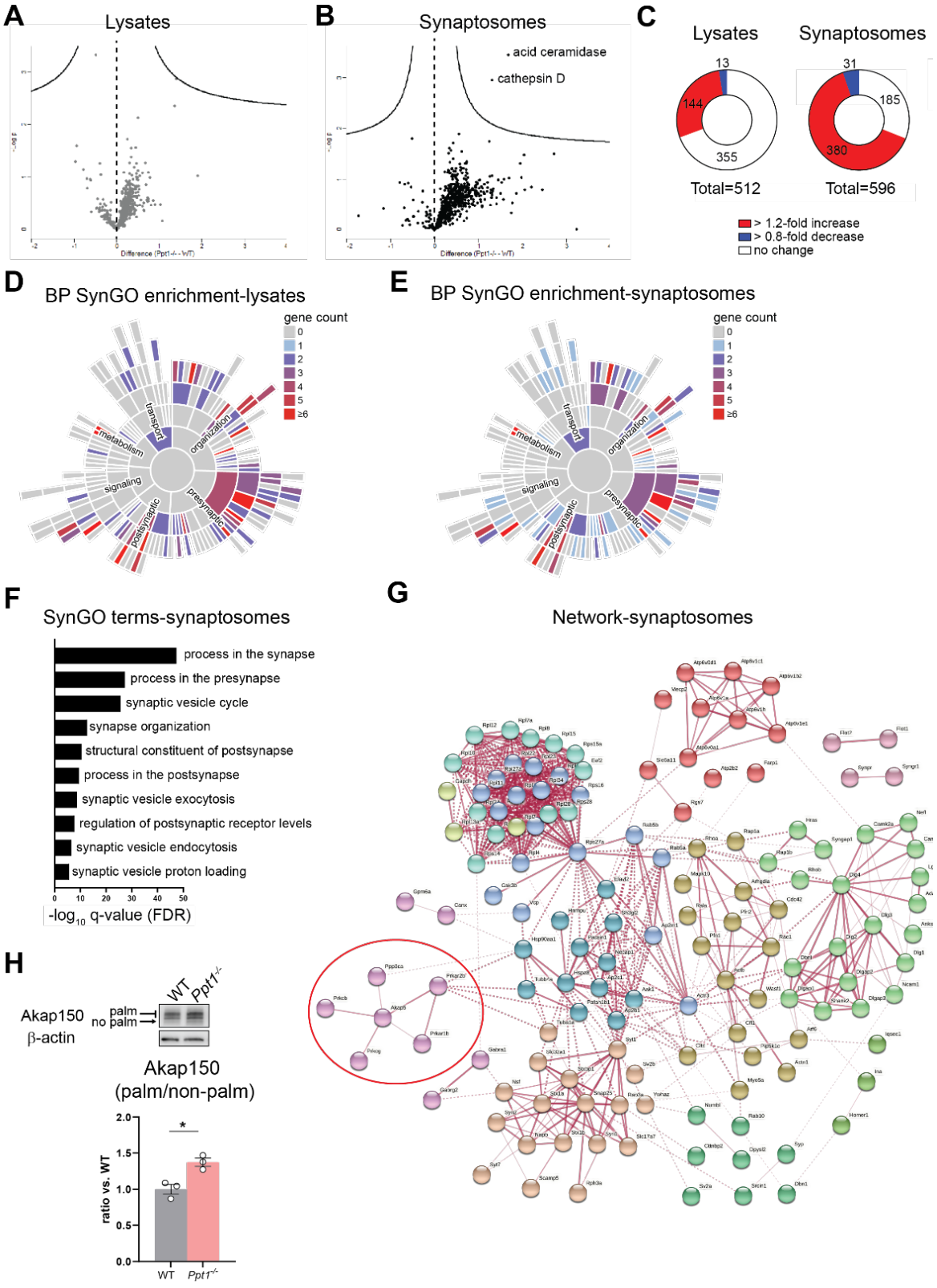

Figure 3.9. No change in developmental Akap5 levels in *Ppt1*$^{-/-}$ visual cortex

(A) Representative immunoblots (left) and quantification (right) of Akap5 levels in visual cortical lysates across age P11-P60.
(B) Representative immunoblots (left) and quantification (right) of Akap5 levels in visual cortical synaptosomes across age P11-P60.
(C) Representative blots of APEGS-processed synaptosomes (left) and quantification of the palmitoylated/non-palmitoylated ratio (right) of GluA1, GluA2, and GluN2B in visual cortical synaptosomes across age P11-P60. *$p<0.05$ by t-test.

Figure 3.9. No change in developmental Akap5 levels in *Ppt1*$^{-/-}$ visual cortex

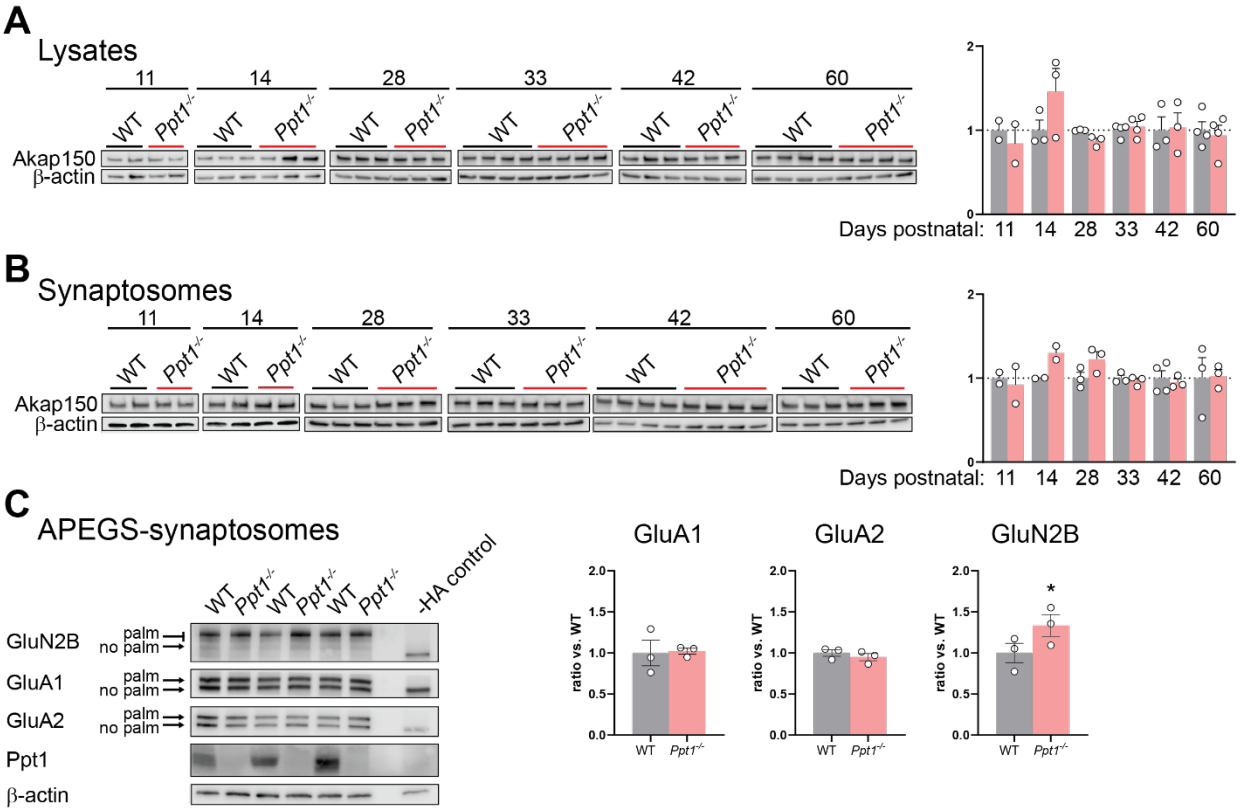

3.3.8. Nuclear factor of activated T-cells (NFAT) nuclear translocation is increased in *Ppt1*$^{-/-}$ neurons

Akap5, PKA and calcineurin represent a key postsynaptic signaling hub that regulates synaptic scaling of CP-AMPARs (Sanderson et al., 2018). Upon activation of Akap5-anchored calcineurin, it is free to dephosphorylate the downstream transcription factor nuclear factor activated in T cells NFAT (NFATc3)(Li et al., 2012; Murphy et al., 2019; Sanderson and Dell'Acqua, 2011), which influences the transcription of cytokines, including the proinflammatory molecule and inducer of synaptic scaling, tumor necrosis factor α (TNFα)(Canellada et al., 2006; Stellwagen and Malenka, 2006). Further, neuroinflammation is a key feature of CLN1 in humans and mouse models (Anderson et al., 2013; Macauley et al., 2014; Radke et al., 2015). Therefore, we reasoned that an overload of palmitoylated Akap5 leads to this CP-AMPAR-calcineurin-NFATc3 pathway bring sensitized in *Ppt1*$^{-/-}$ neurons.

To determine if overly palmitoylated Akap5 leads to hyperactivation of the CaN-NFAT downstream pathway in *Ppt1*$^{-/-}$ neurons, we performed a nuclear translocation assay as described in Murphy et al., (2014). Briefly, WT and *Ppt1*$^{-/-}$ neurons were exposed to an isotonic, high K^+ (50mM) Tyrode's solution to depolarize the culture and allowed to recover for a total of 15 minutes before fixation and immunolabeling for NFATc3-GFP (**Figure 3.10A**). The ratio of the integrated fluorescence signal of nuclear to somatic NFATc3-GFP was measured as a proxy for the activation of NFATc3 transcription. While high K^+-induced depolarization caused the nuclear translocation of NFATc3-GFP in both WT and *Ppt1*$^{-/-}$ neurons, the nuclear/soma ratio was significantly higher in *Ppt1*$^{-/-}$ cells, indicating a greater responsiveness to depolarization (**Figure 3.10B, C**). To test whether this effect resulted from an increased contribution of CP-AMPARs in *Ppt1*$^{-/-}$ neurons, we performed the same assay after induction of synaptic upscaling (TTX incubation) and treated a subset of neurons with NASPM during the depolarization period. We found that NASPM reduced NFATc3 nuclear translocation to a greater degree in *Ppt1*$^{-/-}$ cells

compared to WT (**Figure 3.10B, C**), although neither group reached non-depolarized levels, indicating there is contribution of other calcium sources, such as voltage-gated calcium channels, to NFAT activation that is not blocked by NASPM.

3.3.9. Dark rearing exacerbates neuroinflammation in the visual cortex of *Ppt1*$^{-/-}$ mice

Given NFATc3 activation is enhanced in *Ppt1*$^{-/-}$ neurons and induction of synaptic scaling *in vivo* by dark rearing leads to exacerbated disease symptoms in *Ppt1*$^{-/-}$ visual cortex, we reasoned that dark rearing would worsen the neuroinflammation characteristic of CLN1. To test this hypothesis, we stained WT, *Ppt1*$^{-/-}$, DR-WT, and DR-*Ppt1*$^{-/-}$ brains for the microglia marker, Iba1 (**Figure 3.10D**), and performed Sholl analysis (**Figure 3.10E**) on individual cells in the visual cortex (**Figure 3.10F**), since a classical sign of inflammatory microglial activation is a loss of ramification and ameboid shape (Gehrmann et al., 1995; Giulian, 1987). At P33, there were no differences between any group in either the number of intersections as a function of distance from the cell soma (**Figure 3.10G**) or in terms of the total number of intersections (**Figure 3.10H**). However, at P42, and especially P78 (with a trending decrease at P60), DR-*Ppt1*$^{-/-}$ mice exhibited significantly reduced microglial processes compared to WT, DR-WT, and *Ppt1*$^{-/-}$ animals (**Figure 3.10G, H**). These data demonstrate that dark rearing accelerates neuroinflammation in the visual cortex of *Ppt1*$^{-/-}$ mice.

Figure 3.10. Sensitization of NFAT nuclear translocation in *Ppt1*$^{-/-}$ neurons and exacerbated neuroinflammation in dark reared *Ppt1*$^{-/-}$ visual cortex.

(A) Schematic representation of the experimental design for depolarization (K^+) induction of NFAT activity (nuclear translocation), as in Murphy et al., 2014.
(B) Representative images of NFAT localization from WT and *Ppt1*$^{-/-}$ neurons in response to either sham or K^+-induced depolarization. Outline of the nucleus (saturated DAPI signal) is drawn in each image. Scale bar= 20μm.
(C) Quantification of the nucleus/soma ratio of NFAT fluorescence in WT and *Ppt1*$^{-/-}$ neurons in sham depolarization, K^+ depolarization, and K^+ depolarization + NASPM (10μM) conditions. *p < 0.05, ***p < 0.001, ****p < 0.0001.
(D) Representative low magnification images of Iba1 immunostaining in the visual cortex of WT and *Ppt1*$^{-/-}$ visual cortex at P78. Scale bar=100μm
(E) Representative thresholded microglia image and Scholl analysis overlay.
(F) Representative high magnification images of Iba1 immunostaining for visual cortical (layer 2/3) microglia in WT, *Ppt1*$^{-/-}$, DR-WT, and DR-*Ppt1*$^{-/-}$ mice across age (P28-P78). Scale bar=20μm
(G) Quantification of microglia branching by Sholl analysis in WT, *Ppt1*$^{-/-}$, DR-WT, and DR-*Ppt1*$^{-/-}$ mice across age, where the number of intersections (y-axis) are averaged across cells at the specified distance from the soma (x-axis). N=27-60cells, 2-3 animals per group. Number of cells/animals for each group is listed in panel (H).
(H) Quantification of the total number of intersections for each group of animals across age. Number of cells/animals in each group are listed on the graph. *p < 0.05, **p<0.01, ****p < 0.0001.

Figure 3.10. Sensitization of NFAT nuclear translocation in *Ppt1*$^{-/-}$ neurons and exacerbated neuroinflammation in dark reared *Ppt1*$^{-/-}$ visual cortex.

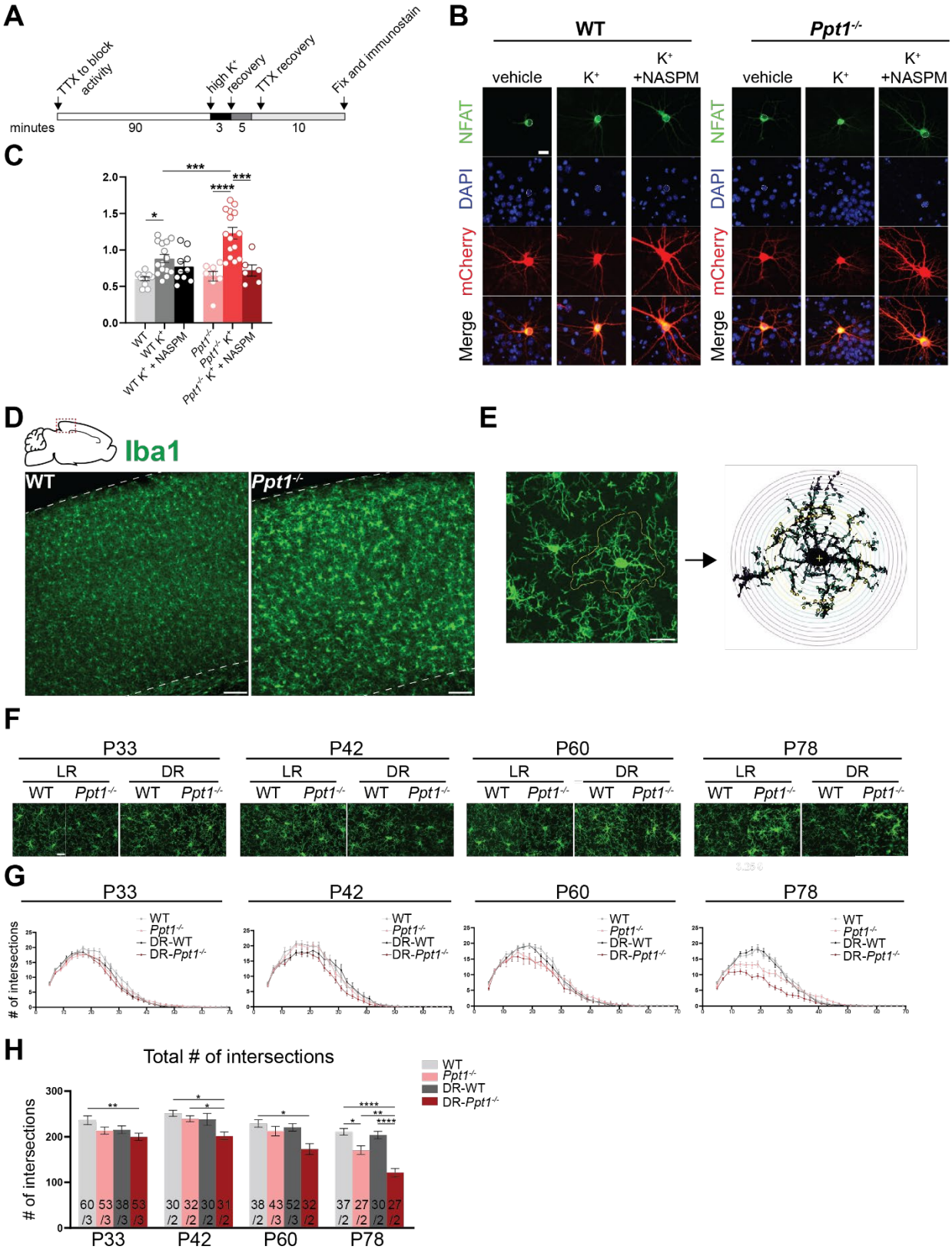

3.4. Discussion

We demonstrate herein that synaptic upscaling is exaggerated in *Ppt1*$^{-/-}$ neurons and that this contributes to disrupted excitatory synapse formation in the visual cortex of developing mice. In addition to biochemical and immunofluorescence data showing a heightened membrane incorporation of GluA1 in up scaled *Ppt1*$^{-/-}$ neurons, calcium imaging data showed an increased contribution of NASPM-sensitive, CP-AMPARs to spontaneous activity in dissociated *Ppt1*$^{-/-}$ neurons (**Figures 3.2-4**). Synaptic upscaling was associated with an increase in GluA1 palmitoylation solely in *Ppt1*$^{-/-}$ neurons (**Figure 3.5**). Dark rearing *Ppt1*$^{-/-}$ animals exacerbated CLN1 disease pathology (**Figure 3.7**). Palmitoyl-proteomic profiling revealed a widespread over-palmitoylation of synaptic proteins in the *Ppt1*$^{-/-}$ visual cortex at a young age (~1.5 months) but pointed to the Akap5 scaffold and associated signaling molecules as collectively showing increases in the palmitoylated fraction (**Figures 3.8**). Correspondingly, the NFAT transcriptional pathway was sensitized in *Ppt1*$^{-/-}$ neurons in response to stimulated neuronal activity and *in vivo* induction of synaptic scaling exacerbated microgliosis (**Figure 3.10**). Our results indicate loss of lysosomal depalmitoylation disrupts proteostasis CP-AMPAR and Akap5, thereby exaggerating synaptic upscaling and leading to neuroinflammation.

Interestingly, although we did not pursue it in detail here, our biochemical and immunolabeling assays show that surface expression of GluA1 is not reduced in *Ppt1*$^{-/-}$ neurons in response to bicuculline treatment (**Figure 3.2**), suggesting a failure to scale down synapses.

3.4.1. Proposed mechanisms of disrupted synaptic upscaling in *Ppt1*$^{-/-}$ neurons.

One of the major findings of the current study is that synaptic upscaling of CP-AMPARs is exaggerated in *Ppt1*$^{-/-}$ neurons. There are two primary explanations; 1) over-palmitoylation of GluA1 itself causes its increased surface expression during upscaling or 2) overly palmitoylated Akap5 disrupts the physiological turnover of CP-AMPARs, resulting in their surface retention during scaling.

An initial study describing the phenomenon of synaptic scaling by O'Brien and colleagues showed that the synaptic accumulation of GluA1-containing AMPARs was due, in part, from an increased half-life of GluA1 protein (O'Brien et al., 1998). Gorenberg et al., recently reported that the extracellular cysteine, C323, is likely to be the site of depalmitoylation by Ppt1 (Gorenberg et al., 2020). The authors of this study speculate that the C323 palmitoylation site represents a latent signal, whereby unmodified GluA1 is palmitoylated at C323 during trafficking to the synapse but forms a disulfide bond with C75 upon exposure to the synaptic cleft. Though it is not yet known how palmitoylation at this site affects GluA1 trafficking, it is possible that the excessive palmitoylation of newly synthesized GluA1 during upscaling due to lack of depalmitoylation by Ppt1 leads to its increased retention at the membrane. It is also established that palmitoylation influences the turnover of specific proteins by inhibiting their ubiquitination (Linder and Deschenes, 2007), either directly or by limiting their endocytosis and exposure to ubiquitination enzymes prior to lysosomal degradation. GluA1 ubiquitination increases during synaptic downscaling (Jewett et al., 2015; Scudder et al., 2014). Consequently, one possibility is that increased GluA1 palmitoylation in upscaled *Ppt1*$^{-/-}$ neurons reduces its degradation and promotes a synaptic accumulation of CP-AMPARs.

Alternatively, the aberrant trafficking of CP-AMPARs during synaptic scaling may not arise from palmitoylation of GluA1 directly, as we also observe excessive palmitoylation of Akap5 and its associated signaling molecules. A series of elegant experiments directly implicates Akap5 in the regulation of CP-AMPARs during synaptic scaling (Sanderson et al., 2018). These authors show that palmitoylated Akap5 limits the basal synaptic incorporation of CP-AMPARs but is required for their postsynaptic insertion during LTP (Purkey et al., 2018). Further, Akap5 requires depalmitoylation for its removal from the postsynapse and undergoes ubiquitination to downregulate GluA1-containing AMPARs during chemical LTD (Cheng et al., 2020; Woolfrey et al., 2018). Therefore, we anticipate that Akap5 undergoes depalmitoylation-dependent

degradation (Cheng et al., 2020) that is diminished in *Ppt1*$^{-/-}$ neurons and that overly-palmitoylated Akap5 harbors an enlarged perisynaptic pool of CP-AMPARs (either at the extrasynapse or dendritic endosomes) that is mobilized during synaptic upscaling.

Lastly, we demonstrate that the hyperpalmitoylation of Akap5 leads to a sensitization of the NFAT transcriptional program in *Ppt1*$^{-/-}$ neurons (**Figure 3.10**). Not only does this likely represent a link to the induction of neuroinflammation that is a predominant feature of CLN1 (Anderson et al., 2013; Radke et al., 2015) and CLN1 mouse models (Jalanko et al., 2005; Kielar et al., 2007; Macauley et al., 2009, 2011, 2014), but a target of NFAT in neural cells is TNFα (Canellada et al., 2006). TNFα is required for synaptic scaling (Stellwagen and Malenka, 2006), acting as a permissive signal to maintain a plastic state that allows for scaling of postsynaptic responses (Steinmetz and Turrigiano, 2010). Furthermore, the calcineurin-NFAT pathway mediates synaptic scaling through the turnover of CP-AMPARs (Kim and Ziff, 2014). Therefore, it is plausible that mis-localization of Akap5 or impaired interactions with calcineurin drive over-activation of NFAT and transcription of TNFα, permitting an exaggerated scaling response of CP-AMPARs in the *Ppt1*$^{-/-}$ brain. Therefore, several related mechanisms may conspire to drive exaggeration of CP-AMPAR incorporation during synaptic upscaling in *Ppt1*$^{-/-}$ neurons.

3.4.2. Ppt1 regulates developmental excitatory synapse formation: Implications for CLN1 progression and therapeutic intervention.

The function of Ppt1 in neuronal circuit function remains incompletely characterized and understanding its role at the synapse is of critical importance to identifying and eventually correcting pathophysiology in CLN1. Typically, sensory cortical networks desynchronize during development, likely expanding the information encoding capability of the neuronal network (Golshani et al., 2009; He et al., 2018; Rochefort et al., 2009). In our previous study, we show

that a developmental maturation of NMDA receptors is disrupted in the visual cortex, favoring the synaptic incorporation of GluN2B, which is associated with an increase in the neuronal plasticity threshold (Abraham, 2008; Yashiro and Philpot, 2008). The current study adds another layer of synaptic dysregulation and shows that synaptic upscaling of CP-AMPARs is exaggerated in *Ppt1*$^{-/-}$ visual cortical neurons. Interestingly, in a computational study, artificial deafferentiation of a population of synthetic neurons drives a pathological synchrony in their activity due to synaptic scaling (Fröhlich et al., 2008). Therefore, the disruption of these molecular synaptic plasticity mechanisms likely contributes to the network hypersynchrony we observe in the *Ppt1*$^{-/-}$ visual cortex (**Figure 3.6**). Whether this manifests in *Ppt1*$^{-/-}$ visual cortex as a failure to desynchronize during development, or a resynchronization because of disrupted plasticity is not clear. Nevertheless, we postulate that this pathological network activity eventually contributes to seizure activity in *Ppt1*$^{-/-}$ mice. Indeed, this failure to desynchronize is observed in another neurodevelopmental disorder associated with seizures, Fragile X syndrome (Gonçalves et al., 2013). Taken together, we propose a model by which disrupted NMDA and AMPA receptor trafficking underlies network desynchronization, driving excitotoxic cell death and synaptic scaling of the afferent brain region. A similar framework has been proposed to contribute to the pathogenesis of Alzheimer disease (Small, 2008). In this way, sequential scaling-synchronization cycles leads to a spreading neurodegeneration in parallel with seizure activity, as observed in CLN1.

Intervention at the molecular level to improve this synchronous oscillatory activity, which has been recently performed by targeting NMDA receptors in models of Alzheimer disease (Hanson et al., 2020), may prove beneficial in CLN1. On the other hand, if the consequence of Ppt1 mutation is a loss of developmental desynchronization, perhaps a therapeutic strategy targeted at the circuit level, such as deep brain stimulation or emerging technologies that can correct network activity (Rowan et al., 2014; Tye, 2014) might prove beneficial. At minimum, our

findings related to the dysregulation of CP-AMPARs and GluA1 in particular lend credence to the recent clinical use of Perampanel as a second line treatment for CLN1 (Augustine et al., 2021).

In parallel, our data implicate the hyperpalmitoylation of Akap5 in the pathogenesis of the *Ppt1*$^{-/-}$ brain through its regulation of CP-AMPAR trafficking and downstream signaling through the calcineurin-NFAT axis. This finding links aberrant calcium activity to a neuroinflammatory cascade and gliosis in CLN1 for the first time (**Figure 3.10**). Further, Calcineurin-NFAT activity represents a new therapeutic target in CLN1 that has a history of being inhibited in other conditions requiring immunosuppression with FDA-approved drugs such as FK506 and cyclosporin A. Future studies focused on testing the efficacy of these (or other) calcineurin-directed therapeutics will be of great interest to the CLN1 field and patient population.

CHAPTER 3 CITED LITERATURE

Abraham, W.C. (2008). Metaplasticity: tuning synapses and networks for plasticity. Nat Rev Neurosci *9*, 387–387.

Ahtiainen, L., Diggelen, O.P., Jalanko, A., and Kopra, O. (2003). Palmitoyl protein thioesterase 1 is targeted to the axons in neurons. Journal of Comparative Neurology *455*.

Ahtiainen, L., Luiro, K., Kauppi, M., Tyynelä, J., Kopra, O., and Jalanko, A. (2006). Palmitoyl protein thioesterase 1 (PPT1) deficiency causes endocytic defects connected to abnormal saposin processing. Experimental Cell Research *312*, 1540–1553.

Anderson, G.W., Goebel, H.H., and Simonati, A. (2013). Human pathology in NCL. Biochimica Et Biophysica Acta Bba - Mol Basis Dis *1832*, 1807–1826.

Atiskova, Y., Bartsch, S., Danyukova, T., Becker, E., Hagel, C., Storch, S., and Bartsch, U. (2019). Mice deficient in the lysosomal enzyme palmitoyl-protein thioesterase 1 (PPT1) display a complex retinal phenotype. Sci Rep-Uk *9*, 14185.

Augustine, E.F., Adams, H.R., Reyes, E. de los, Drago, K., Frazier, M., Guelbert, N., Laine, M., Levin, T., Mink, J.W., Nickel, M., et al. (2021). Management of CLN1 Disease: International Clinical Consensus. Pediatr Neurol *120*, 38–51.

Barnes, S.J., Franzoni, E., Jacobsen, R.I., Erdelyi, F., Szabo, G., Clopath, C., Keller, G.B., and Keck, T. (2017). Deprivation-Induced Homeostatic Spine Scaling In Vivo Is Localized to Dendritic Branches that Have Undergone Recent Spine Loss. Neuron *96*, 871-882.e5.

Blackman, M.P., Djukic, B., Nelson, S.B., and Turrigiano, G.G. (2012). A Critical and Cell-Autonomous Role for MeCP2 in Synaptic Scaling Up. J Neurosci *32*, 13529–13536.

Burnashev, N., Monyer, H., Seeburg, P.H., and Sakmann, B. (1992). Divalent ion permeability of AMPA receptor channels is dominated by the edited form of a single subunit. Neuron *8*, 189–198.

Camp, L., and Hofmann, S. (1993). Purification and properties of a palmitoyl-protein thioesterase that cleaves palmitate from H-Ras. The Journal of Biological Chemistry *268*.

Canellada, A., Cano, E., Sánchez-Ruiloba, L., Zafra, F., and Redondo, J.M. (2006). Calcium-dependent expression of TNF-alpha in neural cells is mediated by the calcineurin/NFAT pathway. Mol Cell Neurosci *31*, 692–701.

Cantu, D.A., Wang, B., Gongwer, M.W., He, C.X., Goel, A., Suresh, A., Kourdougli, N., Arroyo, E.D., Zeiger, W., and Portera-Cailliau, C. (2020). EZcalcium: Open-Source Toolbox for Analysis of Calcium Imaging Data. Front Neural Circuit *14*, 25.

Chandra, G., Bagh, M.B., Peng, S., Saha, A., Sarkar, C., Moralle, M., Zhang, Z., and Mukherjee, A.B. (2015). Cln1 gene disruption in mice reveals a common pathogenic link between two of the most lethal childhood neurodegenerative lysosomal storage disorders. Hum Mol Genet *24*, 5416–5432.

Cheng, W., Siedlecki-Wullich, D., Català-Solsona, J., Fábregas, C., Fadó, R., Casals, N., Solé, M., Unzeta, M., Saura, C.A., Rodríguez-Alvarez, J., et al. (2020). Proteasomal-mediated degradation of AKAP150 accompanies AMPAR endocytosis during cLTD. Eneuro *7*, ENEURO.0218-19.2020.

Colledge, M., Dean, R.A., Scott, G.K., Langeberg, L.K., Huganir, R.L., and Scott, J.D. (2000). Targeting of PKA to Glutamate Receptors through a MAGUK-AKAP Complex. Neuron *27*, 107–119.

Desai, N.S., Cudmore, R.H., Nelson, S.B., and Turrigiano, G.G. (2002). Critical periods for experience-dependent synaptic scaling in visual cortex. Nature Neuroscience *5*.

Diering, G.H., Gustina, A.S., and Huganir, R.L. (2014). PKA-GluA1 coupling via AKAP5 controls AMPA receptor phosphorylation and cell-surface targeting during bidirectional homeostatic plasticity. Neuron *84*, 790–805.

Drisdel, R.C., and Green, W.N. (2004a). Labeling and quantifying sites of protein palmitoylation. BioTechniques *36*, 276–285.

Drisdel, R.C., and Green, W.N. (2004b). Labeling and quantifying sites of protein palmitoylation. Biotechniques *36*, 276–285.

Ehlers, M. (2000). Reinsertion or degradation of AMPA receptors determined by activity-dependent endocytic sorting. Neuron *28*.

Fröhlich, F., Bazhenov, M., and Sejnowski, T.J. (2008). Pathological Effect of Homeostatic Synaptic Scaling on Network Dynamics in Diseases of the Cortex. J Neurosci *28*, 1709–1720.

Fukata, Y., and Fukata, M. (2010). Protein palmitoylation in neuronal development and synaptic plasticity. Nature Reviews Neuroscience *11*.

Gehrmann, J., Matsumoto, Y., and Kreutzberg, G.W. (1995). Microglia: Intrinsic immuneffector cell of the brain. Brain Res Rev *20*, 269–287.

Gilbert, J., Shu, S., Yang, X., Lu, Y., Zhu, L.-Q., and Man, H.-Y. (2017). Erratum to: β-Amyloid triggers aberrant over-scaling of homeostatic synaptic plasticity. Acta Neuropathologica Commun *5*, 20.

Giulian, D. (1987). Ameboid microglia as effectors of inflammation in the central nervous system. J Neurosci Res *18*, 155–171.

Goel, A., and Lee, H.-K. (2007). Persistence of experience-induced homeostatic synaptic plasticity through adulthood in superficial layers of mouse visual cortex. J Neurosci Official J Soc Neurosci *27*, 6692–6700.

Goel, A., Jiang, B., Xu, L.W., Song, L., Kirkwood, A., and Lee, H.-K. (2006). Cross-modal regulation of synaptic AMPA receptors in primary sensory cortices by visual experience. Nat Neurosci *9*, 1001–1003.

Goel, A., Xu, L.W., Snyder, K.P., Song, L., Goenaga-Vazquez, Y., Megill, A., Takamiya, K., Huganir, R.L., and Lee, H.-K. (2011). Phosphorylation of AMPA receptors is required for sensory deprivation-induced homeostatic synaptic plasticity. Plos One *6*, e18264.

Golshani, P., Gonçalves, J.T., Khoshkhoo, S., Mostany, R., Smirnakis, S., and Portera-Cailliau, C. (2009). Internally Mediated Developmental Desynchronization of Neocortical Network Activity. J Neurosci *29*, 10890–10899.

Gonçalves, J.T., Anstey, J.E., Golshani, P., and Portera-Cailliau, C. (2013). Circuit level defects in the developing neocortex of Fragile X mice. Nat Neurosci *16*, 903–909.

Gordon, J., and Stryker, M. (1996). Experience-dependent plasticity of binocular responses in the primary visual cortex of the mouse. The Journal of Neuroscience : The Official Journal of the Society for Neuroscience *16*.

Gorenberg, E.L., Zhao, H.R., Bishai, J., Chou, V., Wirak, G.S., Lam, T.T., and Chandra, S.S. (2020). Identification of palmitoyl protein thioesterase 1 substrates defines roles for synaptic depalmitoylation. Biorxiv 2020.05.02.074302.

Gupta, P., Soyombo, A., Atashband, A., Wisniewski, K., Shelton, J., Richardson, J., Hammer, R., and Hofmann, S. (2001). Disruption of PPT1 or PPT2 causes neuronal ceroid lipofuscinosis in knockout mice. Proceedings of the National Academy of Sciences *98*.

Haltia, M. (2003). The Neuronal Ceroid-Lipofuscinoses. J Neuropathology Exp Neurology *62*, 1–13.

Hanson, J.E., Ma, K., Elstrott, J., Weber, M., Saillet, S., Khan, A.S., Simms, J., Liu, B., Kim, T.A., Yu, G.-Q., et al. (2020). GluN2A NMDA Receptor Enhancement Improves Brain Oscillations, Synchrony, and Cognitive Functions in Dravet Syndrome and Alzheimer's Disease Models. Cell Reports *30*, 381-396.e4.

He, C.X., Arroyo, E.D., Cantu, D.A., Goel, A., and Portera-Cailliau, C. (2018). A Versatile Method for Viral Transfection of Calcium Indicators in the Neonatal Mouse Brain. Front Neural Circuit *12*, 56.

Holtmaat, A., Bonhoeffer, T., Chow, D.K., Chuckowree, J., Paola, V.D., Hofer, S.B., Hübener, M., Keck, T., Knott, G., Lee, W.-C.A., et al. (2009). Long-term, high-resolution imaging in the mouse neocortex through a chronic cranial window. Nat Protoc *4*, 1128–1144.

Jalanko, A., Vesa, J., Manninen, T., Schantz, C. von, Minye, H., Fabritius, A.-L., Salonen, T., Rapola, J., Gentile, M., Kopra, O., et al. (2005). Mice with Ppt1Deltaex4 mutation replicate the INCL phenotype and show an inflammation-associated loss of interneurons. Neurobiol Dis *18*, 226–241.

Jewett, K.A., Zhu, J., and Tsai, N. (2015). The tumor suppressor p53 guides GluA1 homeostasis through Nedd4-2 during chronic elevation of neuronal activity. J Neurochem *135*, 226–233.

Ju, W., Morishita, W., Tsui, J., Gaietta, G., Deerinck, T.J., Adams, S.R., Garner, C.C., Tsien, R.Y., Ellisman, M.H., and Malenka, R.C. (2004). Activity-dependent regulation of dendritic synthesis and trafficking of AMPA receptors. Nat Neurosci *7*, 244–253.

Kanadome, T., Yokoi, N., Fukata, Y., and Fukata, M. (2019). Systematic Screening of Depalmitoylating Enzymes and Evaluation of Their Activities by the Acyl-PEGyl Exchange Gel-Shift (APEGS) Assay. Methods Mol Biology Clifton N J *2009*, 83–98.

Katz, L.C., and Shatz, C.J. (1996). Synaptic Activity and the Construction of Cortical Circuits. Science *274*, 1133–1138.

Keck, T., Toyoizumi, T., Chen, L., Doiron, B., Feldman, D.E., Fox, K., Gerstner, W., Haydon, P.G., Hübener, M., Lee, H.-K., et al. (2017). Integrating Hebbian and homeostatic plasticity: the current state of the field and future research directions. Philosophical Transactions Royal Soc B Biological Sci *372*, 20160158.

Keith, D.J., Sanderson, J.L., Gibson, E.S., Woolfrey, K.M., Robertson, H.R., Olszewski, K., Kang, R., El-Husseini, A., and Dell'acqua, M.L. (2012). Palmitoylation of A-kinase anchoring protein 79/150 regulates dendritic endosomal targeting and synaptic plasticity mechanisms. J Neurosci Official J Soc Neurosci *32*, 7119–7136.

Kielar, C., Maddox, L., Bible, E., Pontikis, C.C., Macauley, S.L., Griffey, M.A., Wong, M., Sands, M.S., and Cooper, J.D. (2007). Successive neuron loss in the thalamus and cortex in a mouse model of infantile neuronal ceroid lipofuscinosis. Neurobiology of Disease *25*, 150–162.

Kim, S., and Ziff, E.B. (2014). Calcineurin Mediates Synaptic Scaling Via Synaptic Trafficking of Ca2+-Permeable AMPA Receptors. Plos Biol *12*, e1001900.

Koopmans, F., Nierop, P. van, Andres-Alonso, M., Byrnes, A., Cijsouw, T., Coba, M.P., Cornelisse, L.N., Farrell, R.J., Goldschmidt, H.L., Howrigan, D.P., et al. (2019). SynGO: An Evidence-Based, Expert-Curated Knowledge Base for the Synapse. Neuron *103*, 217-234.e4.

Kopec, C.D., Li, B., Wei, W., Boehm, J., and Malinow, R. (2006). Glutamate Receptor Exocytosis and Spine Enlargement during Chemically Induced Long-Term Potentiation. J Neurosci *26*, 2000–2009.

Koster, K.P., Francesconi, W., Berton, F., Alahmadi, S., Srinivas, R., and Yoshii, A. (2019). Developmental NMDA receptor dysregulation in the infantile neuronal ceroid lipofuscinosis mouse model. ELife *8*.

Lee, H.-K. (2012). Ca2+-permeable AMPA receptors in homeostatic synaptic plasticity. Front Mol Neurosci *5*, 17.

Lehtovirta, M., Kyttälä, A., Eskelinen, E., Hess, M., Heinonen, O., and Jalanko, A. (2001). Palmitoyl protein thioesterase (PPT) localizes into synaptosomes and synaptic vesicles in neurons: implications for infantile neuronal ceroid lipofuscinosis (INCL). Human Molecular Genetics *10*.

Li, H., Pink, M.D., Murphy, J.G., Stein, A., Dell'Acqua, M.L., and Hogan, P.G. (2012). Balanced interactions of calcineurin with AKAP79 regulate Ca2+–calcineurin–NFAT signaling. Nat Struct Mol Biol *19*, 337–345.

Linder, M.E., and Deschenes, R.J. (2007). Palmitoylation: policing protein stability and traffic. Nature Reviews. Molecular Cell Biology *8*, 74–84.

Lyly, A., Schantz, C. von, Salonen, T., Kopra, O., Saarela, J., Jauhiainen, M., Kyttälä, A., and Jalanko, A. (2007). Glycosylation, transport, and complex formation of palmitoyl protein thioesterase 1 (PPT1)--distinct characteristics in neurons. BMC Cell Biology *8*, 22.

Macauley, S.L., Wozniak, D.F., Kielar, C., Tan, Y., Cooper, J.D., and Sands, M.S. (2009). Cerebellar pathology and motor deficits in the palmitoyl protein thioesterase 1-deficient mouse. Exp Neurol *217*, 124–135.

Macauley, S.L., Pekny, M., and Sands, M.S. (2011). The role of attenuated astrocyte activation in infantile neuronal ceroid lipofuscinosis. J Neurosci Official J Soc Neurosci *31*, 15575–15585.

Macauley, S.L., Wong, A.M.S., Shyng, C., Augner, D.P., Dearborn, J.T., Pearse, Y., Roberts, M.S., Fowler, S.C., Cooper, J.D., Watterson, D.M., et al. (2014). An Anti-Neuroinflammatory That Targets Dysregulated Glia Enhances the Efficacy of CNS-Directed Gene Therapy in Murine Infantile Neuronal Ceroid Lipofuscinosis. J Neurosci *34*, 13077–13082.

Murphy, J.G., Crosby, K.C., Dittmer, P.J., Sather, W.A., and Dell'Acqua, M.L. (2019). AKAP79/150 recruits the transcription factor NFAT to regulate signaling to the nucleus by neuronal L-type Ca 2+ channels. Mol Biol Cell *30*, 1743–1756.

Nguyen TTA, Li W, Park TJ, Gong LW, & Cologna SM (2019) Investigating Phosphorylation Patterns of the Ion Channel TRPM7 Using Multiple Extraction and Enrichment Techniques Reveals New Phosphosites. *J Am Soc Mass Spectrom* 30(8):1359-1367

Nita, D.A., Mole, S.E., and Minassian, B.A. (2016). Neuronal ceroid lipofuscinoses. Epileptic Disorders *18*.

O'Brien, R.J., Kamboj, S., Ehlers, M.D., Rosen, K.R., Fischbach, G.D., and Huganir, R.L. (1998). Activity-dependent modulation of synaptic AMPA receptor accumulation. Neuron *21*, 1067–1078.

Philpot, B., Sekhar, A., Shouval, H., and Bear, M. (2001). Visual experience and deprivation bidirectionally modify the composition and function of NMDA receptors in visual cortex. Neuron *29*.

Pratt, K.G., Zimmerman, E.C., Cook, D.G., and Sullivan, J.M. (2011). Presenilin 1 regulates homeostatic synaptic scaling through Akt signaling. Nat Neurosci *14*, 1112–1114.

Purkey, A.M., Woolfrey, K.M., Crosby, K.C., Stich, D.G., Chick, W.S., Aoto, J., and Dell'Acqua, M.L. (2018). AKAP150 Palmitoylation Regulates Synaptic Incorporation of Ca2+-Permeable AMPA Receptors to Control LTP. Cell Reports *25*, 974-987.e4.

Qiu, Z., Sylwestrak, E.L., Lieberman, D.N., Zhang, Y., Liu, X.-Y., and Ghosh, A. (2012). The Rett Syndrome Protein MeCP2 Regulates Synaptic Scaling. J Neurosci *32*, 989–994.

Radke, J., Stenzel, W., and Goebel, H.H. (2015). Human NCL Neuropathology. Biochimica Et Biophysica Acta Bba - Mol Basis Dis *1852*, 2262–2266.

Rittenhouse, C.D., Shouval, H.Z., Paradiso, M.A., and Bear, M.F. (1999). Monocular deprivation induces homosynaptic long-term depression in visual cortex. Nature *397*, 347–350.

Robertson, H.R., Gibson, E.S., Benke, T.A., and Dell'Acqua, M.L. (2009). Regulation of Postsynaptic Structure and Function by an A-Kinase Anchoring Protein–Membrane-Associated Guanylate Kinase Scaffolding Complex. J Neurosci *29*, 7929–7943.

Rochefort, N.L., Garaschuk, O., Milos, R.-I., Narushima, M., Marandi, N., Pichler, B., Kovalchuk, Y., and Konnerth, A. (2009). Sparsification of neuronal activity in the visual cortex at eye-opening. Proc National Acad Sci *106*, 15049–15054.

Roth, A.F., Wan, J., Green, W.N., Yates, J.R., and Davis, N.G. (2006). Proteomic identification of palmitoylated proteins. Methods *40*, 135–142.

Rowan, M.S., Neymotin, S.A., and Lytton, W.W. (2014). Electrostimulation to reduce synaptic scaling driven progression of Alzheimer's disease. Front Comput Neurosc *8*, 39.

Sanderson, J.L., and Dell'Acqua, M.L. (2011). AKAP Signaling Complexes in Regulation of Excitatory Synaptic Plasticity. Neurosci *17*, 321–336.

Sanderson, J.L., Scott, J.D., and Dell'Acqua, M.L. (2018). Control of Homeostatic Synaptic Plasticity by AKAP-Anchored Kinase and Phosphatase Regulation of Ca 2+ -Permeable AMPA Receptors. J Neurosci *38*, 2863–2876.

Sapir, T., Segal, M., Grigoryan, G., Hansson, K.M., James, P., Segal, M., and Reiner, O. (2019). The Interactome of Palmitoyl-Protein Thioesterase 1 (PPT1) Affects Neuronal Morphology and Function. Frontiers in Cellular Neuroscience *13*, 92.

Scudder, S.L., Goo, M.S., Cartier, A.E., Molteni, A., Schwarz, L.A., Wright, R., and Patrick, G.N. (2014). Synaptic Strength Is Bidirectionally Controlled by Opposing Activity-Dependent Regulation of Nedd4-1 and USP8. J Neurosci *34*, 16637–16649.

Shepherd, J.D., Rumbaugh, G., Wu, J., Chowdhury, S., Plath, N., Kuhl, D., Huganir, R.L., and Worley, P.F. (2006). Arc/Arg3.1 mediates homeostatic synaptic scaling of AMPA receptors. Neuron *52*.

Sleat, D.E., Tannous, A., Sohar, I., Wiseman, J.A., Zheng, H., Qian, M., Zhao, C., Xin, W., Barone, R., Sims, K.B., et al. (2017). Proteomic Analysis of Brain and Cerebrospinal Fluid from the Three Major Forms of Neuronal Ceroid Lipofuscinosis Reveals Potential Biomarkers. J Proteome Res *16*, 3787–3804.

Small, D.H. (2008). Network dysfunction in Alzheimer's disease: does synaptic scaling drive disease progression? Trends Mol Med *14*, 103–108.

Steinmetz, C.C., and Turrigiano, G.G. (2010). Tumor Necrosis Factor-α Signaling Maintains the Ability of Cortical Synapses to Express Synaptic Scaling. J Neurosci *30*, 14685–14690.

Stellwagen, D., and Malenka, R.C. (2006). Synaptic scaling mediated by glial TNF-alpha. Nature *440*, 1054–1059.

Styr, B., and Slutsky, I. (2018). Imbalance between firing homeostasis and synaptic plasticity drives early-phase Alzheimer's disease. Nat Neurosci *21*, 463–473.

Thiagarajan, T.C., Lindskog, M., and Tsien, R.W. (2005). Adaptation to Synaptic Inactivity in Hippocampal Neurons. Neuron *47*, 725–737.

Turrigiano, G.G. (1999). Homeostatic plasticity in neuronal networks: the more things change, the more they stay the same. Trends Neurosci *22*, 221–227.

Turrigiano, G.G. (2017). The dialectic of Hebb and homeostasis. Philosophical Transactions Royal Soc B Biological Sci *372*, 20160258.

Turrigiano, G.G., and Nelson, S.B. (2004). Homeostatic plasticity in the developing nervous system. Nature Reviews Neuroscience *5*.

Turrigiano, G., Leslie, K., Desai, N., Rutherford, L., and Nelson, S. (1998). Activity-dependent scaling of quantal amplitude in neocortical neurons. *391*.

Tye, K.M. (2014). Neural Circuit Reprogramming: A New Paradigm for Treating Neuropsychiatric Disease? Neuron *83*, 1259–1261.

Verkruyse, L., and Hofmann, S. (1996). Lysosomal targeting of palmitoyl-protein thioesterase. The Journal of Biological Chemistry *271*.

Vesa, J., Hellsten, E., Verkruyse, L., Camp, L., Rapola, J., Santavuori, P., Hofmann, S., and Peltonen, L. (1995). Mutations in the palmitoyl protein thioesterase gene causing infantile neuronal ceroid lipofuscinosis. Nature *376*.

Wan, J., Roth, A.F., Bailey, A.O., and Davis, N.G. (2007). Palmitoylated proteins: purification and identification. Nat Protoc *2*, 1573–1584.

Wenthold, R., Petralia, R., J, I.B., and Niedzielski, A. (1996). Evidence for multiple AMPA receptor complexes in hippocampal CA1/CA2 neurons. J Neurosci *16*, 1982–1989.

Woolfrey, K.M., O'Leary, H., Goodell, D.J., Robertson, H.R., Horne, E.A., Coultrap, S.J., Dell'Acqua, M.L., and Bayer, K.U. (2018). CaMKII regulates the depalmitoylation and synaptic removal of the scaffold protein AKAP79/150 to mediate structural long-term depression. J Biol Chem *293*, 1551–1567.

Yang, G., Xiong, W., Kojic, L., and Cynader, M.S. (2009). Subunit-selective palmitoylation regulates the intracellular trafficking of AMPA receptor. Eur J Neurosci *30*, 35–46.

Yashiro, K., and Philpot, B.D. (2008). Regulation of NMDA receptor subunit expression and its implications for LTD, LTP, and metaplasticity. Neuropharmacology *55*, 1081–1094.

Yashiro, K., Riday, T.T., Condon, K.H., Roberts, A.C., Bernardo, D.R., Prakash, R., Weinberg, R.J., Ehlers, M.D., and Philpot, B.D. (2009). Ube3a is required for experience-dependent maturation of the neocortex. Nat Neurosci *12*, 777–783.

Yokoi, N., Fukata, Y., Sekiya, A., Murakami, T., Kobayashi, K., and Fukata, M. (2016). Identification of PSD-95 Depalmitoylating Enzymes. The Journal of Neuroscience *36*.

Yoshii, A., Zhao, J.-P.P., Pandian, S., Zundert, B. van, and Constantine-Paton, M. (2013). A Myosin Va mutant mouse with disruptions in glutamate synaptic development and mature plasticity in visual cortex. The Journal of Neuroscience *33*.

4. CONCLUSIONS AND DISCUSSION

In Chapters 2 and 3, I determined that two forms of synaptic plasticity important for neurodevelopment, the GluN2 subunit switch and homeostatic synaptic scaling, respectively, are disrupted in the *Ppt1*$^{-/-}$ mouse model of CLN1. These findings suggest that Ppt1 plays a central role in the developmental wiring of neural circuits that is corrupted in CLN1.

4.1. PPT1 function in developmental plasticity—the role of silent synapses

One interesting piece of the puzzle in attempting to understand the pathophysiology of CLN1 is the period of seemingly typical development during the first few months of life in humans. During this time, patients not only fail to reach specific milestones, but appear to achieve earlier checkpoints and subsequently regress. This suggest that there may be an early developmental period that does not strictly require PPT1 function, followed by events in synaptic or neuronal functions that do—making neurons unable to tolerate the future paradigms of plasticity that go on to wire the brain. Indeed, in Chapter 2, similar to previous findings (Isosomppi et al., 1999; Suopanki et al., 2000), I found that Ppt1 is developmentally expressed and reaches peak levels in synaptosomes during the first few weeks postnatal (**Figure 2.1**). This is roughly a time where the brain, especially sensory cortical areas, shift from spontaneous synchronous activity to that arising from more complex, experience-driven stimuli (Katz and Shatz, 1996). These environmental stimuli drive experience-dependent plasticity, which includes the GluN2B to GluN2A switch, the maturation of inhibitory circuitry, and the disappearance of silent synapses (discussed below)—classical plasticity mechanisms that refines neuronal circuitry to reflect the complexities of environmental stimuli. Whether PPT1 expression in humans mirrors what is observed in the rodent brain remains unclear but represents an important question for future study. If Ppt1 expression increases perinatally and peaks near 6 months of age in humans, this would be a strong indicator that it is critical for the molecular synaptic plasticity that is set to occur then, especially experience-dependent plasticity. However, the fact that milder mutations in PPT1 cause a slowed disease pathology indicates that PPT1 function is still important for the

maintenance of neuronal health, likely in its broader regulation of proteostasis. Taken together, I suspect that PPT1 plays a prominent role during critical periods of developmental synaptic plasticity and, upon maturation of these neural circuits, shifts into a role in the ongoing trafficking and degradation of synaptic molecules that, albeit important, is not relied upon as strongly as during critical period plasticity.

A potential focal point of the effect of Ppt1 during neurodevelopmental plasticity is at silent synapses—synapses that contain NMDA but no AMPA receptors. In **Chapter 2**, I demonstrated that *Ppt1*$^{-/-}$ neurons have an increased dendritic spine density; however, in **Chapter 3**, it was shown that sEPSP frequency, typically taken as a proxy for the number of AMPA receptor-containing synapses, in layer 2/3 cortical neurons was decreased. Of note, the increased spine density in *Ppt1*$^{-/-}$ neurons was largely made up of immature, filipodia-type protrusions, which commonly harbor silent synapses and are important for the heightened plasticity of the developing brain (Hanse et al., 2013; Matsuzaki et al., 2001; Ozcan, 2017). Therefore, my findings from Chapters 2 and 3 are reconciled by the hypothesis that compared to the WT brain, where many initially silent synapses are converted to mature, AMPA receptor-containing synapses, GluN2B membrane stabilization (due to over-palmitoylation) and hyperactivity in the *Ppt1*$^{-/-}$ cortical neurons suppresses this conversion. This also leaves more vacant synapses available for AMPA receptor insertion during synaptic scaling in *Ppt1*$^{-/-}$ neurons, as observed in **Chapter 3**.

As evidence for this hypothesis, it is established that NMDA receptor activity in the developing brain suppresses unsilencing of synapses (Adesnik et al., 2008). In fact, GluN2B-NMDA receptor activity specifically maintains silent synapses (Gray et al., 2011; Hall et al., 2007), indicating the switch from GluN2B- to GluN2A-containig receptors is crucial for the conversion of silent to functionally mature synapses (Hanse et al., 2013). This process is stagnated in the *Ppt1*$^{-/-}$ visual cortex as measured by the lack of GluN2A and PSD-95 in *Ppt1*$^{-/-}$ synaptosomes (**Chapter 2**). Moreover, dark rearing mice extends the presence of silent synapses in the visual cortex (layer

2/3) (Funahashi et al., 2013), consistent with the observed dark rearing-induced predominance of GluN2B-containing NMDA receptors (Guo et al., 2012; Quinlan et al., 1999b) and in line with our results that CLN1 pathophysiology is exacerbated in DR-*Ppt1*$^{-/-}$ mice (**Figure 3.7**). This also explains the finding that *Ppt1*$^{-/-}$ neurons are vulnerable to NMDA-induced, but not AMPA-induced, excitotoxicity (Finn et al., 2012).

The developmental regulation of silent synapse conversion (maturation) governs the closure of critical period plasticity (Huang et al., 2015) and is important for the appropriate wiring of neural connections (Hanse et al., 2013). As such, silent synapse dysregulation is a feature of neurodevelopmental and neurodegenerative diseases (Hanse et al., 2013). Intriguingly, a mouse model of Fragile X syndrome, which also presents with intellectual disability and seizure in humans, demonstrates increased dendritic spine density and persistence of silent synapses in the primary somatosensory cortex, echoing our results (Harlow et al., 2010). Therefore, developmental Ppt1 activity is likely to be important for the NMDA receptor-dependent molecular mechanisms that unsilence synapses, which are disrupted in CLN1. The convergence of these findings with those from other neurodevelopmental disease models point to common patterns of failed plasticity present across several disorders.

4.2. Disrupted synaptic plasticity and neural synchrony—contributions from NMDA and AMPA receptors

The findings herein identified two plasticity mechanisms disrupted by loss of Ppt1 in visual cortical development. Importantly, I also demonstrated that the spontaneous population activity of visual cortical neurons is more synchronous in *Ppt1*$^{-/-}$ animals. While my work did not establish a direct, or quantitative relationship between the disruption of these mechanisms and their effect on cortical synchrony, I speculate that they contribute significantly to this circuit-level finding.

Ppt1$^{-/-}$ neurons exhibited hyperpalmitoylation of GluN2B, lack of GluN2A-NMDARs, and an overabundance of GluN2B-dependent extrasynaptic calcium transients (**Chapter 2**). There is considerable consensus that increases in the GluN2B/GluN2A ratio of NMDA receptors lowers the threshold for associative plasticity, biasing synapses toward induction of LTP and away from LTD (Yashiro and Philpot, 2008). This has been demonstrated *in vivo*, as visual cortical neurons in dark reared rodents demonstrate LTP at a stimulus frequency that would typically be neutral in wild type animals (e.g., 40Hz stimulation), and exhibit no LTD at 1Hz, which is a standard paradigm for LTD induction (Guo et al., 2012; Kirkwood et al., 1996). Further study revealed that this effect is largely dependent on an increased contribution of GluN2B-containing NMDA receptor function (decrease in the GluN2A/GluN2B ratio) (Cho et al., 2009; Guo et al., 2012; Philpot et al., 2003, 2007). Moreover, the integration window for spike-timing dependent plasticity is also increased as a function of the incorporation of GluN2B-containing NMDA receptors (Guo et al., 2012). I anticipate, therefore, that the failure to complete the GluN2B to GluN2A shift renders the CLN1 visual cortical circuitry in a high plasticity state. Early life experience in *Ppt1*$^{-/-}$ mice, such as eye opening, may drive activity of these GluN2B-dominated NMDA receptors to facilitate LTP of a relatively small number of strong synapses. This increase in associative plasticity between neuronal populations in the CLN1 brain would lead to increased co-activity between interconnected neurons in the *Ppt1*$^{-/-}$ visual cortex, due to their enhanced synaptic coupling. Interestingly, this type of runaway potentiation has been a theoretical concern of the potentially pathological effects of a system with unchecked Hebbian plasticity (Miller, 1996; Miller and MacKay, 1994; Turrigiano, 1999) and is hypothesized to play a role in seizure (Hsu et al., 2008). In fact, this was the fertile ground that sprouted the conceptualization and experimental identification of synaptic scaling.

However, adding another layer to the route toward runaway excitatory synapse potentiation, we also identified an exaggerated synaptic upscaling and a failure to scale down

synaptic responses in *Ppt1*$^{-/-}$ neurons (**Chapter 3**). These homeostatic mechanisms would typically tune neuronal sensitivity to correct for runaway potentiation but are unable to in *Ppt1*$^{-/-}$ cells (Turrigiano, 2017; Turrigiano and Nelson, 2004). Therefore, simultaneous enhancement in the NMDA receptor-dependent Hebbian coupling of neurons with the failure to scale down synapses in response to prolonged potentiation results is likely to enhance connectivity and the coactivity of a greater number of neurons in the *Ppt1*$^{-/-}$ brain. These are the primary reasons I suspect that layer 2/3 neurons exhibit hypersynchrony in the *Ppt1*$^{-/-}$ cortex.

A recent series of studies suggests that the failure of the GluN2B to GluN2A shift and exaggerated synaptic scaling response in *Ppt1*$^{-/-}$ neurons may be synthesized into a unified mechanism (Bridi et al., 2018; Rodriguez et al., 2019). It was originally proposed that synaptic scaling is independent of NMDA receptor activity (Turrigiano et al., 1998). However, using a single-cell knockout approach, Rodriguez and colleagues showed that dark rearing-induced synaptic upscaling in the visual cortex of mice is dependent on NMDA receptors (Rodriguez et al., 2019). This indicates that synaptic upscaling, at least in the dark rearing paradigm, is explained by the "sliding scale" or BCM model of plasticity that is dictated by the recent history of afferent activity (Cooper and Bear, 2012), such that reduced afferent activity biases visual cortical neurons toward an LTP-like upregulation of AMPA receptors (Lee and Kirkwood, 2019). Interestingly, this is a refinement of the mechanism proposed by the original studies demonstrating increased plasticity in the visual cortex due to GluN2B-predominance following visual deprivation (Philpot et al., 2001, 2003; Quinlan et al., 1999a, 1999b). Moreover, the same chronic activity blockade that induces synaptic scaling *in vitro* selectively upregulates GluN2B-containing NMDA receptors and silent synapse formation (Nakayama et al., 2005). Taken together, reducing network activity simultaneously enhances activity of GluN2B-contianing NMDA receptors and biases neurons toward synaptic incorporation of AMPA receptors, perhaps at silent synapses(Lee and Kirkwood, 2019). The results herein suggest that loss of Ppt1 disrupts this

grand mechanism by stagnating developmental GluN2B and GluA1 trafficking, either directly or through the dysregulation of related postsynaptic molecules like Fyn (**Chapter 2**) and Akap5 (**Chapter 3**)

4.3. Sequential scaling and runaway potentiation in CLN1

An intriguing feature of CLN1 pathophysiology, at least in the *Ppt1*$^{-/-}$ mouse brain, is the spreading degeneration pattern (Koster and Yoshii, 2019). In the visual system, for instance, the visual thalamus (dLGN) degenerates before the visual cortex, which degenerates before the motor cortex (Kielar et al., 2007; Koster and Yoshii, 2019). This may also be due, in part, to dysregulated synaptic scaling in *Ppt1*$^{-/-}$ neurons. As neurons serving as first order relays, such as dLGN neurons order nuclei of the thalamus (Sherman, 2016), begin to degenerate in the *Ppt1*$^{-/-}$ brain, the remaining neurons are forced to undergo synaptic upscaling to compensate for the declining activity. Since this upscaling is exaggerated in *Ppt1*$^{-/-}$ neurons, perhaps at previously silent synapses, this would also drive strong connectivity between the remaining cells, resulting in sequentially amplified synchrony. In turn, this has the potential to drive further excitotoxic cell death. Indeed, a computational study determined that deafferentation of simulated pyramidal neurons leads to their pathological synaptic scaling and strong synchrony of the network (Fröhlich et al., 2008). Whether such a volley between disrupted plasticity mechanisms is the major driver of CLN1 is yet to be tested, but a closely related models have been proposed to propel Alzheimer disease (Small, 2008; Styr and Slutsky, 2018).

While this model may explain a portion of the pathophysiology in *Ppt1*$^{-/-}$ mice, it is unlikely that these are the only neuronal disruptions in CLN1 given the impact of PPT1 mutation on the severity of neurodegeneration.

4.4. Additional implications from palmitoyl proteomics

An important finding from my work in **Chapter 3** using palmitoyl proteomics is the modest but broad over-palmitoylation of synaptic proteins (see **Figure 3.8**). While we focused on the Akap5 pathway and its implications in synaptic scaling, there are many other pathways suggested to be disrupted by the data.

Studies both *in vitro* and *in vivo* demonstrate a marked reduction in the presynaptic vesicle pool size with increasing age in *Ppt1*$^{-/-}$ neurons, manifesting a robust decrease by roughly six months of age in the *Ppt*$^{-/-}$ cortex (Kim et al., 2008; Virmani et al., 2005). *In vivo*, this decrease is associated with a retention of presynaptic vesicle proteins (e.g. SNAP25, VAMP2) in the presynaptic membrane (Kim et al., 2008), suggestive of their hyperpalmitoylation. My palmitoyl-proteomic data show a modest increase in the palmitoylation level of many presynaptic proteins, including those identified in previous studies, SNAP25 and syntaxin 1 (A and B) for example, as well as canonical vesicle cycle proteins such as synaptic vesicle glycoprotein 2A and 2B, and N-ethylmaleimide sensitive fusion protein. When analyzed using the online tool for synaptic proteomic data, SynGO (Koopmans et al., 2019), presynaptic proteins were highly enriched, such that the SynGO terms “process in the presynapse” and “synaptic vesicle cycle” represent the second and third top enriched biological process GO terms, respectively (**Figure 3.8**). Therefore, our results corroborate previous findings showing a disruption of presynaptic vesicle function at several points in the synaptic vesicle cycle and point to additional proteins that are likely to be substrates of this disruption *in vivo*.

Subcomponents of the synapse responsible for structural maintenance and the physical transport of molecules were also overrepresented in *Ppt1*$^{-/-}$ visual cortices (**Figure 3.8**). Indeed, “structural constituent of the postsynapse” was the fifth most enriched biological process SynGO term in synaptosomes. Proteins in this category include Homer1, multiple membrane-associated guanylate kinases (Dlg1, Dlg2, Dlg3), and Shank2. Proteins involved in transport of synaptic

molecules include myosin 5a, flotillin 2. Intriguingly, many of these proteins are implicated in neurological diseases, especially neurodevelopmental disorders presenting with intellectual disability and seizure, suggesting common pathways of synaptic dysregulation across multiple diseases (Berkel et al., 2010; Hamdan et al., 2011; Luo et al., 2012; Yoshii et al., 2013; Zaslavsky et al., 2019). Future studies might use these data, in addition to other recent proteomic studies (Gorenberg et al., 2020; Sapir et al., 2019; Scifo et al., 2015; Tikka et al., 2016), as a starting point for identifying the primary pathways disrupted by loss of Ppt1 and understanding in detail their regulation by Ppt1-mediated depalmitoylation.

4.5. Potential underpinnings of widespread failure of depalmitoylation

Our data herein point to the disturbance of postsynaptic receptor function through the hyperpalmitoylation of postsynaptic receptor subunits, signaling molecules, and synaptic scaffolds, while previous studies find a similar phenomenon at the presynapse (albeit, at a later age). Considering the breadth of protein disruption, and the number of proteins showing modest hyperpalmitoylation in our proteomic data, it might be considered that CLN1 proceeds as a function of the widespread accumulation of palmitoylated proteins in membranous compartments where they would typically be removed. Mutations in Ppt1 shift the balance of palmitoylation toward an extensive hyperpalmitoylation of proteins akin to that of how the mutation of a central kinase shifts the balance of cellular signaling in favor of growth, allowing the uncorrected proliferative potential that characterizes cancer. This lack of depalmitoylation manifests in severe neurological symptoms due to the robust enrichment of palmitoylated proteins at synapses (Gorenberg et al., 2020; Sanders et al., 2015). Given enough attention, many proteins and thus forms of synaptic function would likely be discovered to be disrupted in CLN1 due to lack of depalmitoylation, which only compound with age. Perhaps many of these changes are associated with the high demand of developmental synaptic plasticity (Patterson and Skene, 1999). The key to understanding the drivers of disease pathogenesis is to identify mechanisms that show

aberrations first (or at least, early on in the disease). These mechanisms will be disrupted due to the circumstance that they occur ontologically earlier and require some depalmitoylation function by Ppt1. That is, the earliest developmental mechanism that requires Ppt1 activity begins the disease cascade, and each subsequent mechanism will face the add to the neuronal dysregulation.

This broad overpalmitoylation of proteins across studies of *Ppt1*$^{-/-}$ neurons suggests 1) that Ppt1 has many substrates in neurons (leading directly to their hyperpalmitoylation), 2) loss of Ppt1 compromises the endolysosomal machinery, removing the compartment within which depalmitoylation typically occurs for these proteins or 3), that loss of Ppt1 influences the palmitoylation machinery itself, thereby indirectly dysregulating many palmitoylated proteins.

Recent work shows that, indeed, Ppt1 acts on roughly 10% of palmitoylated proteins, which can plausibly account for the robust cellular defects in CLN1. Indeed, as discussed, our proteomic data show a widespread hyperpalmitoylation (>1.2-fold increase) of approximately 300 proteins. However, proteomic studies profiling the palmitoylome of *Ppt1*$^{-/-}$ cells show some disagreement among the substrate profile of Ppt1. In part, this disagreement is surely due to widely different biological systems (e.g., cell lines vs. dissociated neurons vs. brain lysates and synaptosomes) and palmitoylation labeling techniques (acyl biotin exchange vs. acyl resin-assisted capture) utilized for the analysis. Since Ppt1 is developmentally regulated, the timing of the sampling is also likely to cause divergent results. Further, little experimental evidence has verified that Ppt1 interacts with the proposed substrates. Therefore, while the proteomic evidence suggests that the loss of direct depalmitoylation by Ppt1 may explain a large fraction of the deficits observed at Ppt1 synapses, future studies will need to systematically screen potential Ppt1 substrates for direct interactions and depalmitoylase activity to verify these studies.

Among the consistently identified substrates of Ppt1 are Rab GTPases involved in all aspects of endolysosomal protein trafficking and other members of the vesicular machinery, such as cysteine string protein α (CSPα) or dynamin 1 (Aby et al., 2013; Bagh et al., 2018; Gorenberg et al., 2020; Segal-Salto et al., 2017). Ppt1 may drive broad hyperpalmitoylation of proteins by limiting the proper endolysosomal trafficking of proteins, where they would typically interact with a subset of PATs and depalmitoylases. Related to this, several high-confidence Ppt1 substrates contain the palmitoylated motif that is specific to zDHHC17, also known as huntingtin interacting protein 14, indicating that there is a specific interplay between these enzymes (zDHHC17-PPT1 may represent a PAT-depalmitoylase pair)(Gorenberg et al., 2020). zDHHC17 substrates are principally involved in clathrin-mediated endocytosis. Loss of Ppt1 would strongly disrupt this pathway, preventing endocytosis of proteins at the plasma membrane and their subsequent trafficking through the endolysosomal system, where much posttranslational modification occurs. In this way, loss of Ppt1 would block the modification and degradation of large numbers of proteins outside of those it directly interacts with due to their reliance on endolysosomal trafficking. A similar relationship may also be true for other zDHHCs, and thereby other functional modules, but the preferred enzymatic motifs of PATs has not been sufficiently defined to cross-examine with the putative substrate list of Ppt1.

Alternatively, PATs can regulate the palmitoylation state of whole groups of substrates indirectly by palmitoylating and thereby effecting the function of downstream PATs or depalmitoylases. This is true for zDHHC6, which regulates many key proteins in the endoplasmic reticulum and whose palmitoylation by zDHHC16, paired with its dynamic depalmitoylation by APT2, influences activity on its substrates (Abrami et al., 2017). Presumably the same is true for depalmitoylases, i.e., they can depalmitoylate PATs or other depalmitoylases to affect their downstream substrates. Indeed, APTs undergo autodepalmitoylation that dictates access to their substrates (Vartak et al., 2014). Further, though their depalmitoylase is unknown, ABHD17s

palmitoylation is important for access to its substrates (Lin and Conibear, 2015). It is possible then that Ppt1 acts indirectly by depalmitoylating PATs or other depalmitoylases to influence the palmitoylation state of such a broad spectrum of proteins. Interestingly, a pharmacological screen indicated ABHD16A is a depalmitoylase (Lin and Conibear, 2015) and this enzyme was later identified as a potential substrate of Ppt1 (Gorenberg et al., 2020), suggesting this as one potential cascade by which Ppt1 exerts indirect control of the palmitoylation of synaptic proteins. Future studies will need to delineate direct effects of Ppt1 (substrates) vs. indirect effects due to alterations in the other members of the palmitoylation machinery, as this will have major implications for treatment strategies, especially those that act promiscuously.

4.6. Treating CLN1

As discussed in **Chapter 1**, current therapeutics for CLN1 are palliative and the sole class of disease-modifying therapeutics that has been attempted thus far (beside gene therapy) centers on the reduction of lysosomal storage material (Gavin et al., 2013; Levin et al., 2014). However, like the targeted removal of amyloid plaques in Alzheimer disease, eradicating lysosomal storage material in CLN1 may be too far downstream from the initial functional insult for intervention to prove beneficial. This is one potential reason for the limited success of substrate reduction therapies to date. My work and others point to the synapse as a primary locus of dysfunction that represents a large class of novel targets for the treatment of CLN1.

This does not rule out a central role for the endolysosomal system in CLN1 pathophysiology and future therapies, however, since it is indeed crucial for synaptic function. Instead, further pursuit of this strategy might shift toward correcting the function of endolysosomes to support synapses, rather than narrowly preventing buildup of waste material. One example to leverage this system is the use an agonist of the transcription factor EB (TFEB), which induces lysosomal biogenesis and autophagy (Sardiello et al., 2009; Settembre et al., 2011). It is plausible that boosting the number and function of lysosomes can compensate for synaptic functions lost

by Ppt1, while simultaneous enhancement of autophagy would lead to the removal of storage material as well. Indeed, this approach has proven beneficial in models of common neurodegenerative diseases (Decressac et al., 2013; Kilpatrick et al., 2015; Polito et al., 2014; Tsunemi et al., 2012; Xiao et al., 2014, 2015), lysosomal storage disorders (Costa et al., 2021; Medina et al., 2011; Song et al., 2013; Spampanato et al., 2013), and even a mouse model of CLN3 (Palmieri et al., 2017). Refining this strategy may therefore prove beneficial in a multitude of disorders where protein accumulation and lysosomal storage are prominent features, including CLN1.

In addition, the palmitoylation of proteins can be directly targeted using chemical mimetics of depalmitoylation enzymes. One such example, called N-(tert-Butyl) hydroxylamine (NtBuHA), reaches the brain, removes lysosomal storage material, prevents neuronal death, and extends the lifespan of *Ppt1*$^{-/-}$ mice (Sarkar et al., 2013). This is due in part to NtBuHa correcting the trafficking defect of the lysosomal ATPase subunit and Ppt1 substrate, V0a1, in *Ppt1*$^{-/-}$ cells (Bagh et al., 2017). Due to the broad reactivity of the drug, it is likely that NtBuHa acts on multiple substrates to exert beneficial effects; profiling its targets more comprehensively might provide insight into which are crucial for the observed benefits in *Ppt1*$^{-/-}$ mice. However, NtBuHa only extends the lifespan of *Ppt1*$^{-/-}$ mice by ~2 months, suggesting that next generation small molecules are required to make this treatment strategy viable. One therapeutic class that circumvents shortcomings of the pharmacological approach is gene or enzyme replacement therapy, which delivers functional Ppt1 directly to cells in the brain.

The first gene therapy developed for CLN1 consists of the human PPT1 protein under the CAG promoter and encapsulated in an AAV2 viral vector. When delivered to *Ppt1-/-* mice, the treatment resulted in localized PPT1 expression, reduced lysosomal storage material, reduced microcephaly, and improved motor behavior, but had no effect on the lifespan (Griffey et al., 2004, 2006). Improvements in design of the vector (AAV2 with AAV5 capsid protein) and in the treatment

protocols led to similar functional improvements and extended lifespan by 10-20 weeks (Macauley et al., 2012, 2014; Roberts et al., 2012). Interestingly, pairing gene therapy with bone marrow transplant was particularly effective, dramatically enhancing the lifespan of *Ppt1*$^{-/-}$ mice by 7-12 months (Macauley et al., 2012). More recent study employing a third-generation AAV2/9 vector (hybrid of AAV2 and AAV9 capsid protein) and treating both the spinal cord and brain in *Ppt1*$^{-/-}$ mice has demonstrated profound efficacy, correcting much of the histopathological and behavioral phenotype of these animals and extending lifespan to nearly 20 months (Shyng et al., 2017). This body of work prompted adaptation of gene therapy technology for use in humans and has resulted in the recent initiation of clinical trials in CLN1 patients with the FDA Fast Track designated ABO-202, an AAV9-mediated PPT1 delivery system. However, the gene therapy approach has yet to be proven effective in CLN1 patients and will certainly require refinement before it is wholly successful.

In summary, the current and near-future therapeutic landscape for CLN1 includes leveraging lysosomal biogenesis, targeting protein palmitoylation directly, and correcting the loss of PPT1 with enzyme replacement or gene therapies. As a number of studies demonstrate a synergy of multifaceted treatment strategies and diagnosis of CLN1 in human patients is often not made until several symptoms have presented, preemptive use pharmacological agents might prove beneficial to slow disease and enhance the efficacy of gene therapy, once the diagnosis is confirmed.

4.7. Targeting palmitoylation in neurological diseases

Treating neurological diseases remains a largely unsuccessful endeavor, making unresponsiveness and relapse common occurrences for many treatment strategies, including for epilepsy, depression, and especially neurodegeneration (Jakobsen et al., 2017; Mehta et al., 2017; Schmidt and Löscher, 2005). This is partly due to the prevention of drug entry into the brain

by the blood brain barrier (Neuwelt et al., 2008). However, treatment options are also hindered by side effects due to off-target consequences in the periphery.

One potential benefit of targeting the balance of protein palmitoylation and depalmitoylation for the treatment of neurological diseases is the enrichment of palmitoylated proteins in neurons and at synapses. The specialized role for palmitoylation in neurons suggests that successful modulation of this posttranslational modification might provide specific benefit in the brain with limited side effects in the periphery. The palmitoylation of disease-relevant proteins, such as GluA1 in epilepsy (Itoh et al., 2018; Yang et al., 2018), BACE1 in Alzheimer disease (Andrew et al., 2017), or huntingtin in Huntington disease (Huang et al., 2004; Yanai et al., 2006) represent the first line in a growing class of potential therapeutic targets (Naumenko and Ponimaskin, 2018). Thus, though there remain many obstacles, the palmitoylation state of neuronal proteins represents a novel category of therapeutic approaches that might provide penetrant and specific effects on CNS function across diseases. Effective palmitoylation-targeted therapies in CLN1 will serve as a proof of principle for this strategy.

CHAPTER 4 CITED LITERATURE

Abrami, L., Dallavilla, T., Sandoz, P.A., Demir, M., Kunz, B., Savoglidis, G., Hatzimanikatis, V., and Goot, F.G. van der (2017). Identification and dynamics of the human ZDHHC16-ZDHHC6 palmitoylation cascade. ELife *6*.

Aby, E., Gumps, K., Roth, A., Sigmon, S., Jenkins, S.E., Kim, J.J., Kramer, N.J., Parfitt, K.D., and Korey, C.A. (2013). Mutations in palmitoyl-protein thioesterase 1 alter exocytosis and endocytosis at synapses in Drosophila larvae. Fly *7*, 267–279.

Adesnik, H., Li, G., During, M.J., Pleasure, S.J., and Nicoll, R.A. (2008). NMDA receptors inhibit synapse unsilencing during brain development. Proc National Acad Sci *105*, 5597–5602.

Andrew, R.J., Fernandez, C.G., Stanley, M., Jiang, H., Nguyen, P., Rice, R.C., Buggia-Prévot, V., Rossi, P.D., Vetrivel, K.S., Lamb, R., et al. (2017). Lack of BACE1 S-palmitoylation reduces amyloid burden and mitigates memory deficits in transgenic mouse models of Alzheimer's disease. Proceedings of the National Academy of Sciences of the United States of America *114*, E9665–E9674.

Bagh, M.B., Peng, S., Chandra, G., Zhang, Z., Singh, S.P., Pattabiraman, N., Liu, A., and Mukherjee, A.B. (2017). Misrouting of v-ATPase subunit V0a1 dysregulates lysosomal acidification in a neurodegenerative lysosomal storage disease model. Nature Communications *8*, 14612.

Bagh, M.B., Sadhukhan, T., Appu, A.P., Casey, S., Zhang, Z., and Mukherjee, A.B. (2018). Inactivation of dynamin 1 in Cln1−/− mouse brain contributes to declining synaptic pool size. Faseb J *32*, 542.11-542.11.

Berkel, S., Marshall, C.R., Weiss, B., Howe, J., Roeth, R., Moog, U., Endris, V., Roberts, W., Szatmari, P., Pinto, D., et al. (2010). Mutations in the SHANK2 synaptic scaffolding gene in autism spectrum disorder and mental retardation. Nat Genet *42*, 489–491.

Bridi, M.C.D., Pasquale, R. de, Lantz, C.L., Gu, Y., Borrell, A., Choi, S.-Y., He, K., Tran, T., Hong, S.Z., Dykman, A., et al. (2018). Two distinct mechanisms for experience-dependent homeostasis. Nat Neurosci *21*, 843–850.

Cho, K.K.A., Khibnik, L., Philpot, B.D., and Bear, M.F. (2009). The ratio of NR2A/B NMDA receptor subunits determines the qualities of ocular dominance plasticity in visual cortex. Proc National Acad Sci *106*, 5377–5382.

Cooper, L.N., and Bear, M.F. (2012). The BCM theory of synapse modification at 30: interaction of theory with experiment. Nat Rev Neurosci *13*, 798–810.

Costa, A., Metais, T., Mouthon, F., Kerkovich, D., and Charvériat, M. (2021). Evaluating and modulating TFEB in the control of autophagy: toward new treatments in CNS disorders. Fundam Clin Pharm *35*, 539–551.

Decressac, M., Mattsson, B., Weikop, P., Lundblad, M., Jakobsson, J., and Björklund, A. (2013). TFEB-mediated autophagy rescues midbrain dopamine neurons from α-synuclein toxicity. Proc National Acad Sci *110*, E1817–E1826.

Finn, R., Kovács, A.D., and Pearce, D.A. (2012). Altered glutamate receptor function in the cerebellum of the Ppt1-/- mouse, a murine model of infantile neuronal ceroid lipofuscinosis. Journal of Neuroscience Research *90*, 367–375.

Fröhlich, F., Bazhenov, M., and Sejnowski, T.J. (2008). Pathological Effect of Homeostatic Synaptic Scaling on Network Dynamics in Diseases of the Cortex. J Neurosci *28*, 1709–1720.

Funahashi, R., Maruyama, T., Yoshimura, Y., and Komatsu, Y. (2013). Silent synapses persist into adulthood in layer 2/3 pyramidal neurons of visual cortex in dark-reared mice. J Neurophysiol *109*, 2064–2076.

Gavin, M., Wen, G.Y., Messing, J., Adelman, S., Logush, A., Jenkins, E.C., Brown, W.T., and Velinov, M. (2013). Substrate Reduction Therapy in Four Patients with Milder CLN1 Mutations and Juvenile-Onset Batten Disease Using Cysteamine Bitartrate. JIMD Reports *11*, 87–92.

Gorenberg, E.L., Zhao, H.R., Bishai, J., Chou, V., Wirak, G.S., Lam, T.T., and Chandra, S.S. (2020). Identification of palmitoyl protein thioesterase 1 substrates defines roles for synaptic depalmitoylation. Biorxiv 2020.05.02.074302.

Gray, J.A., Shi, Y., Usui, H., During, M.J., Sakimura, K., and Nicoll, R.A. (2011). Distinct Modes of AMPA Receptor Suppression at Developing Synapses by GluN2A and GluN2B: Single-Cell NMDA Receptor Subunit Deletion In Vivo. Neuron *71*, 1085–1101.

Griffey, M., Bible, E., Vogler, C., Levy, B., Gupta, P., Cooper, J., and Sands, M.S. (2004). Adeno-associated virus 2-mediated gene therapy decreases autofluorescent storage material and increases brain mass in a murine model of infantile neuronal ceroid lipofuscinosis. Neurobiology of Disease *16*, 360–369.

Griffey, M.A., Wozniak, D., Wong, M., Bible, E., Johnson, K., Rothman, S.M., Wentz, A.E., Cooper, J.D., and Sands, M.S. (2006). CNS-directed AAV2-mediated gene therapy ameliorates functional deficits in a murine model of infantile neuronal ceroid lipofuscinosis. Mol Ther *13*, 538–547.

Guo, Y., Huang, S., Pasquale, R. de, McGehrin, K., Lee, H.-K., Zhao, K., and Kirkwood, A. (2012). Dark Exposure Extends the Integration Window for Spike-Timing-Dependent Plasticity. J Neurosci *32*, 15027–15035.

Hall, B.J., Ripley, B., and Ghosh, A. (2007). NR2B Signaling Regulates the Development of Synaptic AMPA Receptor Current. J Neurosci *27*, 13446–13456.

Hamdan, F.F., Gauthier, J., Araki, Y., Lin, D.-T., Yoshizawa, Y., Higashi, K., Park, A., Spiegelman, D., Dobrzeniecka, S., Piton, A., et al. (2011). Excess of De Novo Deleterious Mutations in Genes Associated with Glutamatergic Systems in Nonsyndromic Intellectual Disability. Am J Hum Genetics *88*, 516.

Hanse, E., Seth, H., and Riebe, I. (2013). AMPA-silent synapses in brain development and pathology. Nat Rev Neurosci *14*, 839–850.

Harlow, E.G., Till, S.M., Russell, T.A., Wijetunge, L.S., Kind, P., and Contractor, A. (2010). Critical Period Plasticity Is Disrupted in the Barrel Cortex of Fmr1 Knockout Mice. Neuron *65*, 385–398.

Hsu, D., Chen, W., Hsu, M., and Beggs, J.M. (2008). An open hypothesis: Is epilepsy learned, and can it be unlearned? Epilepsy Behav *13*, 511–522.

Huang, K., Yanai, A., Kang, R., Arstikaitis, P., Singaraja, R.R., Metzler, M., Mullard, A., Haigh, B., Gauthier-Campbell, C., Gutekunst, C.-A.A., et al. (2004). Huntingtin-interacting protein HIP14 is a palmitoyl transferase involved in palmitoylation and trafficking of multiple neuronal proteins. Neuron *44*, 977–986.

Huang, X., Stodieck, S.K., Goetze, B., Cui, L., Wong, M.H., Wenzel, C., Hosang, L., Dong, Y., Löwel, S., and Schlüter, O.M. (2015). Progressive maturation of silent synapses governs the duration of a critical period. Proc National Acad Sci *112*, E3131–E3140.

Isosomppi, J., Heinonen, O., Hiltunen, J.O., Greene, N.D., Vesa, J., Uusitalo, A., Mitchison, H.M., Saarma, M., Jalanko, A., and Peltonen, L. (1999). Developmental expression of palmitoyl protein thioesterase in normal mice. Brain Research. Developmental Brain Research *118*, 1–11.

Itoh, M., Yamashita, M., Kaneko, M., Okuno, H., Abe, M., Yamazaki, M., Natsume, R., Yamada, D., Kaizuka, T., Suwa, R., et al. (2018). Deficiency of AMPAR-Palmitoylation Aggravates Seizure Susceptibility. The Journal of Neuroscience : The Official Journal of the Society for Neuroscience *38*, 10220–10235.

Jakobsen, J.C., Katakam, K.K., Schou, A., Hellmuth, S.G., Stallknecht, S.E., Leth-Møller, K., Iversen, M., Banke, M.B., Petersen, I.J., Klingenberg, S.L., et al. (2017). Selective serotonin reuptake inhibitors versus placebo in patients with major depressive disorder. A systematic review with meta-analysis and Trial Sequential Analysis. BMC Psychiatry *17*, 58.

Katz, L.C., and Shatz, C.J. (1996). Synaptic Activity and the Construction of Cortical Circuits. Science *274*, 1133–1138.

Kielar, C., Maddox, L., Bible, E., Pontikis, C.C., Macauley, S.L., Griffey, M.A., Wong, M., Sands, M.S., and Cooper, J.D. (2007). Successive neuron loss in the thalamus and cortex in a mouse model of infantile neuronal ceroid lipofuscinosis. Neurobiology of Disease *25*, 150–162.

Kilpatrick, K., Zeng, Y., Hancock, T., and Segatori, L. (2015). Genetic and Chemical Activation of TFEB Mediates Clearance of Aggregated α-Synuclein. Plos One *10*, e0120819.

Kim, S.-J.J., Zhang, Z., Sarkar, C., Tsai, P.-C.C., Lee, Y.-C.C., Dye, L., and Mukherjee, A.B. (2008). Palmitoyl protein thioesterase-1 deficiency impairs synaptic vesicle recycling at nerve terminals, contributing to neuropathology in humans and mice. Journal of Clinical Investigation *118*.

Kirkwood, A., Rioult, M.G., and Bear, M.F. (1996). Experience-dependent modification of synaptic plasticity in visual cortex. Nature *381*, 526–528.

Koopmans, F., Nierop, P. van, Andres-Alonso, M., Byrnes, A., Cijsouw, T., Coba, M.P., Cornelisse, L.N., Farrell, R.J., Goldschmidt, H.L., Howrigan, D.P., et al. (2019). SynGO: An Evidence-Based, Expert-Curated Knowledge Base for the Synapse. Neuron *103*, 217-234.e4.

Koster, K.P., and Yoshii, A. (2019). Depalmitoylation by Palmitoyl-Protein Thioesterase 1 in Neuronal Health and Degeneration. Frontiers Synaptic Neurosci *11*, 25.

Lee, H.-K., and Kirkwood, A. (2019). Mechanisms of Homeostatic Synaptic Plasticity in vivo. Front Cell Neurosci *13*, 520.

Levin, S.W., Baker, E.H., Zein, W.M., Zhang, Z., Quezado, Z.M., Miao, N., Gropman, A., Griffin, K.J., Bianconi, S., Chandra, G., et al. (2014). Oral cysteamine bitartrate and N-acetylcysteine for patients with infantile neuronal ceroid lipofuscinosis: a pilot study. The Lancet Neurology *13*.

Lin, D.T., and Conibear, E. (2015). ABHD17 proteins are novel protein depalmitoylases that regulate N-Ras palmitate turnover and subcellular localization. ELife *4*, e11306.

Luo, P., Li, X., Fei, Z., and Poon, W. (2012). Scaffold protein Homer 1: Implications for neurological diseases. Neurochem Int *61*, 731–738.

Macauley, S.L., Roberts, M.S., Wong, A.M., McSloy, F., Reddy, A.S., Cooper, J.D., and Sands, M.S. (2012). Synergistic effects of central nervous system-directed gene therapy and bone marrow transplantation in the murine model of infantile neuronal ceroid lipofuscinosis. Ann Neurol *71*, 797–804.

Macauley, S.L., Wong, A.M.S., Shyng, C., Augner, D.P., Dearborn, J.T., Pearse, Y., Roberts, M.S., Fowler, S.C., Cooper, J.D., Watterson, D.M., et al. (2014). An Anti-Neuroinflammatory That Targets Dysregulated Glia Enhances the Efficacy of CNS-Directed Gene Therapy in Murine Infantile Neuronal Ceroid Lipofuscinosis. J Neurosci *34*, 13077–13082.

Matsuzaki, M., Ellis-Davies, G.C.R., Nemoto, T., Miyashita, Y., Iino, M., and Kasai, H. (2001). Dendritic spine geometry is critical for AMPA receptor expression in hippocampal CA1 pyramidal neurons. Nat Neurosci *4*, 1086–1092.

Medina, D.L., Fraldi, A., Bouche, V., Annunziata, F., Mansueto, G., Spampanato, C., Puri, C., Pignata, A., Martina, J.A., Sardiello, M., et al. (2011). Transcriptional Activation of Lysosomal Exocytosis Promotes Cellular Clearance. Dev Cell *21*, 421–430.

Mehta, D., Jackson, R., Paul, G., Shi, J., and Sabbagh, M. (2017). Why do trials for Alzheimer's disease drugs keep failing? A discontinued drug perspective for 2010-2015. Expert Opinion on Investigational Drugs *26*, 735–739.

Miller, K.D. (1996). Synaptic Economics: Competition and Cooperation in Synaptic Plasticity. Neuron *17*, 371–374.

Miller, K.D., and MacKay, D.J.C. (1994). The Role of Constraints in Hebbian Learning. Neural Comput *6*, 100–126.

Nakayama, K., Kiyosue, K., and Taguchi, T. (2005). Diminished Neuronal Activity Increases Neuron-Neuron Connectivity Underlying Silent Synapse Formation and the Rapid Conversion of Silent to Functional Synapses. J Neurosci *25*, 4040–4051.

Naumenko, V.S., and Ponimaskin, E. (2018). Palmitoylation as a Functional Regulator of Neurotransmitter Receptors. Neural Plasticity *2018*, 5701348.

Neuwelt, E., Abbott, N.J., Abrey, L., Banks, W.A., Blakley, B., Davis, T., Engelhardt, B., Grammas, P., Nedergaard, M., Nutt, J., et al. (2008). Strategies to advance translational research into brain barriers. Lancet Neurology *7*, 84–96.

Ozcan, A.S. (2017). Filopodia: A Rapid Structural Plasticity Substrate for Fast Learning. Frontiers Synaptic Neurosci *9*, 12.

Palmieri, M., Pal, R., Nelvagal, H.R., Lotfi, P., Stinnett, G.R., Seymour, M.L., Chaudhury, A., Bajaj, L., Bondar, V.V., Bremner, L., et al. (2017). mTORC1-independent TFEB activation via Akt inhibition promotes cellular clearance in neurodegenerative storage diseases. Nat Commun *8*, 14338.

Patterson, S.I., and Skene, J.H. (1999). A shift in protein S-palmitoylation, with persistence of growth-associated substrates, marks a critical period for synaptic plasticity in developing brain. Journal of Neurobiology *39*, 423–437.

Philpot, B., Sekhar, A., Shouval, H., and Bear, M. (2001). Visual experience and deprivation bidirectionally modify the composition and function of NMDA receptors in visual cortex. Neuron *29*.

Philpot, B.D., Espinosa, J.S., and Bear, M.F. (2003). Evidence for Altered NMDA Receptor Function as a Basis for Metaplasticity in Visual Cortex. J Neurosci *23*, 5583–5588.

Philpot, B.D., Cho, K.K.A., and Bear, M.F. (2007). Obligatory Role of NR2A for Metaplasticity in Visual Cortex. Neuron *53*, 495–502.

Polito, V.A., Li, H., Martini-Stoica, H., Wang, B., Yang, L., Xu, Y., Swartzlander, D.B., Palmieri, M., Ronza, A., Lee, V.M., et al. (2014). Selective clearance of aberrant tau proteins and rescue of neurotoxicity by transcription factor EB. Embo Mol Med *6*, 1142–1160.

Quinlan, E., Philpot, B., Huganir, R., and Bear, M. (1999a). Rapid, experience-dependent expression of synaptic NMDA receptors in visual cortex in vivo. Nature Neuroscience *2*.

Quinlan, E.M., Olstein, D.H., and Bear, M.F. (1999b). Bidirectional, experience-dependent regulation of N-methyl-d-aspartate receptor subunit composition in the rat visual cortex during postnatal development. Proceedings of the National Academy of Sciences *96*.

Roberts, M.S., Macauley, S.L., Wong, A.M., Yilmas, D., Hohm, S., Cooper, J.D., and Sands, M.S. (2012). Combination small molecule PPT1 mimetic and CNS-directed gene therapy as a treatment for infantile neuronal ceroid lipofuscinosis. J Inherit Metab Dis *35*, 847–857.

Rodriguez, G., Mesik, L., Gao, M., Parkins, S., Saha, R., and Lee, H.-K. (2019). Disruption of NMDAR Function Prevents Normal Experience-Dependent Homeostatic Synaptic Plasticity in Mouse Primary Visual Cortex. J Neurosci *39*, 7664–7673.

Sanders, S.S., Martin, D.D., Butland, S.L., Lavallée-Adam, M., Calzolari, D., Kay, C., Yates, J.R., and Hayden, M.R. (2015). Curation of the Mammalian Palmitoylome Indicates a Pivotal Role for Palmitoylation in Diseases and Disorders of the Nervous System and Cancers. PLoS Computational Biology *11*, e1004405.

Sapir, T., Segal, M., Grigoryan, G., Hansson, K.M., James, P., Segal, M., and Reiner, O. (2019). The Interactome of Palmitoyl-Protein Thioesterase 1 (PPT1) Affects Neuronal Morphology and Function. Frontiers in Cellular Neuroscience *13*, 92.

Sardiello, M., Palmieri, M., Ronza, A. di, Medina, D.L., Valenza, M., Gennarino, V.A., Malta, C.D., Donaudy, F., Embrione, V., Polishchuk, R.S., et al. (2009). A Gene Network Regulating Lysosomal Biogenesis and Function. Science *325*, 473–477.

Sarkar, C., Chandra, G., Peng, S., Zhang, Z., Liu, A., and Mukherjee, A.B. (2013). Neuroprotection and lifespan extension in Ppt1(-/-) mice by NtBuHA: therapeutic implications for INCL. Nature Neuroscience *16*, 1608–1617.

Schmidt, D., and Löscher, W. (2005). Drug resistance in epilepsy: putative neurobiologic and clinical mechanisms. Epilepsia *46*, 858–877.

Scifo, E., Szwajda, A., Soliymani, R., Pezzini, F., Bianchi, M., Dapkunas, A., Dębski, J., Uusi-Rauva, K., Dadlez, M., Gingras, A.-C.C., et al. (2015). Proteomic analysis of the palmitoyl protein thioesterase 1 interactome in SH-SY5Y human neuroblastoma cells. Journal of Proteomics *123*, 42–53.

Segal-Salto, M., Hansson, K., Sapir, T., Kaplan, A., Levy, T., Schweizer, M., Frotscher, M., James, P., and Reiner, O. (2017). Proteomics insights into infantile neuronal ceroid lipofuscinosis (CLN1) point to the involvement of cilia pathology in the disease. Hum Mol Genet *26*, 1678–1678.

Settembre, C., Malta, C.D., Polito, V.A., Arencibia, M.G., Vetrini, F., Erdin, S., Erdin, S.U., Huynh, T., Medina, D., Colella, P., et al. (2011). TFEB Links Autophagy to Lysosomal Biogenesis. Science *332*, 1429–1433.

Sherman, S.M. (2016). Thalamus plays a central role in ongoing cortical functioning. Nat Neurosci *19*, 533–541.

Shyng, C., Nelvagal, H.R., Dearborn, J.T., Tyynelä, J., Schmidt, R.E., Sands, M.S., and Cooper, J.D. (2017). Synergistic effects of treating the spinal cord and brain in CLN1 disease. Proceedings of the National Academy of Sciences of the United States of America *114*, E5920–E5929.

Small, D.H. (2008). Network dysfunction in Alzheimer's disease: does synaptic scaling drive disease progression? Trends Mol Med *14*, 103–108.

Song, W., Wang, F., Savini, M., Ake, A., Ronza, A. di, Sardiello, M., and Segatori, L. (2013). TFEB regulates lysosomal proteostasis. Hum Mol Genet *22*, 1994–2009.

Spampanato, C., Feeney, E., Li, L., Cardone, M., Lim, J., Annunziata, F., Zare, H., Polishchuk, R., Puertollano, R., Parenti, G., et al. (2013). Transcription factor EB (TFEB) is a new therapeutic target for Pompe disease. Embo Mol Med *5*, 691–706.

Styr, B., and Slutsky, I. (2018). Imbalance between firing homeostasis and synaptic plasticity drives early-phase Alzheimer's disease. Nat Neurosci *21*, 463–473.

Suopanki, J., Partanen, S., Ezaki, J., Baumann, M., Kominami, E., and Tyynelä, J. (2000). Developmental Changes in the Expression of Neuronal Ceroid Lipofuscinoses-Linked Proteins. Mol Genet Metab *71*, 190–194.

Tikka, S., Monogioudi, E., Gotsopoulos, A., Soliymani, R., Pezzini, F., Scifo, E., Uusi-Rauva, K., Tyynelä, J., Baumann, M., Jalanko, A., et al. (2016). Proteomic Profiling in the Brain of CLN1 Disease Model Reveals Affected Functional Modules. Neuromolecular Medicine *18*, 109–133.

Tsunemi, T., Ashe, T.D., Morrison, B.E., Soriano, K.R., Au, J., Roque, R.A.V., Lazarowski, E.R., Damian, V.A., Masliah, E., and Spada, A.R.L. (2012). PGC-1α Rescues Huntington's Disease Proteotoxicity by Preventing Oxidative Stress and Promoting TFEB Function. Sci Transl Med *4*, 142ra97-142ra97.

Turrigiano, G.G. (1999). Homeostatic plasticity in neuronal networks: the more things change, the more they stay the same. Trends Neurosci *22*, 221–227.

Turrigiano, G.G. (2017). The dialectic of Hebb and homeostasis. Philosophical Transactions Royal Soc B Biological Sci *372*, 20160258.

Turrigiano, G.G., and Nelson, S.B. (2004). Homeostatic plasticity in the developing nervous system. Nature Reviews Neuroscience *5*.

Turrigiano, G., Leslie, K., Desai, N., Rutherford, L., and Nelson, S. (1998). Activity-dependent scaling of quantal amplitude in neocortical neurons. *391*.

Vartak, N., Papke, B., Grecco, H.E., Rossmannek, L., Waldmann, H., Hedberg, C., and Bastiaens, P.I. (2014). The autodepalmitoylating activity of APT maintains the spatial organization of palmitoylated membrane proteins. Biophysical Journal *106*, 93–105.

Virmani, T., Gupta, P., Liu, X., Kavalali, E.T., and Hofmann, S.L. (2005). Progressively reduced synaptic vesicle pool size in cultured neurons derived from neuronal ceroid lipofuscinosis-1 knockout mice. Neurobiology of Disease *20*.

Xiao, Q., Yan, P., Ma, X., Liu, H., Perez, R., Zhu, A., Gonzales, E., Burchett, J.M., Schuler, D.R., Cirrito, J.R., et al. (2014). Enhancing Astrocytic Lysosome Biogenesis Facilitates Aβ Clearance and Attenuates Amyloid Plaque Pathogenesis. J Neurosci *34*, 9607–9620.

Xiao, Q., Yan, P., Ma, X., Liu, H., Perez, R., Zhu, A., Gonzales, E., Tripoli, D.L., Czerniewski, L., Ballabio, A., et al. (2015). Neuronal-Targeted TFEB Accelerates Lysosomal Degradation of APP, Reducing Aβ Generation and Amyloid Plaque Pathogenesis. J Neurosci *35*, 12137–12151.

Yanai, A., Huang, K., Kang, R., Singaraja, R.R., Arstikaitis, P., Gan, L., Orban, P.C., Mullard, A., Cowan, C.M., Raymond, L.A., et al. (2006). Palmitoylation of huntingtin by HIP14 is essential for its trafficking and function. Nature Neuroscience *9*, 824–831.

Yang, Q., Zheng, F., Hu, Y., Yang, Y., Li, Y., Chen, G., Wang, W., He, M., Zhou, R., Ma, Y., et al. (2018). ZDHHC8 critically regulates seizure susceptibility in epilepsy. Cell Death & Disease *9*, 795.

Yashiro, K., and Philpot, B.D. (2008). Regulation of NMDA receptor subunit expression and its implications for LTD, LTP, and metaplasticity. Neuropharmacology *55*, 1081–1094.

Yoshii, A., Zhao, J.-P.P., Pandian, S., Zundert, B. van, and Constantine-Paton, M. (2013). A Myosin Va mutant mouse with disruptions in glutamate synaptic development and mature plasticity in visual cortex. The Journal of Neuroscience *33*.

Zaslavsky, K., Zhang, W.-B., McCready, F.P., Rodrigues, D.C., Deneault, E., Loo, C., Zhao, M., Ross, P.J., Hajjar, J.E., Romm, A., et al. (2019). SHANK2 mutations associated with autism spectrum disorder cause hyperconnectivity of human neurons. Nat Neurosci *22*, 556–564.

VITA

Name

Kevin Patrick Koster

Education

- PhD, Graduate Program in Neuroscience, University of Illinois at Chicago, Chicago, Illinois. GPA 3.81/4.0. 2015-2021
- B.S. Neuroscience, University of Illinois at Chicago, Chicago, Illinois. GPA: 3.54/4.0 2009-2014

Research Experience

- PhD Student/candidate, Dr. Akira Yoshii's Laboratory 2016-2021
- Research rotation student under Drs. Leon M Tai, Akira Yoshii, and Simon Alford 2015-2016
- Research Assistant/Research Associate, Dr. Mary Jo LaDu's Laboratory 2012–2015

Grants and Fellowships

- Dean's Scholar Fellowship, University of Illinois at Chicago (UIC) Graduate College 2020
- Provost's Award for Graduate Research, UIC Graduate College 2018
- Pre-doctoral Education for Clinical and Translational Scientists (PECTS) Fellowship 2018
- Chancellor's Undergraduate Research Award, UIC 2014

Awards and Honors

- Dr. Harry and Mildred R. Monsen Award for Excellence, UIC Department of Anatomy and Cell Biology (awarded to graduate academically distinguished students) 2019
- First place, graduate poster competition, UIC College of Medicine Research Forum 2019
- Third place, graduate poster competition, Chicago Society for Neuroscience 2018
- Second place, graduate poster competition, Graduate Program in Neuroscience Research day 2017
- Selected to represent the University of Illinois at Chicago for the inaugural *Posters Under the Dome Research Day* in Springfield, Illinois (ten students encompassing all disciplines were selected to present their research to state representatives) 2014
- Second place, undergraduate poster competition, Chicago Society for Neuroscience 2014
- First place, undergraduate poster competition, UIC Research Forum 2014

Publications

- **Koster, K. P.**, & Yoshii, A. (2019). Depalmitoylation by Palmitoyl-Protein Thioesterase 1 in Neuronal Health and Degeneration. *Frontiers in synaptic neuroscience*, 11, 25. https://doi.org/10.3389/fnsyn.2019.00025

- **Koster K. P.** (2019). AMPAR Palmitoylation Tunes Synaptic Strength: Implications for Synaptic Plasticity and Disease. *The Journal of neuroscience, 39*(26), 5040–5043. https://doi.org/10.1523/JNEUROSCI.0055-19.2019

- **Koster, K. P.**, Francesconi, W., Berton, F., Alahmadi, S., Srinivas, R., & Yoshii, A. (2019). Developmental NMDA receptor dysregulation in the infantile neuronal ceroid lipofuscinosis mouse model. *eLife*, *8*, e40316. https://doi.org/10.7554/eLife.40316

- Marottoli, F. M., Katsumata, Y., **Koster, K. P.**, Thomas, R., Fardo, D. W., & Tai, L. M. (2017). Peripheral Inflammation, Apolipoprotein E4, and Amyloid-β Interact to Induce Cognitive and Cerebrovascular Dysfunction. *ASN neuro*, *9*(4), 1759091417719201. https://doi.org/10.1177/1759091417719201

- Thomas, R., Diaz, K., **Koster, K. P.**, & Tai, L. M. (2017). In Vitro Assays to Assess Blood-brain Barrier Mesh-like Vessel Formation and Disruption. Journal of visualized experiments: JoVE, (124), 55846. https://doi.org/10.3791/55846

- **Koster, K. P.,** Thomas, R., Morris, A., & Tai, L. M. (2016). Epidermal growth factor prevents oligomeric amyloid-β induced angiogenesis deficits in vitro. *Journal of cerebral blood flow and metabolism, 36*(11), 1865–1871. https://doi.org/10.1177/0271678X16669956

- **Koster KP,** Smith C, Valencia-Olvera AC, Thatcher GR, Tai LM, LaDu MJ. Rexinoids as Therapeutics for Alzheimer's Disease: Role of APOE. *Curr Top Med Chem*. 2017;17(6):708-720. doi:10.2174/1568026616666160617090227

- Tai, L. M., Thomas, R., Marottoli, F. M., **Koster, K. P.**, Kanekiyo, T., Morris, A. W., & Bu, G. (2016). The role of APOE in cerebrovascular dysfunction. *Acta neuropathologica*, *131*(5), 709–723. https://doi.org/10.1007/s00401-016-1547-z

- Luo, J., Lee, S. H., VandeVrede, L., Qin, Z., Ben Aissa, M., Larson, J., Teich, A. F., Arancio, O., D'Souza, Y., Elharram, A., **Koster, K.**, Tai, L. M., LaDu, M. J., Bennett, B. M., & Thatcher, G. R. (2016). A multifunctional therapeutic approach to disease modification in multiple familial mouse models and a novel sporadic model of Alzheimer's disease. *Molecular neurodegeneration*, *11*, 35. https://doi.org/10.1186/s13024-016-0103-6

- Liu, D. S., Pan, X. D., Zhang, J., Shen, H., Collins, N. C., Cole, A. M., **Koster, K. P.**, Ben Aissa, M., Dai, X. M., Zhou, M., Tai, L. M., Zhu, Y. G., LaDu, M., & Chen, X. C. (2015). APOE4 enhances age-dependent decline in cognitive function by down-regulating an NMDA receptor pathway in EFAD-Tg mice. *Molecular neurodegeneration*, *10*, 7. https://doi.org/10.1186/s13024-015-0002-2

- Tai, L. M., Ghura, S., **Koster, K. P.**, Liakaite, V., Maienschein-Cline, M., Kanabar, P., Collins, N., Ben-Aissa, M., Lei, A. Z., Bahroos, N., Green, S. J., Hendrickson, B., Van Eldik, L. J., & LaDu, M. J. (2015). APOE-modulated Aβ-induced neuroinflammation in Alzheimer's disease: current landscape, novel data, and future perspective. *Journal of neurochemistry*, *133*(4), 465–488. https://doi.org/10.1111/jnc.13072

- Tai, L. M., **Koster, K. P.**, Luo, J., Lee, S. H., Wang, Y. T., Collins, N. C., Ben Aissa, M., Thatcher, G. R., & LaDu, M. J. (2014). Amyloid-β pathology and APOE genotype modulate retinoid X receptor agonist activity in vivo. *The Journal of biological chemistry*, *289*(44), 30538–30555.

https://doi.org/10.1074/jbc.M114.600833

Research Skills

- Stereotaxic viral injection, cranial window implantation, and two-photon microscopy in awake mice.
- *in utero* electroporation, intraocular injection.
- Primary neuron culture, transfection, and live-cell imaging with confocal microscopy.
- Familiarity with preparation of *ex vivo* slice for electrophysiology and limited experience obtaining electrophysiological recordings (whole-cell patch) in primary neuron culture and in visual cortical slices.
- Biochemical assays: labeling of protein palmitoylation sites, biotin-streptavidin protein isolation methods, synaptosomal enrichment, Western blotting.
- Immunofluorescence in cell culture and tissue, transcardial perfusion.
- Proficient with analytical and imaging processing software: Fiji, Zen, Imaris, Prism, restricted use of Matlab.
- Transgenic colony management, organizing and executing preclinical drug studies in mice.

Recent Presentations

- Koster, K. P., Francesconi, W., Berton, F.,Yoshii, A. Developmental NMDA receptor dysregulation in the infantile neuronal ceroid lipofuscinosis mouse model. 2019. *College of Medicine Research Forum, University of Illinois at Chicago*. Chicago, Illinois.
- Koster, K. P., Francesconi, W., Berton, F.,Yoshii, A. ***Selected talk***. Developmental Synapse Maturation is Impaired in a Mouse Model of Infantile Neuronal Ceroid Lipofuscinosis. 2018. *16th International Conference on Neuronal Ceroid Lipofuscinoses (Batten Disease)*. London, England.
- Koster, K. P., Francesconi, W., Berton, F.,Yoshii, A. Developmental Synapse Maturation is Impaired in a Mouse Model of Infantile Neuronal Ceroid Lipofuscinosis. 2018. *Chicago Society for Neuroscience Annual Meeting*, Chicago, Illinois.
- Koster, K. P., Francesconi, W., Berton, F.,Yoshii, A. Developmental Synapse Maturation is Impaired in a Mouse Model of Infantile Neuronal Ceroid Lipofuscinosis. 2018. *Brain Research Foundation Neuroscience Day*, Chicago, Illinois.
- Koster, K. P., Francesconi, W., Berton, F.,Yoshii, A. Investigating synaptic plasticity and the balance of protein palmitoylation-depalmitoylation in the pathogenesis of a pediatric neurodegenerative disorder. 2017. *Society for Neuroscience Annual Meeting,* Washington D.C.
- Koster, K. P., Yoshii, A. Defining Synaptic Pathology of Infantile Neuronal Ceroid Lipofuscinosis. 2017. *Brain Research Foundation Neuroscience Day*, Chicago, Illinois.
- Koster, K. P., Yoshii, A. Defining Synaptic Pathology of Infantile Neuronal Ceroid Lipofuscinosis. 2017. *Chicago Society for Neuroscience Annual Meeting*, Chicago, Illinois.
- Koster, K., Thomas R., Morris A., Marottoli F., L.M. Tai. Epidermal growth factor prevents amyloid-beta-induced angiogenesis deficits *in vitro* and prevents cognitive deficits *in vivo.* 2016. *Chicago Society for Neuroscience Annual Meeting*, Chicago, Illinois.
- Koster, K., York J., Ghura S., Collins N., Neumann F., Tai L.M., and M. LaDu. Novel, potent TLR4 antagonists attenuate oAβ-induced neuroinflammation in vitro. 2016. *Graduate Program in Neuroscience annual Neuroscience Day*, Chicago, Illinois.